

University of Alberta

Surface Modification from Aryl Diazonium Reduction

by

Aaron W. Skelhorne



A thesis submitted to the Faculty of Graduate Studies and Research in partial
fulfillment of the requirements for the degree of Doctor of Philosophy

Department of Chemistry

Edmonton, Alberta

Spring 2008



Library and
Archives Canada

Bibliothèque et
Archives Canada

Published Heritage
Branch

Direction du
Patrimoine de l'édition

395 Wellington Street
Ottawa ON K1A 0N4
Canada

395, rue Wellington
Ottawa ON K1A 0N4
Canada

Your file *Votre référence*
ISBN: 978-0-494-45600-2
Our file *Notre référence*
ISBN: 978-0-494-45600-2

NOTICE:

The author has granted a non-exclusive license allowing Library and Archives Canada to reproduce, publish, archive, preserve, conserve, communicate to the public by telecommunication or on the Internet, loan, distribute and sell theses worldwide, for commercial or non-commercial purposes, in microform, paper, electronic and/or any other formats.

The author retains copyright ownership and moral rights in this thesis. Neither the thesis nor substantial extracts from it may be printed or otherwise reproduced without the author's permission.

AVIS:

L'auteur a accordé une licence non exclusive permettant à la Bibliothèque et Archives Canada de reproduire, publier, archiver, sauvegarder, conserver, transmettre au public par télécommunication ou par l'Internet, prêter, distribuer et vendre des thèses partout dans le monde, à des fins commerciales ou autres, sur support microforme, papier, électronique et/ou autres formats.

L'auteur conserve la propriété du droit d'auteur et des droits moraux qui protègent cette thèse. Ni la thèse ni des extraits substantiels de celle-ci ne doivent être imprimés ou autrement reproduits sans son autorisation.

In compliance with the Canadian Privacy Act some supporting forms may have been removed from this thesis.

Conformément à la loi canadienne sur la protection de la vie privée, quelques formulaires secondaires ont été enlevés de cette thèse.

While these forms may be included in the document page count, their removal does not represent any loss of content from the thesis.

Bien que ces formulaires aient inclus dans la pagination, il n'y aura aucun contenu manquant.


Canada

Abstract

The modification of material's surface is a convenient method to change the interfacial behaviour of a material while maintaining the desirable bulk properties. This field of research spans multiple disciplines including science, engineering and medicine.

This thesis will characterize a newer carbon film material prepared from electron beam evaporation of carbon onto a silicon support. These carbon films are extremely flat having nominal roughness of less than 1 nm, they are also robust and compatible with well-established diazonium chemistry modification schemes. An extensive characterization of as-prepared and diazonium-modified surfaces is discussed and encompasses electrochemical methods, scanning force microscopy, X-ray photoelectron spectroscopy, Raman spectroscopy, and infrared spectroscopy. The potential uses of modified films in such areas as molecular electronics and as a model bioimplant material are also discussed. The electron transport properties of the created films are reported. Additionally, the electron transport dependence on the contact force with the external circuit, a conductive atomic force microscope tip, is also discussed. A novel method to tether biomolecules, such as heparin, to a carbon surface is presented along with preliminary interactions with a heparin-binding protein, fibronectin.

Furthermore, the electrochemical and spontaneous diazonium modification of platinum is also discussed with emphasis on the effect on a platinum counter electrode during a typical electrochemical diazonium reduction. The resulting diazonium-modified platinum surfaces showed unique electrochemical behaviour.

Table of Contents

Chapter I: Introduction

1	General Introduction	1
2	Carbon Electrodes	5
3	Atomic Force Microscopy	11
4	Conductive Atomic Force Microscopy	19
5	Cyclic Voltammetry	21
6	Infrared Spectroscopy	26
7	Intention	28

Chapter II: Characterization of Ultra-flat Carbon

1	Introduction	36
2	Experimental	38
3	Results and Discussion	41
3.1	Topography	41
3.2	Electrical Characterization	44
3.3	Electrochemical Properties	55
3.4	Elemental and Chemical Analysis	75
4	Conclusions	79

Chapter III: Attachment of Aryl Molecules to Ultra-flat Carbon

1	Introduction	82
2	Experimental	86
3	Results and Discussion	90
3.1	Electrochemical Deposition of Aryl Molecules	90
3.2	Elemental and Chemical Analysis	97
3.3	Measurement of Film Thicknesses	107
3.4	Electrical Characterization	112
4	Conclusions	122

Chapter IV: Attachment of Aryl Molecules to Platinum

1	Introduction	127
2	Experimental	130
3	Results and Discussion	133
3.1	Topography and Electrochemistry of Bare Platinum Substrates	133
3.2	Electrochemical Reduction of Fast Black K	139
3.3	Spontaneous Attachment of Fast Black K	147
3.4	Electrochemical behaviour of Diazonium Modified Platinum	159
4	Conclusions	173

Chapter V: Conjugation of Anticoagulants to Carbon Surfaces

1	Introduction	180
2	Experimental	184
3	Results and Discussion	187
3.1	Electrochemical Deposition of Aryl Molecules	187
3.2	Interaction of Surface Bound Heparin with Fibronectin	199
4	Conclusions	205

Chapter VI: Conclusions

1	Overall Conclusions	208
2	Future Work	209

Chapter VII: Appendix

1	Appendix	212
---	----------	-----

List of Tables

2.01	Root-mean-square roughness of 50 nm thick non-pyrolyzed carbon films.	42
2.02	ΔE_p of dopamine on EB50 in 0.1 M H ₂ SO ₄ .	63
2.03	Summarized electrochemical data for Eu ^{3+/2+} on EB50.	66
2.04	Summarized electrochemical data for ferrocene on EB50.	68
2.05	Summarized electrochemical data for Ru(NH ₃) ₆ ^{3+/2+} on EB50.	70
2.06	Summarized electrochemical data for Fe(CN) ₆ ^{3-/4-} on EB50.	72
2.07	Heterogeneous electron-transfer rate constants of studied redox systems on EB50 and similar materials.	74
2.08	X-Ray Photoelectron Spectroscopy of 50 nm thick electron beam evaporated carbon.	75
3.01	Reduction potential of diazonium precursors.	95
3.02	XPS data of Fast Black K modified EB50.	102
3.03	XPS data of p-nitrobenzene modified EB50.	102
3.04	Elemental theoretical mass percent of Fast Black K and p-nitrobenzene, omitting the mass contribution from hydrogen	103
3.05	Film thicknesses.	110
3.06	Feature shift in force-distance-current plots for studied films	113
4.01	ΔE_p of Fe(CN) ₆ ^{3-/4-} on platinum.	137
4.02	Infrared Reflection Absorbance Spectroscopy peak assignments for electrochemically immobilized Fast Black K	140

4.03	Infrared Reflection Absorbance Spectroscopy peak assignments for spontaneously attached Fast Black K and 1-dodecanethiol.	151
4.04	Infrared Reflection Absorbance Spectroscopy peak assignments for spontaneously attached Fast Black K and 1-dodecanethiol displaced.	153
4.05	ΔE_p of hydrogen on platinum.	161
4.06	ΔE_p of hydrogen on FBK modified platinum.	163
4.07	ΔE_p of $\text{Fe}(\text{CN})_6^{3-/4-}$ on various platinum based electrodes.	169
4.08	FBK peak changes after hydrogen evolution.	171
5.01	Infrared peak assignments for powdered heparin.	193
5.02	Infrared peak assignments for heparin bound to gold.	195
5.03	Infrared peak assignments for heparin bound to glassy carbon.	197
7.01	Noise of RMS roughness measurements of Nanoman Atomic Force Microscope.	212
7.02	Noise of RMS roughness measurements of Multimode Atomic Force Microscope, "E" scanner.	212

List of Figures

1.01	Schematic illustration of the crystal structure of graphite.	7
1.02	Schematic representation of the structure of A) Highly oriented pyrolytic graphite (HOPG) and B) Glassy Carbon (GC).	8
1.03	Electrochemical reduction and subsequent attachment of aryl diazonium.	11
1.04	Schematic representation of the basic principles of a sample-scanning Atomic Force Microscope.	13
1.05	Contact mode AFM.	15
1.06	Feedback in intermittent contact AFM.	17
1.07	Intermittent contact mode AFM.	18
1.08	Schematic of C-AFM.	20
1.09	Potential program for cyclic voltammetry.	21
1.10	Typical cyclic voltammogram with essential features labeled.	22
1.11	The six modes of IR.	27
2.01	Atomic force microscopy image of 50 nm thick electron beam deposited carbon film.	43
2.02	Scanning electron micrograph of a typical DNP atomic force microscope probe coated in-house with 30 nm chromium followed by 300 nm of gold.	45
2.03	Force-distance and distance-current curves of EB50 100 mV potential.	46

2.04	Atomic force microscopy images of 50 nm thick electron beam evaporated carbon film.	49
2.05	Atomic force microscopy images of 50 nm thick pyrolyzed electron beam evaporated carbon films.	50
2.06	Atomic force microscopy images of highly doped, <100> oriented, prime silicon.	53
2.07	IV curves of EB50 measured with C-AFM at a tip-sample contact force of 28 nN.	54
2.08	Cyclic voltammetry of $\text{Fe}(\text{CN})_6^{3-/4-}$ on EB50.	57
2.09	Cyclic voltammetry of $\text{Fe}(\text{CN})_6^{3-/4-}$ on EB50.	58
2.10	Cyclic voltammetry of $\text{Fe}(\text{CN})_6^{3-/4-}$ on EB50.	59
2.11	Cyclic voltammetry of $\text{Fe}(\text{CN})_6^{3-/4-}$ on EB50.	60
2.12	ΔE_p and current for CV's of $\text{Fe}(\text{CN})_6^{3-/4-}$.	61
2.13	Cyclic voltammetry of dopamine on EB50.	64
2.14	Cyclic voltammetry of $\text{Eu}^{3+/2+}$ on EB50.	67
2.15	Cyclic voltammetry of ferrocene on EB50.	69
2.16	Cyclic voltammetry of $\text{Ru}(\text{NH}_3)_6^{3+/2+}$ on EB50.	71
2.17	Cyclic voltammetry of $\text{Fe}(\text{CN})_6^{3-/4-}$ on EB50.	73
2.18	X-ray Photoelectron Spectroscopy of 50 nm thick electron beam evaporated carbon film	76
2.19	Raman spectrum of unmodified 50 nm thick electron beam evaporated carbon	78
3.01	Schematic illustration of the formation of aryl diazonium	84

	derived multilayers	
3.02	Cyclic voltammogram for the electrochemical attachment of Fast Black K to EB50.	91
3.03	Cyclic voltammogram for the electrochemical attachment of Biphenyl to EB50.	93
3.04	Cyclic voltammograms for the electrochemical attachment of p-nitrobenzene (solid) and phenyl acetic acid (dashed) to EB50.	94
3.05	Cyclic voltammograms for the blocking of dopamine in 0.1 M H ₂ SO ₄ for modified EB50.	96
3.06	Purposed final attachment configuration of diazonium derived layers as presented by Bélanger.	100
3.07	Survey XPS of Fast Black K and p-nitrobenzene modified EB50.	104
3.08	High resolution XPS of Fast Black K on EB50.	105
3.09	High resolution XPS of p-nitrobenzene on EB50.	106
3.10	Electrochemical deposition onto a photo patterned surface.	108
3.11	Tapping mode AFM measurement of film thickness.	109
3.12	Cyclic voltammogram for the electrochemical attachment of Fast Black K to photolithographic patterned EB50.	111
3.13	Force vs distance curves for Fast Black K at 0.500 V and resulting current	114
3.14	Force vs distance curves for Fast Black K at 1.000 V and	115

	resulting current.	
3.15	Force vs distance curves for p-nitrobenzene at 0.500 V and resulting current.	116
3.16	Force vs distance curves for p-nitrobenzene at 1.000 V and resulting current.	117
3.17	Current-voltage curve of Fast Black K modified EB50.	119
3.18	Current-voltage curve of p-nitrobenzene modified EB50.	120
3.19	Current-voltage curves of Fast Black K modified EB50, p-nitrobenzene modified EB50 and bare EB50.	121
4.01	Atomic force microscopy image of unmodified glass supported platinum, 25 μm^2 image size.	134
4.02	Atomic force microscopy image of unmodified glass supported platinum, 6.25 μm^2 image size.	135
4.03	Cyclic voltammetry of $\text{Fe}(\text{CN})_6^{3-/4-}$ on glass-slide platinum.	138
4.04	Cyclic voltammogram for the electrochemical reduction of Fast Black K on a platinum electrode.	142
4.05	Infrared reflection absorbance spectroscopy spectra of Fast Black K electrochemically deposited on platinum.	143
4.06	Infrared reflection absorbance spectroscopy spectra of Fast Black K electrochemically deposited on platinum.	144
4.07	Atomic force microscopy image of Fast Black K modified glass supported platinum, 25 μm^2 image size.	145
4.08	Atomic force microscopy image of Fast Black K modified	146

	glass supported platinum.	
4.09	Infrared reflection absorbance spectroscopy spectra of Fast Black K self-assembled on platinum, fingerprint region.	148
4.10	Infrared reflection absorbance spectroscopy spectra of Fast Black K self-assembled on platinum.	149
4.11	Infrared reflection absorbance spectroscopy spectra of A) 1-dodecanethiol and B) Fast Black K self-assembled on platinum.	152
4.12	Infrared reflection absorbance spectroscopy spectra of A) 1-dodecanethiol displaced by Fast Black K and B) Fast Black K displaced by 1-dodecanethiol.	157
4.13	Infrared reflection absorbance spectroscopy spectra of Fast Black K on a platinum working electrode and counter electrode after an electrochemical reduction of Fast Black K.	158
4.14	Cyclic voltammograms for the evolution of hydrogen on glass-slide platinum electrode.	160
4.15	Cyclic voltammograms for the evolution of hydrogen on FBK modified glass-slide platinum electrode.	162
4.16	Cyclic voltammograms for the evolution of hydrogen on FBK modified glass-slide platinum electrode and bare glass-slide platinum electrode at 0.100 V/s.	164
4.17	Cyclic voltammogram for platinum electrode scanned in blank.	166

4.18	Cyclic voltammetry of $\text{Fe}(\text{CN})_6^{3-/4-}$ on FBK modified glass-slide platinum.	167
4.19	Cyclic voltammetry of $\text{Fe}(\text{CN})_6^{3-/4-}$ on FBK modified glass-slide platinum after hydrogen evolution.	168
4.20	Infrared reflection absorbance spectroscopy spectra of Fast Black K on platinum	172
5.01	Structure of heparin, repeating dimer unit	182
5.02	Immobilization of heparin on glassy carbon.	183
5.03	Cyclic voltammogram for the electrochemical attachment of p-phenyl acetic acid to glassy carbon.	189
5.04	Cyclic voltammogram for the electrochemical attachment of p-nitrobenzene to glassy carbon.	190
5.05	Electrochemical reduction of surface nitro group to amine.	191
5.06	Infrared spectrum of powdered heparin.	194
5.07	Infrared reflection absorption spectrum of heparin on gold.	196
5.08	Infrared reflection absorption spectrum of heparin on glassy carbon	198
5.09	Laser Scanning Confocal Image of FITC labeled fibronectin and bovine serum albumin with heparin immobilized on carboxylic acid terminated diazonium with a 1,6-hexane diamine linker.	201
5.10	Laser Scanning Confocal Image of FITC labeled fibronectin and bovine serum albumin with heparin immobilized on	202

	amine terminated diazonium.	
5.11	Surface plasmon resonance image, and corresponding cross section, of the interactions of bovine serum albumin and human fibronectin with a heparin modified gold SPR sensor.	204
6.01	Nanogap fabricated from pyrolyzed electron beam lithography.	211
7.01	Power spectrum density of Nanoman noise at normal feedback.	214
7.02	Power spectrum density of Nanoman noise at low feedback	215
7.03	Scanning electron micrograph of a typical DNP atomic force microscope probe coated in-house with 30 nm chromium followed by 300 nm of gold.	216
7.04	Cyclic voltammograms for electrochemical attachment of variamine blue RT to EB50.	217
7.05	Cyclic voltammograms for the blocking of dopamine by Variamine Blue RT on EB50.	218
7.06	Infrared spectrum of powdered Fast Black K	219
7.07	Infrared spectrum of Fast Black K displaced by 1-dodecane thiol	220

List of Symbols

α	Transfer coefficient
Å	Ångström
C_O	Concentration of oxidized species
C_R	Concentration of reduced species
D_O	Diffusion coefficient of the oxidized species
D_R	Diffusion coefficient of the reduced species
ΔE_p	Peak separation potential
$\Delta E_{p,corr}$	Corrected peak separation potential
$\Delta E_{p,obs}$	Observed peak separation potential
E	Potential of the electrode
E^0	Standard potential of the electrode
E_p	Peak potential
$E_{p/2}$	Half-peak potential
$E_{p,a}$	Anodic peak potential
$E_{p,c}$	Cathodic peak potential
E_λ	Switching potential
eV	Electron volt
F	Faraday constant
G	Siemen
I	Current
i_p	Peak current
$i_{p,a}$	Anodic peak current

$i_{p,c}$	Cathodic peak current
k°	Heterogeneous electron transfer rate constant
L_a	Intraplanar distance
L_c	Interplanar distance
N	Number of atoms in a molecule or functional group
n	number of electrons
R	Resistance
R_g	Universal gas constant
r^2	Correlation coefficient
T	Temperature
V	Volt
ψ	Kinetic parameter
v	Scan rate
\square	Sheet resistance
Ω	Ohm

List of Abbreviations

ACSES	Alberta Centre for Surface Engineering and Science
AFM	Atomic force microscope
BE	Binding energy
BP	Biphenyl
BSA	Bovine serum albumin
C-AFM	Conductive atomic force microscope
CP-AFM	Conducting probe atomic force microscope, interchangeable with C-AFM
CPS	Counts per second
CV	Cyclic voltammetry
EB	Electron beam
EB50	Electron beam evaporated carbon film, nominal thickness of 50 nm
EDC	1-Ethyl-3-(3-dimethylaminopropyl) carbodiimide hydrochloride
FBK	Fast Black K
FITC	Fluorescein isothiocyanate
Fn	Fibronectin
FWHM	Full width at half maximum
GC	Glassy Carbon
HOPG	Highly oriented pyrolytic graphite
IV	Current-voltage
IR	Infrared
IRRAS	Infrared reflection absorption spectroscopy

LTIC	Low temperature isotropic carbon
PDMS	Polydimethylsiloxane
PPF	Pyrolyzed photoresist film
RMS	Root mean square
RPM	Revolutions per minute
RSD	Relative standard deviation
RSF	Relative sensitivity factor
PBS	Phosphate buffered saline
SD	Standard deviation
SEM	Scanning Electron microscope
SFM	Scanning force microscope, interchangeable with AFM
SPM	Scanning probe microscope
SPR	Surface plasmon resonance
STM	Scanning tunneling microscope
TOF-SIMS	Time of flight secondary ion mass spectrometry
XPS	X-ray photoelectron spectroscopy

Chapter I

Introduction

1 General Introduction

The modification of material's surface is a convenient method to change the interfacial behaviour of a material while maintaining the desirable bulk properties. This area of research spans multiple disciplines including science, engineering and medical fields. Current searches of literature databases such as the ISI Web of Science¹ for the keywords "surface" and "modification" returns over 29 000 results. This huge genre encompasses such topics as textiles,^{2, 3} electronics,^{4, 5} sensors,^{6, 7} biocompatibility,^{8, 9} separations,^{10, 11} materials,^{12, 13} and chemical and wear resistance.¹⁴⁻¹⁶ Despite the vast differences in applications, the quintessential goal is to develop reproducible and well-defined modification schemes. Once a method is developed, it can be tailored to impart a plethora of chemical moieties onto the interface. The combinations and permutations of bulk properties and interfacial properties are nearly limitless. Materials that are hydrophobic can be prepared with a hydrophilic interface; bio-implants that would be traditionally be rejected by the human immune system can be made compatible. With modern knowledge of chemical principles and rational design, one can create an interface to perform any reasonable function.

One of the newer, and relevant to this thesis, applications of the knowledge generated by the preceding years of surface modification research is in molecular electronic devices. As the components of electronic devices, such as transistors,

become smaller and smaller, fabrication processes approach a fundamental limit, namely the size of an individual molecule or atom. The often referred to example for this trend is the transistor size of microprocessors. In 1982 Intel introduced a new microprocessor, the 80286 or 286, which ushered in a new era for personal computers and made IBM compatible computers available in mass quantities. These 1982 state of the art microprocessors had fabricated features as small as 1.5 μm . Recently Intel announced a new line of microprocessors with features as small as 45 nm¹⁷ with 65 nm feature processors in mass production. As we are surely approaching the size limit of fabricated devices using traditional techniques, radical new design methods are being created. One such design goal is to use molecules, single molecules or ensembles, as discrete devices in electrical devices. The term “Molecular Electronics” has been around since at least 1961 when Herwald published a short communication aptly named “Molecular Electronics.”¹⁸ This early version of molecular electronics would later become what we now refer to as solid-state electronics. It wasn’t until 1974 that the first computational studies indicated that a single molecule could successfully be used as an electronic device were performed.^{19,}
²⁰ In this publication Ratner and Aviram presented computational arguments that a single molecule could behave as a rectifier.

The newly formed field of molecular electronics received little attention until recently. This interest was indubitably influenced by the impending fundamental device size limitation as discussed above as well as the proliferation of instrumentation capable of analyzing and interacting with devices on the atomic scale, such as the atomic force microscope (AFM) invented in 1986 and the scanning

tunneling microscope (STM) invented in 1981. Both of these nanotools are now commonplace in many laboratories.

The first series of experiments related to molecular electronics was performed with STMs by a team with IBM.²¹⁻²³ In this work Crommie and coworkers manipulated 48 individual iron atoms to create a circular quantum corral with a radius of 71.3 Å. They were also able to use the STM to visualize the standing-wave patterns of electrons in a Cu(111) surface. Scanning tunneling microscopy continued to be the experiment method of choice for a number of years. In 1995 Chavy and coworkers used the STM to probe the electrical characteristics of a single C₆₀ molecule.²⁴ Chavy investigated the current flowing through the C₆₀ molecule as the tip distance was varied and determined the resistance, at point of contact, to be 54.80 MΩ. The technique of STM was put to further use by Reifenberger.^{25, 26} Dithiol monolayers on a gold surface were created. Gold clusters were introduced to the surface and were bound to the exposed surface thiol. The gold clusters were located with the imaging feature of the STM and once found, current-voltage curves were performed. By fitting the experimental data to a model, Reifenberger and coworkers were able to estimate the electrical resistance of a single dithiol molecule. With the recent adaptation of STM as a popular choice for molecular scale electric measurements, Weiss and Tour developed rationally designed candidates for molecular wires. The earliest of their candidates was a highly conjugated thiolacetate, 4,4'-di(phenylene-ethynylene)benzenethioacetate.²⁷ These candidates were randomly dispersed in a normal alkyl chain thiol monolayer. After locating the molecules of interest in imaging mode, they were probed to assess their electrical

properties. The embedded molecular wires showed very high conductivity when compared to the surrounding alkanethiol matrix.

Analogous to how atomic force microscope was invented shortly after the scanning force microscope, conductive atomic force microscopy (C-AFM) followed STM as a method to probe nano-scale electrical properties. For a more detailed discussion on the technique of C-AFM see section 1.3. Conductive atomic force microscopy has been shown to be a viable tool for measurement of nano-scale electrical properties. Frisbie has used C-AFM to measure the electrical response of a variety of self-assembled thiol monolayers on gold.²⁸⁻³⁰ Frisbie was able to detect and measure single molecules and report electrical features such as current-voltage response and resistance.

Although the measurement of a single molecule is an elegant method and is easily compared to single molecule computational calculations, it is arguable that the immediate future of molecular electronics relies on ensembles of molecules as opposed to single molecules. There is a substantial amount of research in which molecular films are sandwiched between two electrodes. The top and bottom electrodes serve as the contact between the molecular films and the rest of the system. The work in this area most relevant to this thesis is that of McCreery.³¹⁻⁴² McCreery developed an ultra-flat carbon surface by pyrolyzation of commercial photoresists.^{41,}
⁴² These new, ultra-flat carbon surfaces served as a platform to create molecular junctions when coupled with a top contact.⁴⁰ In this case the top contact was created using a mercury drop^{37, 39} or evaporated titanium/gold.³⁴ Initial results were promising, with stable and repeatable current-voltage curves. The most significant of

the results was the observed hysteresis and rectification in the current-voltage cycle. As the molecular junctions were scanned in one direction, the reverse scan showed a significant difference in measured current at a particular voltage. This hysteresis is the beginning of a logic gate, with it being able to be turned “on” and “off” at the potential limits, and the state being read at a lesser potential. Rectification can similarly be exploited for such uses as a diode. Despite the promising behaviour of these fabricated junctions, McCreery later reported that the observed behaviour was heavily influenced by the presence of oxygen and the subsequent formation of a metal oxide layer.³¹ Molecular junctions were prepared identically to those described above, except the top contact was changed from copper to titanium. The resulting copper topped junctions proved to be insensitive to trace oxygen and the current voltage curves were symmetrical and showed no hysteresis.

2 Carbon Electrodes

Carbon electrodes are consistently used in electrochemical applications such as electroanalysis, electrosynthesis, and energy conversion.^{43, 44} Of the many available forms of carbon, sp^2 hybridized graphitic carbon is the ubiquitous choice for electrode material, although sp^3 hybridized diamond carbon has recently gained popularity as an electrode material.⁴⁵⁻⁵⁴ Graphitic carbon is widely used due to the inherent low cost, relatively large potential window, compatibility with a wide range of solvents and electrolytes, and excellent mechanical stability. These factors make carbon a viable, and often preferred, alternative to metals for many electrochemical

applications. Graphitic carbon can be acquired in a variety of forms, with all of them being electrochemically active. Common forms include glassy carbon (GC), low temperature isotropic carbon (LTIC), highly oriented pyrolytic graphite (HOPG), and carbon black. Somewhat lesser known, but discussed in this thesis, are thin carbon films created from electron beam evaporation or pyrolyzation of polymers. All forms of graphitic carbon share the same basic structure; each sp^2 carbon atom is covalently bound to three other carbon atoms to form a two dimensional network of carbon atoms. These two dimensional carbon networks are known as graphene. Graphite consists of alternating, offset, layers of graphene sheets in an AB, AB pattern, such that, every second sheet lines up, forming a three dimensional structure. A schematic illustration of the basic crystal structure of carbon is presented in figure 1.01. The individual sheets are held together by relatively weak Van der Waals forces when compared to the covalent bonds between carbon atoms of the same sheet. The relative interaction forces are echoed in the atom spacing; 3.4 Å carbon-carbon spacing for intrasheet^{55, 56} whereas the intersheet carbon-carbon spacing is only 1.42 Å.⁵⁶ Single crystal graphite is anisotropic. Due to the delocalization of the π -electrons, single crystal graphite is good conductor of electricity along the graphene planes but is a poor conductor of electricity between the planes.

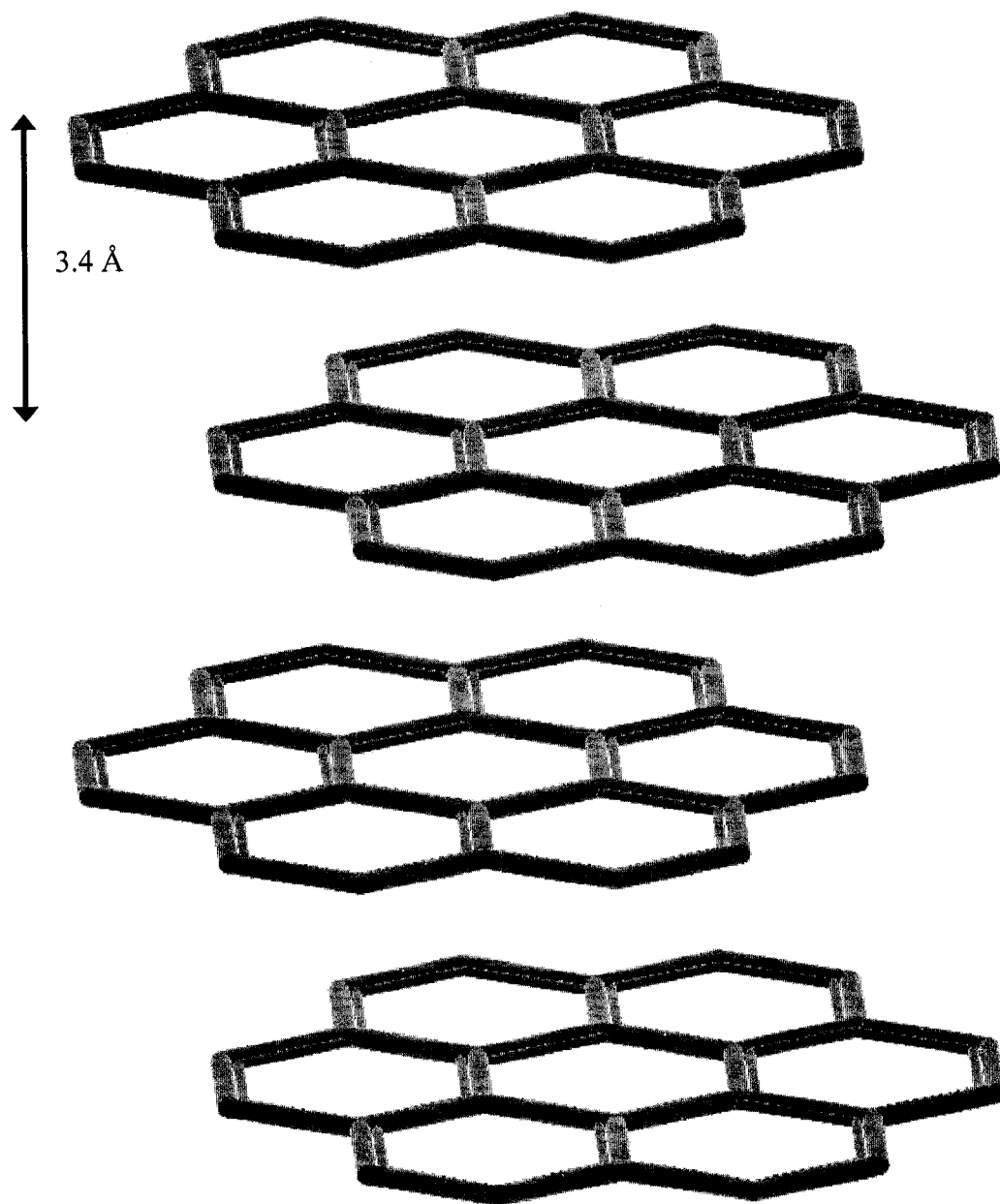


Figure 1.01. Schematic illustration of the crystal structure of graphite.

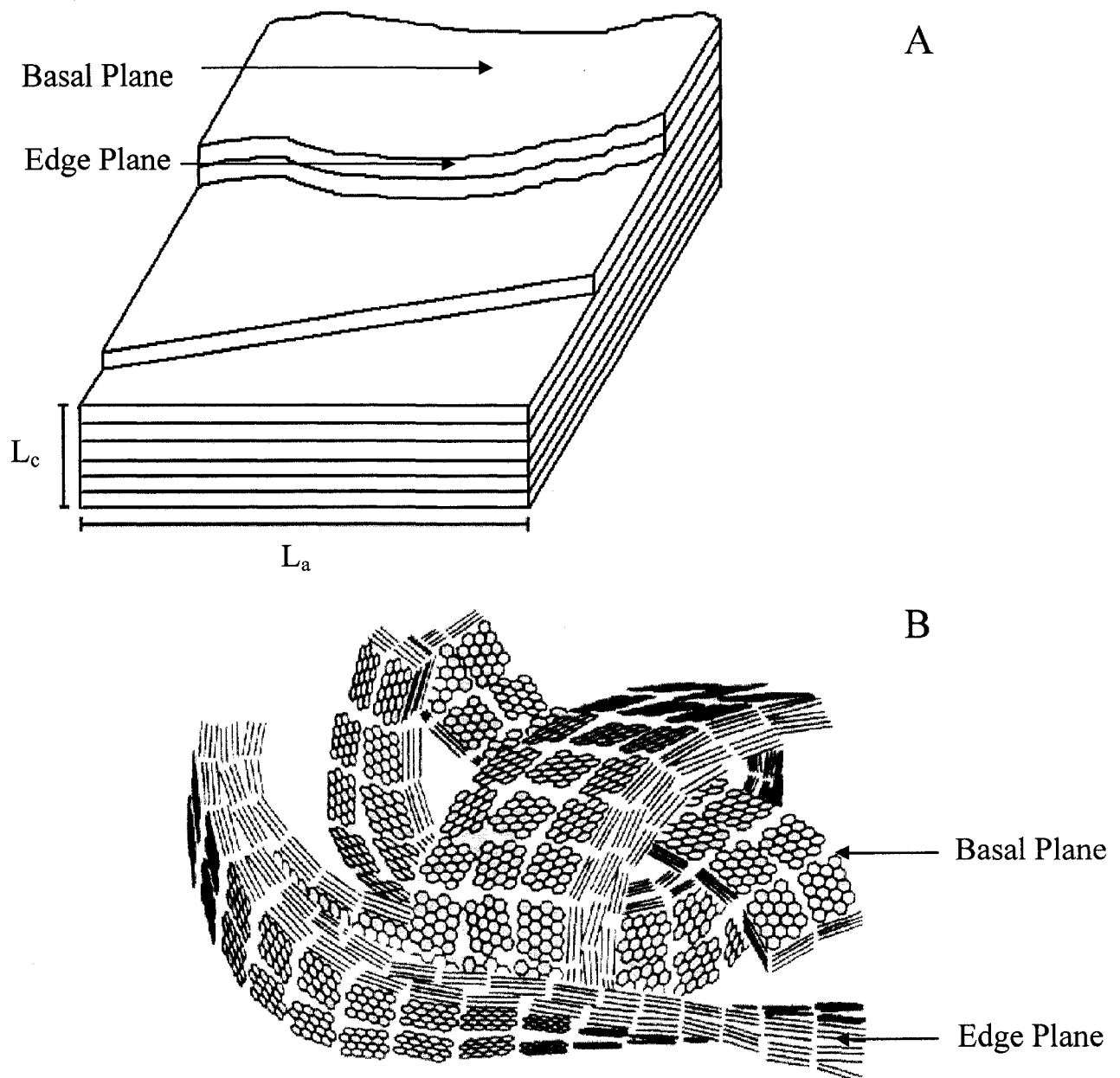


Figure 1.02. Schematic representation of the structure of A) Highly oriented pyrolytic graphite (HOPG) and B) Glassy Carbon (GC).

Although all forms of graphitic carbon share the same basic structure, the physical and electrical properties vary dramatically. The differences observed in various graphitic carbon substrates are due to the differences in the size and orientation of graphitic crystallites.⁴⁴ The microcrystallite size of graphite is defined by two parameters; the width of the microcrystallite, L_a , also known as the intraplanar distance and the thickness of the microcrystallite, L_c , also known as the interplanar distance. Figure 1.02A illustrates both L_a and L_c on HOPG. Apart from defects, highly oriented pyrolytic graphite, as illustrated in figure 1.02A, maintains the basic crystal structure, shown in figure 1.01, over very long ranges. Overall, HOPG makes for a poor electrode in terms of electroanalytical chemistry. The advantage in using HOPG is that one is able to selectively probe the basal or edge planes. These separate planes represent an ideal surface and have attracted a plethora of researchers.^{54, 57-61} The most commonly used carbon material for electrodes is likely GC. Glassy carbon is named due to its fracture characteristics; when stressed it shatters similar to glass. Glassy Carbon was first reported in 1962 by employees of Tokai Electrode Manufacturing Plant when Yamada and Sato provided a detailed list of the physical properties of a then-new type of carbon; glassy carbon.⁶² Due to corporate concerns, no manufacturing details about the starting materials or the carbonization process were provided with the initial. In 1970 the preparation of glassy carbon was independently reproduced by Jenkins and Kawamura⁶³ via the pyrolysis of a phenolic resin under pressure. In the following year they also reported the structure as determined by X-ray diffraction and electron microscopy.⁶⁴ They reported the structure as a long, narrow ribbon of cross-linked aromatic molecules that are highly

tangled and randomly oriented. The random orientation of the graphite ribbons imparts the isotropic behaviour of bulk glassy carbon when the individual subunits are entirely anisotropic. A schematic illustration of the structure of GC is presented in figure 1.02B.

Carbon is a widely used and universally accepted electrode material, however the desire to alter and adjust the surface chemistry for specific tasks is a widespread area of research.^{65, 66} Modification of carbon surfaces has historically been performed via reaction with the native oxide layer.⁶⁷⁻⁷⁰ Carbon surfaces exposed to ambient conditions undergo spontaneous oxidation to form an excess of oxygen containing moieties on the surface. These oxygen containing functional groups are susceptible to traditional chemical methods and provided a means by which to tailor the carbon surface. This thesis will discuss a relatively new reductive method for the modification of surfaces, such as carbon, introduced by Savéant in 1992.⁷¹ This new method involves the electrochemical reduction of an aryl diazonium to form a highly reactive intermediate that readily attaches to carbon surfaces. The initial reports identified the reactive intermediate as an aryl radical. The reported films were described as quite robust and durable. Due to the facile nature of film preparation, the resilience of the created layers, and the relatively simple synthesis^{72, 73} the use of aryl diazoniums was the exclusive method of initial carbon derivatization in this thesis. The general structure and use of aryl diazoniums in surface modification is illustrated in figure 1.03.

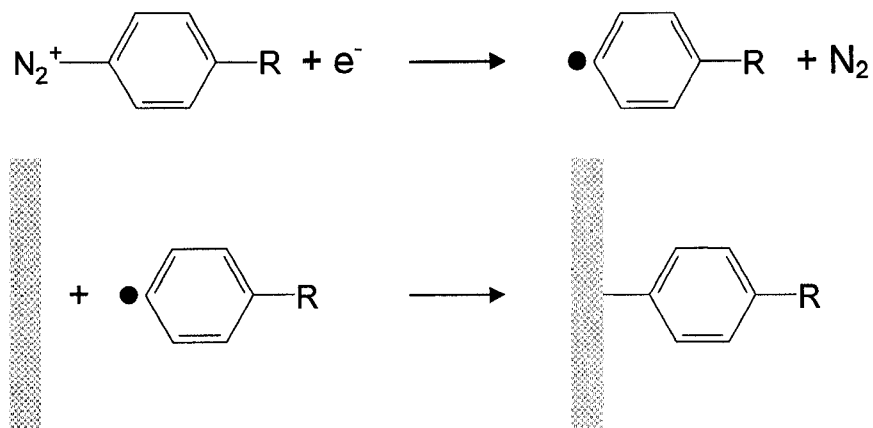


Figure 1.03. Electrochemical reduction and subsequent attachment of aryl diazonium.

3 Atomic Force Microscopy

Atomic force microscopy (AFM), also known as scanning force microscopy (SFM), is a variety of scanning probe microscopy (SPM) originally designed as high-resolution surface mapping technique. The heart of the atomic force microscope is the cantilever and tip. The length of the cantilever is in the range of hundreds of micrometers while the tip provides the entirety of the interactions between the sample being probed and the microscope. Probes typically consist of micro fabricated silicon or silicon nitride. Cantilever tip shapes and sizes are quite varied; tip radii of curvatures may be as low as a few nanometers. Mapping of the surface occurs by monitoring the movement of the tip as it traces the surface. The movement is tracked by reflecting an optical beam, typically from a diode laser, off the back of the cantilever and onto a position sensitive detector. With specialized equipment, modern atomic force microscopes are capable of scanning in a plethora of

environments. Possible scanning environments include, but are not limited to, acidic and caustic aqueous solutions, organic solvents, ambient air and ultra-high vacuum.

All AFM techniques rely on the interactions between the tip and the sample being investigated. A variety of forces contribute to the deflection of the attached cantilever and therefore the generated image. The force most commonly associated with the tip-sample interactions is the interatomic force known as Van der Waals. When the tip is located far from the surface, tens to hundreds of angstroms (\AA), the experienced forces are attractive. A tip located at this distance enables one to perform a variety of non-contact AFM measurements. When the tip is brought sufficiently close to the surface, a few angstroms or less, the net forces are repulsive and the tip is considered to be in contact with the surface. A typical sample-scanning AFM is illustrated in figure 1.04.

3.1 Contact Mode

The first, and conceptually most simple, method of imaging with an atomic force microscope is contact mode. In this method the tip is scanned laterally across the sample in a raster pattern and the deflection of the cantilever is recorded. Typical contact mode imaging employs the use of feedback to maintain a near constant load on the surface. The four-quadrant position sensitive detector records the deflection of the cantilever. The feedback loop adjusts the voltage of the Z piezo, thereby adjusting the vertical position of the sample to maintain the set cantilever deflection, and therefore a constant force. Topographical maps are created by mapping the distance calibrated Z piezo voltage versus the X-Y position. In contact mode with feedback turned on, the cantilever deflection is also known as the “error

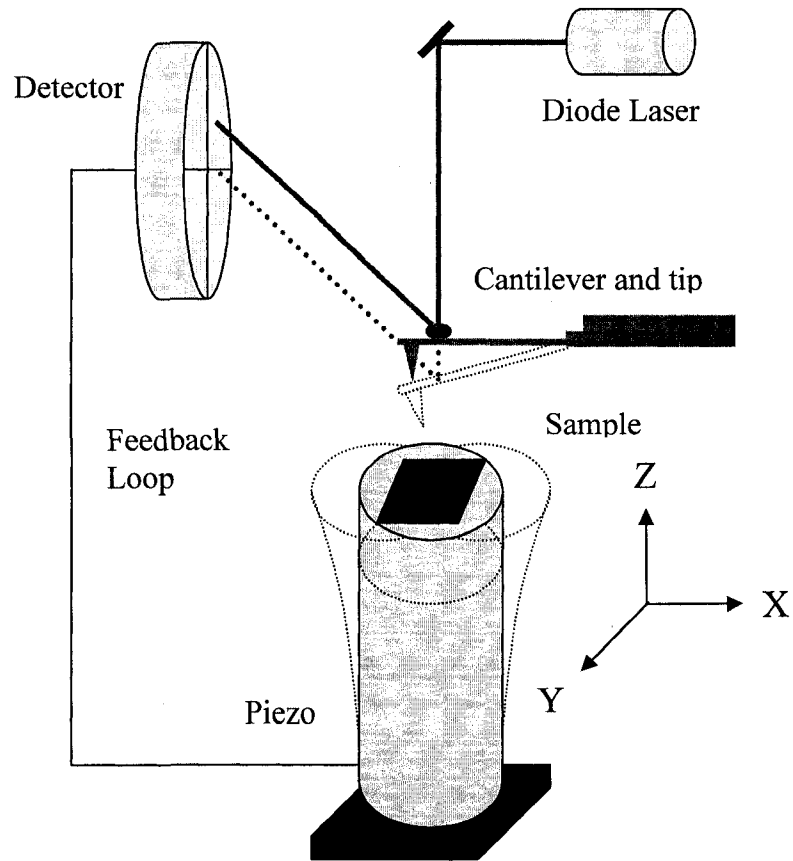


Figure 1.04. Schematic representation of the basic principles of a sample-scanning Atomic Force Microscope.

signal". The error signal reflects the time between the cantilever deflecting and the response of the feedback loop adjusting the Z piezo voltage to maintain a constant cantilever deflection. The error signal during contact mode is useful for optimizing imaging conditions as well as highlighting sample edge features. Under certain experimental conditions, involving relatively flat samples, the feedback may be turned off. Under this condition the measured cantilever deflection is no longer the error signal and is instead the sample topography.

Another advantageous feature of contact mode is the ability to measure the torsion twisting of the cantilever. When the tip is scanned across the surface frictional forces between the tip and the sample torque the cantilever. The frictional forces have been shown to be sensitive to the surface chemistry of the sample. Modern atomic force microscopes have the ability to simultaneously measure all three of the mentioned imaging modes during a single scan, generating a large portion of data from a single image scan. Figure 1.05 illustrates the three main data channels that are available in a typical contact mode imaging scan.

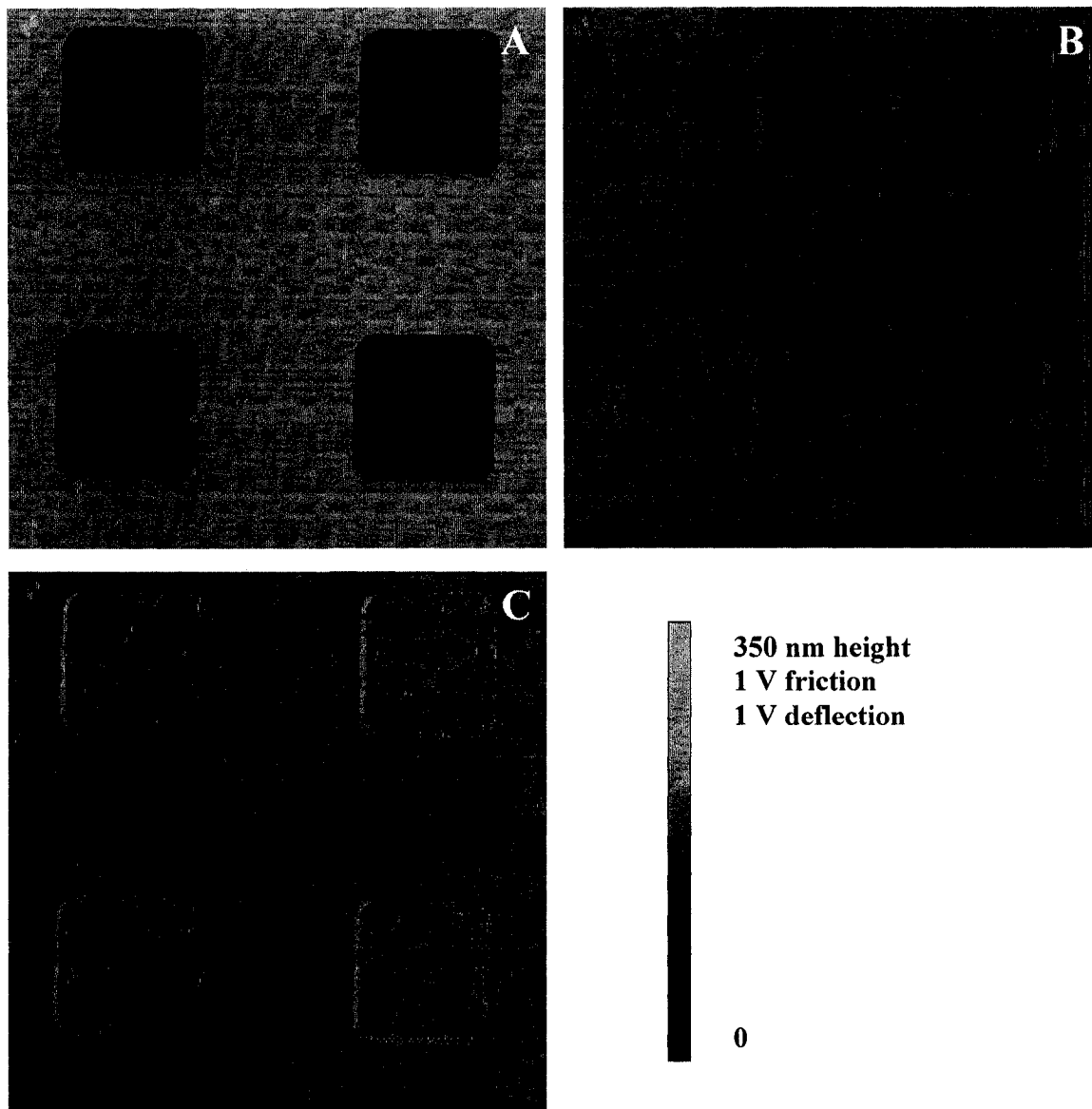


Figure 1.05. Contact mode AFM images. Three main data channels A) height, B) friction, C) deflection, 50 x 50 μm images. The images are of a standard calibration grid.

3.2 Intermittent Contact Mode

An additional common mode of operation is one in which the cantilever is oscillated at or near its resonance frequency and the tip is in intermittent contact with the sample surface. As a result of the intermittent contact the shear forces experienced by the sample are minimized, thus, intermittent contact mode is well suited for applications with easily damaged samples, such as biological samples and delicate organic films. Intermittent contact is a bistable state in which the interactions between the tip and sample vary between attractive and repulsive. Attractive mode occurs when the resonance frequency of the cantilever and the measured phase are shifted to a lower frequency. Conversely repulsive mode occurs when the resonance frequency of the cantilever and the measured phase are shifted to a higher frequency. Quantitative height measurements are performed in intermittent contact mode using the cantilever oscillation amplitude. Feedback electronics are employed to produce a constant, pre-set oscillation amplitude. When the tip encounters a topographic feature the amplitude is altered, in the case of an increase in topography the amplitude is dampened and in the case of a depression the amplitude increases upto the free oscillation amplitude. In both cases, the piezo voltage is adjusted to change the height accordingly and therefore restore the set oscillation amplitude. The feedback mechanism of intermittent contact mode AFM is illustrated in figure 1.06. Similar to contact mode, intermittent contact mode has three primary sources of data. As mentioned above, the topography of the sample may be measured and mapped by plotting the distance the piezo travels versus the X-Y position. Another easily

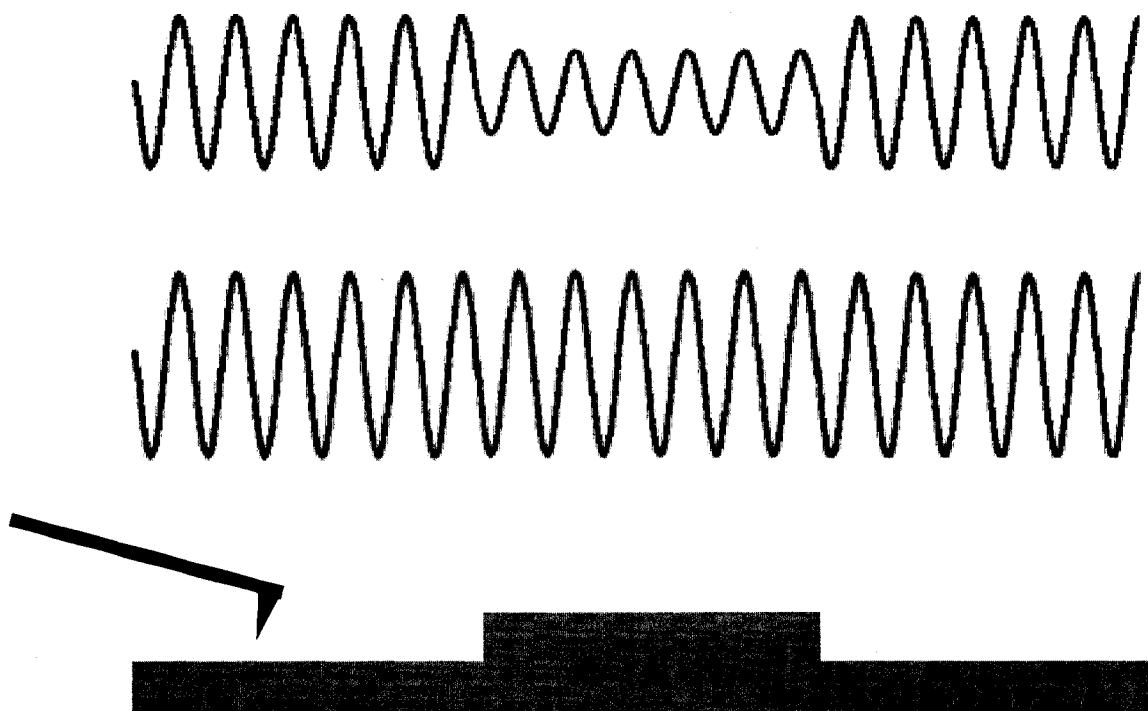


Figure 1.06. Schematic of feedback in intermittent contact AFM, top wave is oscillation trace without feedback, the bottom trace is with perfect feedback.

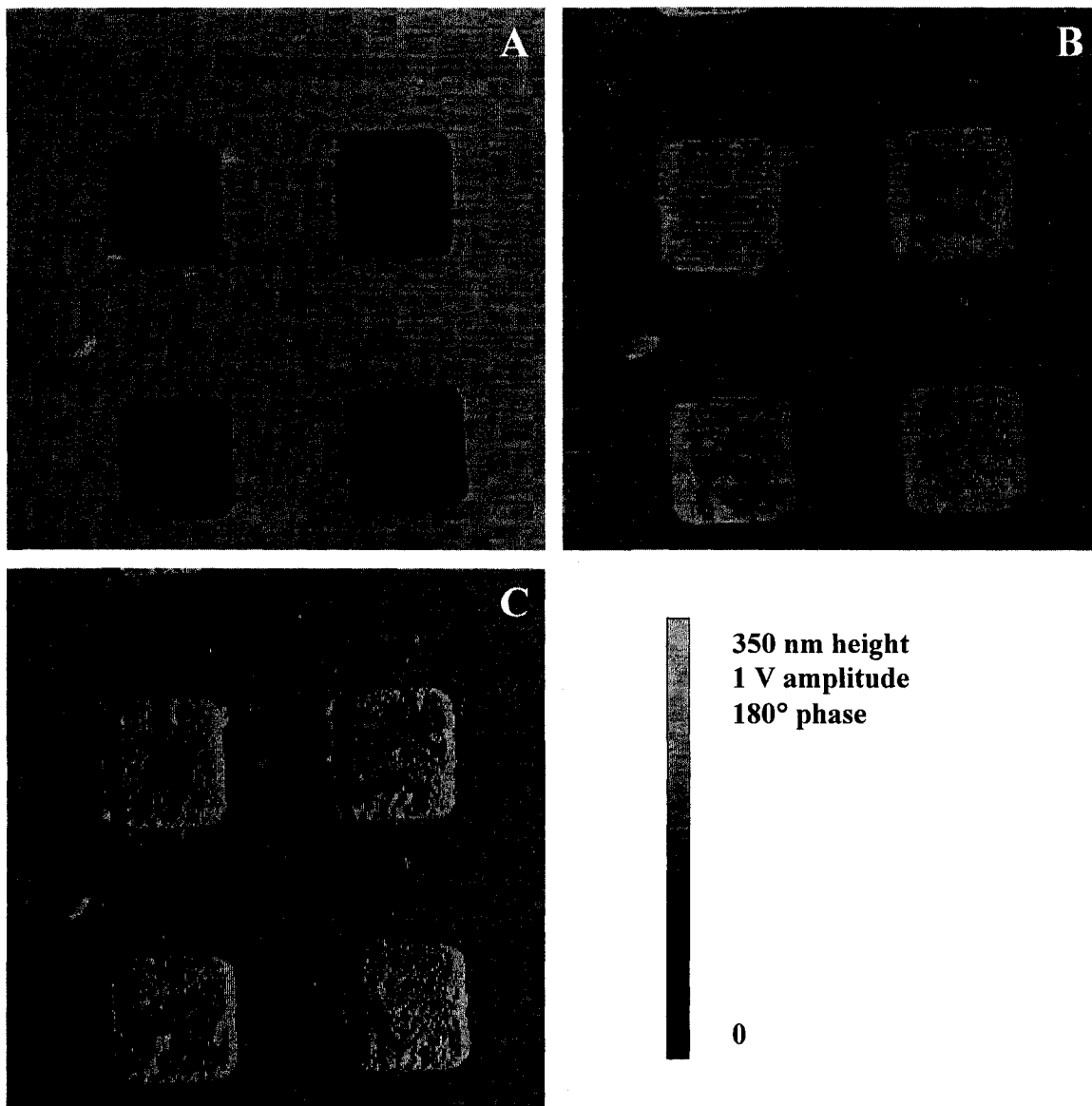


Figure 1.07. Intermittent contact mode AFM images. Three main data channels A) height, B) phase, C) amplitude, 50 x 50 μm images. The images are of a standard calibration grid.

obtained parameter is the amplitude. The feedback works to maintain constant amplitude and therefore amplitude is referred to as the error signal in intermittent contact mode, analogous to deflection in contact mode. With the use of a lock-in amplifier, the frequency shift of the cantilever with respect to the drive frequency can be measured. This frequency shift is known as phase and is a reflection of power dispersion of the sample. It has been shown that under certain circumstances phase imaging can detect different functional groups on a surface.⁷⁴ The three main data channels for intermittent contact mode AFM are presented in figure 1.07.

4 Conductive Atomic Force Microscopy

Conductive atomic force microscopy (C-AFM or conducting probe atomic force microscopy, CP-AFM) is a variant of AFM that probes electrical properties. The small contact area between the tip and the sample allows for electrical probing of the sample on the nano-scale. In its simplest form, C-AFM applies a controlled potential to the tip or sample, and the resulting current that flows between the tip and sample is measured. By ensuring the probe, sample holder, and employed electronics are sufficiently conductive, the measured resistance is due exclusively to the sample and the tip-sample interface. Conductive atomic force microscopy has a large window of detection, with current detection spanning seven orders of magnitude, from hundreds of fA to μ A. Conductive atomic force microscopy has two standard modes of operation. The first uses a constant applied potential as the surface is scanned in contact mode. The collected data can be formed into an image, much like topography, friction, and deflection, but the plotted data are representative of the local

conductivity. The second common method for C-AFM data collection uses a stationary tip, in contact with the surface, and passes a programmed potential sweep through the tip. The current is plotted as a function of the applied voltage; these plots are known as current-voltage (IV) curves. A third, but less often used, method for data collection via C-AFM are force-current curves. Standard force curves are performed, but in this case a constant potential is applied to the tip and the current is measured with respect to tip travel distance. The tip travel distance can easily be converted to applied force. The basic components of a C-AFM are illustrated below in figure 1.08.

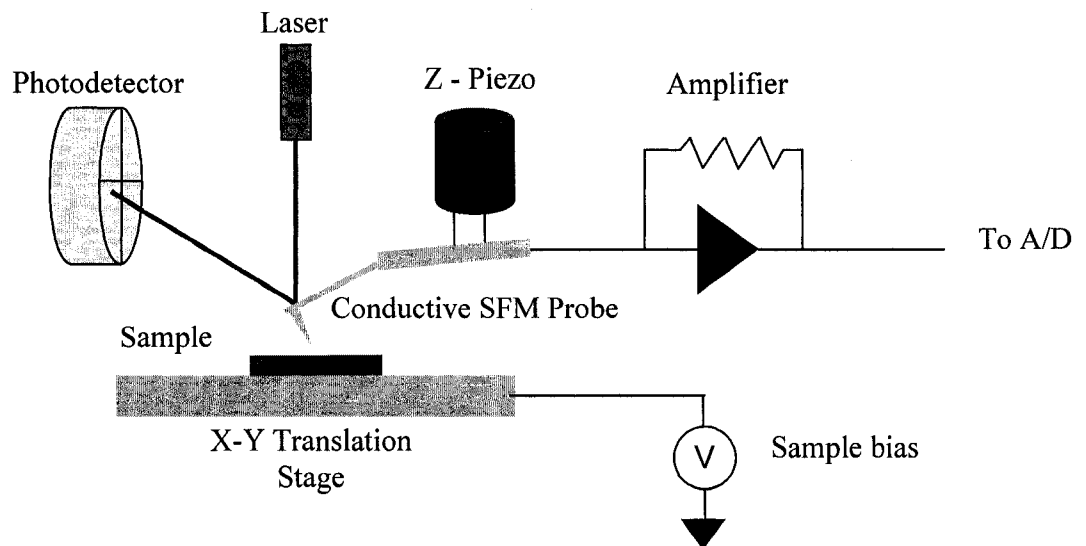


Figure 1.08. Schematic of C-AFM.

5 Cyclic Voltammetry

Cyclic voltammetry is controlled potential electrochemical technique. A linear sweep of the potential to a predefined value is carried out at which point the potential is reversed and a linear potential sweep is performed back to the original starting value. In practice, the electrode is held at a static potential for a period of time before the experiment begins. Figure 1.09 illustrates a typical cyclic voltammetry sweep. Depending on experimental setup, cyclic voltammetry has the potential to offer a plethora of electrochemical data about the system being investigated. Figure 1.10 illustrates a typical cyclic voltammogram, with important features labeled. The peak potential is labeled as E_p , with the cathodic and anodic peaks differentiated, $E_{p,c}$ and $E_{p,a}$ respectively. The peak currents are labeled as i_p , again with the cathodic and anodic currents differentiated. The difference between the peak potentials is labeled as ΔE_p . The half-peak potential is the potential where the current is exactly one half the peak current; this is labeled as $E_{p/2}$. The last value of note is the switching potential E_λ ; this is the potential where the sweep is reversed.

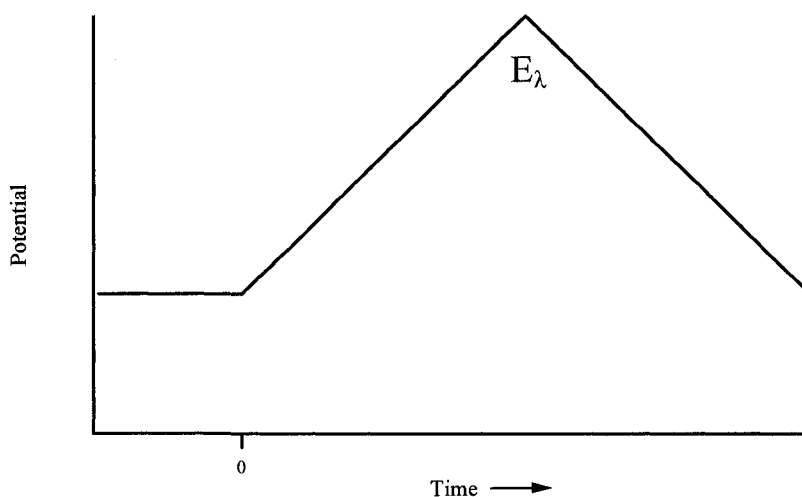


Figure 1.09. Potential program for cyclic voltammetry

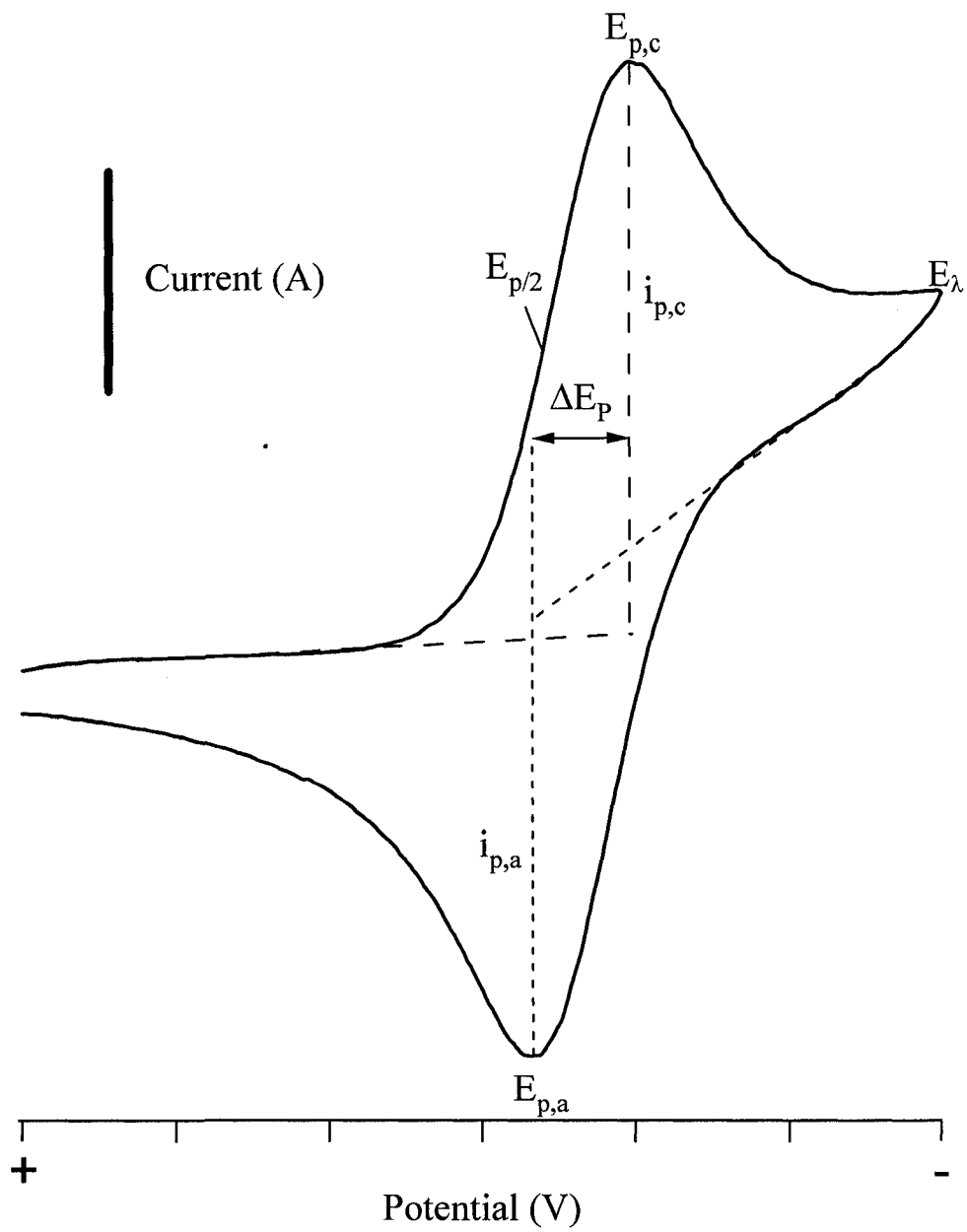


Figure 1.10. Typical cyclic voltammogram with essential features labeled.

Cyclic voltammetry systems can fall into three categories. The first type is a reversible system in which the electron transfer occurs sufficiently fast that the oxidized and reduced species are immediately converted to the concentration ratio as defined by the Nernst equation, equation 1.01

$$E = E^{\circ} + \frac{R_g T}{nF} \ln \frac{C_O}{C_R}$$

Equation 1.01. Nernst Equation: E = potential of the electrode, E° = standard potential of the electrode, R_g = universal gas constant, T = temperature (K), n = number of electrons, F = Faraday constant, C_O = concentration of oxidized species, C_R = concentration of reduced species.

The peak potentials (E_p) for reversible CV waves are independent of scan rate (ν) and the peak currents are proportional to the square root of the applied scan rate ($\nu^{1/2}$).⁷⁵ An additional indication of Nernstian behaviour in cyclic (and linear) voltammetry is the measured difference between E_p and $E_{p/2}$. The relationship is presented in equation 1.02.⁷⁵ It should be noted that the measured peak separation values (ΔE_p) in cyclic voltammetry may also be used as a diagnostic for a Nernstian reaction, but this method suffers from slight complication due to the dependence of ΔE_p on switching potential; however if in general ΔE_p is close to $59/n$ mV at 25° C at all scan rates, the reaction should be considered reversible.⁷⁵

$$|E_p - E_{p/2}| = \frac{2.2R_g T}{nF} = \frac{56.5}{n} \text{ mV at } 25^\circ \text{ C}$$

Equation 1.02. Diagnostic of a reversible wave: E_p = peak potential, $E_{p/2}$ = half-peak potential, R_g = universal gas constant, T = temperature (K), n = number of electrons, F = Faraday constant.

The second behaviour type for cyclic voltammetry is the irreversible system. As the title implies, an irreversible system is kinetically opposite to the reversible system, that is, the electron transport is extremely slow or sluggish. The peak current, i_p , for irreversible waves is proportional to both the bulk concentration of the analyte, C^* , and $v^{1/2}$ while E_p is a function of scan rate. A diagnostic of irreversible behaviour was described by Bard and Faulkner and is given in equation 1.03.⁷⁵

$$|E_p - E_{p/2}| = \frac{1.857R_g T}{\alpha nF} = \frac{47.7}{\alpha n} \text{ mV at } 25^\circ \text{ C}$$

Equation 1.03. Diagnostic of an irreversible wave: E_p = peak potential, $E_{p/2}$ = half-peak potential, R_g = universal gas constant, T = temperature (K), n = number of electrons, F = Faraday constant, α = transfer coefficient.

The third type of possible system in a cyclic voltammetry experiment, and the one most relevant to this thesis, is the quasi-reversible system. In practice, most systems fall into the quasi-reversible regime. Quasi-reversible systems have electron transfer kinetic limitations and the reverse reaction needs to be considered. The quasi-reversible systems were first introduced by Ayabe and Matsuda.⁷⁶ Unlike the

other two systems, the peak current, i_p , of quasi-reversible reactions is not dependent on $v^{1/2}$. Quasi-reversible cyclic voltammograms are a function of the dimensionless kinetic parameter Ψ described by Nicholson as shown in equation 1.04.^{75,77}

$$\Psi = \frac{\left(\frac{D_O}{D_R}\right)^{\alpha/2} k^{\circ}}{[D_o \pi \nu (nF / R_g T)]^{1/2}}$$

Equation 1.04. Definition of a quasi-reversible reaction: ψ = kinetic parameter, D_o = diffusion coefficient of the oxidized species, D_R = diffusion coefficient of the reduced species, R_g = universal gas constant, T = temperature (K), n = number of electrons, F = Faraday constant, α = transfer coefficient, ν = scan rate, k° = heterogeneous electron transfer rate constant.

The peak separation potential, ΔE_p , values in these systems are nearly independent of both α and E_{λ} , and depend only on Ψ . In practice, ΔE_p values are measured and the corresponding values of Ψ are extrapolated from tabulated values.^{75, 77} This allows one to calculate heterogeneous electron transfer rate constants, k° , for quasi-reversible systems by rearrangement of equation 1.04. Although the Nicholson method for determination of rate constants of quasi-reversible reactions from measured ΔE_p values can falter at high cell resistances it was deemed appropriate when used in conjunction with uncompensated cell resistance correction.

6 Infrared Spectroscopy

Infrared spectroscopy (IR) is an optical technique capable of probing rotational and vibrational modes of molecules and functional groups. In terms of spectroscopy, the infrared region is divided into three regions; the far infrared encompasses 400 to 10 cm^{-1} , the mid-IR contains the region between 4000 to 400 cm^{-1} , and the near-IR cover the range from 14000 to 4000 cm^{-1} . The far-IR borders microwaves in the electromagnetic spectrum and, much like microwave spectroscopy, is used for rotational spectroscopy. The near-IR can probe high energy overtone vibrational modes of molecules and functional groups. The most common form of IR spectroscopy uses the mid-IR range. This range probes the primary vibrational mode for many molecules and functional groups. Modern IR instruments are capable of detecting low-picogram amounts of analyte. This thesis will discuss the mid-IR region exclusively; all further references to mid-IR will simply be referred to as IR.

Infrared spectroscopy probes the various modes of vibrations and can be used as a quantitative measurement as well as a means to identify samples. The number of vibration modes, and hence the number of absorption bands, is determined by the number of vibrational degrees of freedom. For non-linear polyatomic molecules the number of degrees of freedom are described by $3N - 6$, where N is the number of atoms in the molecule or functional group. For linear species the degrees of freedom are described by $3N - 5$. For typical octavalent organic compounds, such as those studied in this thesis, up to six vibrational modes are possible. The various modes are illustrated in figure 1.11. By comparing the signal intensity of the observed bands one can extract quantitative information from IR spectra while the positions and

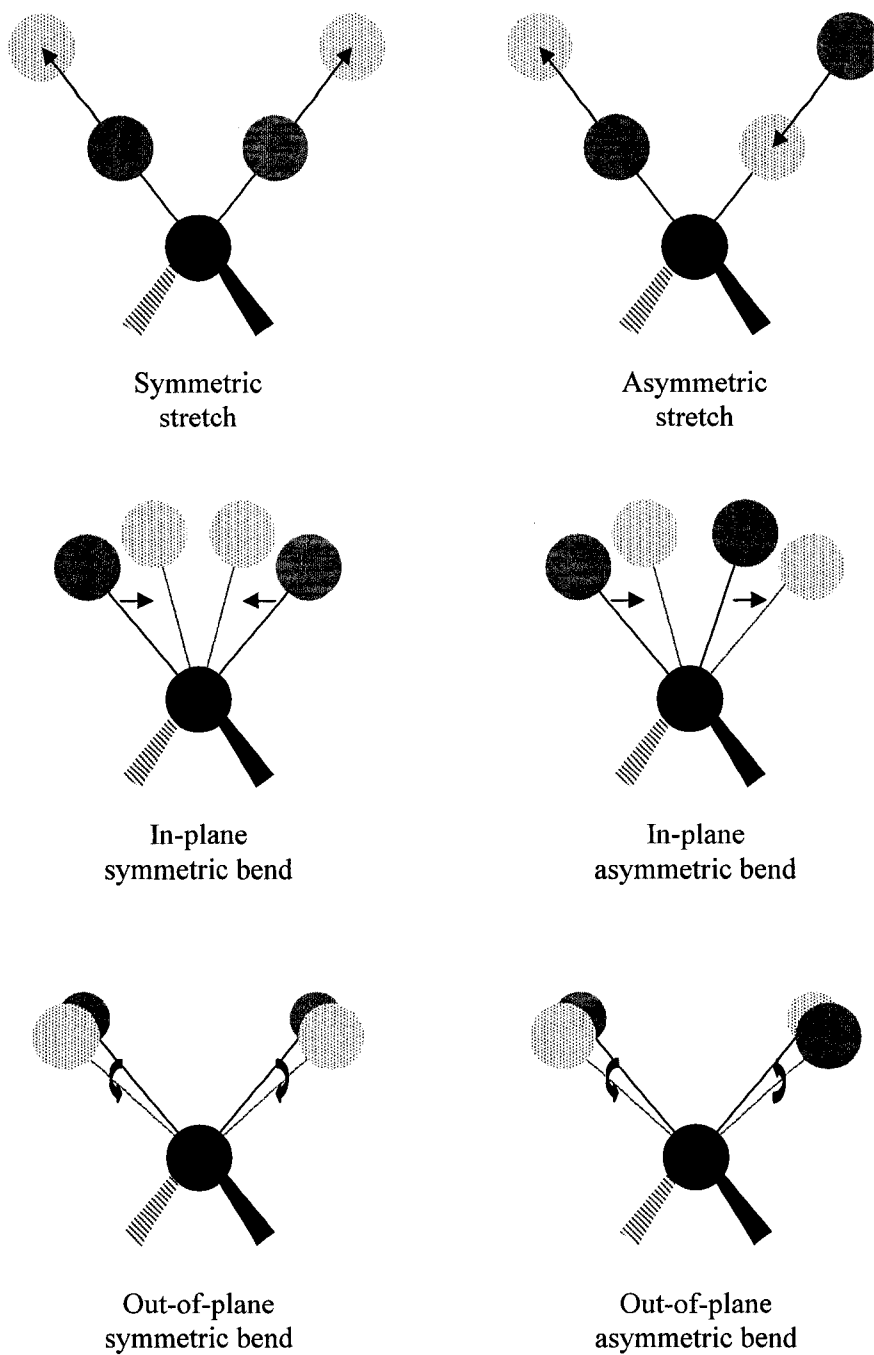


Figure 1.11. The six modes of IR vibrations are illustrated above; symmetric stretch, asymmetric stretch, in-plane symmetric bend, in-plane asymmetric bend, out-of-plane symmetric bend and out-of-plane asymmetric bend.

relative intensities of the various bands may be useful in identifying an unknown compound.

Infrared reflection absorption spectroscopy (IRRAS) is a variant of infrared spectroscopy in which the incident optical beam is reflected off of a surface at an oblique, grazing, angle. The reflective surface is, or contains, the analyte. Although IRRAS conforms to the standard IR rules it also has significant features that make it unique. IRRAS uses light that is polarized perpendicular to the surface, s-polarized light. Due to the polarity of the light, for metallic surfaces, only dipoles perpendicular to the surface will be IR active. This is known as the surface selection rule.⁷⁸ As a result IRRAS may provide orientation information that it is not available with traditional IR sampling techniques.

7 Intention

Throughout this thesis the common theme is surface modification via reduction of aryl diazonium salts. A number of surfaces were studied, including various forms of carbon and platinum for derivatization. In each case multiple methods were used to characterize the resulting structures. The fabricated films were also tested for various uses, including molecular electronics and biocompatibility.

References

- (1) Keyword search “surface” and “modification” retrieved January 15, 2006, from *ISI Web of Science* <http://www.isiknowledge.com/>.
- (2) Qi, K. H.; Daoud, W. A.; Xin, J. H.; Mak, C. L.; Tang, W. Z.; Cheung, W. P. *Journal of Materials Chemistry* **2006**, *16*, 4567-4574.
- (3) Read, R. E.; Culling, G. C. *American Dyestuff Reporter* **1967**, *56*, 42.
- (4) Chou, W. Y.; Mai, Y. S.; Cheng, H. L.; Yeh, C. Y.; Kuo, C. W.; Tang, F. C.; Shu, D. Y.; Yew, T. R.; Wen, T. C. *Organic Electronics* **2006**, *7*, 445-451.
- (5) Kim, J. M.; Lee, J. W.; Kim, J. K.; Ju, B. K.; Kim, J. S.; Lee, Y. H.; Oh, M. H. *Applied Physics Letters* **2004**, *85*, 6368-6370.
- (6) Chen, K. S.; Chen, S. C.; Lin, H. R.; Yan, T. R.; Tseng, C. C. *Materials Science & Engineering C-Biomimetic and Supramolecular Systems* **2007**, *27*, 716-724.
- (7) Jonsson, G.; Gorton, L. *Biosensors* **1985**, *1*, 355-368.
- (8) Chu, P. K. *Surface & Coatings Technology* **2007**, *201*, 5601-5606.
- (9) Ikada, Y. *Macromolecular Symposia* **1996**, *101*, 455-462.
- (10) Bilek, G.; Kremser, L.; Blaas, D.; Kenndler, E. *Electrophoresis* **2006**, *27*, 3999-4007.
- (11) Zlatkis, A.; Walker, J. Q. *Analytical Chemistry* **1963**, *35*, 1359-1362.
- (12) Vesel, A.; Mozetic, M.; Hladnik, A.; Dolenc, J.; Zule, J.; Milosevic, S.; Krstulovic, N.; Klanjsek-Gunde, M.; Hauptmann, N. *Journal of Physics D-Applied Physics* **2007**, *40*, 3689-3696.
- (13) Shi, J. Z.; Schuman, T. P.; Stoffer, J. O. *Jct Research* **2004**, *1*, 225-234.

- (14) Aktary, M.; McDermott, M. T.; MacAlpine, G. *Surface Engineering* **2002**, *18*, 70-74.
- (15) Aktary, M.; McDermott, M. T.; McAlpine, G. A. *Tribology Letters* **2002**, *12*, 155-162.
- (16) Aktary, M.; McDermott, M. T.; Torkelson, J. *Wear* **2001**, *247*, 172-179.
- (17) *Santa Clara California press release* **January 25, 2006**.
- (18) Herwald, S. W. *Current Science* **1961**, *30*, 207.
- (19) Aviram, A.; Ratner, M. A. *Chemical Physics Letters* **1974**, *29*, 277-283.
- (20) Aviram, A.; Ratner, M. A. *Bulletin of the American Physical Society* **1974**, *19*, 341-341.
- (21) Crommie, M. F.; Lutz, C. P.; Eigler, D. M. *Science* **1993**, *262*, 218-220.
- (22) Crommie, M. F.; Lutz, C. P.; Eigler, D. M. *Physical Review B* **1993**, *48*, 2851-2854.
- (23) Crommie, M. F.; Lutz, C. P.; Eigler, D. M. *Nature* **1993**, *363*, 524-527.
- (24) Joachim, C.; Gimzewski, J. K.; Schlittler, R. R.; Chavy, C. *Physical Review Letters* **1995**, *74*, 2102-2105.
- (25) Dorogi, M.; Gomez, J.; Osifchin, R.; Andres, R. P.; Reifenberger, R. *Physical Review B* **1995**, *52*, 9071-9077.
- (26) Andres, R. P.; Bein, T.; Dorogi, M.; Feng, S.; Henderson, J. I.; Kubiak, C. P.; Mahoney, W.; Osifchin, R. G.; Reifenberger, R. *Science* **1996**, *272*, 1323-1325.
- (27) Bumm, L. A.; Arnold, J. J.; Cygan, M. T.; Dunbar, T. D.; Burgin, T. P.; Jones, L.; Allara, D. L.; Tour, J. M.; Weiss, P. S. *Science* **1996**, *271*, 1705-1707.

- (28) Wold, D. J.; Frisbie, C. D. *Journal of the American Chemical Society* **2000**, *122*, 2970-2971.
- (29) Wold, D. J.; Frisbie, C. D. *Journal of the American Chemical Society* **2001**, *123*, 5549-5556.
- (30) Wold, D. J.; Haag, R.; Rampi, M. A.; Frisbie, C. D. *Journal of Physical Chemistry B* **2002**, *106*, 2813-2816.
- (31) McGovern, W. R.; Anariba, F.; McCreery, R. L. *Journal of the Electrochemical Society* **2005**, *152*, E176-E183.
- (32) Anariba, F.; Steach, J. K.; McCreery, R. L. *Journal of Physical Chemistry B* **2005**, *109*, 11163-11172.
- (33) Solak, A. O.; Eichorst, L. R.; Clark, W. J.; McCreery, R. L. *Analytical Chemistry* **2003**, *75*, 296-305.
- (34) McCreery, R.; Dieringer, J.; Solak, A. O.; Snyder, B.; Nowak, A. M.; McGovern, W. R.; DuVall, S. *Journal of the American Chemical Society* **2003**, *125*, 10748-10758.
- (35) Hebert, N. E.; Snyder, B.; McCreery, R. L.; Kuhr, W. G.; Brazill, S. A. *Analytical Chemistry* **2003**, *75*, 4265-4271.
- (36) Anariba, F.; DuVall, S. H.; McCreery, R. L. *Analytical Chemistry* **2003**, *75*, 3837-3844.
- (37) Solak, A. O.; Ranganathan, S.; Itoh, T.; McCreery, R. L. *Electrochemical and Solid State Letters* **2002**, *5*, E43-E46.
- (38) Itoh, T.; McCreery, R. L. *Journal of the American Chemical Society* **2002**, *124*, 10894-10902.

- (39) Anariba, F.; McCreery, R. L. *Journal of Physical Chemistry B* **2002**, *106*, 10355-10362.
- (40) Ranganathan, S.; Steidel, I.; Anariba, F.; McCreery, R. L. *Nano Letters* **2001**, *1*, 491-494.
- (41) Ranganathan, S.; McCreery, R. L. *Analytical Chemistry* **2001**, *73*, 893-900.
- (42) Ranganathan, S.; McCreery, R.; Majji, S. M.; Madou, M. *Journal of the Electrochemical Society* **2000**, *147*, 277-282.
- (43) Kinoshita, K. *Carbon: Electrochemical and Physicochemical Properties*; Wiley: New York, 1988.
- (44) McCreery, R. L. *Electroanalytical Chemistry*; Bard, A J. Ed; Dekker: New York, 1991.
- (45) Ivandini, T. A.; Honda, K.; Rao, T. N.; Fujishima, A.; Einaga, Y. *Talanta* **2007**, *71*, 648-655.
- (46) Zang, J. B.; Wang, Y. H.; Zhao, S. Z.; Bian, L. Y.; Lu, J. *Diamond and Related Materials* **2007**, *16*, 16-20.
- (47) Fischer, A. E.; Swain, G. M. *Journal of the Electrochemical Society* **2005**, *152*, B369-B375.
- (48) Granger, M. C.; Swain, G. M. *Journal of the Electrochemical Society* **1999**, *146*, 4551-4558.
- (49) Granger, M. C.; Xu, J. S.; Strojek, J. W.; Swain, G. M. *Analytica Chimica Acta* **1999**, *397*, 145-161.

- (50) Hupert, M.; Muck, A.; Wang, R.; Stotter, J.; Cvackova, Z.; Haymond, S.; Show, Y.; Swain, G. M. *Diamond and Related Materials* **2003**, *12*, 1940-1949.
- (51) Swain, G. M.; Anderson, A. B.; Angus, J. C. *Mrs Bulletin* **1998**, *23*, 56-60.
- (52) Wang, J.; Swain, G. M.; Mermoux, M.; Lucazeau, G.; Zak, J.; Strojek, J. W. *New Diamond and Frontier Carbon Technology* **1999**, *9*, 317-343.
- (53) Wang, J.; Swain, G. M.; Tachibana, T.; Kobashi, K. *Journal of New Materials for Electrochemical Systems* **2000**, *3*, 75-82.
- (54) Xu, J. S.; Chen, Q. Y.; Swain, G. M. *Analytical Chemistry* **1998**, *70*, 3146-3154.
- (55) Pauling, L. *The Nature of the Chemical Bond*; Cornell University Press, 1960.
- (56) Harrison, W. A. *Electronic Structure and the Properties of Solids: The Physics of the Chemical Bond*; Freeman: San Francisco, 1980.
- (57) Gofer, Y.; Barbour, R.; Luo, Y. Y.; Tryk, D. A.; Jayne, J.; Chottiner, G.; Scherson, D. A. *Journal of Physical Chemistry* **1995**, *99*, 11797-11800.
- (58) Ratcliff, B. B.; Klancke, J. W.; Koppang, M. D.; Engstrom, R. C. *Analytical Chemistry* **1996**, *68*, 2010-2014.
- (59) Chu, A. C.; Josefowicz, J. Y.; Farrington, G. C. *Journal of the Electrochemical Society* **1997**, *144*, 4161-4169.
- (60) Rivera, M.; Holguin, S.; Moreno, A.; Sepulveda-Sanchez, J. D.; Hernandez-Perez, T. *Journal of the Electrochemical Society* **2002**, *149*, E84-E89.
- (61) McDermott, M. T.; Kneten, K.; McCreery, R. L. *Journal of Physical Chemistry* **1992**, *96*, 3124-3130.

- (62) Yamada, S.; Sato, H. *Nature* **1962**, *193*, 261-262.
- (63) Kawamura, K.; Jenkins, G. M. *Journal of Materials Science* **1970**, *5*, 262-267.
- (64) Jenkins, G. M.; Kawamura, K. *Nature* **1971**, *231*, 175-176.
- (65) Murray, R. W. *Electroanalytical Chemistry* **1984**, *13*, 191-368.
- (66) Wrighton, M. S. *Science* **1986**, *231*, 32-37.
- (67) Noel, M.; Anantharaman, P. N. *Surface & Coatings Technology* **1986**, *28*, 161-179.
- (68) Jannakoudakis, A. D.; Jannakoudakis, P. D.; Theodoridou, E.; Besenhard, J. O. *Journal of Applied Electrochemistry* **1990**, *20*, 619-624.
- (69) Lin, A. W. C.; Yeh, P.; Yacynych, A. M.; Kuwana, T. *Journal of Electroanalytical Chemistry* **1977**, *84*, 411-419.
- (70) Donnet, J. B.; Ehrburger, P. *Carbon* **1977**, *15*, 143-152.
- (71) Delamar, M.; Hitmi, R.; Pinson, J.; Saveant, J. M. *Journal of the American Chemical Society* **1992**, *114*, 5883-5884.
- (72) Balz, G.; Schiemann, G. *Berichte Der Deutschen Chemischen Gesellschaft* **1927**, *60*, 1186-1190.
- (73) Dunker, M. F. W.; Starkey, E. B.; Jenkins, G. L. *Journal of the American Chemical Society* **1936**, *58*, 2308-2309.
- (74) Finot, M. O.; McDermott, M. T. *Journal of the American Chemical Society* **1997**, *119*, 8564-8565.
- (75) Bard, A. J.; Faulkner, L. R. *Electrochemical methods : fundamentals and applications*; Wiley: New York ; Chichester, 1980.
- (76) Matsuda, H.; Ayabe, Y. *Zeitschrift Fur Elektrochemie* **1955**, *59*, 494-503.

- (77) Nicholson, R. S. *Analytical Chemistry* **1965**, 37, 1351-1355.
- (78) Sheppard, N.; Erkelens, J. *Applied Spectroscopy* **1984**, 38, 471-485.

Chapter II

Characterization of Ultra-flat Carbon

1. Introduction

Traditionally, carbon has been one of the most widely used materials for solid electrodes. Carbon electrodes are chemically compatible with a wide variety of redox systems, are stable over a relatively large potential window, and exhibit excellent mechanical stability. These advantageous features coupled with the low cost and the wide availability of analytical grade carbon make carbon based electrodes an attractive choice for an assortment of analytical and electrochemical applications. The use of various carbon materials as electrodes and electrochemical sensors has been discussed in detail in chapter 1. Carbon electrodes have traditionally been prepared from a relatively large, solid mass of graphite. Carbon film electrodes possess the beneficial traits of traditional electrodes but can be produced with significantly less graphite. Depending on the choice of support and deposition method, thin carbon films can be mass produced at a significantly lower expense when compared to traditional electrodes.

Of the various methods to produce carbon films, this chapter will focus on the fabrication and characterization of those produced by electron beam evaporation. Electron beam evaporated carbon films similar to those studied in this work were first reported in 1975 when Mattson *et al.* evaporated carbon onto germanium internal reflection elements to study the spectroscopic and electrochemical behaviour of the thin carbon films.¹ Mattson reported the first electron beam evaporated thin carbon films with conductivity high enough to be used as electrodes while maintaining the

initial criteria of being optically transparent. In a subsequent publication Mattson described carbon films on glass and quartz via electron beam evaporation;² again the optical and electrochemical properties were probed. Mattson reported that the electrochemical behaviour of these thin carbon films was similar to that of bulk carbon electrodes.

Research in the area of electron beam deposited carbon films was relatively stagnant until 1997 when Möbius investigated the surface and bulk properties of these films.³ Möbius used glass and Si(100) as the supporting substrate to create electron beam deposited carbon films up to 60 nm thick, then characterized them via X-ray diffraction, scanning electron microscopy, scanning tunneling microscopy, and Raman spectroscopy. The electrical conductance was also measured. Möbius reported an amorphous sp^2 carbon film with graphitic crystallites on the order of 1.5 to 2.5 nm and linear conductance behaviour for film thicknesses greater than 8 nm.

In 2004, McDermott furthered the research of Si(100) supported electron beam evaporated carbon films with a more extensive electrochemical and surface topography investigation.⁴ Films were created with thicknesses varying between 2 and 200 nm, focusing on two film thicknesses of 7 and 200 nm. Samples were also pyrolyzed to increase graphitization in the carbon. The surface topography of the samples was measured via atomic force microscopy and the roughness was reported. This was the first work in which roughness over large areas, greater than 1 μm , was studied. Additionally electrochemical electron transport was measured for a variety of redox systems and reported as heterogeneous electron transport rate constants, k^o . Similar to Möbius' published work, McDermott used Raman spectroscopy to gauge

the degree of disorder of graphitic crystallites present in the film. The published results of McDermott *et al.* showed an extremely flat carbon surface over a wide lateral range for nonpyrolyzed samples while the pyrolyzed samples showed an increase in both the degree of graphitization and the roughness of the surface. The thicker of the studied films, 20 nm and greater, were also excellent electrodes as demonstrated by the reported heterogeneous electron transport rate constants, with the pyrolyzed samples showing similar characteristics to glassy carbon.

The ultra-flat nature of the Si(100) supported electron beam evaporated carbon makes it desirable for further study and modification. The modification of these films and uses for such modified films is discussed in later chapters. This chapter deals with the fabrication and characterization of 50 nm thick electron beam evaporated carbon films. The thickness of 50 nm was chosen to ensure that the films are sufficiently thick to behave as bulk material while also keeping the deposition and required high vacuum time reasonable.

2. Experimental

Electron beam evaporated carbon films were fabricated using $1.5 \times 1.5 \text{ cm}^2$ substrates of highly doped, $\langle 100 \rangle$ oriented, prime silicon wafers (N-type, arsenic doped; resistivity = $40 \text{ } \Omega$; Silicon Valley Microelectronics). The substrates were cleaned with piranha (3:1 (v/v) conc. $\text{H}_2\text{SO}_4/30\% \text{ H}_2\text{O}_2$) for 15 – 20 minutes to remove any organic residue, then rinsed with Nanopure water ($18 \text{ M}\Omega/\text{cm}$, Barnstead, Dubuque, IA). The resulting oxidized surface was stripped by immersion in 49% HF

for 1 – 2 minutes. The substrates were again rinsed with Nanopure water. The silicon was dried with argon and immediately placed into the evaporation vacuum chamber for carbon deposition. The evaporation vacuum chamber was pumped to a pressure of $\sim 1 \times 10^{-6}$ Torr. The carbon source used was a high-purity polycrystalline puck located 43 cm from the sample holder. A quartz crystal microbalance was used to monitor the deposition rate. The deposition rate was controlled via the electron beam current which was adjusted to yield a rate of 0.1 nm/s prior to exposing the samples to the carbon source. The pressure did not rise above 5×10^{-6} Torr during any point of the evaporation. The carbon substrates were sonicated in an ethanol/activated charcoal slurry, sonicated in Nanopure water and then dried with argon prior to characterization.

Electron beam evaporated carbon films were prepared for electrochemical analysis by sonication in a slurry of activated charcoal and isopropyl alcohol for twenty minutes. The samples were removed from the slurry, rinsed with Nanopure water and dried with a gentle stream of argon. The films were immediately placed into the electrochemical cell and the analyte solution was added to help shield the electrode from atmospheric fouling.

Surface topography of the non-pyrolyzed carbon films was measured with a variety of atomic force microscopes including, a MultiMode AFM equipped with an “E” scanner and a NanoScope IIIa controller (Veeco Metrology Group, Santa Barbara, CA), a Dimension 3100 AFM with a NanoScope 4 controller (Veeco Metrology Group, Santa Barbara, CA), and an MFP-3D AFM (Asylum Research, Santa Barbara, CA). The AFMs were used to image and quantify the surface

topography of the non-pyrolyzed carbon films. Due to the higher resolution and lower noise, the MultiMode AFM was used exclusively for quantitative measurements. Imaging was performed in contact mode with standard DNP probes and intermittent contact mode with NSC15/50 silicon cantilevers (MikroMasch USA, Wilsonville, OR). Typical imaging scan rates were one to four Hertz. The applied force was closely monitored to ensure the sample was not damaged from excessive force. For physical characterization the carbon films were rinsed with Nanopure water and dried with a gentle stream of argon. Image analysis was performed with the supplied instrument software, Nanoscope V6.12 for the MultiMode and Dimension AFMs and Igor Pro 5 with MFP3D software for the MFP-3D AFM.

The nano-scale electrical characterization of the carbon films was performed with a Dimension 3100 NanoMan System with a NanoScope IV controller and Conductive Atomic Force Microscopy Application Module. Graphite conductive adhesive 112 (Electron Microscopy Sciences, Hatfield, PA) was used to adhere the carbon film/silicon wafer samples to the steel sample pucks as well as to complete the electrical circuit between the carbon surface and the sample puck. Commercially available Veeco Instruments Inc DNP probes were used. The probes were coated in-house with 30 nm chromium followed by 300 nm of gold via a Torr Thermal Evaporation System (Torr International Inc, New Windsor, NY) while rotating about the long axis to evenly coat all sides of the probe and cantilever to prevent distortion due to thermal expansion. All probes were imaged with scanning electron microscopy (JEOL model 6301FXV, JEOL USA, Inc., Peabody, MA) prior to use to ensure proper, defect-free, tip coverage. Prior to analysis, carbon samples were

sonicated in an ethanol and activated charcoal mixture for twenty minutes; the samples were then rinsed with Nanopure water and dried with a gentle stream of argon.

Elemental analysis of the non-pyrolyzed carbon films was performed with an Axis Ultra XPS (Kratos Analytical, Chestnut Ridge, NY) in energy spectrum mode. Survey spectra were collected from 0 to 1200 eV binding energy to gather elemental information and peaks of interest were then rescanned in high resolution. Carbon samples were sonicated in an ethanol and activated charcoal mixture for twenty minutes; the samples were then rinsed with Nanopure water and dried with a gentle stream of argon before analysis.

3. Results and Discussion

3.1 Topography

The topographical and electrical characterization of 50 nm thick electron beam deposited carbon films (EB50) was performed via conducting probe atomic force microscopy. Topographical-only characterization was also performed using traditional atomic force microscopy. The atomic force microscopy studies indicate the as-prepared non-pyrolyzed carbon films have root-mean-square roughness of less than 1 nm for image areas up to 25 μm^2 and less than 1.3 nm for image areas up to 100 μm^2 , the following table, 2.01, summarizes measured roughness values.

Sample Area	Roughness RMS (nm)	SD (nm)	RSD
10 x 10 μm	1.24	0.08	6%
5 x 5 μm	0.848	0.007	0.9%
1 x 1 μm	0.740	0.068	9.2%
500 nm x 500 nm	0.630	0.09	15%

Table 2.01. Root-mean-square roughness of 50 nm thick non-pyrolyzed carbon films.

The values measured in this work are significantly larger than the previously reported values of similar films.⁴ Previously reported roughness values of similar carbon films of 0.07 nm are at the threshold of the atomic force microscope manufacturer's cantilever noise specification of 0.05 nm and below or near the lowest actual measured noise of 0.279 ± 0.083 nm for the Dimension 3100 NanoMan and 0.065 ± 0.012 nm for the MultoMode equipped with an "E" scanner; for a more in-depth noise analysis see appendix. Throughout this work the newly reported values were used and believed to be correct. The measured root-mean-square roughness represents an extremely flat surface. The increased roughness at the largest scan size is attributed to defects in the film. With the exception of sporadically located defects, the roughness is consistent throughout the film and is not a localized effect. A three dimensional plot of a representative surface is presented in figure 2.01.

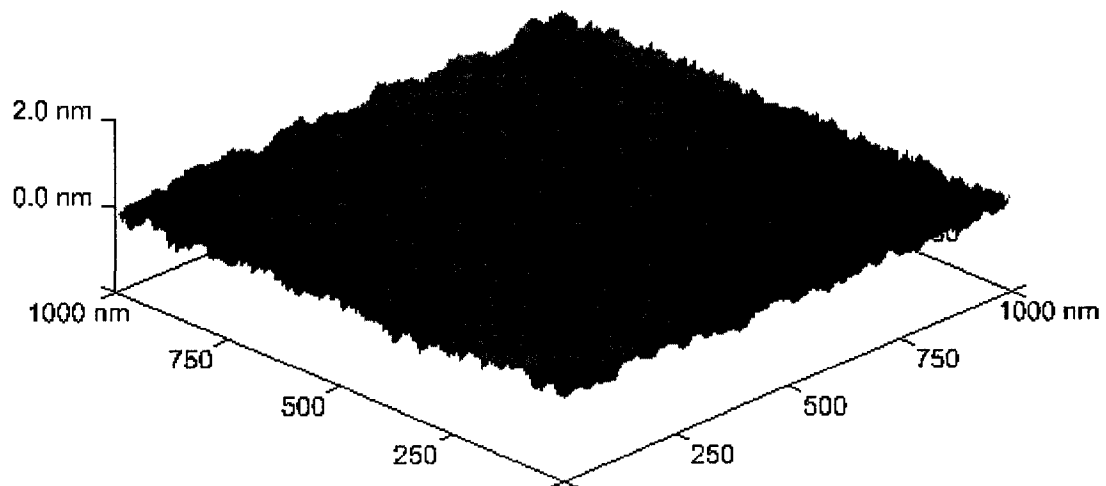


Figure 2.01. Atomic force microscopy image of 50 nm thick electron beam deposited carbon film.

3.2 Electrical Characterization

The nano-scale electrical properties of the electron beam evaporated carbon films were probed with conductive atomic force microscopy (C-AFM). As the name implies, C-AFM requires the use of a conducting probe. Typical contact mode AFM tips are made from insulating silicon nitride and therefore require a coating to provide conductivity. The AFM tips were coated with an adhesion layer of chromium (30 nm) followed by a 300 nm thick layer of gold to provide a conductive and stable coating. To ensure the probes were suitable for C-AFM measurements each probe was imaged via scanning electron microscopy (SEM). Images collected with SEM allowed determination of the shape and size of the probe as well as determination of any defects in their coatings. An example of a tip containing a continuous, regular coating and deemed suitable is shown in figure 2.02, conversely an example of an unusable probe from the same coating batch is presented in the appendix. The presence of an unsuitable probe in the same coating batch as numerous suitable ones validates the need to characterize each in-house coated probe prior to use.

Improper electrical contact is an issue that is easily observed in micro- and macro-electronics. If an adequate contact is not made between two components in a circuit, an abnormally high resistance is observed. To determine the approximate contact force required for good contact between a C-AFM probe and an EB50 film, a set of simple experiments were designed in which the contact force was varied between the probe and film. A constant potential of 100 mV was applied throughout the force loading and the resulting current was monitored. Typical results are presented

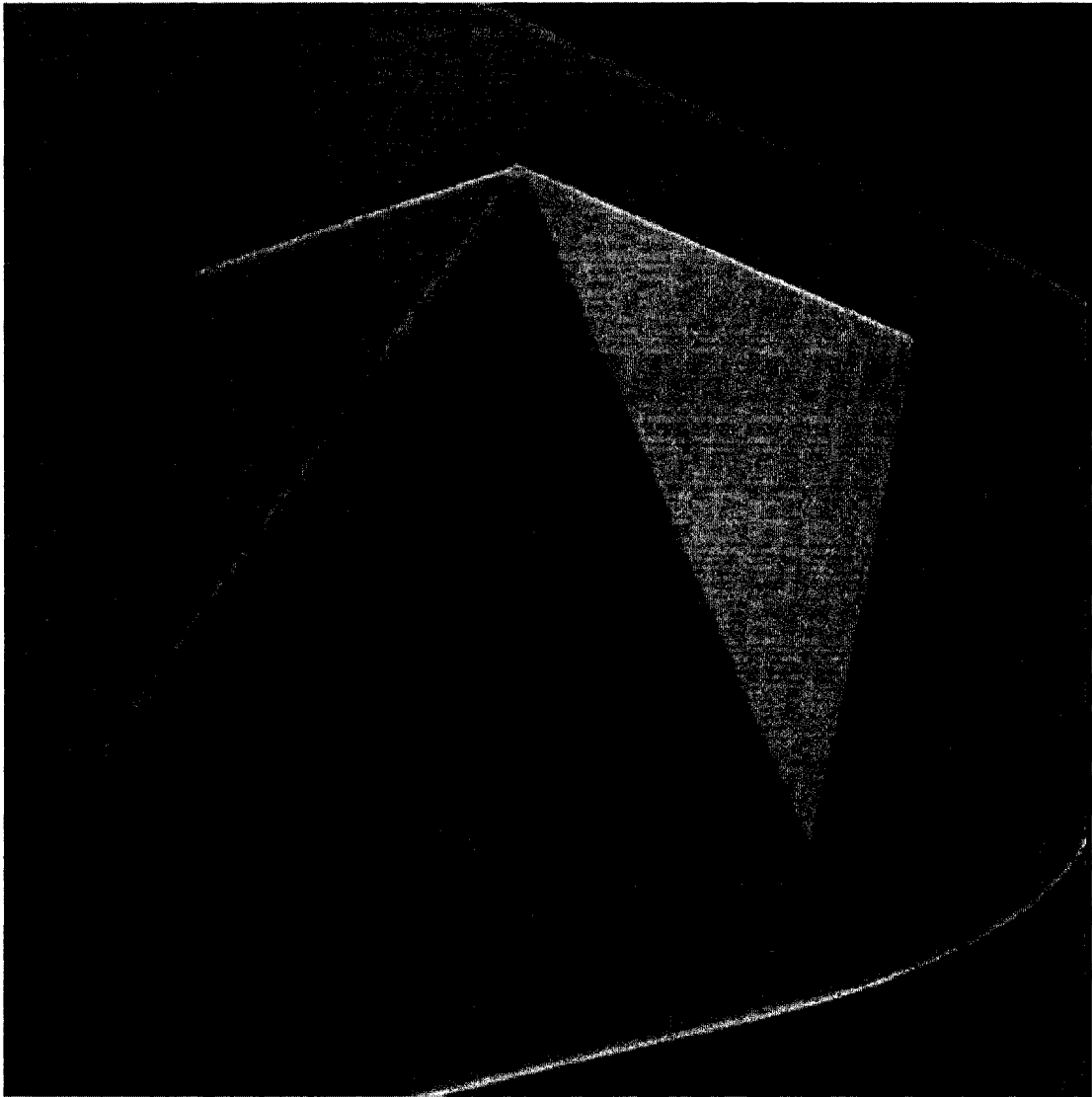


Figure 2.02. Scanning electron micrograph of a typical DNP atomic force microscope probe coated in-house with 30 nm chromium followed by 300 nm of gold. The image is 6.966 x 6.966 μm .

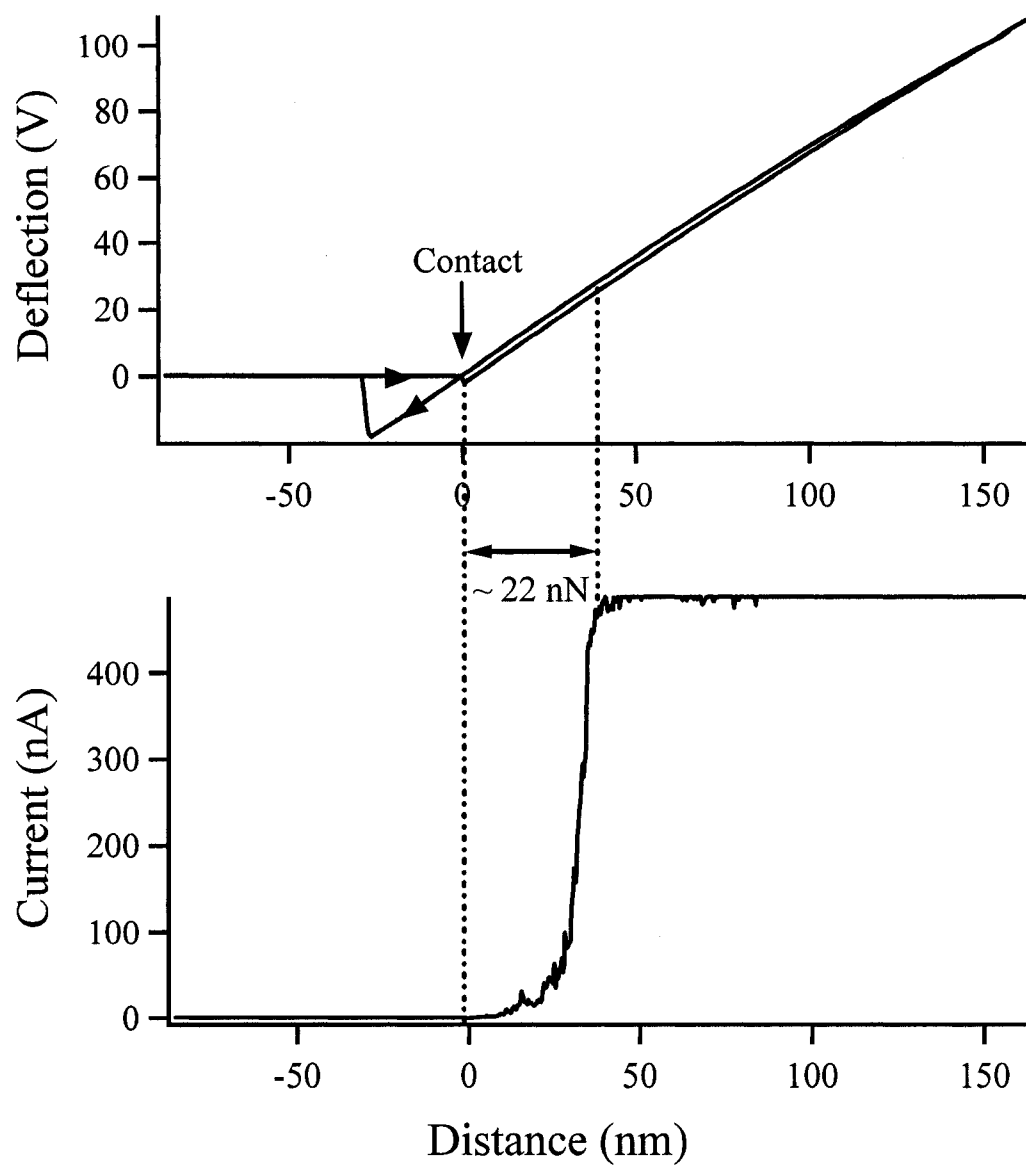


Figure 2.03. Force-distance and distance-current curves of EB50 100 mV potential, average of 50 curves.

in figure 2.03. The top trace represents the deflection (Y-axis) of the cantilever as it approaches (X-axis) and contacts the surface. In this instance, zero on the trace is defined as the sample surface. As the probe is lowered to the surface, no deflection of the cantilever is observed until the probe contacts the surface. In the presented example, snap-to-contact occurs at 0 nm. At the point of contact the cantilever deflection changes linearly with distance traveled, as expected. The bottom trace plots the current between the tip and sample vs distance. Because both the tip and sample are conducting materials, a “good” contact is defined as the point where the current is sufficient to overload the pre-amp of the C-AFM circuit (500 nA). In figure 2.03, this current is not observed until the piezo has traveled an additional 37.8 nm from the point of contact. Using the cantilever’s manufacturer’s specification of the force constant of 0.58 N/m, the measured deflection corresponds to a contact force of approximately 22 nN. All C-AFM carbon film characterization measurements were conducted above 22 nN to ensure decent electrical contact between the probe and sample.

Conductive AFM provides a means to map the surface based on differences in conductivity. As a topographic image is obtained, the gold coated tip is held at a constant potential relative to the sample. Thus, a second image based on current can be obtained. The current flowing in the tip-sample junction is proportional to conductivity, in Siemens, as shown in equation 2.01.

$$G = \frac{I}{V}$$

Equation 2.01 Definition of a Siemen.

A C-AFM current image can therefore be thought of as a map of conductivity of the surface so long as the tip-sample contact remains constant throughout the image. Figure 2.04 shows the topography and current images of nonpyrolyzed EB50 with a tip bias potential of 7 mV. Light colours indicate higher features in the topography image and higher current in the current image. The images show an extremely flat and smooth surface, as discussed in section 3.1, but also show a surface exhibiting uniform conductivity over the bulk of the surface with a number of small, sporadically placed regions of lower conductivity. There appears to be no correlation between the location of the low conductivity regions and topography.

As previously reported by McDermott and coworkers⁴ pyrolyzation of electron beam evaporated carbon films results in greater graphitization. The pyrolyzed carbon films show greater electrochemical reactivity than the nonpyrolyzed films. The process also increases the roughness of the films.

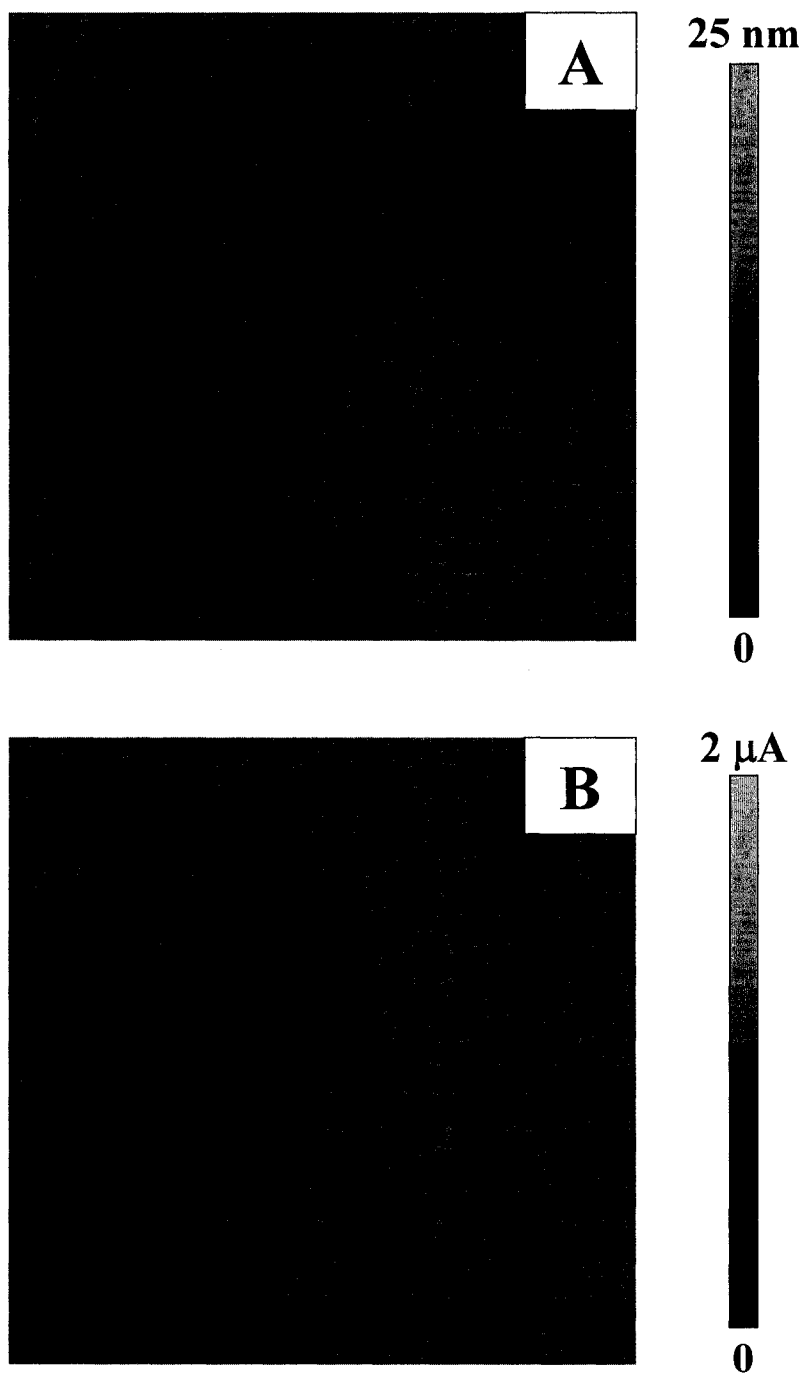


Figure 2.04. Atomic force microscopy images of 50 nm thick electron beam evaporated carbon films A) Topography and B) Current. Images are 10.0 x 10.0 μm.

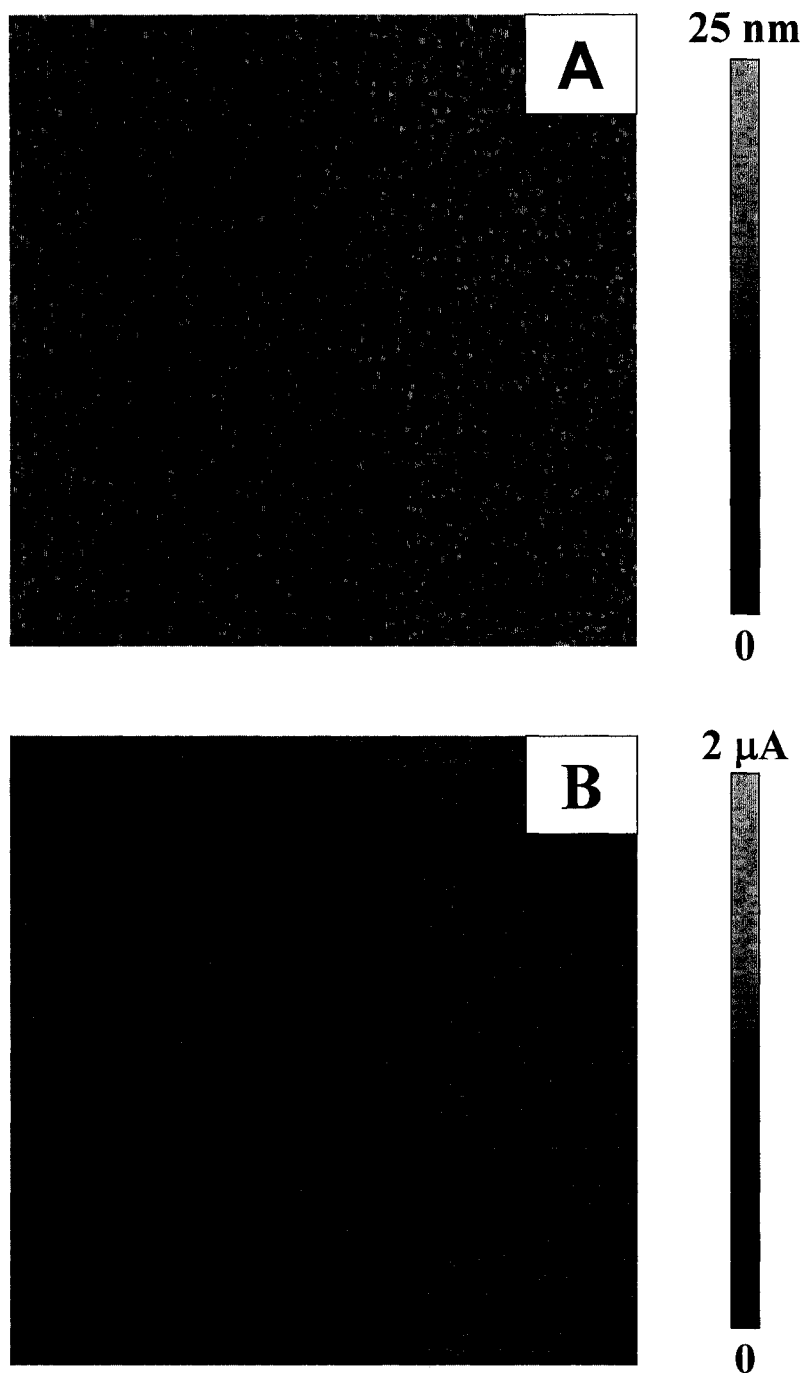


Figure 2.05. Atomic force microscopy images of 50 nm thick pyrolyzed electron beam evaporated carbon films A) Topography and B) Current. Images are 10.0 x 10.0 μm .

Figure 2.05A shows substantially larger variations in topography compared to the non-pyrolyzed film in figure 2.04A. Although a detailed investigation of the roughness of pyrolysed EB50 was not performed here, the RMS roughness of figure 2.05A is about 1.5 nm. This is higher than the RMS listed in table 2.01 for a 10 x 10 μm image for non-pyrolyzed EB50. It is difficult to correlate current variations in figure 2.05B with topography in 2.05A. However, as the tip traces a rough topography such as that shown in figure 2.05A, it is likely that the contact area also changes. It is thus difficult to attribute the changes in current observed in figure 2.05B solely to inherent variations in the conductivity of the pyrolyzed EB50. The average current, and thus conductivity, of the pyrolyzed EB50 is higher than that of non-pyrolyzed EB50 as described above. As a point of reference, the topography and conductivity of the underlying silicon is shown in figure 2.06. The underlying silicon is extremely flat and smooth and exhibits a uniform, low conductivity due to the presence of a silicon oxide coating on the surface.

Quantitative measurements of the conductivity were performed via IV curves. For the IV curves, the C-AFM probe was placed at specific points of interest on the sample. The potential was ramped and the resulting current measured at a constant tip-sample force of about 28 nN. The closed loop XY scanner of the Dimension 3100 allowed for precise and accurate positing of the probe relative to the surface. Various features observed in the C-AFM image of non-pyrolyzed EB50 were measured. The IV curves of non-pyrolyzed EB50 are shown in figure 2.07A. The two curves shown correspond to measurements taken on the bulk of the material as well as measurements taken on the low current areas, or “on spot”, see figure 2.04B. The

slope of the IV curves is the conductivity of the corresponding sample. Conductivity is measured in Siemens and is expressed as G . See equation 2.01. Using the relationship presented in Ohm's Law, equation 2.02, one can easily convert conductivity to resistance by taking the inverse. The concept of resistance is more

$$R = \frac{V}{I}$$

Equation 2.02 Ohm's Law

familiar to most readers and therefore measured conductivities are converted to, and reported as, resistance. The measured C-AFM resistance at the bulk of non-pyrolyzed EB50 is 250 k Ω and the "on spot" is 580 k Ω . The measured C-AFM resistance of pyrolyzed EB50 is 7.4 k Ω . It should be noted that this measured resistance is a series combination of the tip-sample contact resistance and the resistance of the carbon film. The use of C-AFM as a measure of resistivity, despite the presence of contact resistance, was chosen in order to compare directly with C-AFM measurements of modified EB50 films discussed in later sections. Pyrolyzed EB50 was deemed unsuitable for this work due to its greater surface roughness and is not discussed further. For the remainder of this thesis all references to "EB50" will refer to a non-pyrolyzed electron beam evaporated carbon film. Both pyrolyzed and non-pyrolyzed electron beam evaporated carbon films are relatively low resistance and would be expected to behave similar to other sp² carbon electrodes such as glassy carbon.

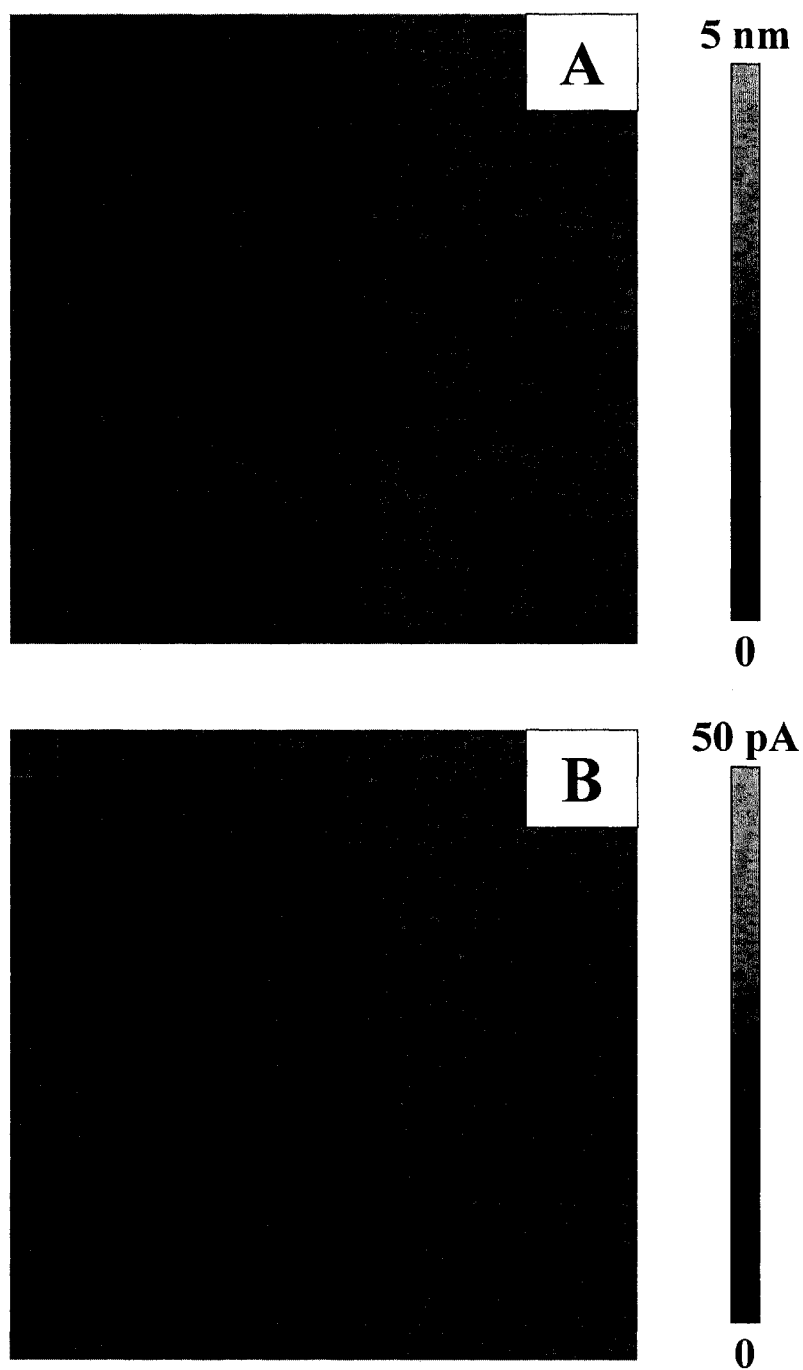


Figure 2.06. Atomic force microscopy images of highly doped, $\langle 100 \rangle$ oriented, prime silicon A) Topography and B) Current. Images are $10.0 \times 10.0 \mu\text{m}$.

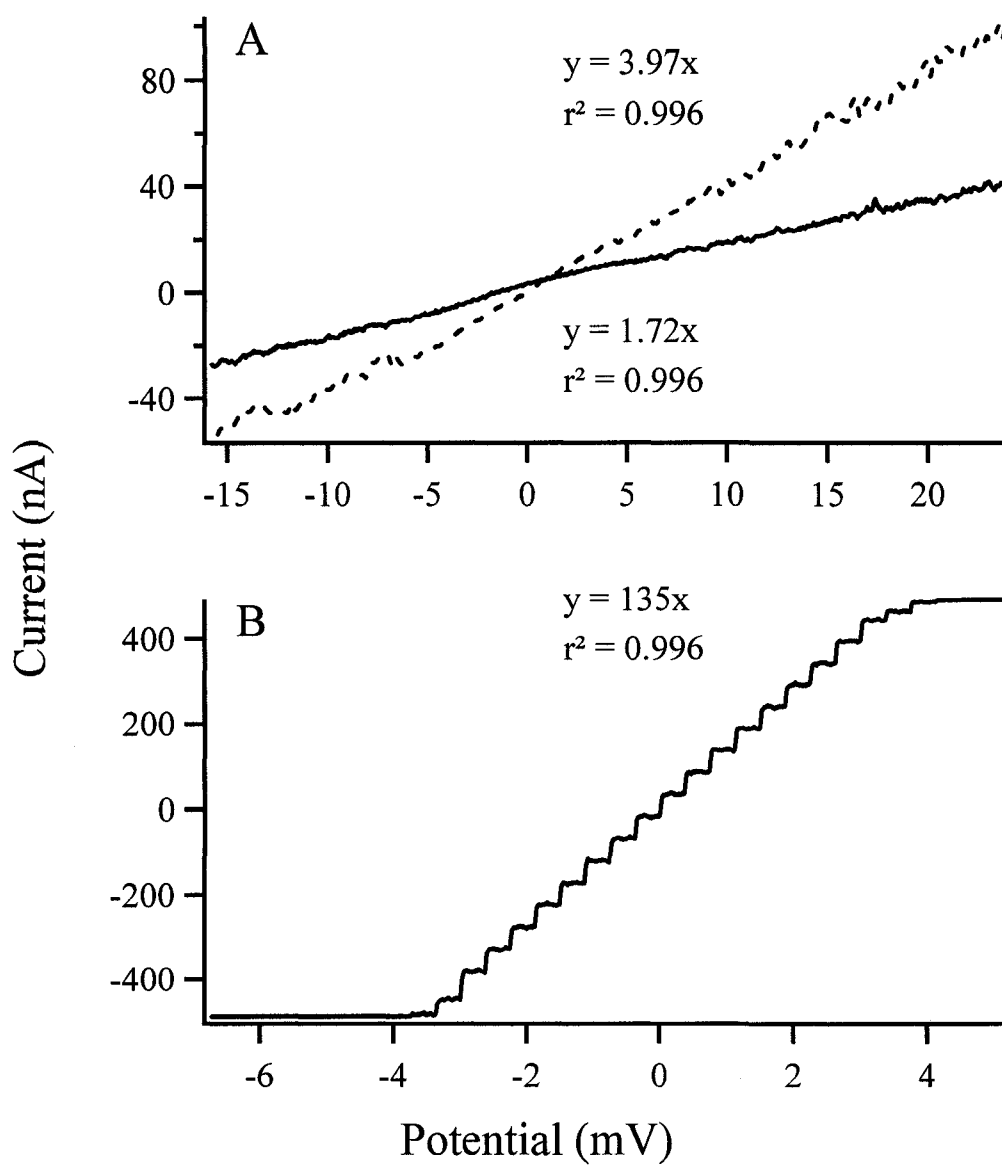


Figure 2.07. IV curves of EB50 measured with C-AFM at a tip-sample contact force of 28 nN. A) non-pyrolyzed, Bulk – dotted and “on spot” - solid B) pyrolysed.

3.3 Electrochemical Properties

Electrochemical characterization was performed by measuring electron transfer and adsorption with standard electrochemical redox systems for carbon electrodes. The heterogeneous electron transfer rate constants, k^o , were calculated from cyclic voltammetric peak separation values (ΔE_p) using the method described by Nicholson.⁵ The relevant expression is given in equation 2.03, where α is transfer coefficient and assumed to be 0.5; D_O is the diffusion coefficient of the oxidized species; D_R is the diffusion coefficient of the reduced species; ν is the scan rate; n is the electrons per molecule oxidized or reduced and is equal to one; F is Faraday's constant and is $96485.31 \text{ C}\cdot\text{mol}^{-1}$, R_g is the molar gas constant and is $8.31451 \text{ J}\cdot\text{mol}^{-1}\text{K}^{-1}$; T is the temperature, and ψ is the kinetic parameter as described by Nicholson.⁵ In practice, ΔE_p values are used to find tabulated ψ values. The heterogeneous electron transfer rate constant, k^o , is then calculated from equation 2.03.

$$\psi = \frac{\left(\frac{D_O}{D_R}\right)^{\alpha/2} k^o}{[D_O \pi \nu (nF / R_g T)]^{1/2}}$$

Equation 2.03. Definition of a quasi-reversible reaction.

The measured ΔE_p values used to calculate the heterogeneous electron transfer rate constants were corrected for uncompensated cell resistance using a method previously used for pyrolyzed photoresist films⁶ using equation 2.04 where $\Delta E_{p,corr}$ is the corrected ΔE_p (V), $\Delta E_{p,obs}$ is the measured ΔE_p (V), i is the voltammetric peak current (A) and R_u is the uncompensated cell resistance (Ω).

$$\Delta E_{p,corr} = \Delta E_{p,obs} - 2 |i| R_u$$

Equation 2.04. Uncompensated cell resistance determination

Aqueous solutions of potassium ferricyanide and potassium chloride were used as the redox system to determine the uncompensated cell resistance. The uncompensated cell resistance was calculated from the slopes of the plots of $\Delta E_{p,obs}$ versus i at a variety of concentrations and scan rates near the experimental conditions used for the heterogeneous electron transfer rate constant determination. The cyclic voltammograms used to determine the uncompensated cell resistance are presented in figures 2.08 to 2.11. The resulting plots of $\Delta E_{p,obs}$ versus i is presented in figure 2.12. The uncompensated cell resistance value used to calculate $\Delta E_{p,corr}$ was the average from each of the slopes in figure 2.12, the uncompensated cell resistance was 120 Ω .

The determined heterogeneous electron transfer rate constants for the studied single electron redox systems, and the measured ΔE_p for dopamine, are used to compare the films used in this work to similar electron beam deposited films, pyrolyzed photoresist films, as well as glassy carbon electrodes.

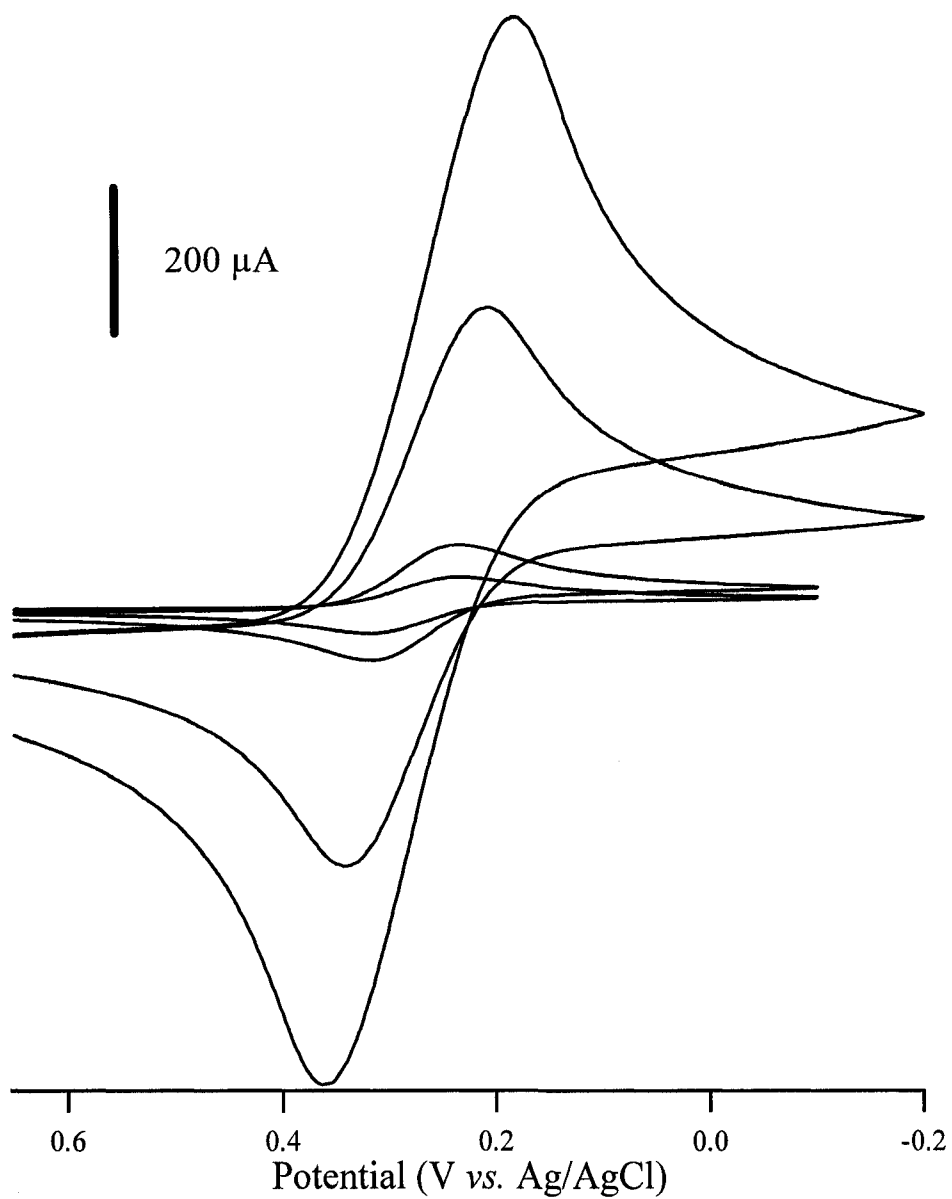


Figure 2.08. Cyclic voltammetry of $\text{Fe}(\text{CN})_6^{3-/4-}$ on EB50 in 1 M KCl. From lowest current to highest current, concentrations of 0.1, 1, 5, and 10 mM at 100 mV/s.

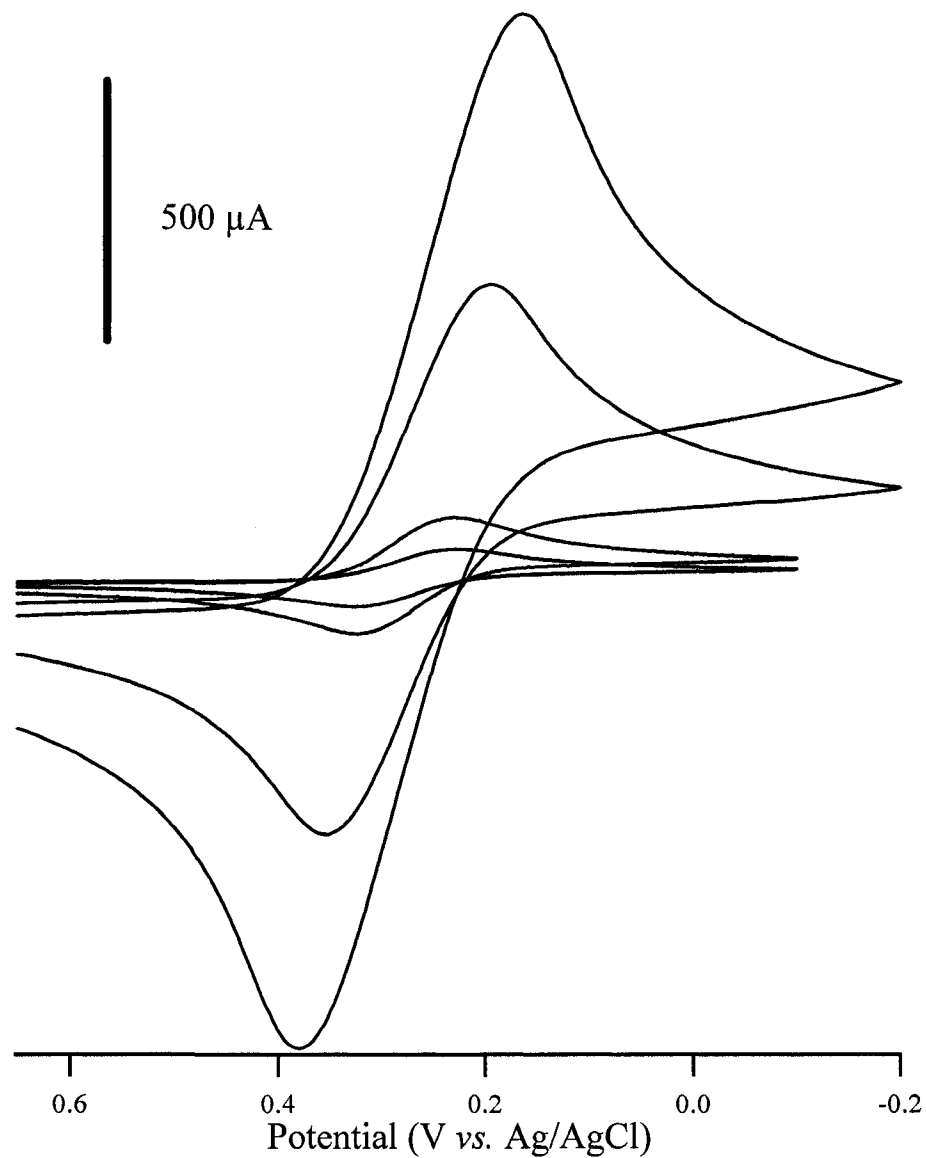


Figure 2.09. Cyclic voltammetry of $\text{Fe}(\text{CN})_6^{3-/4-}$ on EB50 in 1 M KCl. From lowest current to highest current, concentrations of 0.1, 1, 5, and 10 mM at 200 mV/s.

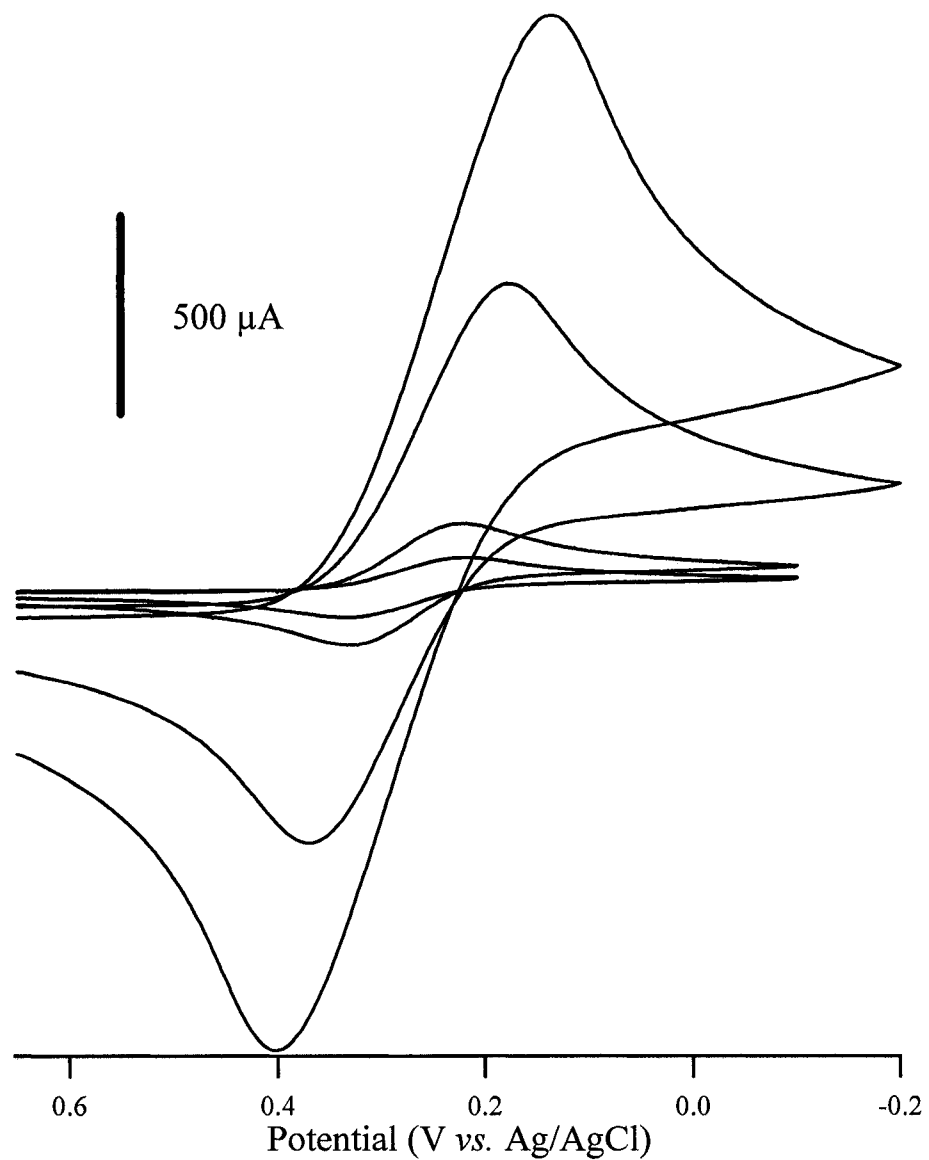


Figure 2.10. Cyclic voltammetry of $\text{Fe}(\text{CN})_6^{3-/4-}$ on EB50 in 1 M KCl. From lowest current to highest current, concentrations of 0.1, 1, 5, and 10 mM at 400 mV/s.

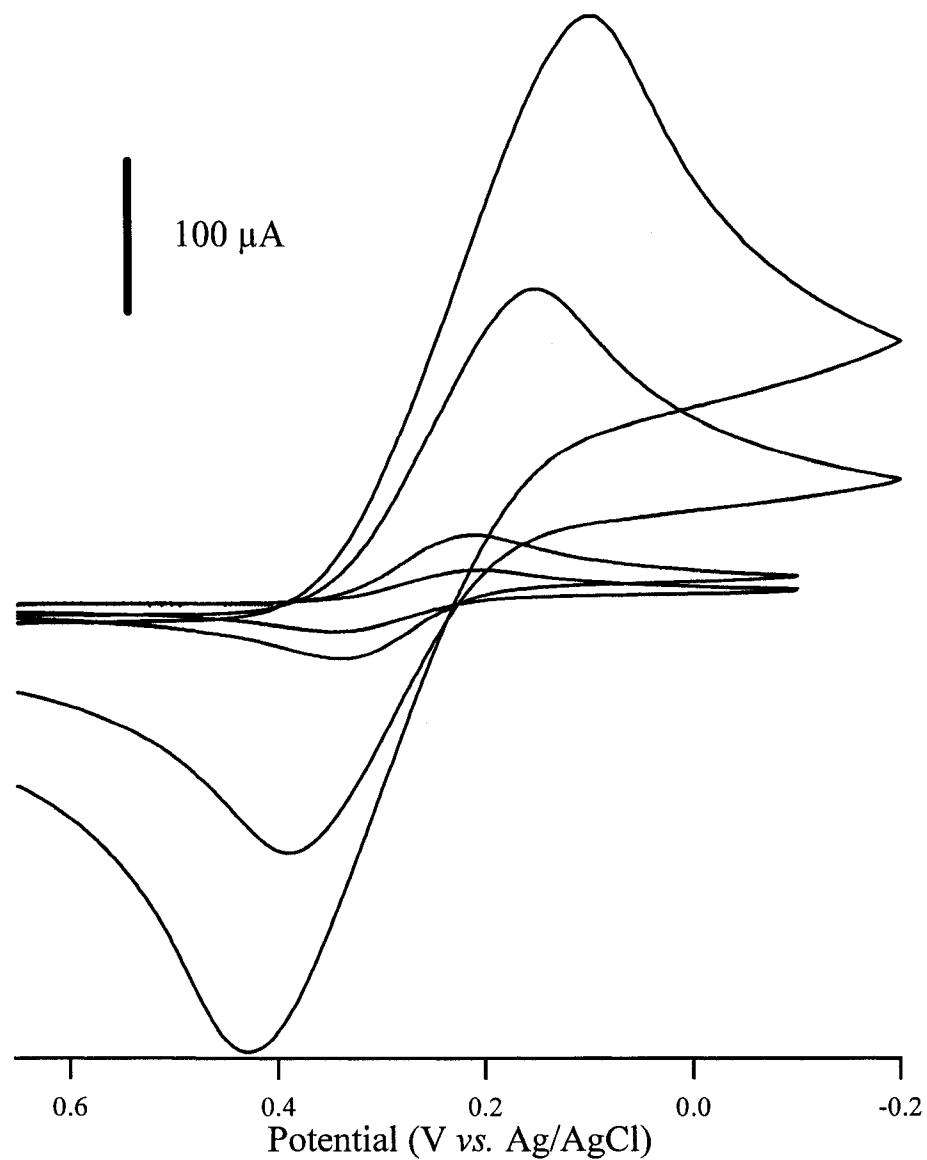


Figure 2.11. Cyclic voltammetry of $\text{Fe}(\text{CN})_6^{3-/4-}$ on EB50 in 1 M KCl. From lowest current to highest current, concentrations of 0.1, 1, 5, and 10 mM at 800 mV/s.

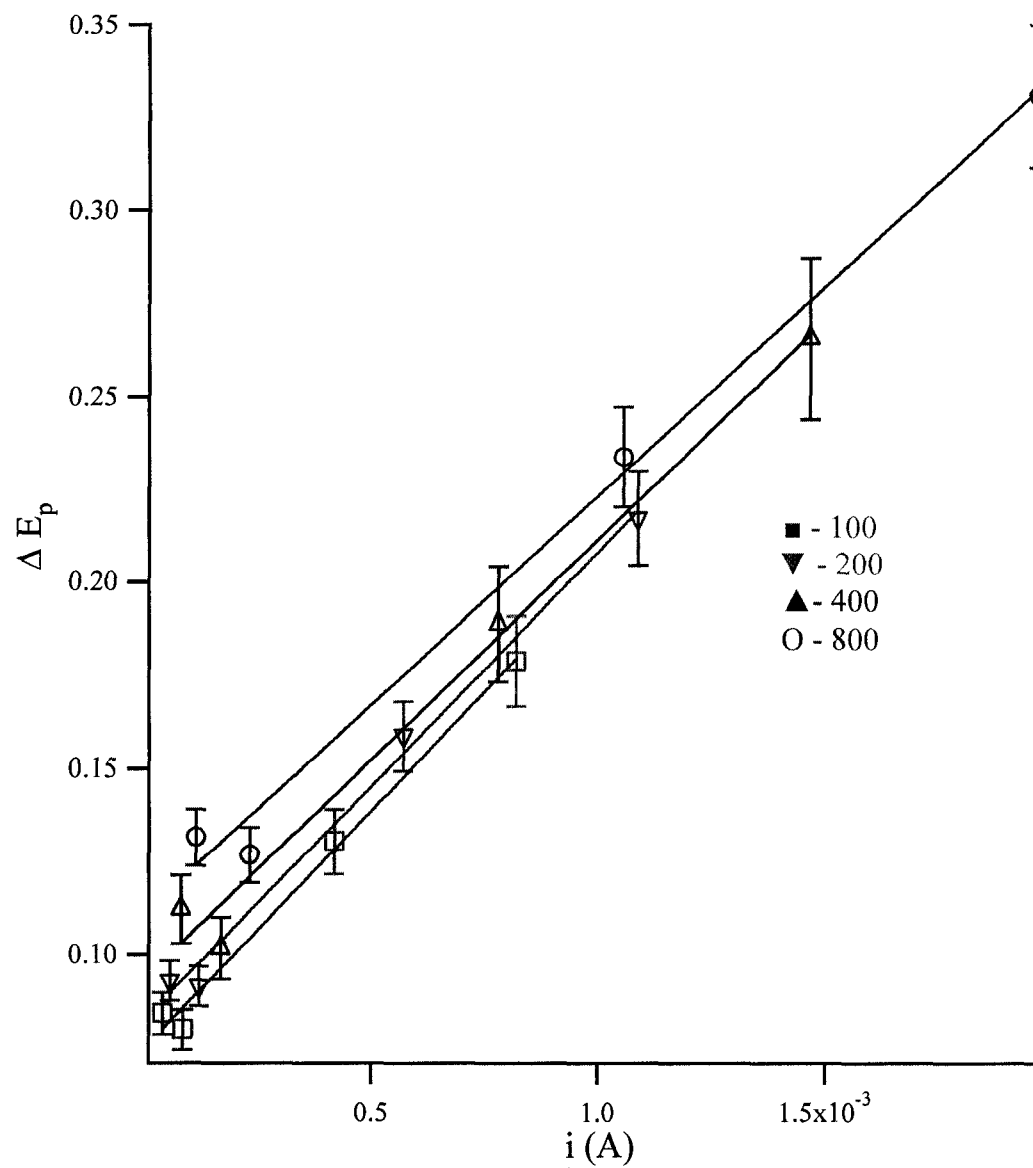


Figure 2.12. ΔE_p and current for CV's of $\text{Fe}(\text{CN})_6^{3-/4-}$ scan rates of 100, 200, 400, and 800 mV/s concentrations of 0.1, 1, 5, and 10 mM.

Redox species for determining the electron transport properties of EB50 films were chosen based on their well-studied and known kinetic behaviour on carbon electrodes. The redox species selected were dopamine, $\text{Eu}^{3+/2+}$, ferrocene, $\text{Ru}(\text{NH}_3)_6^{3+/2+}$, and $\text{Fe}(\text{CN})_6^{3-/4-}$. Dopamine oxidation has been shown to involve adsorption to oxide-free areas of carbon electrodes.⁷ Dopamine is known to be a good probe for detection of pin-holes in films on carbon. Although not directly suitable for quantitative electron transfer determination it is useful for assessing diazonium derived films discussed later in this thesis and thus the response on unmodified EB50 is presented here. The cyclic voltammetry behaviour of dopamine is shown in figure 2.13, with cyclic voltammograms of aqueous dopamine in 0.1 M H_2SO_4 . The measured ΔE_p of dopamine on EB50 at 200 mV/s is 298 mV. Similar 200 nm thick films have ΔE_p of 243 ± 13 mV⁴ for nonpyrolyzed films and glassy carbon has reported dopamine ΔE_p values of 107,⁴ 74,⁶ and 67⁷ mV at 200 mV/s. The results reported in this work are 12% greater than previously published results of similar films.⁴ Full ΔE_p results for dopamine, both uncorrected and corrected, are listed in table 2.02.

Scan Rate (mV/s)	ΔE_p (mV)	Standard Deviation (mV)	ΔE_p Corrected (mV)	Standard Deviation (mV)
800	380	60	330	60
400	340	6	300	60
200	300	70	270	70
100	260	70	240	70
50	240	80	220	80

Table 2.02. ΔE_p of dopamine on EB50 in 0.1 M H₂SO₄.

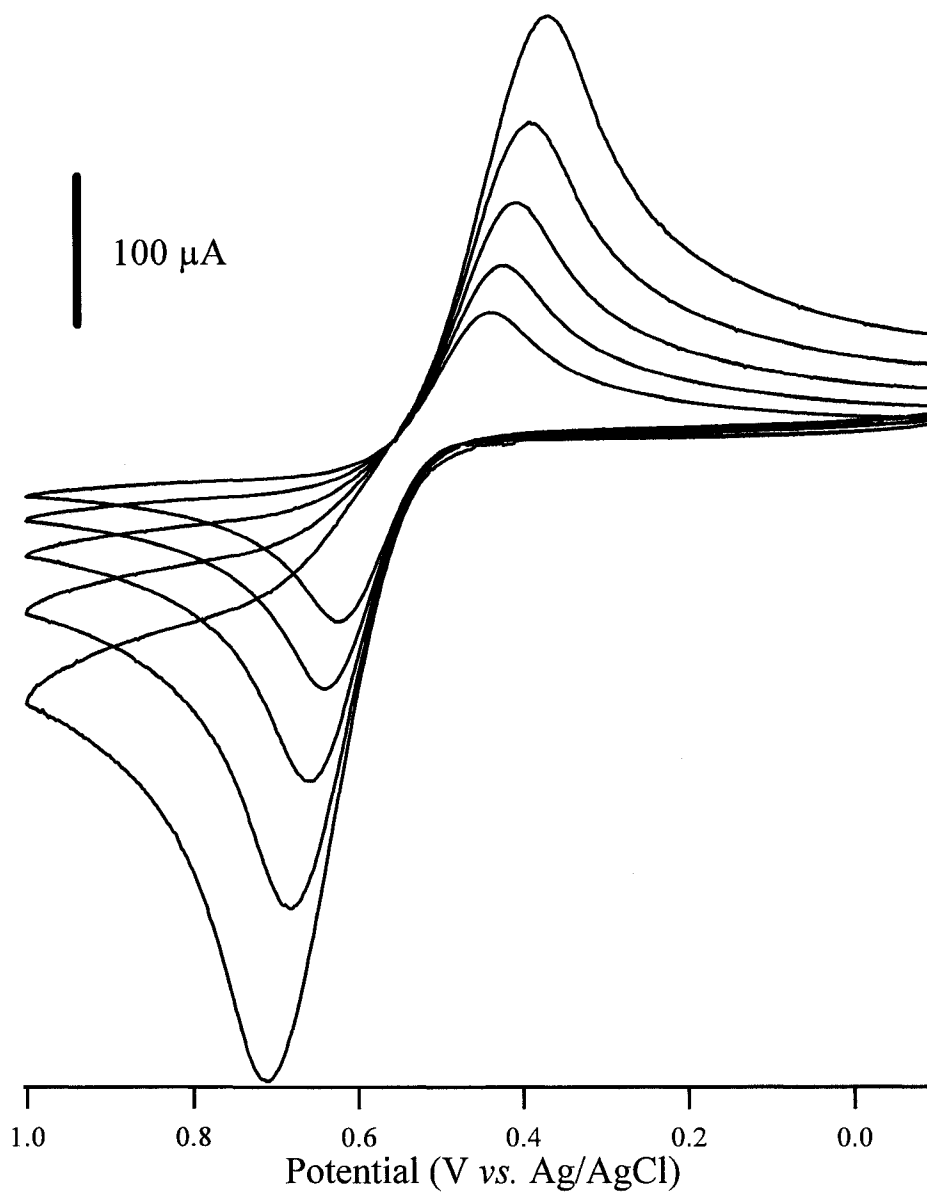


Figure 2.13. Cyclic voltammetry of dopamine on EB50 in 0.1 M H₂SO₄. (from lowest peak current to highest current) at 50, 100, 200, 400 and 800 mV/s.

Cyclic voltammograms for $\text{Eu}^{3+/2+}$ (in 0.2 M NaClO_4) are shown in figure 2.14. The calculated heterogeneous electron-transfer rate constants for $\text{Eu}^{3+/2+}$ are $< 1.6 \pm 0.8 \times 10^{-3}$ uncorrected as well as $< 1.6 \pm 0.8 \times 10^{-3}$ corrected. No change in heterogeneous electron-transfer rate constant is observed when comparing the corrected to the uncorrected value due to the shape of the Ψ vs. ΔE_p graph⁵ at large ΔE_p values. The graph plateaus near ΔE_p of 120 mV, in the irreversible region, thus a large change in ΔE_p results in a very small change in the Ψ value. The diffusion coefficient for both the reduced and oxidized form of europium is $7.90 \times 10^{-6} \text{ cm}^2 \text{ s}^{-1}$.⁴ The electroactivity of $\text{Eu}^{2+/3+}$ has been shown to be very sensitive to, and dependent on the presence of surface bound carbonyl functionalities on carbon electrodes.^{8,9} The oxygen contained in the EB50 was determined to be about 4% by mass. The reported values of oxygen content for polished glassy carbon are typically around 8%.^{6, 10} Under the conditions used in these experiments the heterogeneous electron-transfer rate constant for $\text{Eu}^{3+/2+}$ could not be quantitatively determined and is reported as a “less than” value, nonetheless it agrees with the literature values reported for similar electron-beam deposited films⁴ as well as polished glassy carbon electrodes that contain approximately twice the amount of oxygen. Summarized electrochemical data for $\text{Eu}^{3+/2+}$ on EB50 is presented in table 2.03.

Scan Rate (mV/s)	ΔE_p (mV)	ΔE_p Corrected (mV)	k^0	k^0 Corrected
800	670	613	0.00278	0.00278
400	547	504	0.00197	0.00197
200	443	418	0.00139	0.00139
100	355	335	0.000983	0.000983
50	283	263	0.000695	0.000695

Table 2.03. Summarized electrochemical data for $\text{Eu}^{3+/2+}$ on EB50.

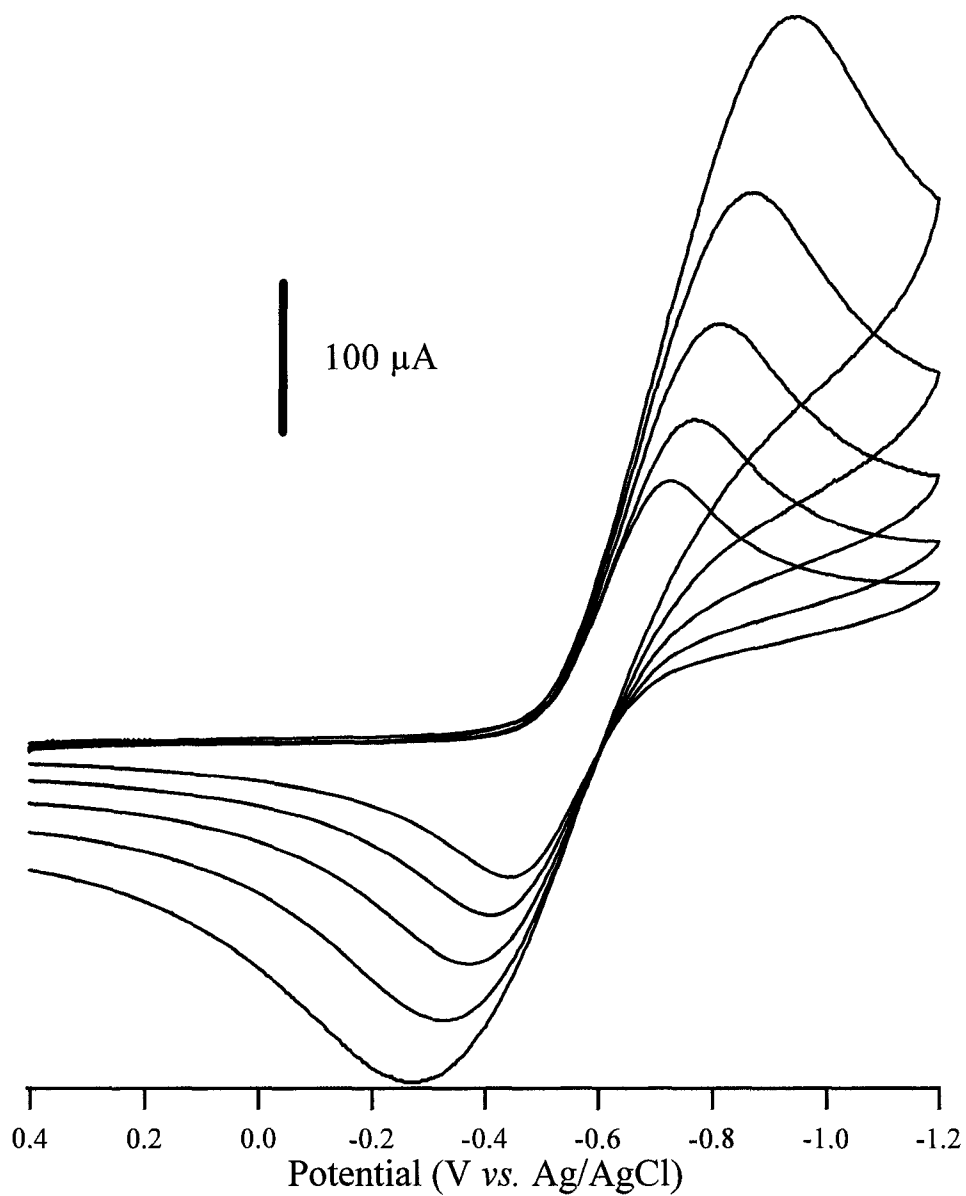


Figure 2.14. Cyclic voltammetry of Eu^{3+/2+} on EB50 in 0.2 M NaClO₄ (from lowest peak current to highest current) at 50, 100, 200, 400 and 800 mV/s.

Cyclic voltammograms for ferrocene (in 0.1 M tetrabutylammonium tetrafluoroborate in acetonitrile) are shown in figure 2.15. Ferrocene is an outer-sphere redox system and has been shown to be relatively insensitive to surface preparation.¹¹⁻¹³ The diffusion coefficient used for both the reduced and oxidized form of ferrocene was $2.40 \times 10^{-5} \text{ cm}^2 \text{ s}^{-1}$.⁴ The measured ΔE_p values, corrected ΔE_p values, and calculated heterogeneous electron-transfer rate constants for ferrocene are presented in table 2.04. The calculated heterogeneous electron-transfer rate constants for ferrocene are $5.1 \pm 0.5 \times 10^{-3}$ uncorrected as well as $6.5 \pm 1 \times 10^{-3}$ corrected. The literature values for k^o on glassy carbon is 1.8×10^{-3} and 2.1×10^{-3} for 200 nm thick electron beam deposited carbon films. Thus, EB50 films show similar electrochemical reactivity to outer-sphere redox systems on GC and other carbon film electrodes.

Scan Rate (mV/s)	ΔE_p (mV)	ΔE_p Corrected (mV)	k^o	k^o Corrected
800	243	204	0.00485	0.00569
400	196	166	0.00461	0.00677
200	160	145	0.00507	0.00588
100	134	124	0.00485	0.00574
50	102	95.76	0.00593	0.00821

Table 2.04. Summarized electrochemical data for ferrocene on EB50.

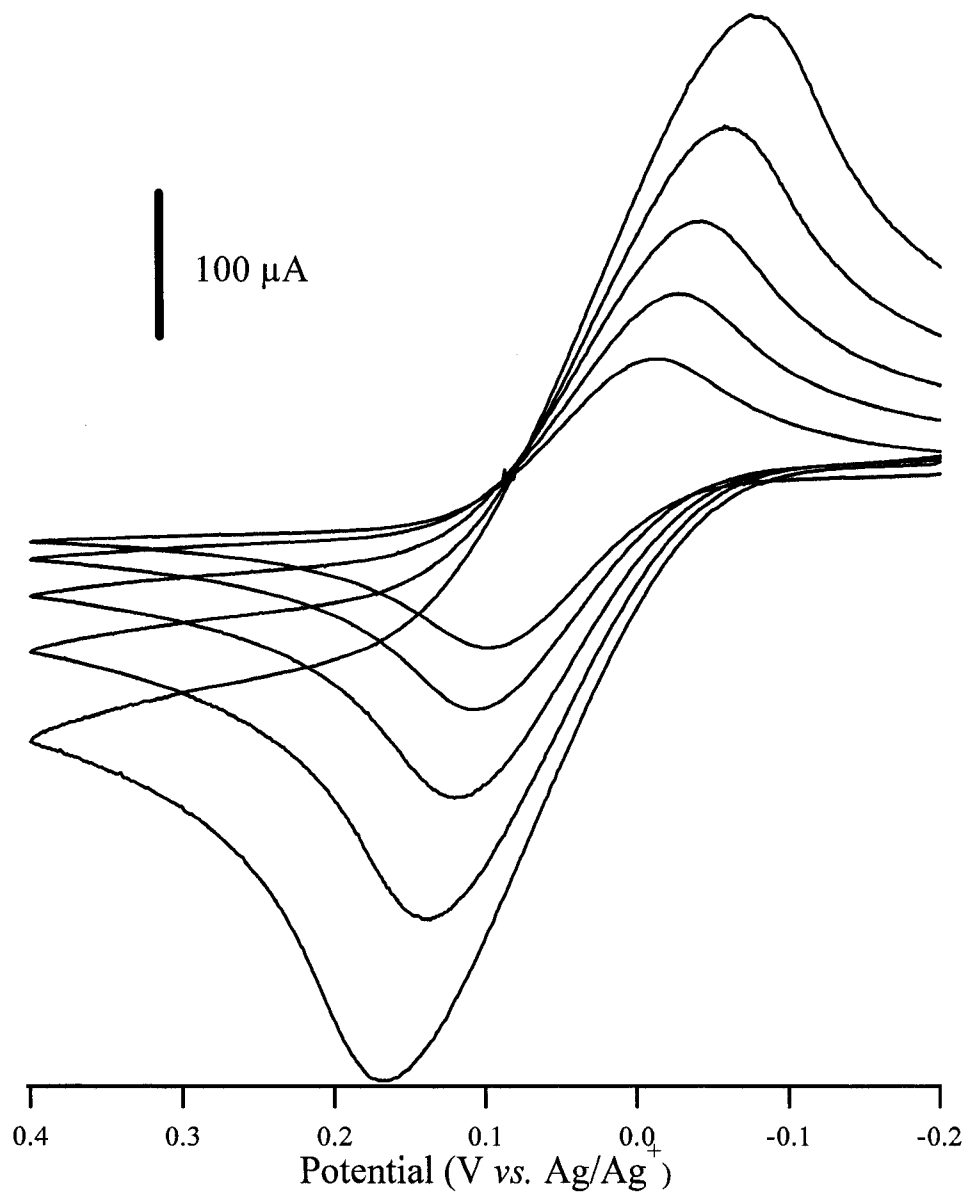


Figure 2.15. Cyclic voltammetry of ferrocene on EB50 and 0.1 M tetrabutylammonium tetrafluoroborate in acetonitrile (from lowest peak current to highest current) at 50, 100, 200, 400 and 800 mV/s.

Cyclic voltammograms for $\text{Ru}(\text{NH}_3)_6^{3+/2+}$ (in 1M KCl) are shown in figure 2.16. Similar to ferrocene, $\text{Ru}(\text{NH}_3)_6^{3+/2+}$ is an outer-sphere redox system and has also been shown to be relatively insensitive to surface preparation.¹¹⁻¹³ The diffusion coefficient used for both the reduced and oxidized form of ruthenium hexamine was 6.50×10^{-6} .⁴ The measured ΔE_p values, corrected ΔE_p values, and calculated heterogeneous electron-transfer rate constants for $\text{Ru}(\text{NH}_3)_6^{3+/2+}$ are presented in table 2.05. The calculated heterogeneous electron-transfer rate constants for $\text{Ru}(\text{NH}_3)_6^{3+/2+}$ are $4.4 \pm 4.7 \times 10^{-2}$ uncorrected and approach infinity, reversible, for the corrected rate constant. Although electron transport between $\text{Ru}(\text{NH}_3)_6^{3+/2+}$ and EB50 films appears to be reversible for scan rates less than 400 mV/s, the system should still be considered as quasi-reversible as the peak positions, both corrected and uncorrected, change with scan rate. This is a property inherent only to quasi-reversible redox systems in cyclic voltammetry.¹⁴

Scan Rate (mV/s)	ΔE_p (mV)	ΔE_p Corrected (mV)	k^0	k^0 Corrected
800	106	73.2	0.0125	0.0479
400	81	58.3	0.0218	∞
200	73	56.7	0.0241	∞
100	66	54.3	0.0357	∞
50	58	49.5	0.126	∞

Table 2.05. Summarized electrochemical data for $\text{Ru}(\text{NH}_3)_6^{3+/2+}$ on EB50

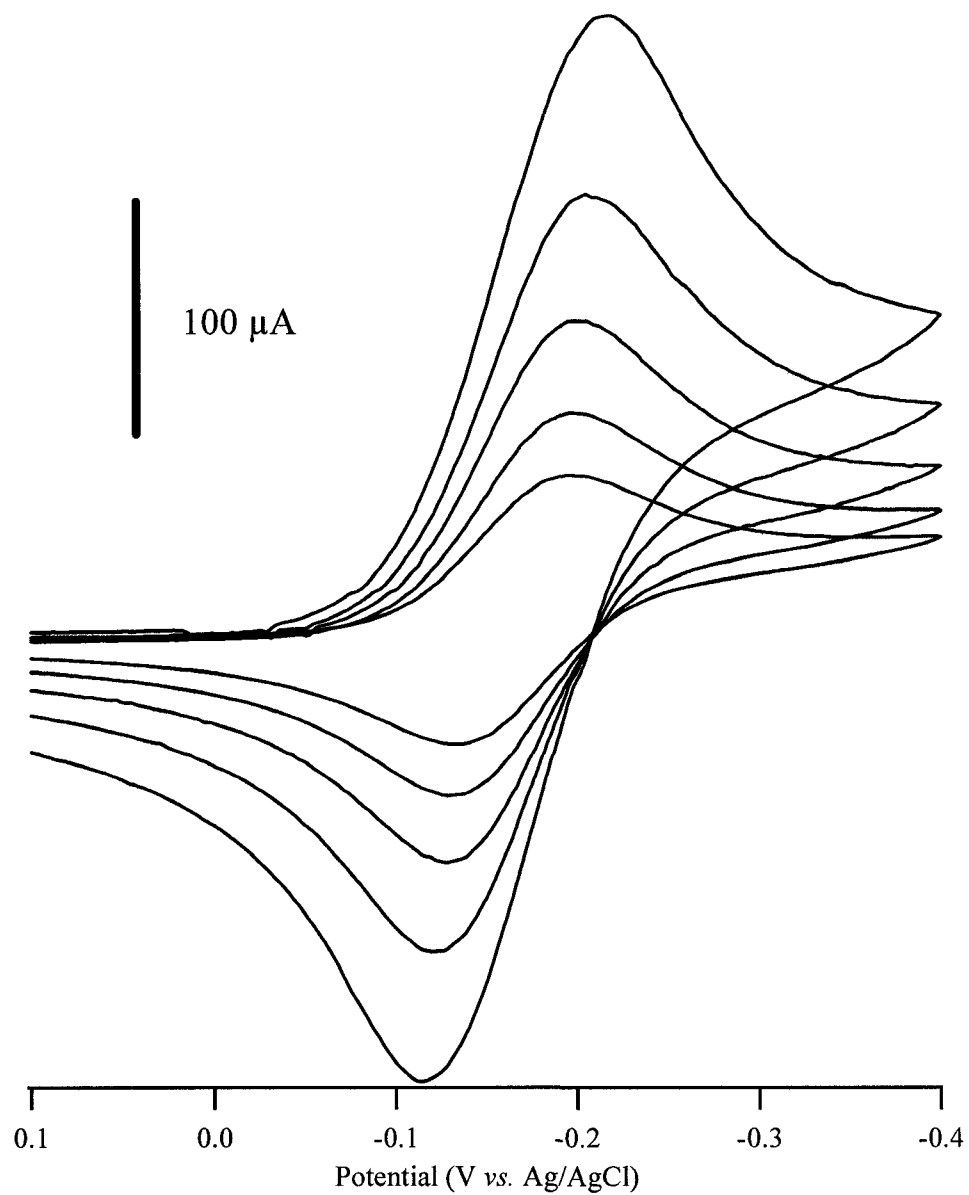


Figure 2.16. Cyclic voltammetry of Ru(NH₃)₆^{3+/2+} on EB50 in 1M KCl (from lowest peak current to highest current) at 50, 100, 200, 400 and 800 mV/s.

Figure 2.17 shows typical cyclic voltammograms for potassium ferrocyanide (in 1M KCl). The diffusion coefficient used for ferricyanide (D_o) was 6.32×10^{-6} and the diffusion coefficient used for ferrocyanide (D_R) was 7.63×10^{-6} .⁴ The measured ΔE_p values, corrected ΔE_p values, and calculated heterogeneous electron-transfer rate constants for $\text{Fe}(\text{CN})_6^{3-/4-}$ are presented in table 2.06. The calculated heterogeneous electron-transfer rate constants for $\text{Fe}(\text{CN})_6^{3-/4-}$ are $2.8 \pm 0.3 \times 10^{-3}$ uncorrected as well as $2.9 \pm 0.2 \times 10^{-3}$ corrected. The literature values for k^o on glassy carbon are 8×10^{-3} and $5.7 \pm 0.97 \times 10^{-3}$ for 200 nm thick electron beam deposited carbon films.

Scan Rate (mV/s)	ΔE_p (mV)	ΔE_p Corrected (mV)	k^o	k^o Corrected
800	248	224	0.00261	0.00261
400	206	188	0.00206	0.00278
200	168	155	0.00252	0.00288
100	137	127	0.00249	0.00294
50	113	106	0.00274	0.00318

Table 2.06. Summarized electrochemical data for $\text{Fe}(\text{CN})_6^{3-/4-}$ on EB50

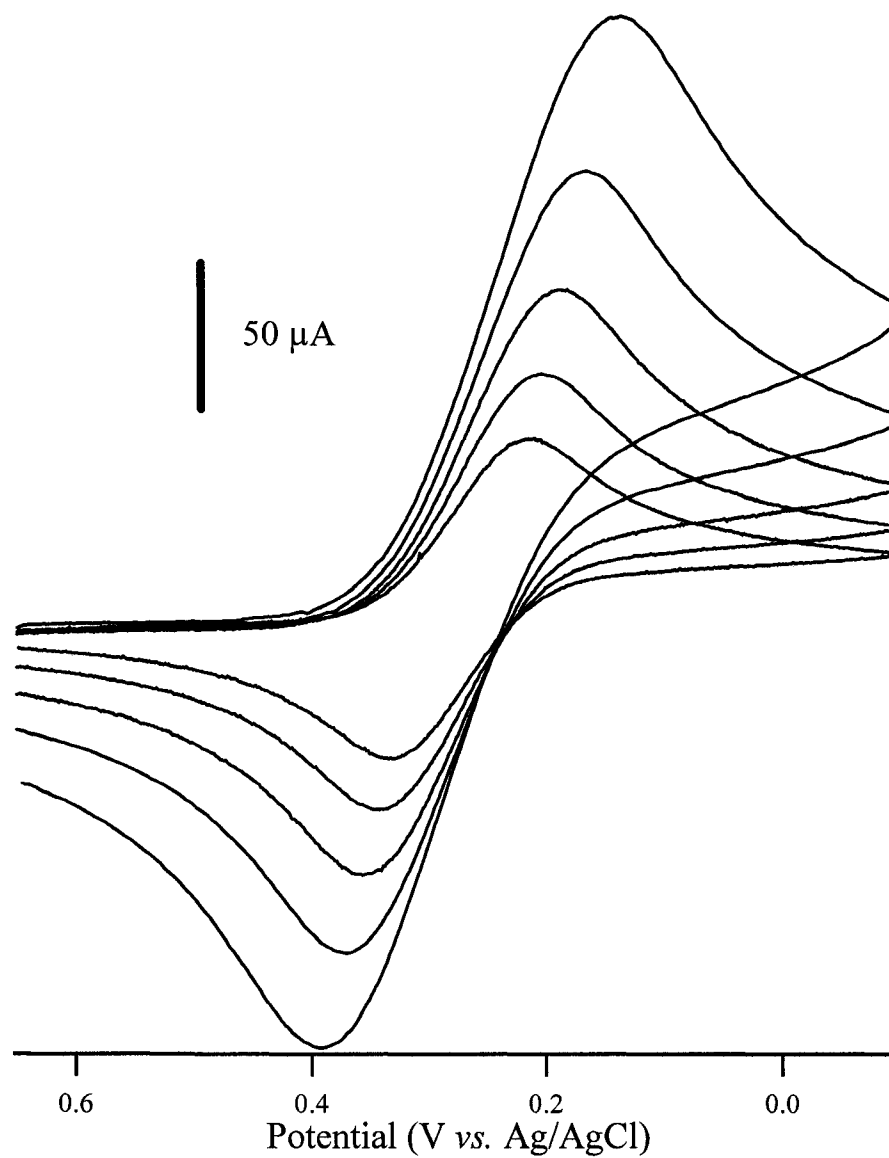


Figure 2.17. Cyclic voltammetry of $\text{Fe}(\text{CN})_6^{3-/4-}$ on EB50 in 1M KCl (from lowest peak current to highest current) at 50, 100, 200, 400 and 800 mV/s.

The electrochemical electron transport data is summarized below in table 2.07. Literature values for similar 200 nm thick electron beam deposited carbon films as well as glassy carbon are also presented. All of the calculated k^o values agree well with the reported values for similar 200 nm thick films. In each case the values are the same order of magnitude and are within a factor of approximately two with respect to each other. The only anomaly is the calculated k^o for $\text{Eu}^{3+/2+}$; the scan rates used in this work were not sufficient to calculate k^o values less than $< 1.6 \pm 0.8 \times 10^{-3}$. Despite the semi-quantitative results for $\text{Eu}^{3+/2+}$, the results do agree with the reported literature values.

Redox System	k^o	k^o corrected	k^o corrected 200 nm film	Ref	k^o Glassy Carbon	Ref
$\text{Eu}^{3+/2+}$	$< 1.6 \pm 0.8 \times 10^{-3}$	$< 1.6 \pm 0.8 \times 10^{-3}$	$5.3 \pm 2.6 \times 10^{-4}$	⁴	3.2×10^{-4}	¹⁰
Ferrocene	$5.1 \pm 0.5 \times 10^{-3}$	$6.5 \pm 1 \times 10^{-3}$	$2.1 \pm 0.63 \times 10^{-3}$	⁴	1.8×10^{-3}	⁴
$\text{Fe}(\text{CN})_6^{3-/4-}$	$2.8 \pm 0.3 \times 10^{-3}$	$2.9 \pm 0.2 \times 10^{-3}$	$5.7 \pm 0.97 \times 10^{-3}$	⁴	8×10^{-3} (25%)	¹⁰
$\text{Ru}(\text{NH}_3)_6^{3+/2+}$	$4.4 \pm 4.7 \times 10^{-2}$	N/A	$4.3 \pm 0.60 \times 10^{-2}$	⁴	1.9×10^{-2}	¹⁰

Table 2.07. Heterogeneous electron-transfer rate constants of studied redox systems on EB50 and similar materials.

3.4 Elemental and Chemical Analysis

X-ray photoelectron spectroscopy (XPS) was used to perform quantitative elemental analysis of the EB50 carbon films. The films were allowed to equilibrate with atmospheric oxygen for at least 24 hours in a desiccator before analysis. As expected the major detected element measured in the EB50 films was carbon, making up nearly 96% of the total film. The only other detectable element contained in the films was oxygen at about 4%. The summarized XPS data is presented in table 2.08. Represented in the table are the elemental peak, the binding energy (BE) position, the full width at half maximum (FWHM), the peak raw area in counts per second (CPS), the relative sensitivity factor (RSF), the atomic mass of the element, the atomic concentration, and the mass concentration. The survey spectrum for a typical EB50 film is presented in figure 2.18. The relatively low amount of oxygen measured by XPS supports the reduced electrochemical reactivity of the films towards $\text{Eu}^{2+/3+}$, as previously discussed.

Peak	Position BE (eV)	FWHM (eV)	Raw Area (CPS)	RSF	Atomic Mass	Atomic Conc %	Mass Conc %
O 1s	532.293	3.518	50188.6	0.780	15.999	3.07	4.05
C 1s	284.463	2.804	535033.2	0.278	12.011	96.93	95.95

Table 2.08. X-Ray Photoelectron Spectroscopy of 50 nm thick electron beam evaporated carbon.

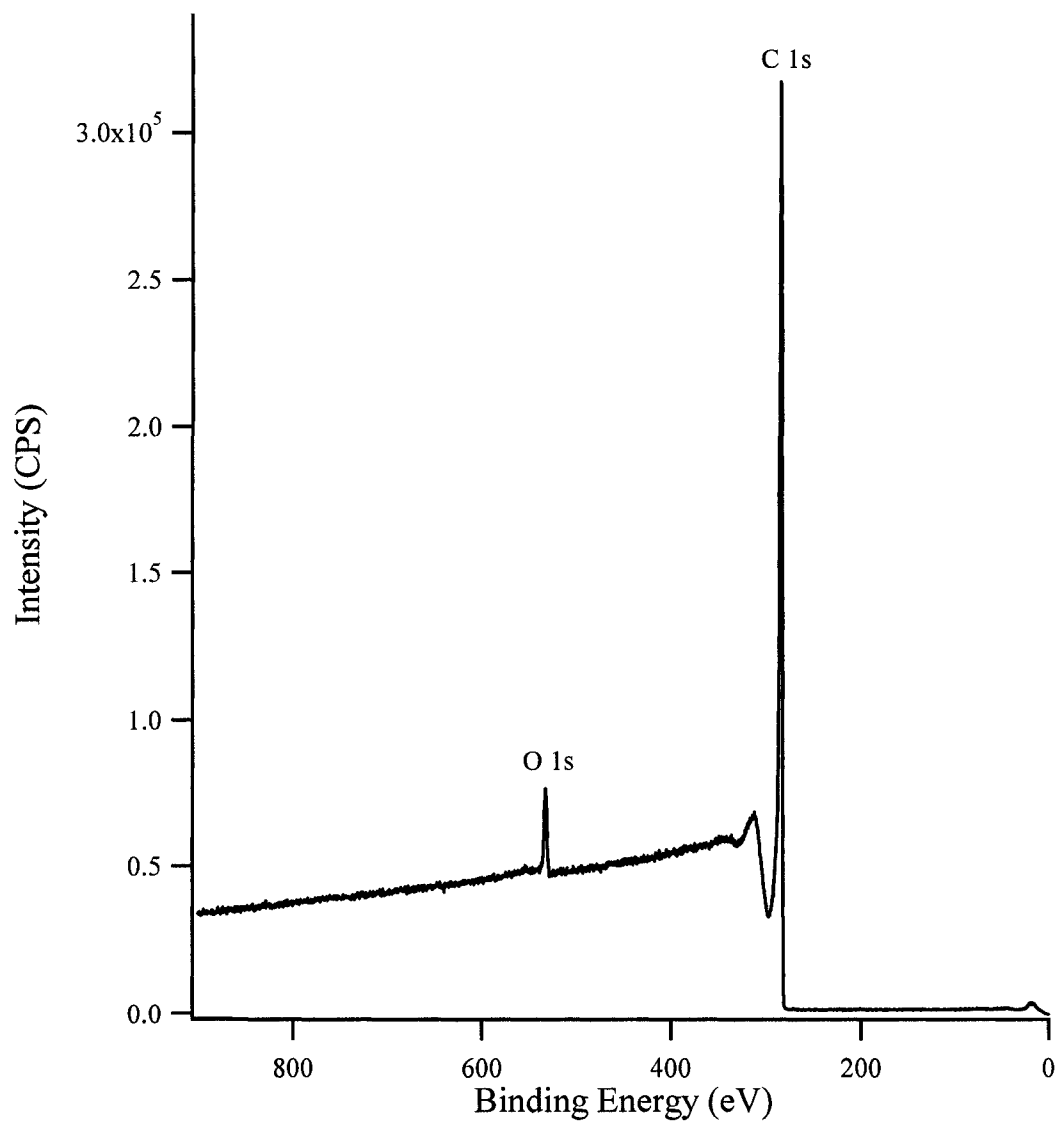


Figure 2.18. X-ray Photoelectron Spectroscopy of 50 nm thick electron beam evaporated carbon film.

Raman spectroscopy was used to elucidate micro-structural information about the EB50 films. In particular, Raman spectroscopy has been shown to be a suitable probe for determining graphitic crystallite sizes. A typical Raman spectrum of EB50 is presented in figure 2.19. The penetration depth of the laser used is greater than the thickness of the films. This is demonstrated by the presence of a Si-O band at 986 cm^{-1} . The Si peak is also observable at 520 cm^{-1} (not shown). The disordered carbon band is visible at 1406 cm^{-1} and the graphitic carbon band is visible at 1574 cm^{-1} . The graphitic carbon band is a near perfect match for the literature value reported for the single Raman peak at 1575 cm^{-1} for single crystal graphite.¹⁵ The disordered carbon band is shifted about 16 cm^{-1} towards higher wavenumbers from the reported literature values of $1350\text{-}1390\text{ cm}^{-1}$.³ The presence of two distinct, yet overlapped carbon peaks present in the Raman spectrum indicates a higher level of graphitization of the 50 nm thick carbon films compared to the 200 nm thick films reported by McDermott.⁴ The peak shift of the disordered carbon band towards the graphitic carbon band indicates the low degree of graphitization in these films compared to more highly graphitized materials such as pyrolyzed electron beam deposited carbon films and glassy carbon. The lack of resolution between the 1406 and 1575 cm^{-1} peaks in figure 2.19 indicates that most of the material is amorphous.

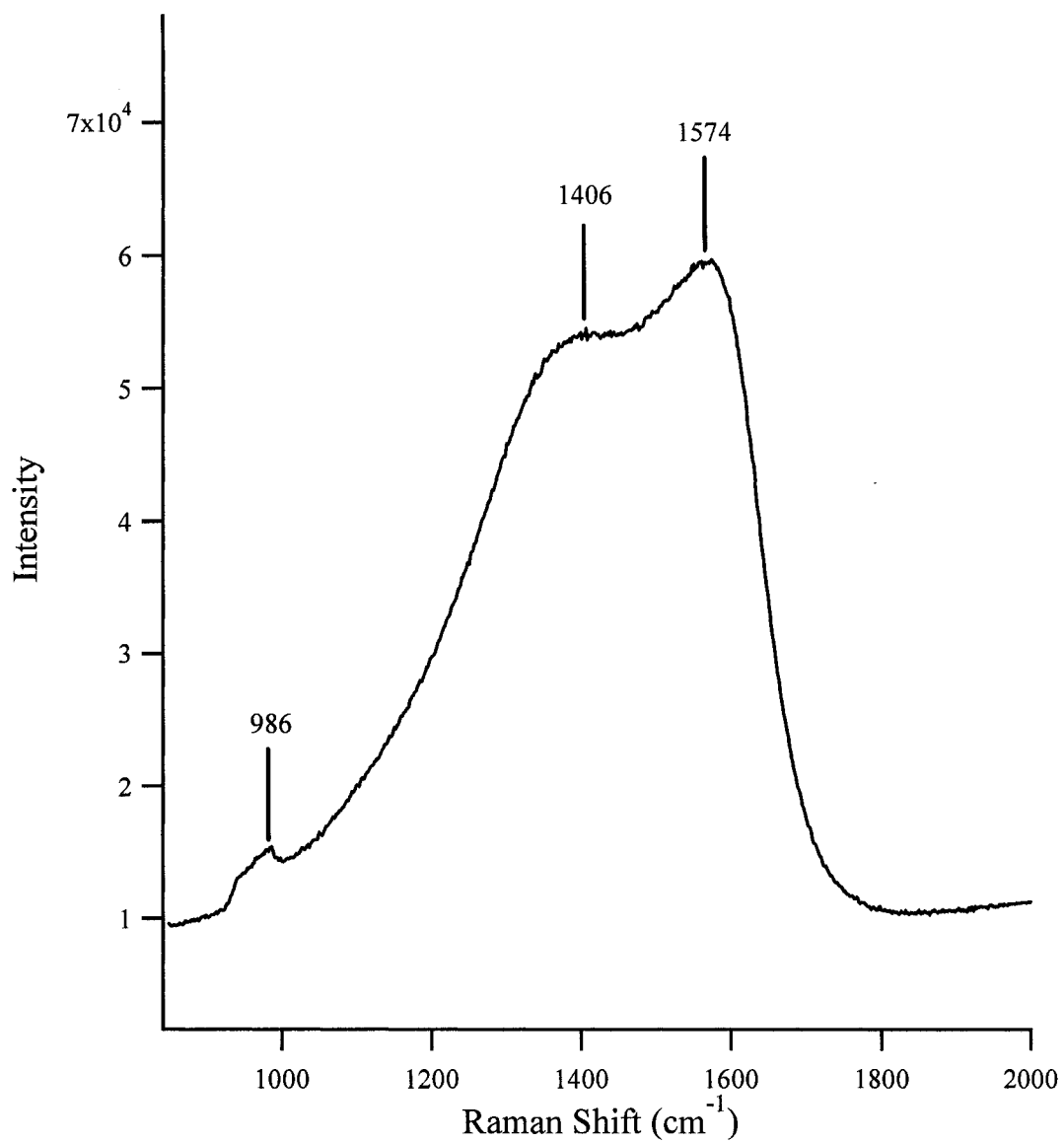


Figure 2.19. Raman spectrum of unmodified 50 nm thick electron beam evaporated carbon. Excitation line = 514.5 nm, exposure time = 10s, average of 64 scans.

4. Conclusions

Electron beam evaporated carbon films supported by Si(100) provide extremely flat (<1 nm RMS) well-behaved electrodes. These films exhibit electrochemical performance just short of that observed for the ubiquitous glassy carbon and agree well with that for similar 200 nm thick films. The films were shown to be highly pure, consisting of approximately 96% carbon and 4% oxygen and contain graphitic crystallite sizes slightly less than pyrolyzed photo resist derived films, which will be discussed in later chapters. The low cost, ease of preparation, and parallel fabrication procedure of EB50 make it amenable to mass production of films for sensors and general electrochemical use.

References

- (1) Mattson, J. S.; Smith, C. A. *Analytical Chemistry* **1975**, *47*, 1122-1125.
- (2) Deangelis, T. P.; Hurst, R. W.; Yacyncych, A. M.; Mark, H. B.; Heineman, W. R.; Mattson, J. S. *Analytical Chemistry* **1977**, *49*, 1395-1398.
- (3) Besold, J.; Thielsch, R.; Matz, N.; Frenzel, C.; Born, R.; Mobius, A. *Thin Solid Films* **1997**, *293*, 96-102.
- (4) Blackstock, J. J.; Rostami, A. A.; Nowak, A. M.; McCreery, R. L.; Freeman, M. R.; McDermott, M. T. *Analytical Chemistry* **2004**, *76*, 2544-2552.
- (5) Nicholson, R. S. *Analytical Chemistry* **1965**, *37*, 1351-1355.
- (6) Ranganathan, S.; McCreery, R. L. *Analytical Chemistry* **2001**, *73*, 893-900.
- (7) DuVall, S. H.; McCreery, R. L. *Journal of the American Chemical Society* **2000**, *122*, 6759-6764.
- (8) McDermott, C. A.; Kneten, K. R.; McCreery, R. L. *Journal of the Electrochemical Society* **1993**, *140*, 2593-2599.
- (9) Chen, P. H.; Fryling, M. A.; McCreery, R. L. *Analytical Chemistry* **1995**, *67*, 3115-3122.
- (10) Kiema, G. K.; Aktay, M.; McDermott, M. T. *Journal of Electroanalytical Chemistry* **2003**, *540*, 7-15.
- (11) Chen, P. H.; McCreery, R. L. *Analytical Chemistry* **1996**, *68*, 3958-3965.
- (12) McCreery, R. L. *Electroanalytical Chemistry*; Bard, A. J. Ed; Dekker: New York, 1991.
- (13) McCreery, R. L. *Interfacial Electrochemistry*; Wieckowski, A., Ed; Dekker: New York, 1999.

- (14) Bard, A. J.; Faulkner, L. R. *Electrochemical methods : fundamentals and applications*; Wiley: New York ; Chichester, 1980.
- (15) Tuinstra, F.; Koenig, J. L. *Journal of Chemical Physics* **1970**, *53*, 1126-1130.

Chapter III

Attachment of Aryl Molecules to Ultra-flat Carbon

1. Introduction

The modification of graphitic carbon surfaces is a growing field in engineering and science. One of the most studied areas of carbon modification is the derivatization of electrodes.¹⁻¹⁶ Prior to 1992, the commonly used methods for covalent modification of carbon electrode surfaces involved attachment via the surface bonded oxygen functional groups. It was also common practice to oxidize the carbon surface to increase the number of surface-bound oxygen functional groups and thus increase the capability for further functionalization.¹⁻⁴ In 1992, Savéant introduced a new reductive method for the modification of carbon surfaces⁵ whereby an aryl diazonium (4-nitrophenyldiazonium tetrafluoroborate) was electrochemically reduced via cyclic voltammetry to a 4-nitrobenzene radical. The nitrobenzene radical then spontaneously attached to the working electrode, glassy carbon. A characteristic irreversible surface adsorption wave was visible followed by a reversible nitro reduction at a more negative potential. The surface adsorption wave was only present on the first scan, indicating the electrode was deactivated towards further radical formation. Savéant was able to modify the bound nitro group via electrochemical reduction to the amine as well as further modification via traditional amine chemistry. The reported diazonium derived layer was extremely stable and robust. The observed resilience was attributed to a covalent bond formed between the nitrobenzene and the carbon surface.

The use of aryl diazonium salts to modify carbon surfaces is a facile and desirable method. The diazoniums are synthesized from the corresponding amine precursor in a one pot reaction followed by crystallization.^{6,7} The initial synthesis of aryl diazoniums used aniline as the precursor leading to the simplest form, a phenyl diazonium ion^{6,7} but a wide variety of derivatives may be synthesized or purchased commercially.

The growth of diazonium derived layers on carbon electrodes, including highly oriented pyrolytic graphite and glassy carbon, was further studied by Kariuki.^{8,9} Thick films of diethylaniline (which has a molecule length of about 0.8 nm) were grown around polystyrene blocked areas of the electrode. The polystyrene was removed and film thicknesses were measured via AFM. The created films were up to 20 nm thick. It was reported that aryl diazonium ions were capable of forming multilayers when electrochemically deposited. As a result of these studies a mechanism, illustrated in figure 3.01, was proposed for the growth of diazonium derived multilayers.

The discovery, and explanation, of multilayer formation furthered the understanding and usefulness of aryl diazonium ions. However, it raised concerns about the ability to control fabricated film thicknesses. One aspiration for many researchers who deal with thin films is the ability to create a true monolayer. This was addressed by McCreery in a publication in 2003.¹⁰ McCreery demonstrated that with careful control of all deposition conditions, diazonium derived aryl monolayers

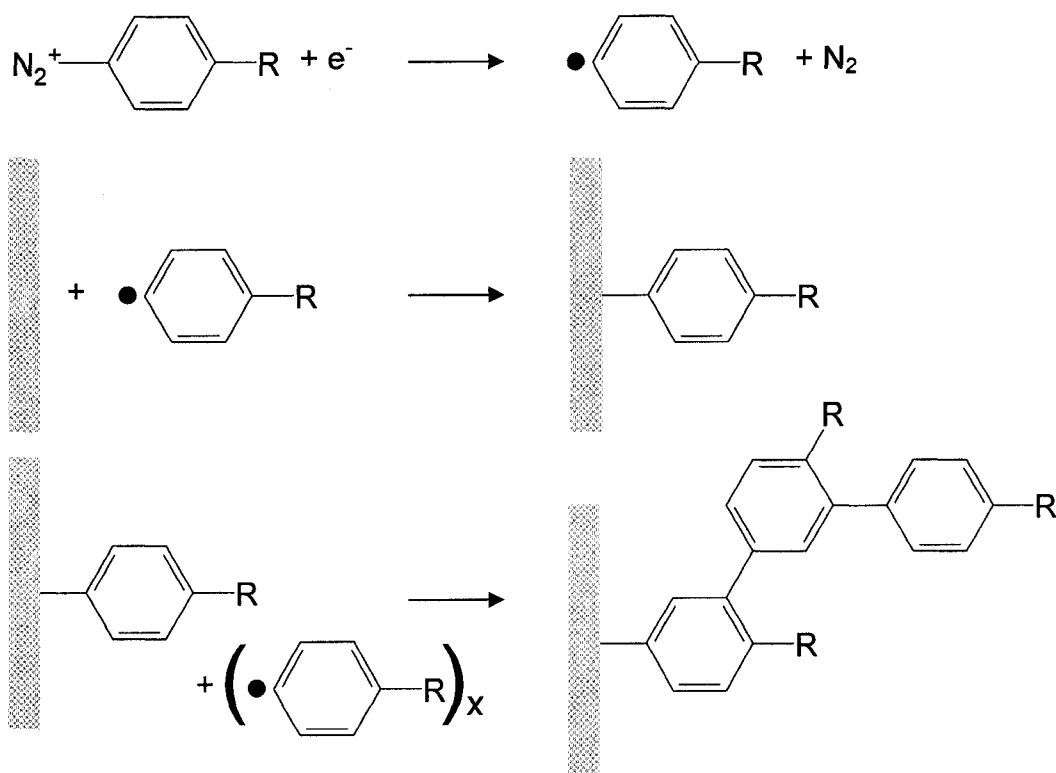


Figure 3.01 Schematic illustration of the formation of aryl diazonium derived multilayers. An electrochemically inserted electron liberates nitrogen and forms an aryl radical that is free to bond to the substrate or a surface-bound molecule.

could be created. Another advancement in the area of diazonium modified carbon surfaces occurred in 2005 when Bélanger published a method to create and deposit aryl diazonium ions *in situ*.¹¹ The electrochemical deposition was performed from the synthesis matrix without the need for isolation or purification of the diazonium. These films were similar, but had measurable differences when compared to those created via the traditional method. This opened up the possibility of grafting molecules that were insoluble in acetonitrile as well as eliminating the need to store volatile diazonium salts such as benzenediazonium tetrafluoroborate, which has been found to be quite explosive in the author's experience.

Of all the uses for diazonium derived aryl films on carbon, this chapter will discuss the potential use in molecular electronics. The concept that a single molecule could be used as a discrete part of an electrical circuit was first suggested by Aviram and Ratner in 1974.^{12, 13} Using the results of semiquantitative calculations, Aviram and Ratner argued that it was feasible for a single organic molecule to act as a rectifier. The model molecules have two separate, unbalanced, π systems separated by multiple σ bonds in order to mimic donor-acceptor behaviour of p-n junctions from traditional silicon based rectifiers. The theoretical current-voltage (IV) response of a molecular rectifier was presented and laid the groundwork for future molecular electronics studies.

Of particular relevance to the work discussed in this chapter is the design, fabrication, characterization and electronic behaviour of diazonium derived aryl films on pyrolyzed photoresist films described by McCreery.^{24, 28-37} While some of the molecules used to create the organic films in these publications are slightly different

from the work described in this chapter, there are also a number that are the same. Another small difference is the choice of supporting substrate. McCreery's carbon electrodes of choice are pyrolyzed photoresist films while the work presented in this chapter is predominately on electron beam deposited carbon films. However, the defining difference is the nature of the top contact in the electrical circuit design. McCreery uses a relatively large metal contact, typically in the range of millimeters, whereas in this work the top contact was achieved via an AFM tip which has an effective surface area in the range of nanometers.

Although a plethora of surfaces have been modified with diazoniums and investigated, including multiple forms of carbon, this is the first reported instance of electron beam evaporated carbon modified via diazonium reduction.

2. Experimental

For aqueous electrochemical experiments, a home-built silver/silver chloride electrode was used as the reference. The electrode consisted of a glass tube with a platinum filament sealed at one end. The inherent microcracks where the platinum spans the glass allows for ion transport between the bulk solution and the reference solution. The leak rate for this design is relatively slow so as to avoid significant cross contamination between the bulk solution and the internal reference solution. The silver wire was cleaned by soaking in concentrated ammonium hydroxide, rinsed with Nanopure water (18 M Ω /cm, Barnstead, Dubuque, IA) and soaked briefly in concentrated nitric acid to roughen the surface. The silver wire was again rinsed with

Nanopure water and then dried with argon (Praxair, Mississauga, Ontario, Canada). The silver wire was coated in silver chloride by anodization in saturated potassium chloride. The presence of silver chloride was confirmed visually by the presence of a grayish-white film on the electrode. The silver/silver chloride wire was placed in the glass electrode body; the electrode was filled with saturated KCl and stoppered at the open end to minimize loss due to evaporation. Electrical contact was made with the silver/silver chloride wire that had been threaded through the stopper.

A similar reference electrode was prepared for electrochemistry performed in acetonitrile. The preparation was the same as described above except the wire was not anodized in saturated potassium chloride. The filling solution used for the acetonitrile reference electrode was 230 mM silver nitrate (Sigma-Aldrich Canada Ltd, Oakville, Ontario, Canada) in acetonitrile.

Solutions of 2,5-Dimethoxy-4-(4-nitrophenylazo)-benzenediazonium salt (Sigma-Aldrich Canada Ltd, Oakville, Ontario, Canada) were prepared at 5 mM concentrations in freshly distilled reagent grade acetonitrile (Caledon Laboratory Chemicals, Georgetown, Ontario) and included 0.1 M tetrabutylammonium tetrafluoroborate (Sigma-Aldrich Canada Ltd, Oakville, Ontario, Canada) as the supporting electrolyte. All solutions were prepared fresh for each experiment set and deaerated with argon prior to use.

Pyrolyzed photoresist films (PPF) were prepared based on the method described by McCreery.¹⁴⁻¹⁸ Silicon (100) was diced into 1.2 x 1.2 cm squares. The silicon was cleaned with piranha (3:1 (v/v) conc. H₂SO₄/30% H₂O₂) for 15 – 20 minutes to remove any organic residue, then rinsed with Nanopure water (18 MΩ/cm,

Barnstead, Dubuque, IA). The resulting oxidized surface was stripped by immersion in 49% HF for 1 to 2 minutes or a buffered oxide etch solution of 10:1 (v/v) 40% NH_4F and 49% HF. The substrates were again rinsed with Nanopure water and dried with argon. The silicon samples were coated with HPR 504, a positive photoresist (Arch Chemical Inc., Norwalk, Connecticut, USA) under the following conditions: 10 seconds at 200 RPM followed by 40 seconds at 2000 RPM. The spin-coating procedure was repeated three times for each silicon substrate. The freshly coated samples were loaded into a quartz tube and then into a tube furnace. The atmosphere was purged and maintained with a forming gas of 95% N_2 , 5% H_2 (Praxair, Mississauga, Ontario, Canada). The temperature of the samples was slowly ramped to 1000 °C where they were then pyrolyzed for 1.5 hours, then slowly cooled to room temperature overnight. The forming gas atmosphere was maintained throughout all stages of heating until the samples reached room temperature. The PPF samples were placed in plastic Petri dishes, wrapped in an optically opaque foil, and stored in a low-vacuum dessicator until use.

Electron beam evaporated carbon films and pyrolyzed photoresist films were prepared for electrochemical analysis by sonication in a slurry of activated charcoal and anhydrous ethanol (Commercial Alcohols Inc, Brampton, Ontario, Canada) for twenty minutes as a standard cleaning step described by Ranganathan and McCreery.¹⁴ The samples were removed from the slurry, rinsed with Nanopure water and dried with a gentle stream of argon. The films were immediately placed into the electrochemical cell and the analyte solution was added to shield the electrode from atmospheric fouling. For samples that were modified with various diazonium salts a

similar cleaning procedure was used. The samples were sonicated in ethanol, without activated charcoal, rinsed and dried as described above.

Samples prepared for X-ray photoelectron spectroscopy and time-of-flight secondary ion mass spectrometry were placed in plastic Petri dishes, sealed, wrapped in an optically opaque foil, and stored in a low-vacuum dessicator until they were analyzed. Storage time prior to analysis was kept under seventy-two hours. X-ray photoelectron spectroscopy and time-of-flight secondary ion mass spectrometry analysis was performed by the Alberta Centre for Surface Engineering and Science (ACSES).

The nano-scale electrical characterization of the modified carbon films was performed with a Dimension 3100 NanoMan System with a NanoScope IV controller and Conductive Atomic Force Microscopy Application Module. Graphite conductive adhesive 112 (Electron Microscopy Sciences, Hatfield, PA) was used to both adhere the carbon film/silicon wafer samples to the steel sample pucks as well as to complete the electrical circuit between the carbon surface and the sample puck. The tips employed for the nano-scale electrical characterization of the films were CSC12/Ti-Pt/50 (Mikromasch, Tallinn, Estonia). The tips contained a 20 nm adhesion layer of titanium and an outermost conductive layer of 10 nm of platinum. The radius of curvature was less than 40 nm and they had a nominal spring constant of 0.95 N/m for the “A” tip.

All photolithography was performed in the clean room of the University of Alberta Nanofab. The EB50 samples were spin coated with IC-28/T3, a negative photoresist (Arch Chemical Inc., Norwalk, CT, USA) under the following conditions:

deposited and spun at 600 RPM for 15 seconds followed by 40 seconds at 4000 RPM. The coated substrates were soft-baked for five minutes at 90 °C then placed under a photolithographic mask and exposed to ultraviolet light for three seconds. The samples were developed with WNRD (Arch Chemical Inc., Norwalk, CT, USA) for 45 seconds followed by a rinse in Rinse 1 (Arch Chemical Inc., Norwalk, CT, USA) for 15 seconds. After patterning the samples were rinsed with distilled, deionized water and dried with plumed clean dry air.

3. Results and Discussion

3.1 Electrochemical Deposition of Aryl Molecules

Electrochemical deposition of aryl moieties from the diazonium ion precursors was performed from a 5 mM solution of the appropriate diazonium and 0.1 M tetrabutylammonium tetrafluoroborate in freshly distilled acetonitrile. The attachment of Fast Black K was achieved by sweeping the potential from +0.400 V to -0.800 V at 0.200 V/s. A typical deposition cyclic voltammogram is shown in figure 3.02. When the potential becomes sufficiently negative a cathodic wave is observed. This wave is due to the one electron reduction of the diazonium to form the aryl radical. For Fast Black K the reduction occurs at -0.222 V with respect to Ag/Ag⁺. The reverse cycle of the voltammogram is absent of any anodic wave; this is indicative of a chemically irreversible reaction.

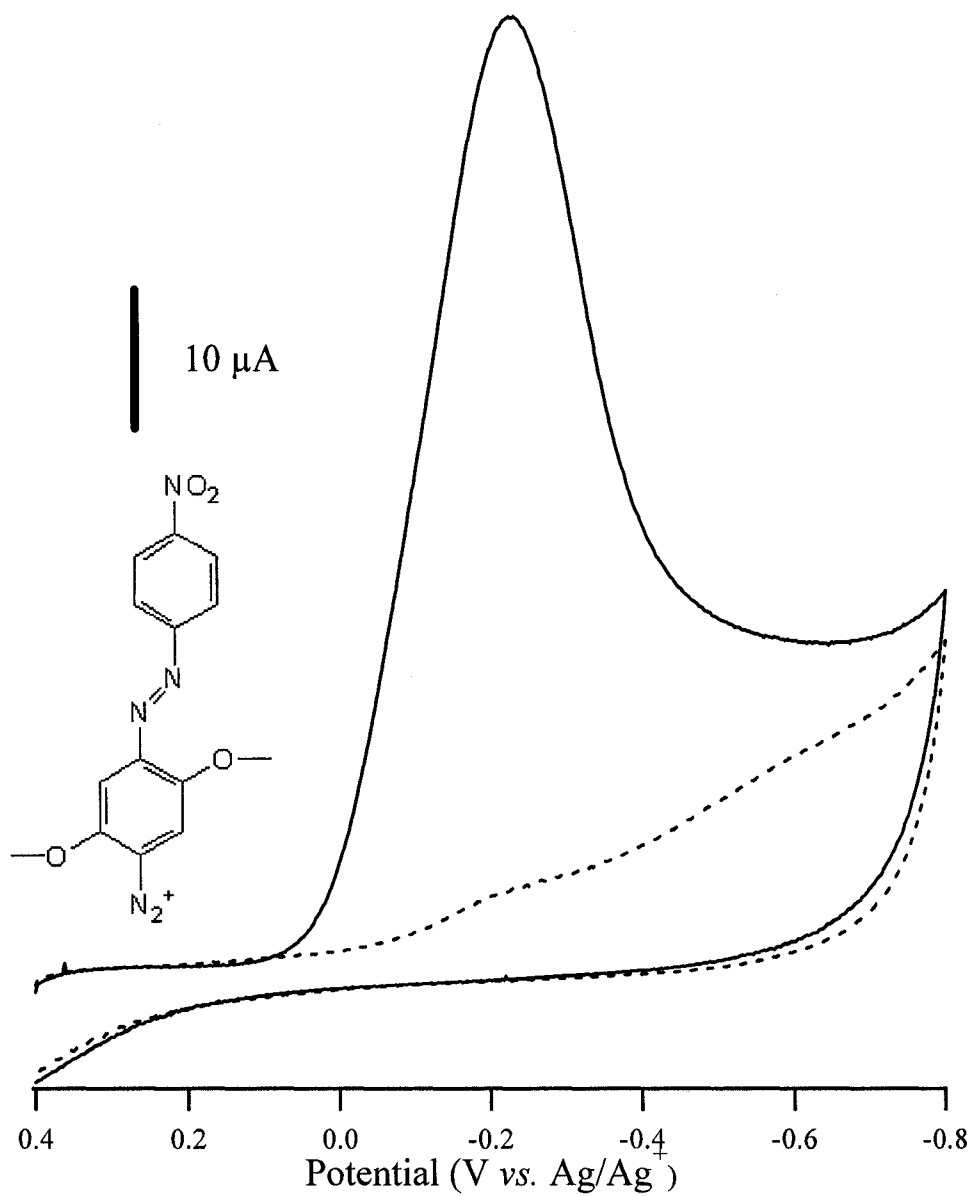


Figure 3.02. Cyclic voltammogram for the electrochemical attachment of Fast Black K to EB50 from TBATFB in acetonitrile. Solid – first sweep; dotted – second sweep.

The second cycle, shown as the dotted trace in figure 3.02, shows very little cathodic current. The lack of electrochemical activity during the second sweep signifies the surface is nearly completely covered and blocked during the first sweep.

An example of the immobilization of biphenyl from its parent diazonium is shown in figure 3.03. The cyclic voltammogram program shown for the deposition of biphenyl is two sweeps from +0.600 V to -0.400 V. Similar to FBK the reduction of the biphenyl diazonium ion to the radical occurs when the potential of the first sweep, solid line, reaches a suitably negative potential of -0.104 V with respect to Ag/Ag^+ . The modification of the electrode surface is for the most part completed during the first cycle, as indicated by the near absence of the reductive peak in the second sweep.

Representative electrochemical attachment cyclic voltammograms of nitrobenzene and phenyl acetic acid moieties to EB50 from their respective diazonium parent ions are shown in figure 3.04 (only the first cycles are shown). The reduction of nitrobenzene diazonium occurs at +0.102 V and the reduction phenyl acetic acid occurs at -0.312 V, both with respect to Ag/Ag^+ . As with the other studied diazoniums, the second sweep for both p-nitrobenzene and phenyl acetic acid is absent of any significant non-capacitance current. The reduction potentials of the four studied diazoniums are summarized in table 3.01.

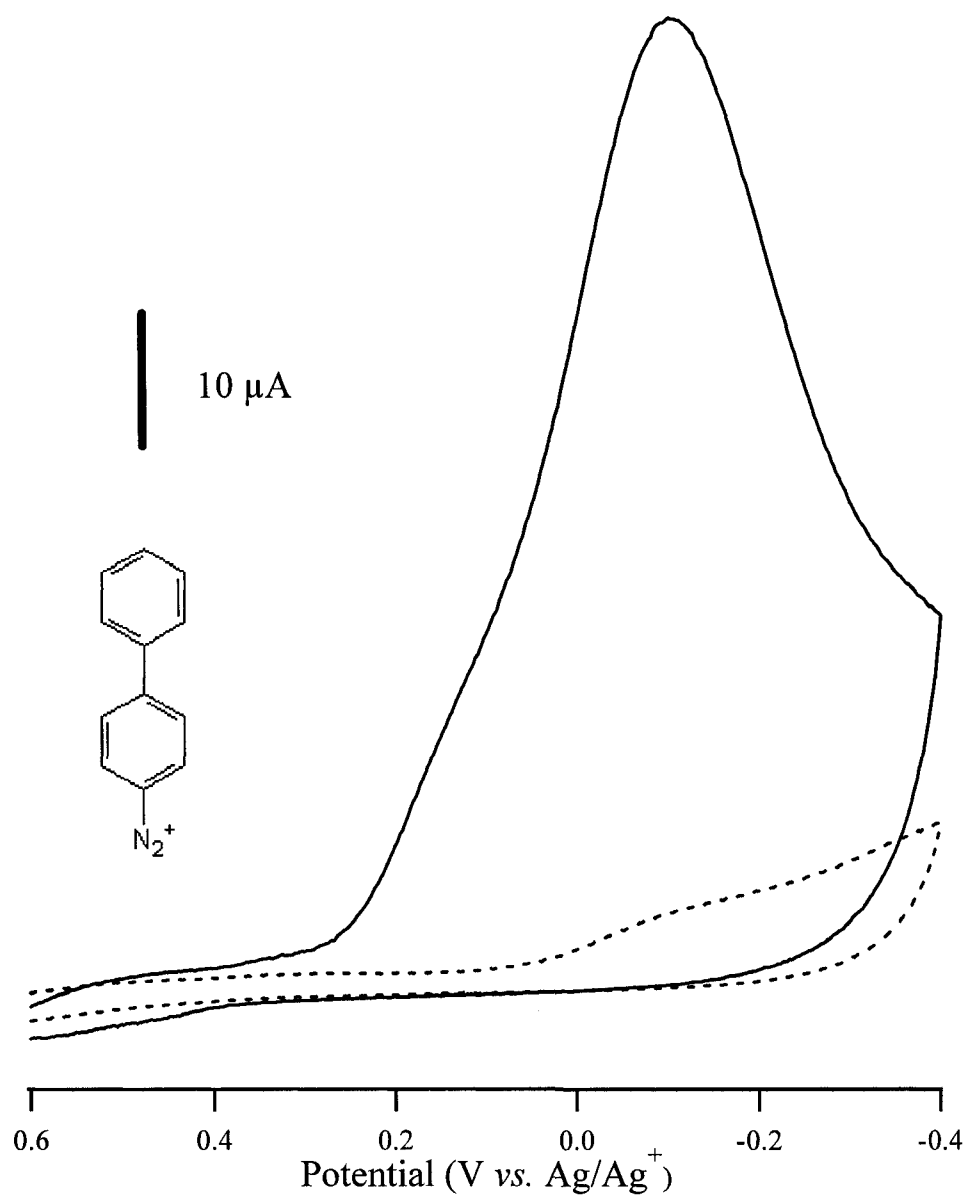


Figure 3.03. Cyclic voltammogram for the electrochemical attachment of Bipheryl to EB50 from TBATFB in acetonitrile. Solid – first sweep; dotted – second sweep

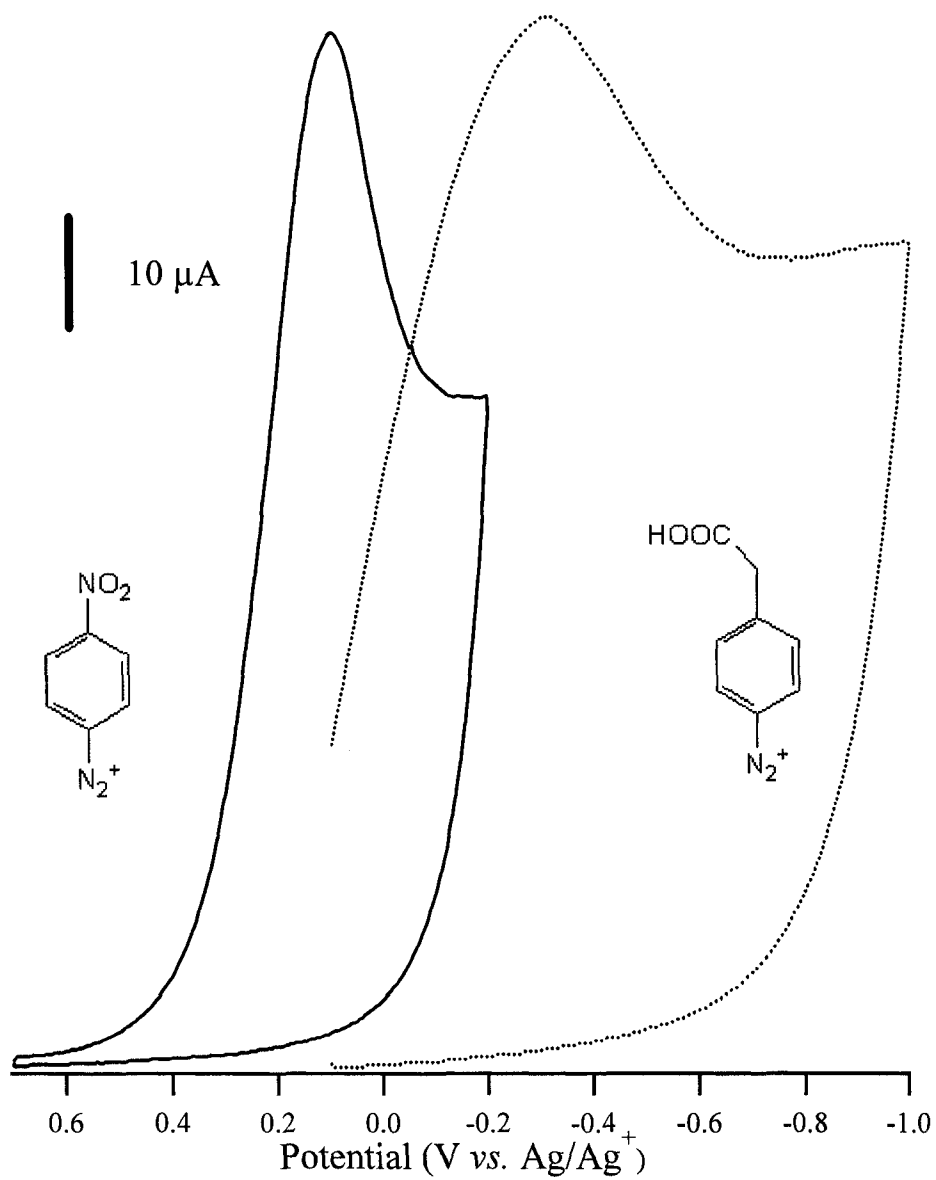


Figure 3.04. Cyclic voltammograms for the electrochemical attachment of p-nitrobenzene (solid) and phenyl acetic acid (dotted) to EB50 from TBATFB in acetonitrile. Second scan omitted.

Modifier	Potential (V vs. Ag/Ag ⁺)
p-nitrobenzene	+0.102
Biphenyl	-0.104
Fast Black K	-0.222
Phenyl acetic acid	-0.312

Table 3.01. Reduction potentials of diazonium precursors.

The standard method for ensuring complete coverage of carbon electrodes with the film of interest is cyclic voltammetry of dopamine in H₂SO₄.¹⁹⁻²¹ Dopamine requires adsorption to a bare, oxide free carbon surface to exhibit facile electron transfer. Modification of carbon surfaces with a thin film can reduce or completely block electron transport to dopamine. Dopamine voltammetry can be used to detect defects or “pinholes” in thin films on carbon electrodes, and such experiments are referred to as “blocking”. This method has been extended to diazonium derived layers.²² The cyclic voltammetry of dopamine on EB50 was discussed in chapter 2 and initially presented in figure 2.13. The electrochemical behaviour of dopamine on bare EB50 is again shown by the solid line in figure 3.05. The dashed trace represents the dopamine response on FBK modified EB50 while the dotted trace is that for biphenyl modified EB50. FBK and biphenyl modified EB50 show no dopamine electrochemical activity. From this it was concluded that the diazonium derived films of FBK and biphenyl contain few, if any, defects.

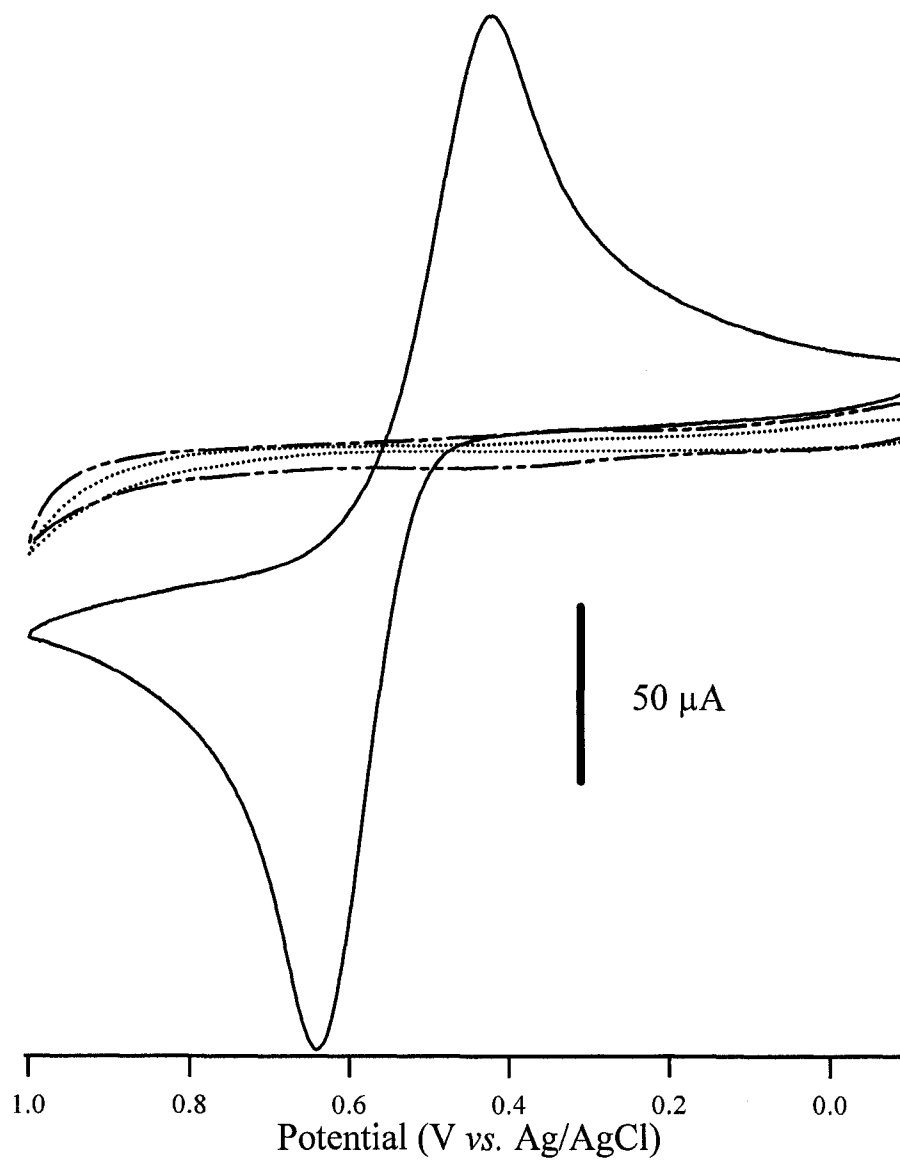


Figure 3.05. Cyclic voltammograms for the blocking of dopamine in 0.1 M H₂SO₄ for modified EB50. Solid – bare EB50, dashed – Fast Black K, and dotted – biphenyl.

This is similar to films created on other carbon based electrodes such as glassy carbon and pyrolysed photoresist derived films.

3.2 Elemental and Chemical Analysis

Elemental and chemical analysis was performed predominantly via X-ray photoelectron spectroscopy. Time-of-flight secondary ion mass spectrometry and Raman spectroscopy were also used. X-ray photoelectron spectroscopy was mainly used to determine elemental composition of modified EB50 films, although some chemical speciation of the nitrogen was also performed. The XPS survey spectra for FBK and p-nitrobenzene modified EB50 are shown in figure 3.07. The XPS of FBK modified EB50 is shown by the solid, top (offset) trace while the XPS for p-nitrobenzene modified EB50 is shown in the dotted, lower, trace. The high resolution XPS for FBK modified EB50 are presented in figure 3.08 while those for p-nitrobenzene are presented in figure 3.09. The summarized quantitative data of the XPS are presented in table 3.02 for FBK and table 3.03 for p-nitrobenzene. The theoretical mass percent of the elements contained in both FBK and p-nitrobenzene are presented in table 3.04. The mass contribution from hydrogen is omitted to facilitate comparison with the XPS data as the XPS is incapable of detecting hydrogen. The sampling depth of the X-ray beam is on the order of the aryl layer thickness, 2.64 nm, which leads to a large carbon signal as both the aryl film and the underlying carbon substrate are simultaneously sampled. As expected, the most abundant element detected in both the FBK and p-nitrobenzene samples was carbon, at about 71% for FBK and 79% for p-nitrobenzene. Due to the sampling depth issue,

this is larger than the theoretical values of 23.34 and 27.10%. The high resolution XPS of the carbon 1s region for FBK, figure 3.08A, contains a shoulder at higher energies. This is most likely due to the carbon-oxygen-carbon contained in the aryl-methoxy groups of FBK.

The other elements detected in significant quantities are nitrogen and oxygen. Due to the large signal from carbon due to the sampling depth, a similar result is expected with oxygen as the underlying EB50 substrate contains 4% oxygen. Although one could attempt to normalize the results based on measured and theoretical carbon ratios, the results would not be quantitative. This is expected as these are both contained in the organic film. The nitrogen 1s signal for FBK, figure 3.08C, contains two emissions; the more intense of the two is located at 400.2 eV while the peak with lesser intensity is located at 406.0 eV. The ratio of the peaks is about 2:1. The larger peak at 400.2 eV is attributed to the two nitrogens in the azo group while the higher energy nitrogen peak at 406.0 eV is attributed to the nitro group.^{23, 24} The peak intensity ratio matches well with the nitrogen content ratio of FBK. The high resolution XPS has no trace of a nitrogen 1s peak that would be expected for the diazonium functional group, 403.8 eV.²⁵ The nitrogen 1s signal for p-nitrobenzene, figure 3.09C, also unexpectedly contains two distinct nitrogen peaks. The larger of the two located at 405.8 eV corresponds to the nitrogen contained in the nitro group. The lower intensity peak is located at 400.3 eV. The lower energy of the second nitrogen peak is indicative of a reduced form of nitrogen as compared to that in the nitro group. According to the previously presented mechanism, figure 3.01, the p-nitrobenzene diazonium derived layer should only contain one nitrogen signal, for

the nitro group. The first possible explanation of the erroneous nitrogen 1s peak is the reduction of the nitro group in the XPS vacuum chamber to an amine.²⁶⁻²⁸ The second possible, but unlikely source of the nitrogen signal is residual tetrabutylammonium from the electrolyte. The presence of electrochemical electrolyte in the form of tetrafluoroborate is confirmed and discussed later in this section, but it is present in very small quantities. If it is assumed that both tetrabutylammonium and tetrafluoroborate are present in similar quantities, this cannot explain the observed signal. Additionally, Murray reports the XPS nitrogen 1s peak of tetraethylammonium to be located at 401.5 eV.²⁹ One would expect the nitrogen XPS signals for tetraethylammonium and tetrabutylammonium to be the same. Another possible explanation was suggested by Bélanger when a 400 eV 1s nitrogen peak was observed for the electrochemical deposition of various aryl layers from diazoniums on gold. This 400 eV peak was observed even in films created from 4-carboxyphenyldiazonium, a molecule that contains no nitrogen other than that present in the diazonium group. This led Bélanger to suggest the possibility of a new mechanism for the attachment of diazonium derived radicals to a gold surface and/or attachment to the existing layer during multilayer growth.²³

This new proposed mechanism involves conversion of the diazonium to an azo group and linkage through this newly formed azo group. The final attachment scheme is presented in figure 3.06. It is still unclear if this mechanism proposed for the electrochemical attachment of aryl molecules from diazoniums to a gold surface

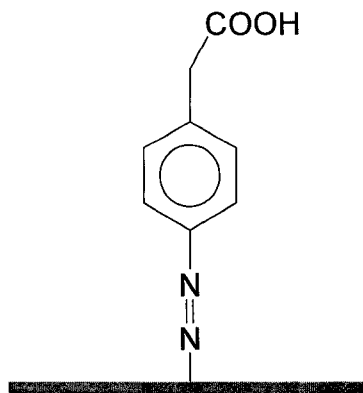


Figure 3.06. Purposed final attachment configuration of diazonium derived layers as presented by Bélanger.

is applicable to carbon surfaces. The mechanism suggest by Bélanger would explain the erroneous 400 eV nitrogen signal observed in the p-nitrobenzene films, it does not agree with the measured nitrogen ratio signal observed for FBK derived films. At this point, it is believed that the p-nitrobenzene 400 eV signal is due to nitrogen reduction occurring in the XPS vacuum chamber.

Of note is the detection of fluorine and chlorine in the FBK modified EB50, figures 3.08D and E, and the detection of fluorine in the p-nitrobenzene modified EB50, figure 3.09D. Both boron and fluorine are present as tetrafluoroborate as the counter ion of the parent diazoniums and as the supporting electrolyte for the electrochemical deposition. The most likely source of the fluorine signal is from the intercalation or adsorption of tetrafluoroborate into the film as, or after, they are electrochemically deposited. The presence of fluorine suggests that boron is also present. High resolution XPS were collected in the boron 1s region, but any signal from boron is below the detection limit of the XPS, figures 3.08F and 3.09F. This is

not surprising as the signal for fluorine is close to the signal-to-noise of the instrument and the expected signal of boron from tetrafluoroborate is one quarter that of fluorine based on the atomic ratio of BF_4 . The presence of chlorine in the XPS for FBK, figure 3.08E, can be explained by the fact that the chloride is the counter ion for commercial FBK and it is coupled with zinc chloride; $\text{C}_{14}\text{H}_{12}\text{ClN}_5\text{O}_4 \cdot 0.5\text{ZnCl}_2$. Although this easily accounts for the presence of detectable chlorine in the FBK modified films, it is possible that chlorine was also observed in the p-nitrobenzene modified film, figure 3.09E, which has no inherent sources of chloride or chlorine. The chlorine 2p region of the high resolution XPS for p-nitrobenzene is ambiguous. The observed signal could be chloride but it is just as likely that the observed signal is entirely noise. Any possible presence of chlorine signal in the XPS can only be attributed to contamination. All glassware used for electrochemical preparation and analysis was stored wet containing a solution of hydrochloric acid. This is the most likely source of any potential chloride contamination.

Time-of-flight secondary ion mass spectrometry was performed by the Alberta Centre for Surface Engineering and Science (ACSES) and was used to support the results seen with XPS. Both boron and tetrafluoroborate were visible in the mass spectrum provided by ACSES. Raman spectroscopy was performed but the resulting spectrum was indistinguishable from that of bare EB50.

Peak	Position BE (eV)	FWHM (eV)	Raw Area (CPS)	RSF	Atomic Mass	Atomic Conc %	Mass Conc %
F 1S	685.300	2.387	5280.0	1.000	18.998	0.29	0.43
O 1s	532.840	2.818	215390.4	0.780	15.999	15.53	19.35
N 1s	399.850	2.890	68755.6	0.477	14.007	8.35	9.11
C 1s	285.010	3.449	353516.5	0.278	12.011	75.46	70.56
Cl 2p	200.860	2.869	1328.9	0.891	35.460	0.09	0.25*
B 1s	184.690	0.736	617.4	0.159	10.823	0.23	0.20*

Table 3.02. XPS data of Fast Black K modified EB50. * indicates values below the limit of quantification.

Peak	Position BE (eV)	FWHM (eV)	Raw Area (CPS)	RSF	Atomic Mass	Atomic Conc %	Mass Conc %
F 1S	685.630	1.272	826.4	1.000	18.998	0.04	0.06*
O 1s	532.510	2.786	168315.1	0.780	15.999	11.34	14.40
N 1s	405.790	2.478	50886.0	0.477	14.007	5.76	6.41
C 1s	284.680	2.917	415278.7	0.278	12.011	82.78	78.91
Cl 2p	200.860	1.547	1265.0	0.891	35.460	0.08	0.22*
B 1s	189.64	0.875	0.0	0.159	10.823	0.00	0.00*

Table 3.03. XPS data of p-nitrobenzene modified EB50. * indicates values below the limit of quantification

Element	Fast Black K Theoretical Mass %	p-Nitrobenzene Theoretical Mass %
Oxygen	23.34	27.10
Nitrogen	15.33	11.86
Carbon	61.37	61.04
Chlorine	0	0
Boron	0	0
Fluorine	0	0

Table 3.04. Elemental theoretical mass percent of Fast Black K and p-nitrobenzene, omitting the mass contribution from hydrogen

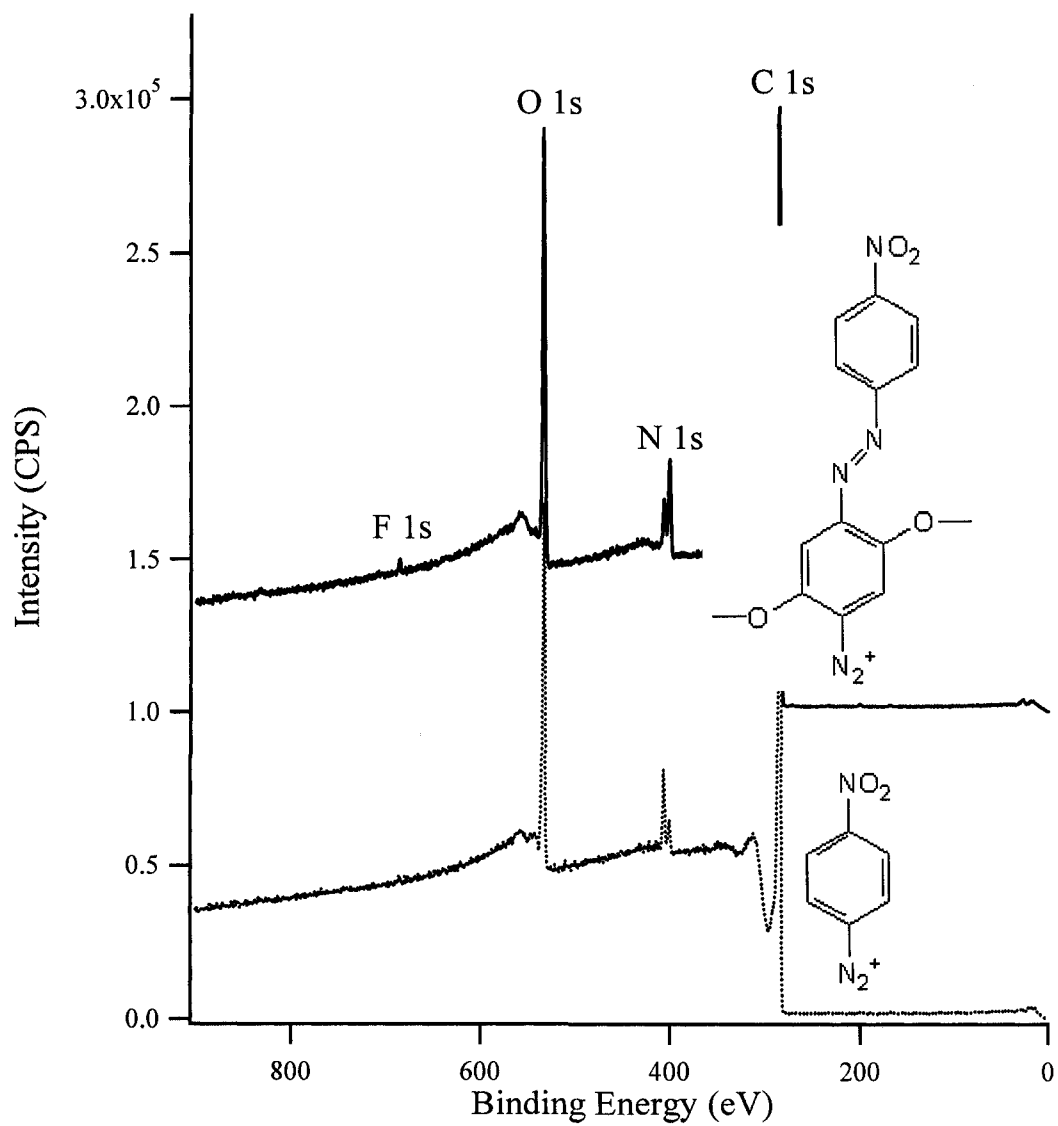


Figure 3.07. Survey XPS of Fast Black K (solid) and p-nitrobenzene (dotted) modified EB50.

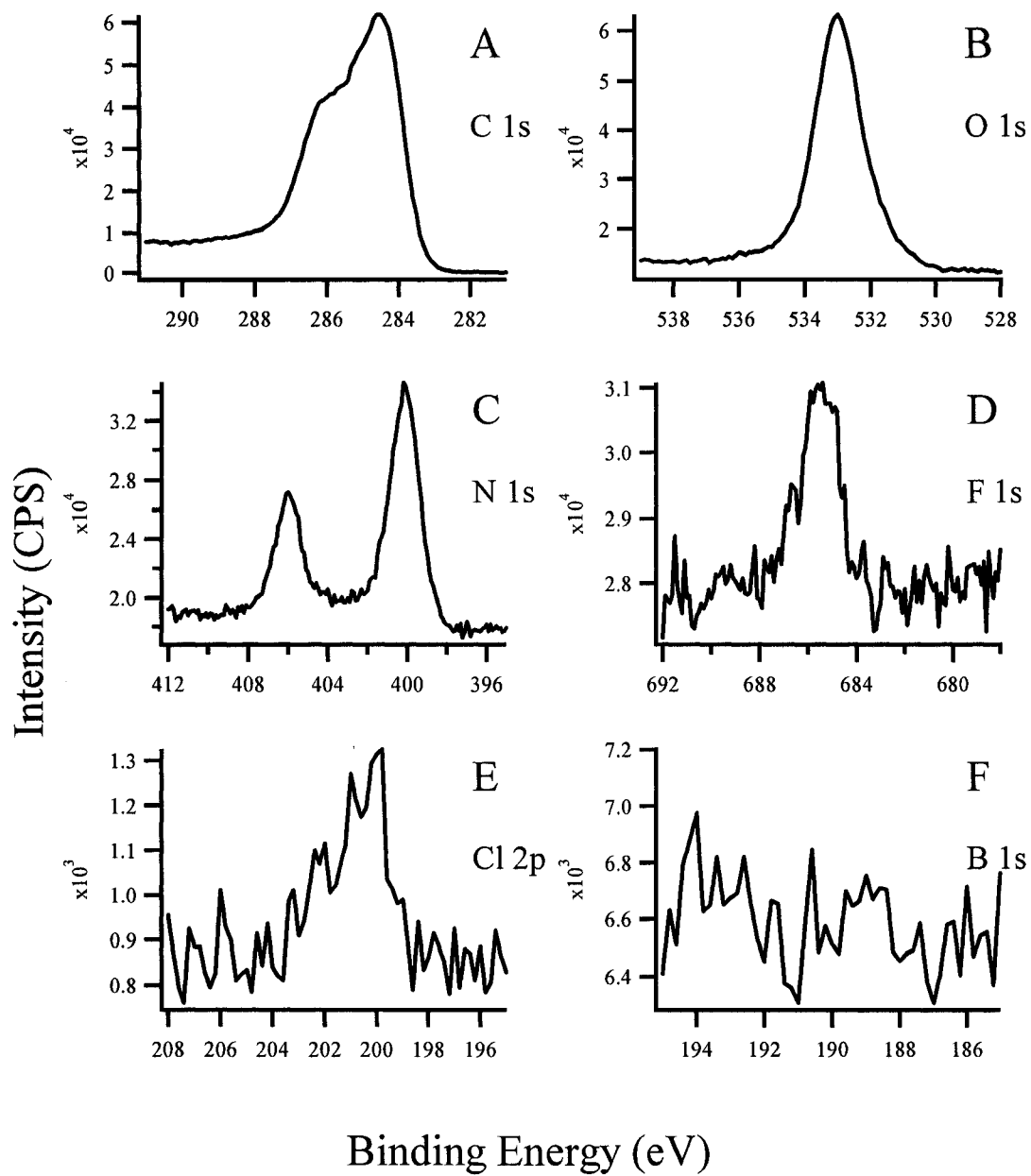


Figure 3.08. High resolution XPS of Fast Black K on EB50. A) carbon 1s B) oxygen 1s C) nitrogen 1s D) fluorine 1s E) chlorine 2p F) boron 1s

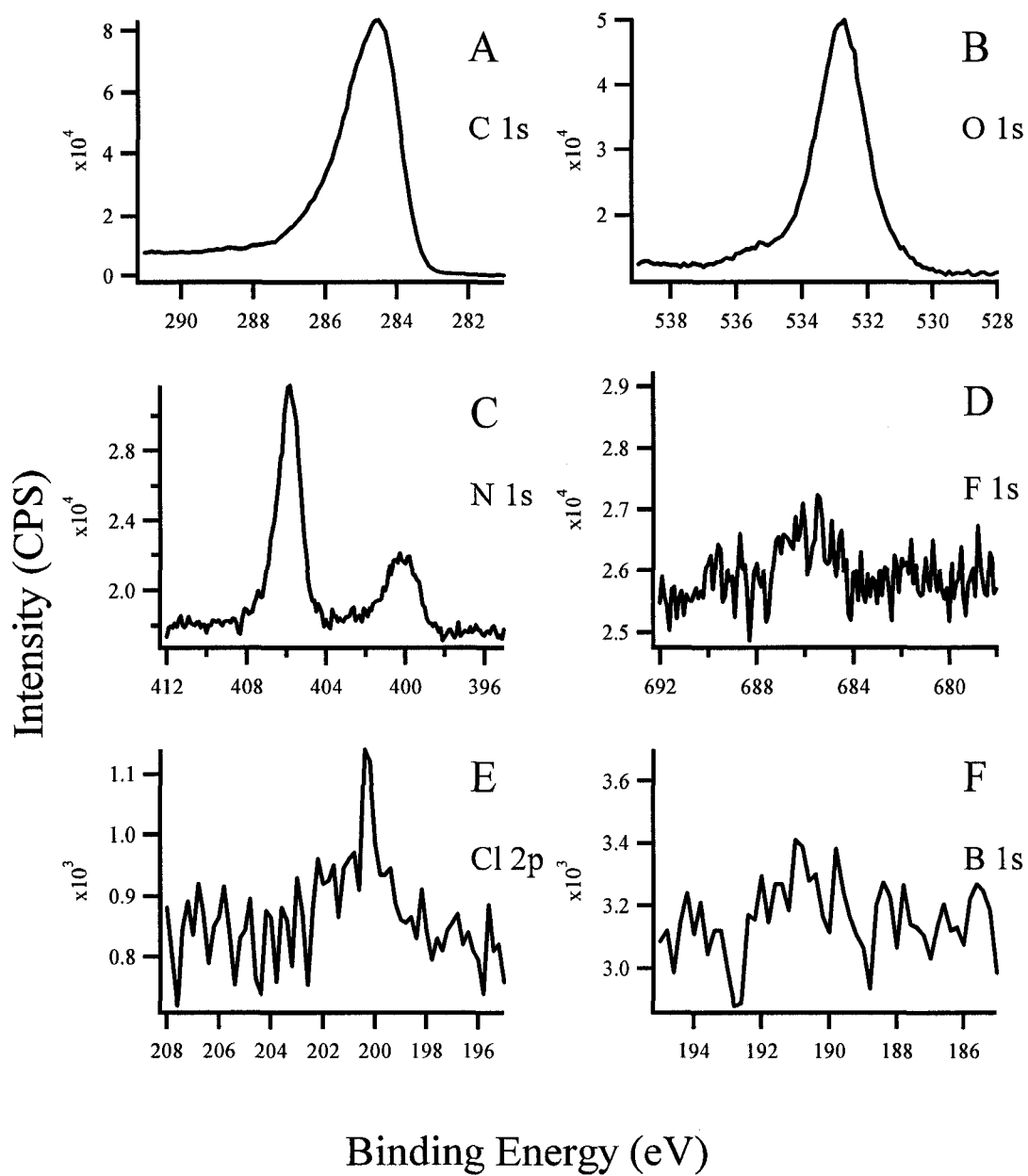


Figure 3.09. High resolution XPS of p-nitrobenzene on EB50. A) carbon 1s B) oxygen 1s C) nitrogen 1s D) fluorine 1s E) chlorine 2p F) boron 1s

3.3 Measurement of Film Thicknesses

In order to facilitate film characterization, a method was developed to measure the film thickness. Similar thickness measurements of films prepared on PPF have been performed by removal of the film in a specific area via AFM “scratching”.¹⁰ This method requires one to account for any damage done to the underlying substrate by the AFM tip under the harsh contact conditions required to completely remove the covalently bound film. One also must ensure that the deposited film is completely removed and that no residual parts of the film remain to skew the measured heights.

The method developed and presented in this chapter involves standard photolithography methods to pattern the EB50 as described in the experimental section. The patterned EB50 had the diazoniums of interest deposited on them through a photoresist pattern via cyclic voltammetry as previously described. This method is similar to the method used by Kariuki to measure aryl film thicknesses on glassy carbon,⁹ but has the advantage of a regular and defined pattern as defined by the mask. Figure 3.10 illustrates the process of depositing aryl moieties around a photolithographic pattern. The diazonium reduction of FBK is shown in figure 3.12. The same behaviour is observed for the deposition through a pattern as deposition on an unmodified sample as previously discussed. The only significant difference is the lower magnitude of current. This is due to the reduced effective surface area of the electrode. The cyclic voltammogram shown in figure 3.12 is highly digitized due to the extremely low current being measured and the employed gain of the potentiostat. After electrochemical deposition, the photoresist was stripped from the samples and the heights of the patterned films were determined via

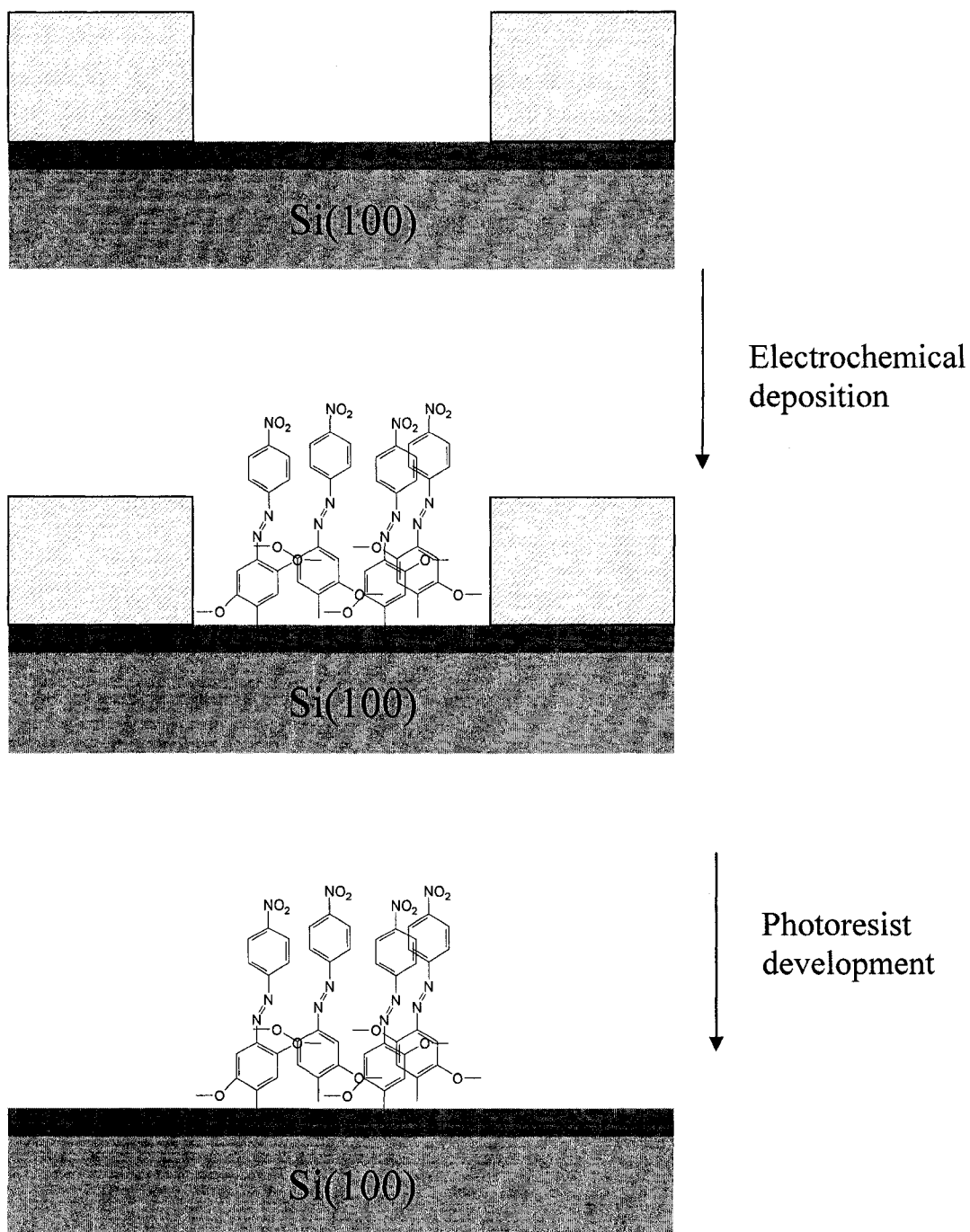


Figure 3.10. Electrochemical deposition onto a photo patterned surface. Standard photolithographic methods are used to create a patterned surface allowing selective modification of the unblocked areas.

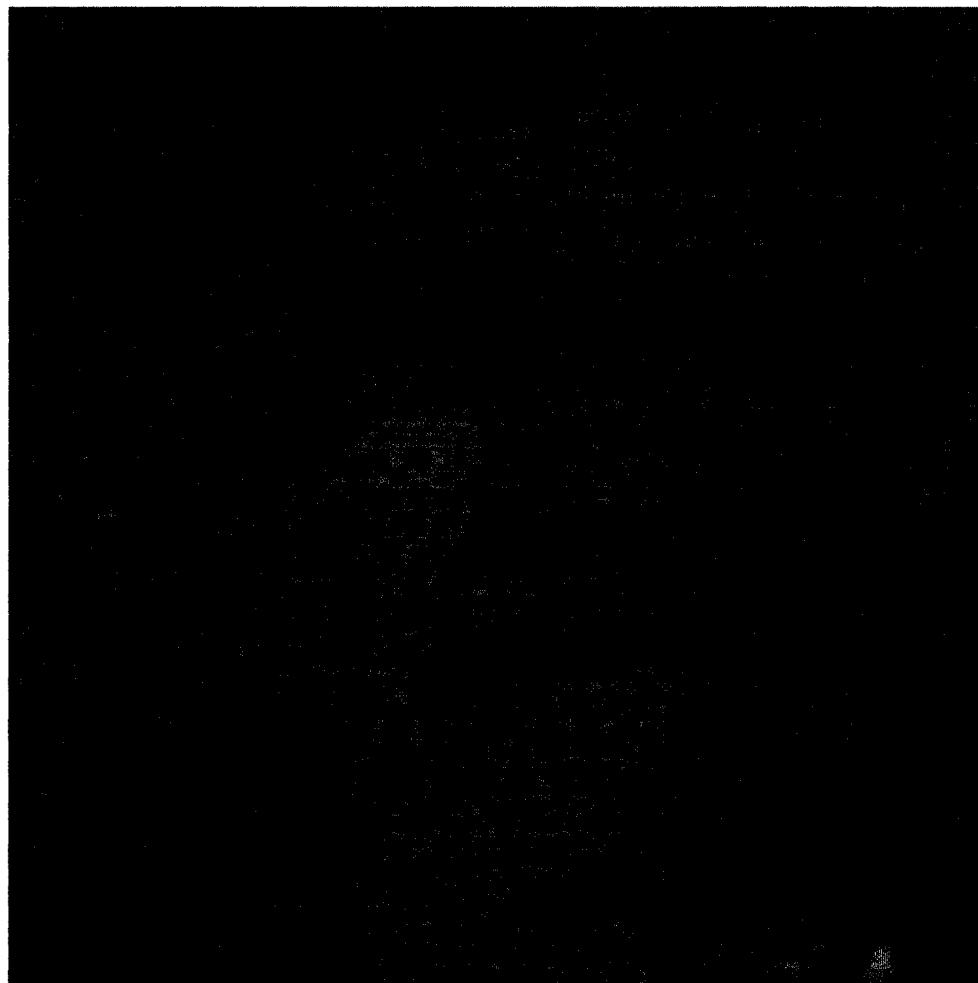


Figure 3.11. Tapping mode AFM measurement of film thickness. The bottom left portion of the image is the area modified from biphenyl diazonium; the top right portion of the image is the area initially blocked by photoresist. Film thicknesses are measured from multiple line profiles, as shown above. The image is 3.0 x 3.0 μm .

intermittent contact mode AFM. The measured values of film thicknesses as measured by the photolithography patterning method are presented in table 3.05. The measured thickness of the FBK films is greater than that of a single monolayer, but less than two molecule lengths stacked end-to-end indicating multilayer formation similar to figure 3.01. The initial focus of this work was on modified PPF but switched exclusively to EB50 soon after the preliminary investigations. For comparison, and demonstration of the technique, the PPF values have been included. This method has since been successfully employed in our lab to measure a variety of film thicknesses deposited from aqueous media.³⁰

Attached moiety	Thickness (nm)	SD	Substrate
Fast Black K	2.6	0.6	EB50
Fast Black K*	6.00	1.0	EB50
Biphenyl	3.0	0.3	EB50
Nitroazobenzene ³¹	2.7	0.4	EB50
Nitrobenzene	2.0	0.2	PPF
Phenyl acetic acid	2.4	0.3	PPF

Table 3.05. Film thicknesses (* denotes 11 cycle deposition run)

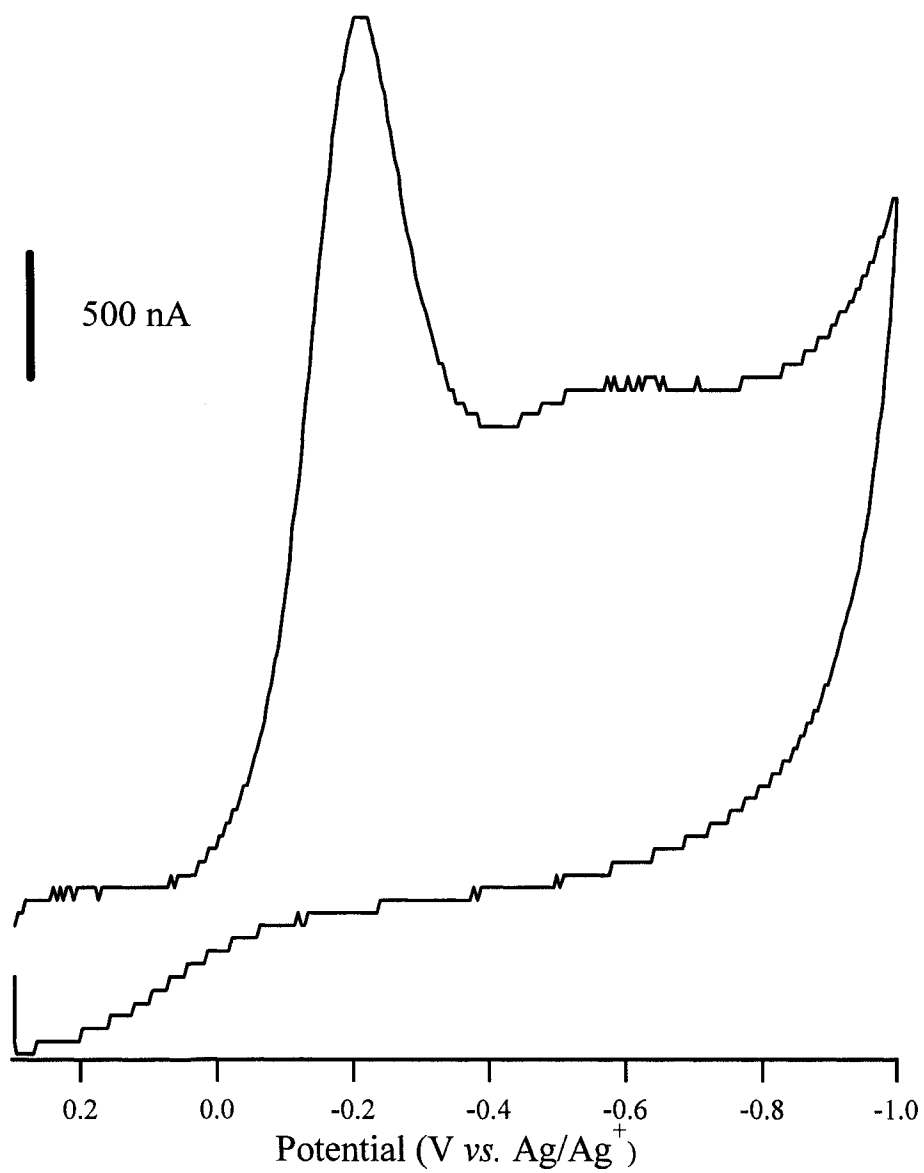


Figure 3.12. Cyclic voltammogram for the electrochemical attachment of Fast Black K to photolithographic patterned EB50 from TBATFB in acetonitrile.

3.4 Electrical Characterization

As with the unmodified EB50 films discussed in chapter 2, the nano-scale electrical properties of the electron beam evaporated carbon films were probed with conductive atomic force microscopy (C-AFM). The aryl layers on the carbon films proved to be more fragile than the underlying carbon substrate. Large normal forces coupled with lateral movement of the C-AFM tip resulted in film damage. As a result, all imaging was performed in intermittent contact mode, when an area containing very few topographic features was found, it was deemed a worthy location for electrical measurements. The tip was withdrawn and the C-AFM was switched to force-distance or potential-current mode. Once in the appropriate operational mode the tip was reengaged and the electrical measurements were performed.

The contribution of molecular orientation and configuration is recognized to play a prominent role in the utility of molecules in electrical devices.³²⁻³⁸ The first set of experiments were designed to gauge how contact force affects the electrical behaviour of the film. It was expected that contact force would alter the orientation and/or configuration of the film and therefore the electrical response. For this investigation a constant potential was applied to the tip, the tip was then lowered to the surface, engaged the surface, and then pressed into it. The tip was then withdrawn from the surface. The deflection of the cantilever, which relates linearly with the applied force, and the current passing through the tip-layer-EB50 junction were monitored. The force-distance and the current-distance curves for FBK probed with a tip held at a potential of +0.500 V are presented in figure 3.13, the solid traces represents the behaviour while as tip is pushing into the surface while the dotted line

is while the probe is pulling away from the surface. Figure 3.13 clearly shows a dramatic change in the measured current as the force is increased on the sample. Interestingly, as the tip is withdrawn from the surface and the force is decreased a similar electrical behaviour is observed, but the response of the withdrawal is consistently shifted 19.7 ± 2.5 nm, which corresponds to 18.7 ± 2.2 nN. The force-distance and resulting current curves were collected again at 1.000 V and the resulting results are presented in figure 3.14. Again, the current response varies dramatically as the force is increased. As with the response at 0.500 V, the behaviour is repeated when the tip is withdrawn, with the features shifted 20.7 ± 4.1 nN. Force-distance-current curves are shown for p-nitrobenzene at 0.500 V and 1.000 V in figures 3.15 and 3.16 respectively. As with the case of FBK, the current response is affected heavily by the applied force. The same feature shift of about 18 nN is seen with the p-nitrobenzene samples as was seen with the FBK samples. For ease of comparison the feature shifts are summarized in table 3.06.

Attached moiety and potential	Shift (nN)	sd (nN)
Fast black K 0.500 V	19	2
Fast black K 1.000 V	21	4
p-Nitrobenzene 0.500 V	18	2
p-Nitrobenzene 1.000 mV	18	3

Table 3.06. Feature shift in force-distance-current plots for studied films.

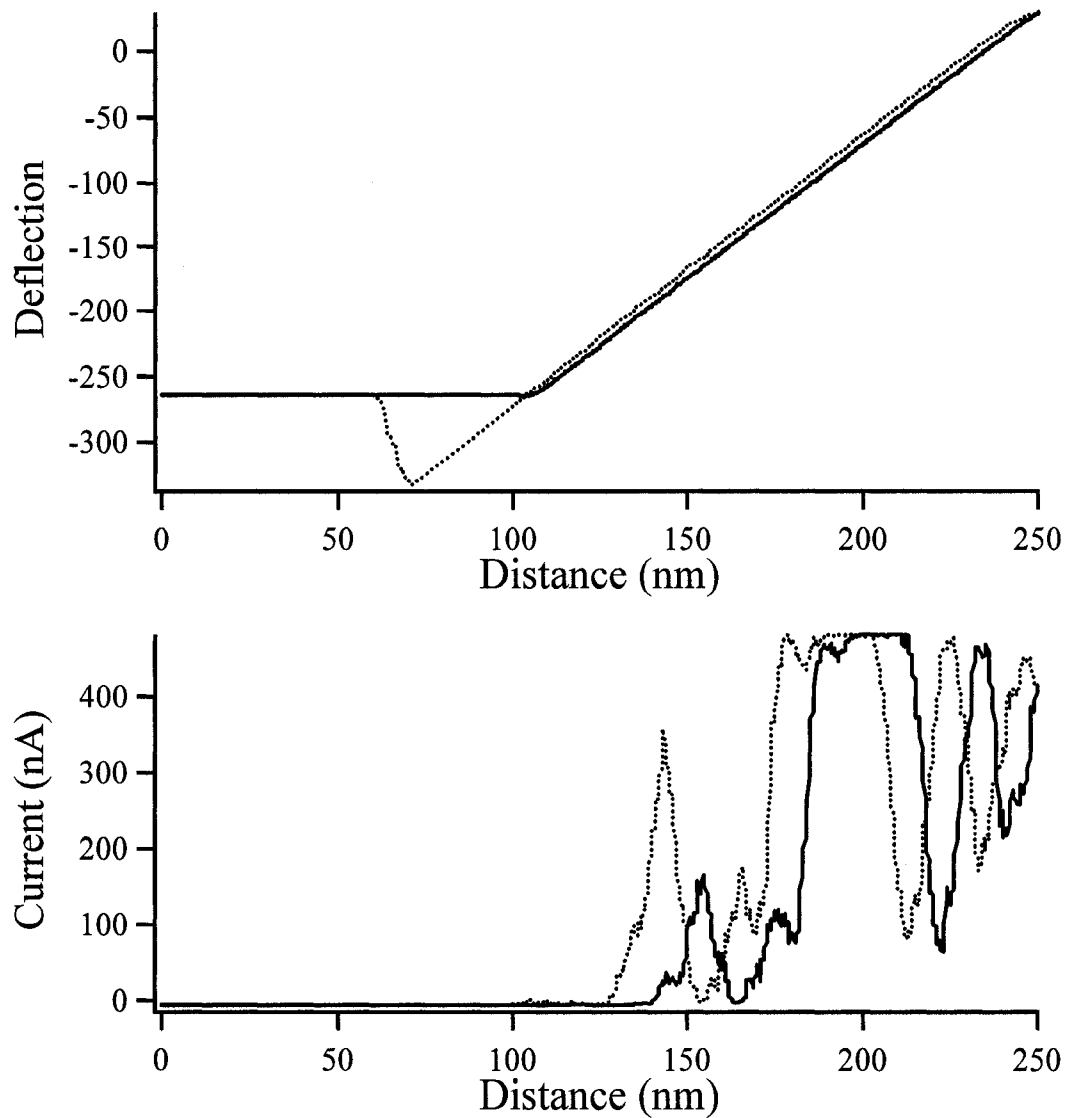


Figure 3.13. Force vs distance curves for Fast Black K at 0.500 V and resulting current (bottom). Solid line pushing in, dashed line pulling out. Average of 25 curves.

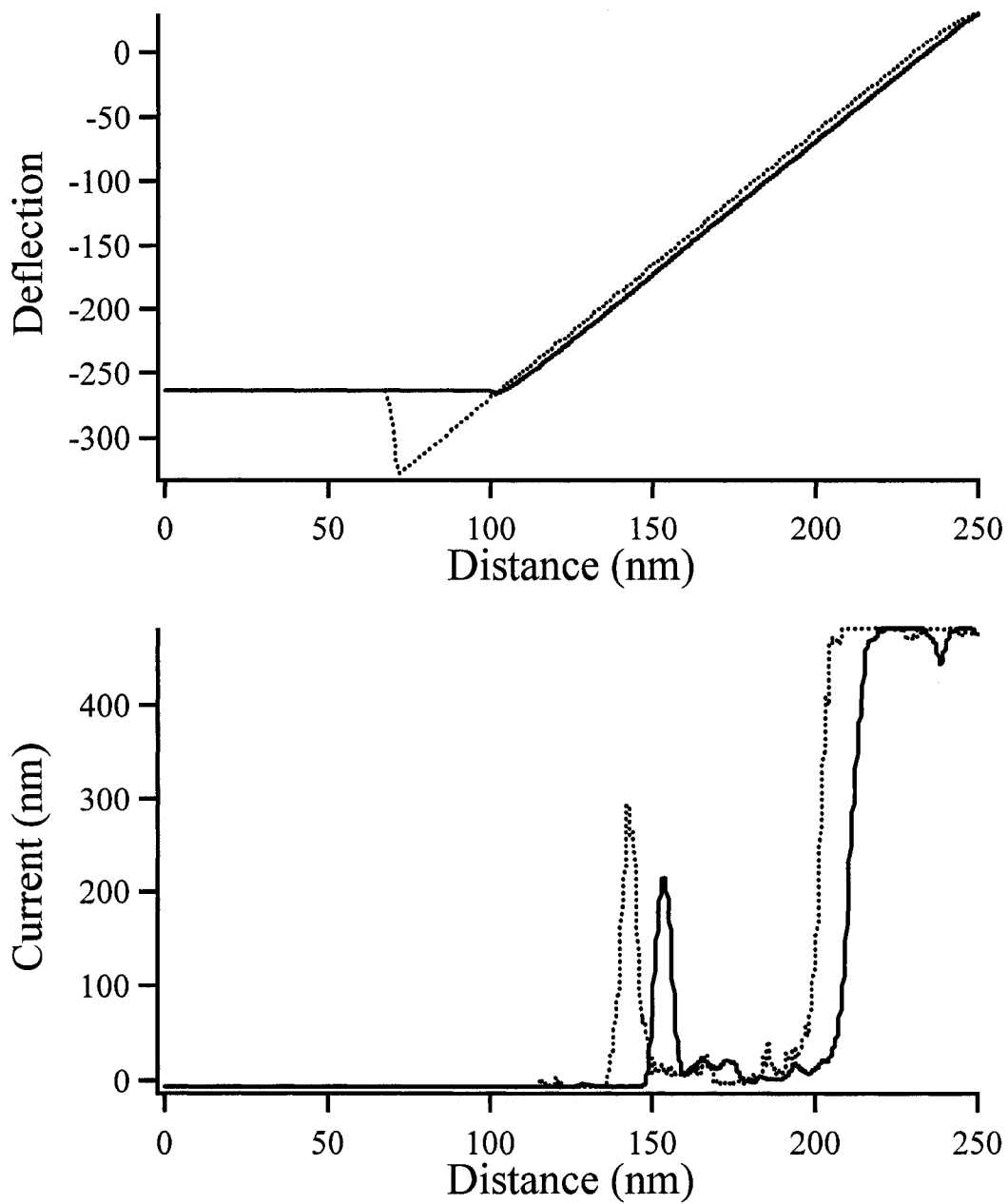


Figure 3.14. Force vs distance curves for Fast Black K at 1.000 V and resulting current (bottom). Solid line pushing in, dashed line pulling out. Average of 25 curves.

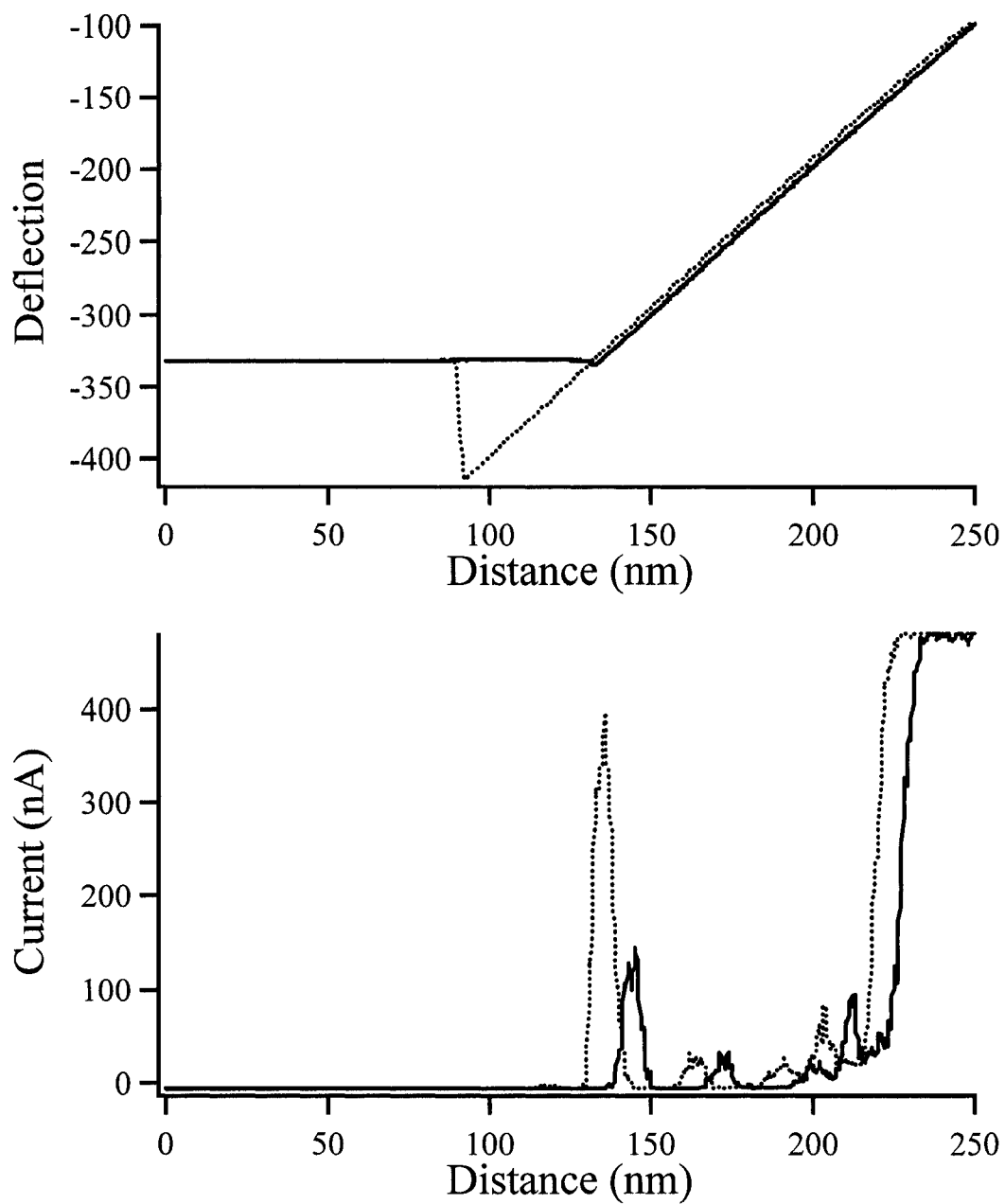


Figure 3.15. Force vs distance curves for p-nitrobenzene at 0.500 V and resulting current (bottom). Solid line pushing in, dashed line pulling out. Average of 25 curves.

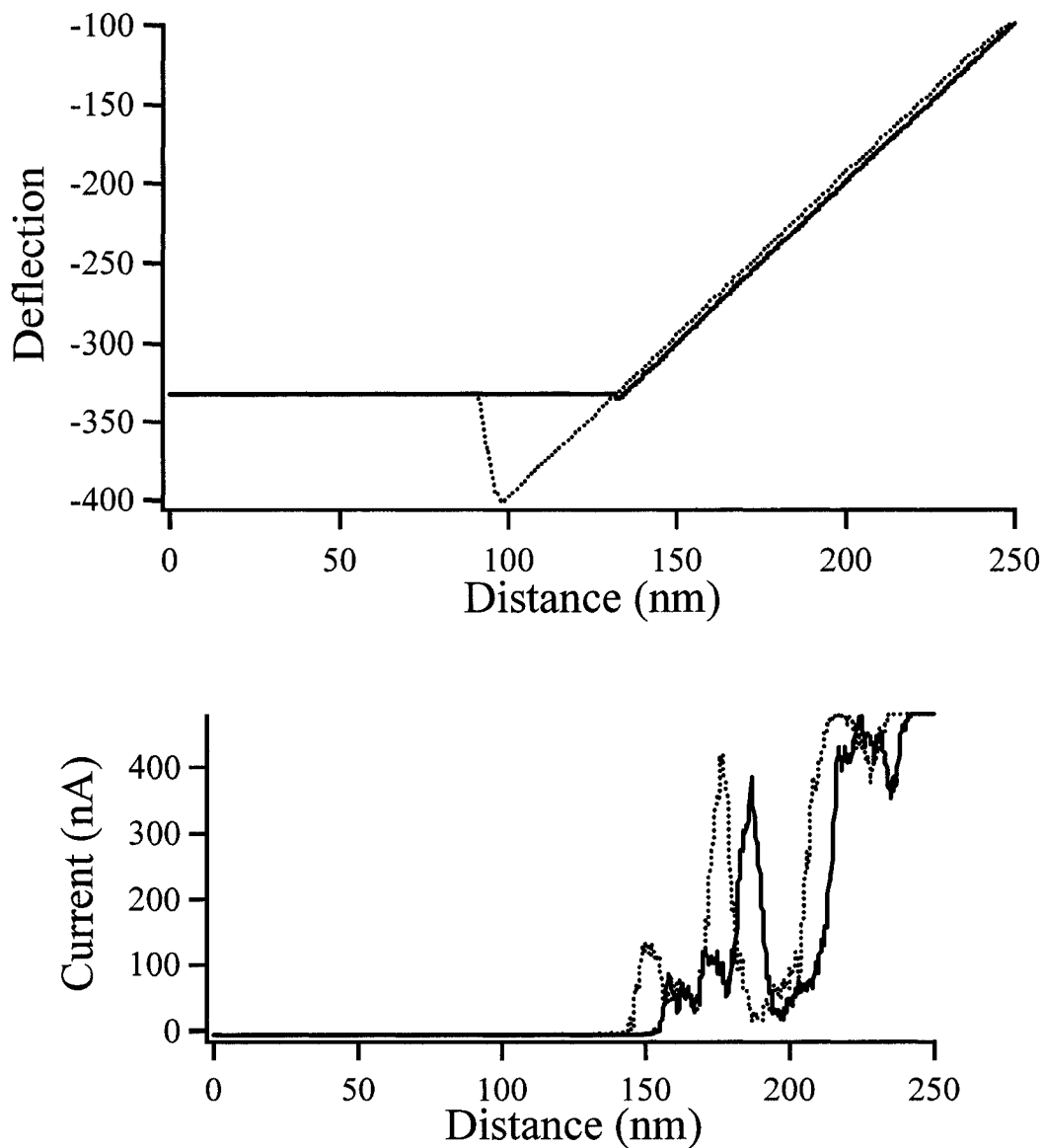


Figure 3.16. Force vs distance curves for p-nitrobenzene at 1.000 V and resulting current (bottom). Solid line pushing in, dashed line pulling out. Average of 25 curves.

All of the force-current curves show a strong dependence of the measured current on the applied force. The p-nitrobenzene films showed an onset of current with less applied force as compared to that of FBK films. The force dependent response is most likely a result of the molecular conformation changes in the films as it is being locally compressed under the tip. These conformation changes appear to be reversible at the studied forces with an equivalent 18 nN hysteresis.

The current-voltage, or IV, characteristics of the prepared films were also probed with C-AFM. The samples were imaged in tapping mode to determine a suitable area for analysis; the C-AFM was then switched to contact mode and the tip was engaged on the surface. The contact force was adjusted to coincide to the initial rising edge of the current as seen in the force-current plots. The potential was slowly ramped at a rate of 0.821 V/s from positive potential to negative potential, with respect to the tip. The current response of FBK is presented in figure 3.17 and that of p-nitrobenzene is presented in figure 3.18. The current-voltage characteristics for these two systems are significantly different. Fast black K shows behaviour indicative of a rectifier over a 2.00 V window. The negative current is greater than positive current, with respect to the tip. This implies that electron transport from the carbon through the FBK film to the tip is preferred over flow from the tip to the film and finally in the carbon. This preferential direction of electron flow is consistent with the work functions of platinum and carbon, 5.65 eV and 5.0 eV respectively.³⁹

Figure 3.18 shows the IV response of p-nitrobenzene over a 0.400 V window. The solid trace is the forward scan from positive to negative potential and the dotted

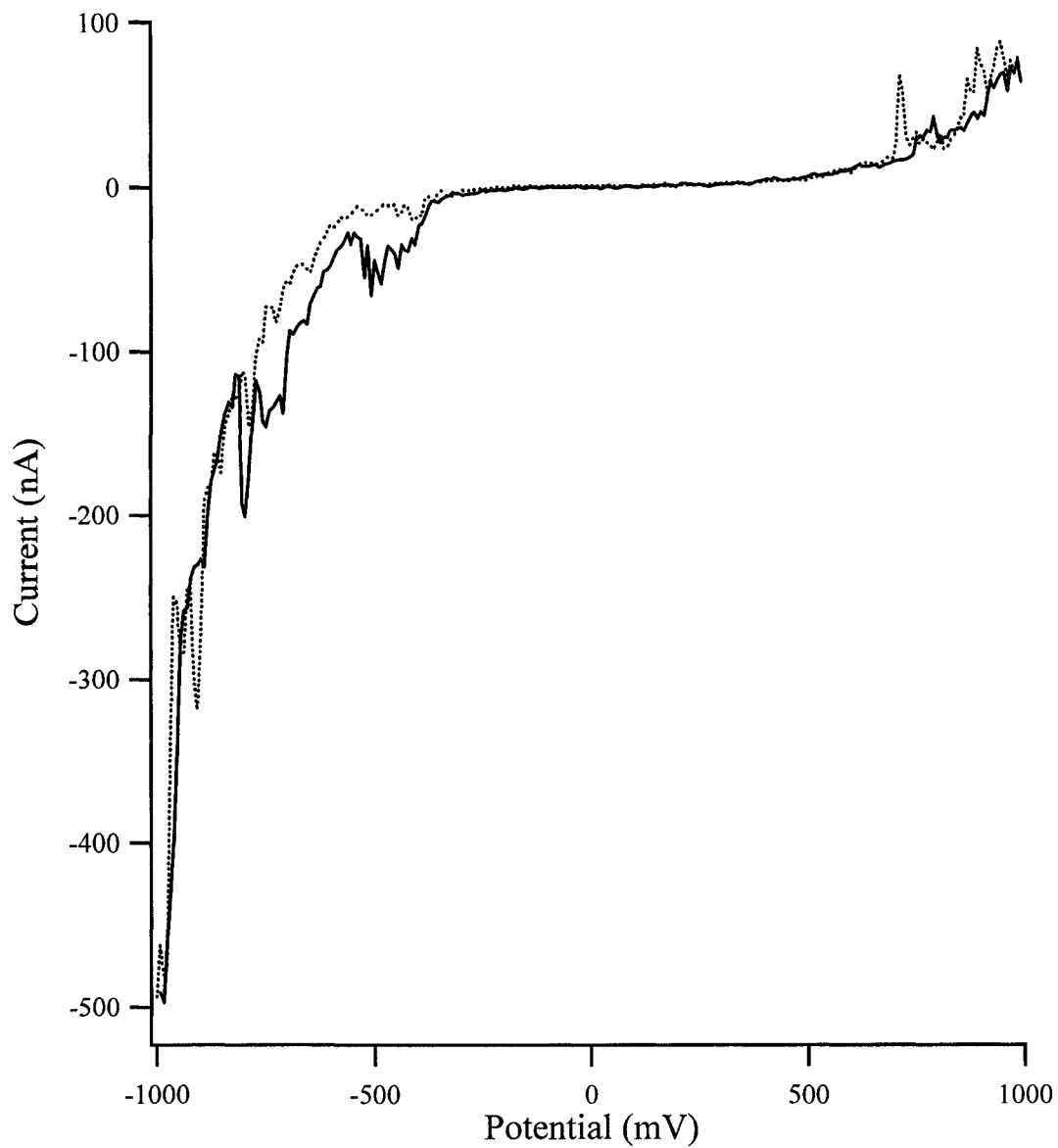


Figure 3.17. Current-voltage curve of Fast Black K modified EB50. Solid black – forward direction. Dotted – reverse direction. Average of 50 scans.

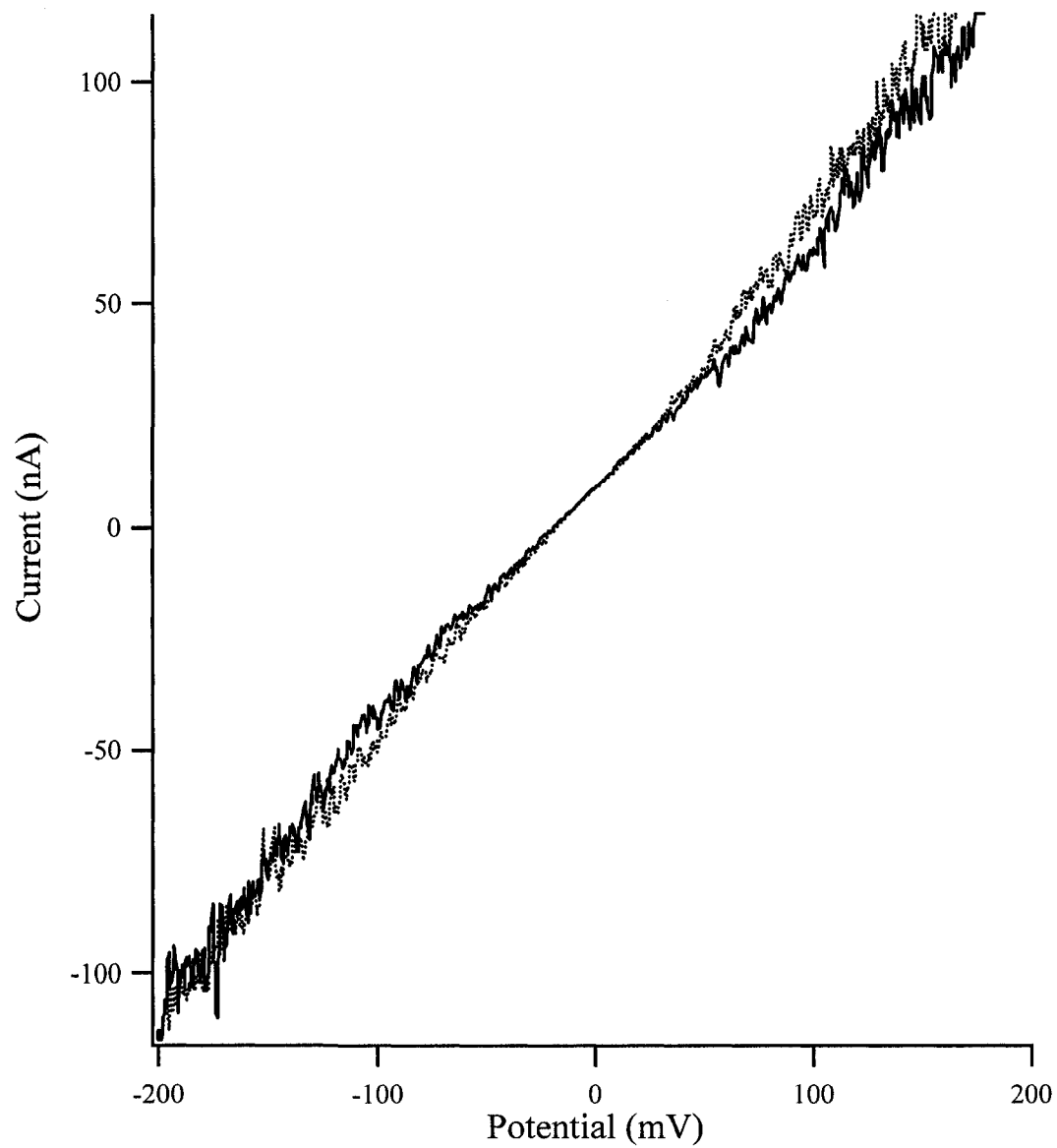


Figure 3.18. Current-voltage curve of p-nitrobenzene modified EB50. Solid black – forward direction. Dotted – reverse direction. Average of 50 scans.

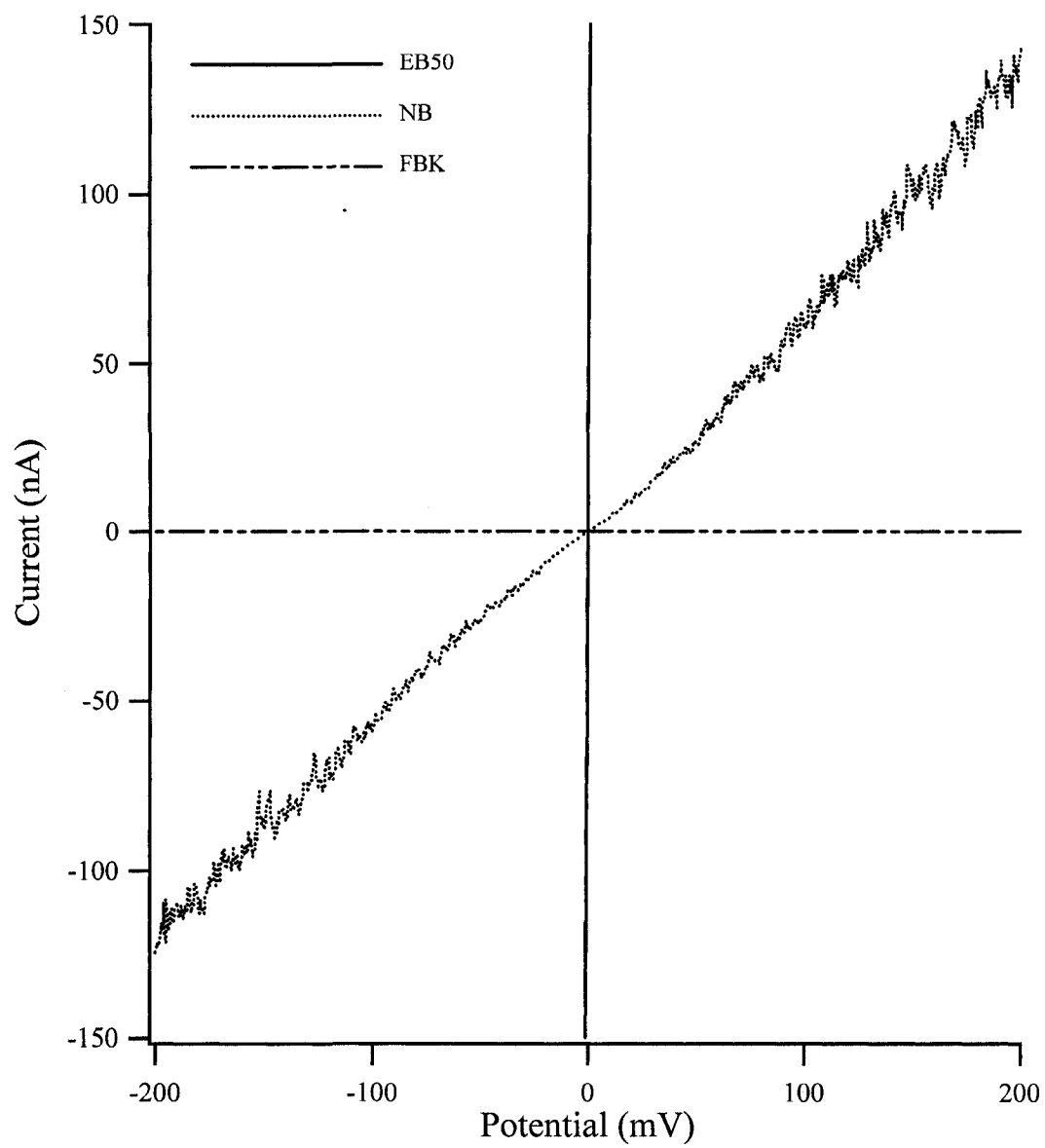


Figure 3.19. Current-voltage curves of Fast Black K modified EB50, p-nitrobenzene modified EB50 and bare EB50.

trace is the reverse scan. The behaviour of p-nitrobenzene is considerably different from that of FBK. The response is linear over the same 2.00 V window, with the center portion displayed in figure 3.18. The slope of the IV curve for p-nitrobenzene is 5.92×10^{-7} S, which is equivalent to a resistance of 1.69 M Ω . For comparison, the linear regions of the current-voltage curves for bare EB50, FBK modified EB50 and p-nitrobenzene modified EB50 are shown in figure 3.19. On this limited scale the different films behave quite differently in regards to electron transport. Bare EB50 behaves as a conductor, p-nitrobenzene has the properties of a resistor, and the FBK film acts like an insulator.

4. Conclusions

Electrochemical deposition of aryl moieties onto electron beam evaporated carbon from the corresponding diazonium was achieved. This deposition occurred similar to deposition on similar graphitic surfaces. A variety of molecules were grafted and presented. A novel method for depositing regularly patterned features on carbon surfaces for the determination of deposited film thicknesses was presented. Finally, the electrical properties of films created from FBK and p-nitrobenzene were probed. The electrical response was shown to have a profound dependence on the applied force to the molecular thin film. An example of a simple molecular resistor and a molecular rectifier were presented. The methods discussed within this chapter can be used to easily screen molecules as candidates for use in molecular electronic devices.

References

- (1) Noel, M.; Anantharaman, P. N. *Surface & Coatings Technology* **1986**, *28*, 161-179.
- (2) Jannakoudakis, A. D.; Jannakoudakis, P. D.; Theodoridou, E.; Besenhard, J. O. *Journal of Applied Electrochemistry* **1990**, *20*, 619-624.
- (3) Lin, A. W. C.; Yeh, P.; Yacynych, A. M.; Kuwana, T. *Journal of Electroanalytical Chemistry* **1977**, *84*, 411-419.
- (4) Donnet, J. B.; Ehrburger, P. *Carbon* **1977**, *15*, 143-152.
- (5) Delamar, M.; Hitmi, R.; Pinson, J.; Saveant, J. M. *Journal of the American Chemical Society* **1992**, *114*, 5883-5884.
- (6) Balz, G.; Schiemann, G. *Berichte Der Deutschen Chemischen Gesellschaft* **1927**, *60*, 1186-1190.
- (7) Dunker, M. F. W.; Starkey, E. B.; Jenkins, G. L. *Journal of the American Chemical Society* **1936**, *58*, 2308-2309.
- (8) Kariuki, J. K.; McDermott, M. T. *Langmuir* **1999**, *15*, 6534-6540.
- (9) Kariuki, J. K.; McDermott, M. T. *Langmuir* **2001**, *17*, 5947-5951.
- (10) Anariba, F.; DuVall, S. H.; McCreery, R. L. *Analytical Chemistry* **2003**, *75*, 3837-3844.
- (11) Baranton, S.; Bélanger, D. *Journal of Physical Chemistry B* **2005**, *109*, 24401-24410.
- (12) Aviram, A.; Ratner, M. A. *Chemical Physics Letters* **1974**, *29*, 277-283.
- (13) Aviram, A.; Ratner, M. A. *Bulletin of the American Physical Society* **1974**, *19*, 341-341.

- (14) Ranganathan, S.; McCreery, R.; Majji, S. M.; Madou, M. *Journal of the Electrochemical Society* **2000**, *147*, 277-282.
- (15) Ranganathan, S.; McCreery, R. L. *Analytical Chemistry* **2001**, *73*, 893-900.
- (16) Ranganathan, S.; Steidel, I.; Anariba, F.; McCreery, R. L. *Nano Letters* **2001**, *1*, 491-494.
- (17) Solak, A. O.; Eichorst, L. R.; Clark, W. J.; McCreery, R. L. *Analytical Chemistry* **2003**, *75*, 296-305.
- (18) Solak, A. O.; Ranganathan, S.; Itoh, T.; McCreery, R. L. *Electrochemical and Solid State Letters* **2002**, *5*, E43-E46.
- (19) DuVall, S. H.; McCreery, R. L. *Journal of the American Chemical Society* **2000**, *122*, 6759-6764.
- (20) Xu, J. S.; Granger, M. C.; Chen, Q. Y.; Strojek, J. W.; Lister, T. E.; Swain, G. M. *Analytical Chemistry* **1997**, *69*, A591-A597.
- (21) DuVall, S. H.; McCreery, R. L. *Analytical Chemistry* **1999**, *71*, 4594-4602.
- (22) Downard, A. J.; Roddick, A. D.; Bond, A. M. *Analytica Chimica Acta* **1995**, *317*, 303-310.
- (23) Laforgue, A.; Addou, T.; Bélanger, D. *Langmuir* **2005**, *21*, 6855-6865.
- (24) Saby, C.; Ortiz, B.; Champagne, G. Y.; Bélanger, D. *Langmuir* **1997**, *13*, 6805-6813.
- (25) Stewart, M. P.; Maya, F.; Kosynkin, D. V.; Dirk, S. M.; Stapleton, J. J.; McGuinness, C. L.; Allara, D. L.; Tour, J. M. *Journal of the American Chemical Society* **2004**, *126*, 370-378.

- (26) Mendes, P.; Belloni, M.; Ashworth, M.; Hardy, C.; Nikitin, K.; Fitzmaurice, D.; Critchley, K.; Evans, S.; Preece, J. *Chemphyschem* **2003**, *4*, 884-889.
- (27) Eck, W.; Stadler, V.; Geyer, W.; Zharnikov, M.; Golzhauser, A.; Grunze, M. *Advanced Materials* **2000**, *12*, 805-808.
- (28) Adenier, A.; Cabet-Deliry, E.; Chausse, A.; Griveau, S.; Mercier, F.; Pinson, J.; Vautrin-UI, C. *Chemistry of Materials* **2005**, *17*, 491-501.
- (29) Elliott, C. M.; Murray, R. W. *Analytical Chemistry* **1976**, *48*, 1247-1254.
- (30) Sajed, B., University of Alberta, Edmonton, 2005.
- (31) Skelhorne, A. W.; Shewchuk, D.; Sajed, B.; McDermott, M. T. In *Electrochemical Society Canadian Section Spring Symposium: Saskatoon, 2005*.
- (32) Aswal, D. K.; Lenfant, S.; Guerin, D.; Yakhmi, J. V.; Vuillaume, D. *Analytica Chimica Acta* **2006**, *568*, 84-108.
- (33) Chaudret, B. *Actualite Chimique* **2005**, 33-43.
- (34) Cuniberti, G.; Gutierrez, R.; Fagas, G.; Grossmann, F.; Richter, K.; Schmidt, R. *Physica E-Low-Dimensional Systems & Nanostructures* **2002**, *12*, 749-752.
- (35) Kastler, M.; Pisula, W.; Laquai, F.; Kumar, A.; Davies, R. J.; Balushev, S.; Garcia-Gutierrez, M. C.; Wasserfallen, D.; Butt, H. J.; Riekkel, C.; Wegner, G.; Mullen, K. *Advanced Materials* **2006**, *18*, 2255-2259.
- (36) Ke, S. H.; Baranger, H. U.; Yang, W. T. *Journal of Chemical Physics* **2005**, *123*, 114701(1)-114701(8).
- (37) Palermo, V.; Palma, M.; Tomovic, Z.; Watson, M. D.; Friedlein, R.; Mullen, K.; Samori, P. *Chemphyschem* **2005**, *6*, 2371-2375.

- (38) Wang, L.; Liu, L.; Chen, W.; Feng, Y. P.; Wee, A. T. S. *Journal of the American Chemical Society* **2006**, *128*, 8003-8007.
- (39) Michaelson, H. B. *Journal of Applied Physics* **1977**, *48*, 4729-4733.

Chapter IV

Attachment of Aryl Molecules to Platinum

1. Introduction

The electrochemical attachment of aryl molecules to carbon surfaces may be performed via the electrochemical reduction of the corresponding diazonium salt as discussed in previous chapters. Since the initial discovery of the electrochemical reactivity of aryl diazoniums on graphitic electrodes,¹ a number of other surfaces have been investigated for modification via aryl diazonium reduction. The electrochemical grafting of aryl diazoniums has become a prominent and widely accepted method for the preparation of organic films on conductors and semiconductors. Wheeler and coworkers used the electrochemical attachment of diazonium derived radicals to silicon(100) and platinum as a standard for comparing films created from aryl iodonium salts.² Electrochemical deposition onto surfaces of silicon,²⁻⁹ iron,^{3, 10-15} diamond,^{3, 16} cobalt, nickel, copper, zinc, gold, and platinum^{2, 3, 17} have all received attention recently.

One of the more interesting potential applications for the modification of platinum surfaces is that for alternative energy source of hydrogen and corresponding hydrogen storage. Hydrogen powered vehicles are becoming increasingly popular when compared to the traditional petroleum burning automobiles. Currently, most of the major consumer automobile manufacturers offer a hydrogen powered vehicle, either fully hydrogen powered or hybrid. Intra-city public transportation in the form

of busses is another popular medium for the testing of hydrogen powered vehicles. A common design for fuel cells is polymer electrolyte membrane. This form uses two electrodes separated by a polymer capable of conducting protons but insulating with respect to electrons. The electrodes are typically carbon supported platinum. Significant research is being done to improve the efficiency of the fuel cell, protect the catalytic platinum as well as find alternatives to pure platinum as a catalyst. In an impossible, but interesting scenario, it is estimated that if all the cars by 2020 were powered by state-of-the-art fuel cells that the world platinum supply would fall 80% short.¹⁸

Diazonium chemistry has been used to modify the catalyst carbon support by Xu and coworkers.¹⁹⁻²¹ Xu used *in situ* diazonium synthesis and deposition to attach a variety of chemical species to the carbon surface, including sulfonic acid, ethanesulfonic acid, and pentafluorophenyl groups. The pentafluorophenyl modification scheme was reported as reducing local flooding; a common pitfall of fuel cell design. The ethanesulfonic and sulfonic group modification provided a 60% increase in performance, attributed to the increased acidity and higher proton conductance.

Poisoning of the platinum catalyst is a major issue in the operation of fuel cells. Purification of the hydrogen prior to use is costly and hydrogen produced at hand typically contains significant impurities, including carbon monoxide.²² It is well known that carbon monoxide binds strongly to the surface of platinum and thereby reduces the number of active surface sites. This has a huge negative impact on the performance and efficiency. Significant research has been performed to develop

platinum based catalysts that are tolerant of contamination. The most abundant of this research uses platinum alloys or metal adatoms and were shown to have a high tolerance to carbon monoxide poisoning.²³⁻²⁷ Direct modification the platinum with organometallic compounds was performed by Yanso and coworkers.²⁸ The authors directly attached *N,N'*-ethylenebis(salicylideneaminato)oxovanadium(IV)²⁹ and *N,N'*-mono-8-quinolyl-*o*-phenylenediamine³⁰ to the platinum. The resulting organic metal complexes were shown to have a tolerance to carbon monoxide higher then that for the ubiquitous ruthenium-platinum. The published results of Yano and coworkers are the first to suggest that direct modification of platinum with organic moieties is a feasible method to develop poison-resistant catalysts.

With the use of established diazonium chemistry to modify the supporting carbon coupled with demonstration of the direct modification of the platinum catalyst with organometallic species to improve the performance of fuel cells, it becomes apparent that the development of attachment schemes that supports both functions is desirable. Diazonium chemistry has the potential to fulfill both of these roles.

The diazonium derived attachment to platinum is directly related to the work presented in this thesis when one considers the counter electrode. The quintessential method for the electrochemical reduction of aryl diazoniums involves using a platinum counter electrode during the deposition. Although platinum is traditionally considered an inert material, recent investigations indicate that aryl diazonium salts will spontaneously attach to a variety of carbon, metal, and semiconductor surfaces including the atomically similar palladium.^{3, 31-35} This phenomenon suggests the possibility of the aryl diazoniums of interest spontaneously attaching to the platinum

counter electrode during the course of the experiments. As discussed in chapter 3, attachment of diazonium derivatives to carbon electrode surfaces will typically passivate the electrode and thus hinder electron transport. The passivation of the platinum surface with respect to the formation of the aryl radical was observed by Pinson when the electrochemical attachment to industrial, coinage and noble metals was investigated; included in this study was platinum.¹⁷

One of the foremost requirements for the use of aryl diazonium salts as a precursor for molecular electronic devices is reproducibility in the molecular attachment scheme. Modification of the counter electrode during the course of the experiment has the potential to alter the results of the experiment as well as add irreproducibility from one experiment to another. Due to this possibility it was deemed crucial to study the attachment of aryl diazoniums to a platinum counter electrode during a typical electrochemical reduction experiment.

This chapter will discuss the electrochemical attachment of Fast Black K, the spontaneous attachment of FBK, and the spontaneous attachment of FBK in the timeframe of a typical diazonium electrochemical experiment, all to platinum.

2. Experimental

Solutions of FBK (2,5-Dimethoxy-4-(4-nitrophenylazo)-benzenediazonium salt, Sigma-Aldrich Canada Ltd, Oakville, Ontario, Canada) were prepared at 5 mM concentration in freshly distilled reagent grade acetonitrile (Caledon Laboratory Chemicals, Georgetown, Ontario). Solutions of 1-dodecanethiol (Sigma-Aldrich

Canada Ltd, Oakville, Ontario, Canada) were prepared at about 1 – 10 mM concentration in anhydrous ethanol (Commercial Alcohols Inc, Brampton, Ontario, Canada). Solutions used for electrochemical attachment contained 0.1 M tetrabutylammonium tetrafluoroborate (Sigma-Aldrich Canada Ltd, Oakville, Ontario, Canada) as the supporting electrolyte. All solutions were prepared fresh for each experiment set and deaerated with argon (Praxair, Mississauga, Ontario, Canada) prior to use.

Platinum coated glass slides (200 nm) with a thin (less than 10 nm) chromium adhesion layer (sputtered at Micralyne Inc, Edmonton, AB, Canada) were ozone cleaned (UVO-Cleaner model 42, Jelight Company Inc, Irvine, CA, USA) for ten minutes, rinsed with anhydrous ethanol (Commercial Alcohols Inc) and dried with argon (Praxair).

For self-assembly investigations, cleaned platinum slides were immersed in solutions of 1-dodecanethiol and 2,5-dimethoxy-4-(4-nitrophenylazo)-benzenediazonium and allowed to self assemble overnight. After twenty-four hours the slides were removed from their respective solution, rinsed with ethanol and dried with argon. The substrates were then analyzed via Infrared Reflection Absorbance Spectroscopy (IRRAS) after purging the sample compartment for twenty minutes. Appropriate infrared peaks were identified and used to compare relative coverage of the platinum by the molecule of interest. After spectra were recorded, each sample was incubated in a displacement solution overnight. The displacement solution for the 2,5-dimethoxy-4-(4-nitrophenylazo)-benzenediazonium/platinum sample was the 1-dodecanethiol solution and the displacement solution for the 1-

dodecanethiol/platinum sample was the 2,5-dimethoxy-4-(4-nitrophenylazo)-benzenediazonium solution. The preparation for analysis via IRRAS was the same as described above, except a thirty-minute sample chamber purge was used. The samples were again analyzed via IRRAS.

For electrochemical attachment studies, two ozone cleaned, platinum coated glass slides were immersed in a solution of 2,5-dimethoxy-4-(4-nitrophenylazo)-benzenediazonium and tetrabutylammonium tetrafluoroborate. The platinum slides were arranged as parallel plates two centimeters apart. The slides were used as the working and counter electrode in a typical three-electrode electrochemical set-up. A home built Ag/Ag⁺ reference electrode, as described in chapter 3, was also used. The potential was cycled once from 400 mV to -900 mV at 100 mV/s and the data was recorded. The potential was then continually cycled with the same parameters ten more times and the data were recorded. Samples were analyzed via IRRAS using the conditions described above. To study displacement by 1-dodecanethiol, the modified working electrode was immersed in a 1-dodecanethiol solution for twenty-four hours and then analyzed via IRRAS using the conditions described above.

Atomic force microscopy was performed with an Asylum Research MFP-3D (Asylum Research, Santa Barbara, CA, USA) in AC mode (intermittent contact). The probes used were NSC15/50 (Mikromasch, Tallinn, Estonia) with a nominal spring constant of 40 N/m and a typical resonance frequency of 325 kHz. Typical scan rates used were 1-2 Hz.

The infrared reflection absorbance spectroscopy spectra were collected at a forward scan rate of 40 kHz and a reverse scan rate of 50 kHz. Data were recorded

during the forward scan. Due to the inherent low signal obtained from monolayer and near-monolayer samples, each spectra and background consisted of an average of 1000 scans to achieve a reasonable signal-to-noise. Spectra were recorded with a resolution of 2.0 cm^{-1} . The additional following parameters were used; double FFT symmetry; triangular apodization; Mertz phase correction; triangular phase apodization; and the phase type used was real.

3. Results and Discussion

3.1 Topography and Electrochemistry of Bare Platinum Substrates

The investigation of spontaneous attachment of aryl diazoniums to platinum was started with the intentional grafting by the standard electrochemical reduction method previously discussed. The electrochemical reduction of diazonium and the resulting attachment of the daughter aryl radical to platinum has previously been performed using para substituted nitro, iodine, trifluoromethyl, fluorinated hexane, and dodecane phenyl diazonium.¹⁷ It was logical to assume the reduction of FBK would similarly attach to platinum. Prior to attachment of FBK, the platinum electrodes were characterized by AFM and electrochemistry. Similar to the preparation for electrochemistry, platinum slides were ozone cleaned and rinsed with

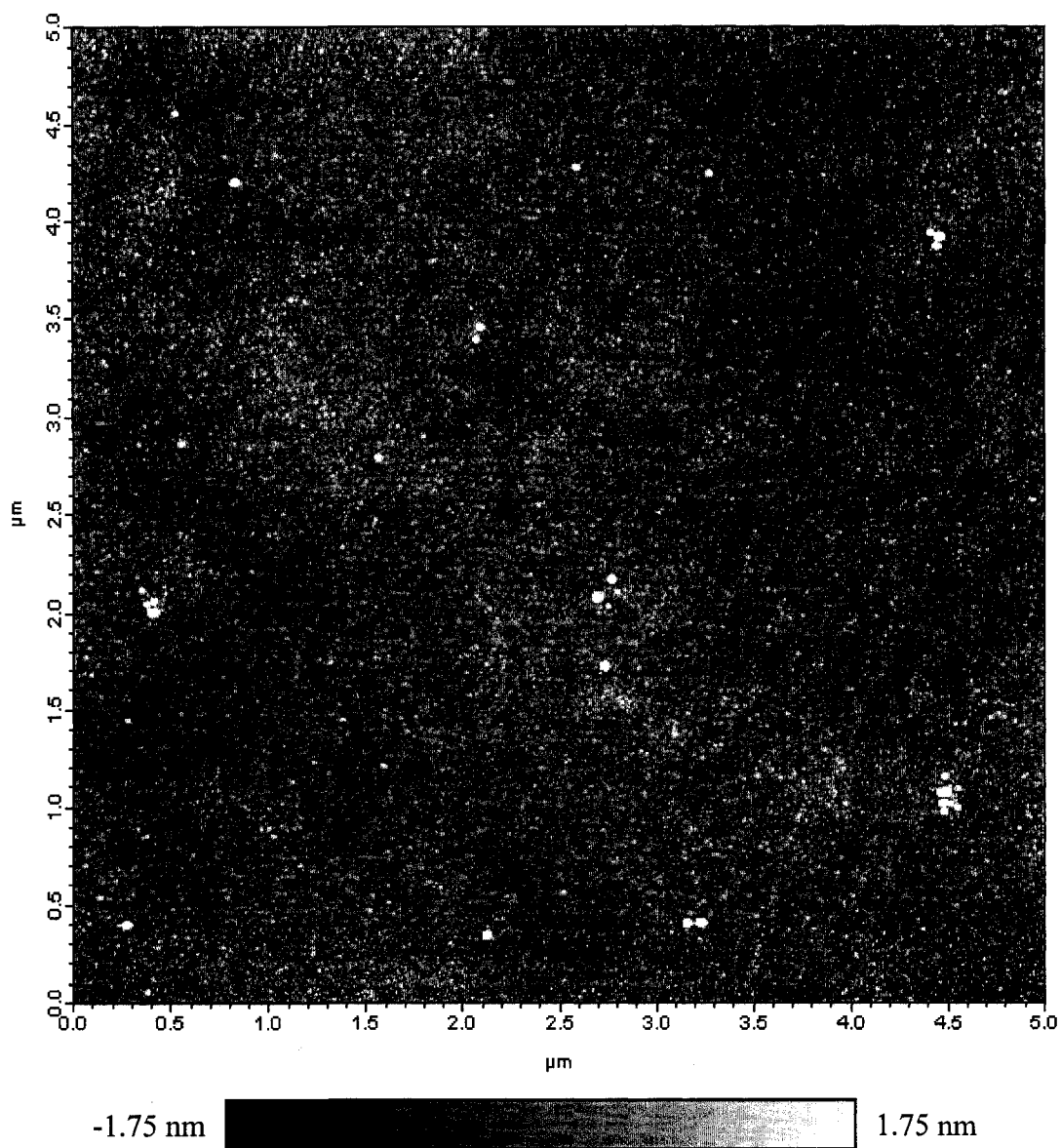


Figure 4.01. Atomic force microscopy image of unmodified glass supported platinum, $25 \mu\text{m}^2$ image size.

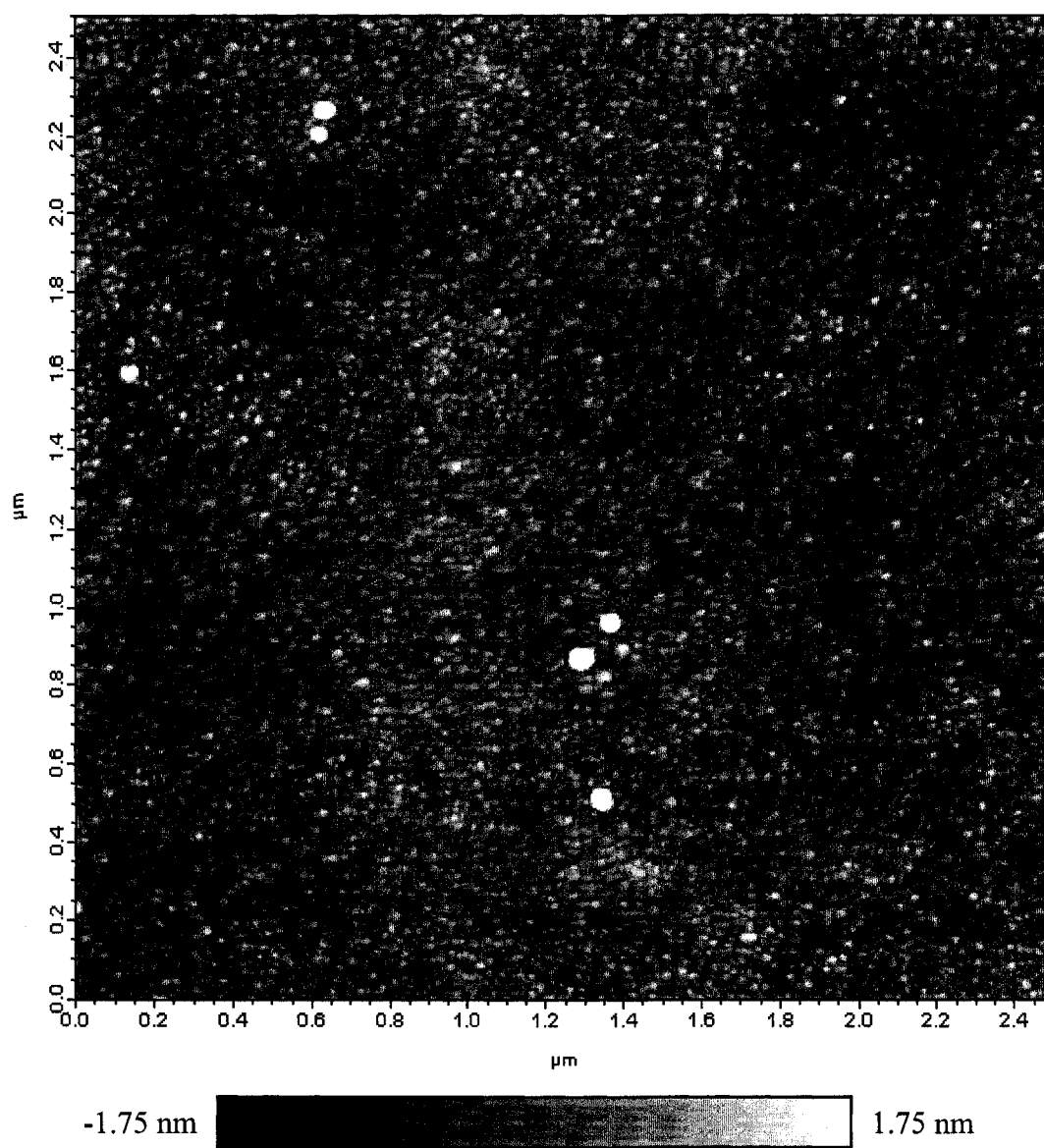


Figure 4.02. Atomic force microscopy image of unmodified glass supported platinum, $6.25 \mu\text{m}^2$ image size.

ethanol. The slides were imaged via AFM; images of unmodified platinum slides, 25 μm^2 and 6.25 μm^2 , are shown in figures 4.01 and 4.02 respectively. The surface consists of platinum grains of about 20-50 nm diameter with sporadically located larger platinum features. This type of distribution is typical for a sputtered metal film.

To facilitate comparison with the electrochemical results discussed in chapter 5 the electrochemical behaviour of platinum towards ferricyanide was also investigated. The heterogeneous electron transport rate constant was calculated via the method described in chapter 2. Representative cyclic voltammograms of ferricyanide on platinum are shown in figure 4.03 and the tabulated peak separations are listed in table 4.01. The calculated k^o of ferricyanide in 1M KCl was 0.38 ± 0.11 cm s^{-1} . The literature value for k^o in 1M NaCl is reported as 0.18 cm s^{-1} on a similar platinum electrode.³⁶ Although our measured value initially appears high, when one considers the influence of ion pairing of the supporting electrolyte, the values agree quite well. It is well established that the choice of supporting electrolyte alters the observed heterogeneous electron transport rate constant of ferricyanide.³⁷⁻³⁹ The general order of observed k^o values with respect to the supporting electrolyte cation follows the following order; $\text{Li}^+ < \text{Na}^+ < \text{K}^+ < \text{Rb}^+ \leq \text{Cs}^+$ for alkali metals.^{37, 39} For ferricyanide on a gold electrode, k^o measured in 1M KCl was reported to be 3.5 to 5 times larger than the k^o measured in 1 M NaCl.³⁹

Scan Rate (V/s)	ΔE_p (V)
0.100	0.072
0.200	0.077
0.300	0.080
0.400	0.083
0.500	0.088
0.600	0.091
0.700	0.091
0.800	0.095

Table 4.01. ΔE_p of $\text{Fe}(\text{CN})_6^{3-/4-}$ on platinum (1 M KCl, 25 °C)

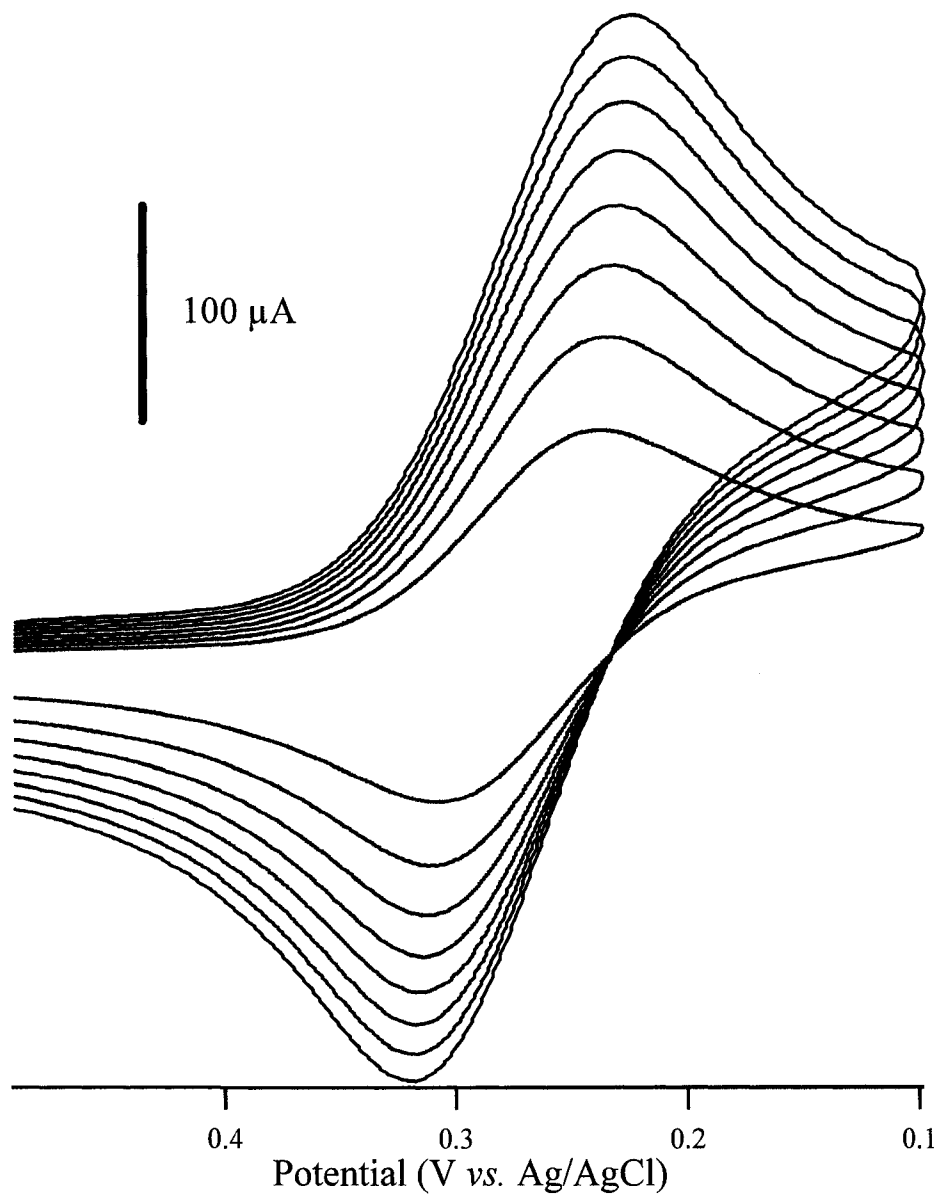


Figure 4.03. Cyclic voltammetry of $\text{Fe(CN)}_6^{3-/4-}$ in 1M KCl on glass-slide platinum (from lowest peak current to highest current) at 0.100, 0.200, 0.300, 0.400, 0.500, 0.600, 0.700, and 0.800 V/s.

3.2 Electrochemical Reduction of Fast Black K

The electrochemical reduction of Fast Black K is shown in figure 4.04. The reduction was achieved by sweeping the potential from 0.400 V to -0.900 V with respect to Ag/Ag⁺. Although there is noticeable current during the second cycle, overall the attachment to platinum is similar to attachment of FBK to carbon surfaces; the grafting to platinum is self passivating as the reduction peak is greatly reduced on the second and subsequent cycles. The attachment of FBK was confirmed by infrared reflection absorbance spectroscopy (IRRAS) and AFM. A presumably thick film was intentionally prepared from 11 cyclic voltammetry sweeps in order to facilitate confirmation of attachment.

The IRRAS spectrum of modified platinum is shown in figures 4.05 and 4.06. The spectrum is split into three regions of interest; the fingerprint region shown in 4.05, the aliphatic region shown in 4.06A, and the diazonium region shown in figure 4.06B. The infrared (IR) peaks are identified and listed in table 4.02, with two of the most prominent peaks being the symmetric stretch, ν_s , and the asymmetric stretch, ν_a , of NO₂ at 1345 and 1525 cm⁻¹ respectively. The identification of all expected IR bands in figures 4.05 and 4.06A confirms the presence of FBK or a similar FBK derivative. The absence of the diazonium peak at 2241 cm⁻¹ in figure 4.06B corroborates the proposed mechanism of diazonium reduction and confirms the observed IR signal is not simply from physisorbed FBK. The powder IR spectra of stock FBK, presented in the appendix, clearly shows the diazonium peak located at 2241 cm⁻¹. The peak located at 1742 cm⁻¹ is due to atmospheric water not purged from the chamber.

Peak Position (cm^{-1})	Group
Figure 4.05	
1037	C-O-C ν_s
1112	Ph-C-H in-plane bend
1223	C-O-C ν_a
1271	Ph-C-H in-plane bend
1345	NO ₂ ν_s
1392	R-CH ₃ symmetric deformation
1467	R-CH ₃ asymmetric deformation
1499	Aromatic ring stretch
1525	NO ₂ ν_a
1591	Aromatic ring stretch
Figure 4.06A	
2841	R-CH ₃ ν_s
2945	R-CH ₃ ν_a
3000	Ph-C-H stretch

Table 4.02. Infrared Reflection Absorbance Spectroscopy peak assignments for electrochemically immobilized Fast Black K.

The electrochemical behaviour and observed IR bands indicate a similar attachment to platinum as to graphite.

Atomic force microscopy images of FBK modified platinum are presented in figures 4.07 and 4.08. The surface topography is nearly indistinguishable from that of the underlying platinum when compared to figures 4.01 and 4.02. This implies that the resulting film is thinner than the horizontal surface features. If a similar film is prepared on platinum as it is on carbon it would be in the range of 6 nm thick as discussed in chapter 3. Compared to the platinum grain sizes of about 20-50 nm, one would expect the resulting film to be not visible on such a rough surface.

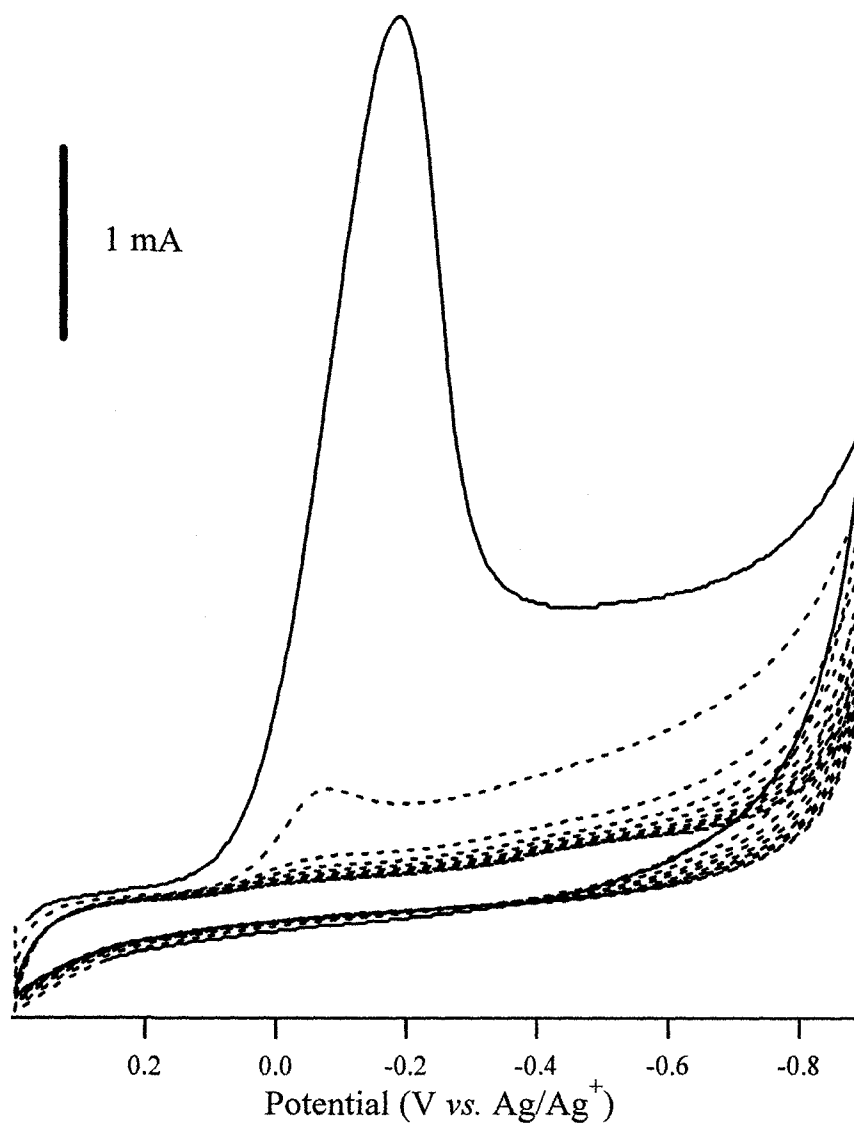


Figure 4.04. Cyclic voltammogram for the electrochemical reduction of Fast Black K on a platinum electrode from TBATFB in acetonitrile. First cycle is shown by the solid trace and subsequent scans are shown by the dashed traces.

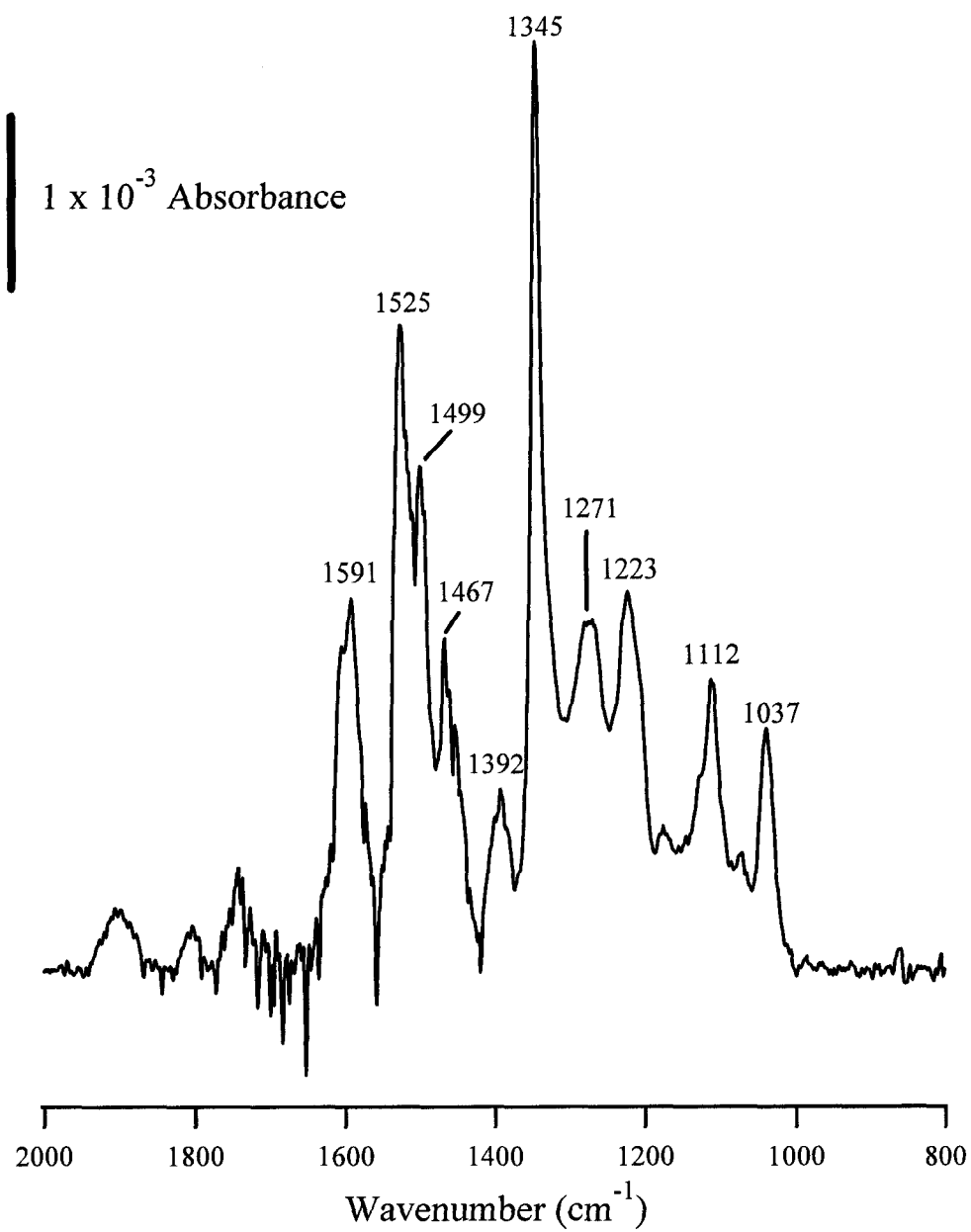


Figure 4.05. Infrared reflection absorbance spectroscopy spectra of Fast Black K electrochemically deposited on platinum.

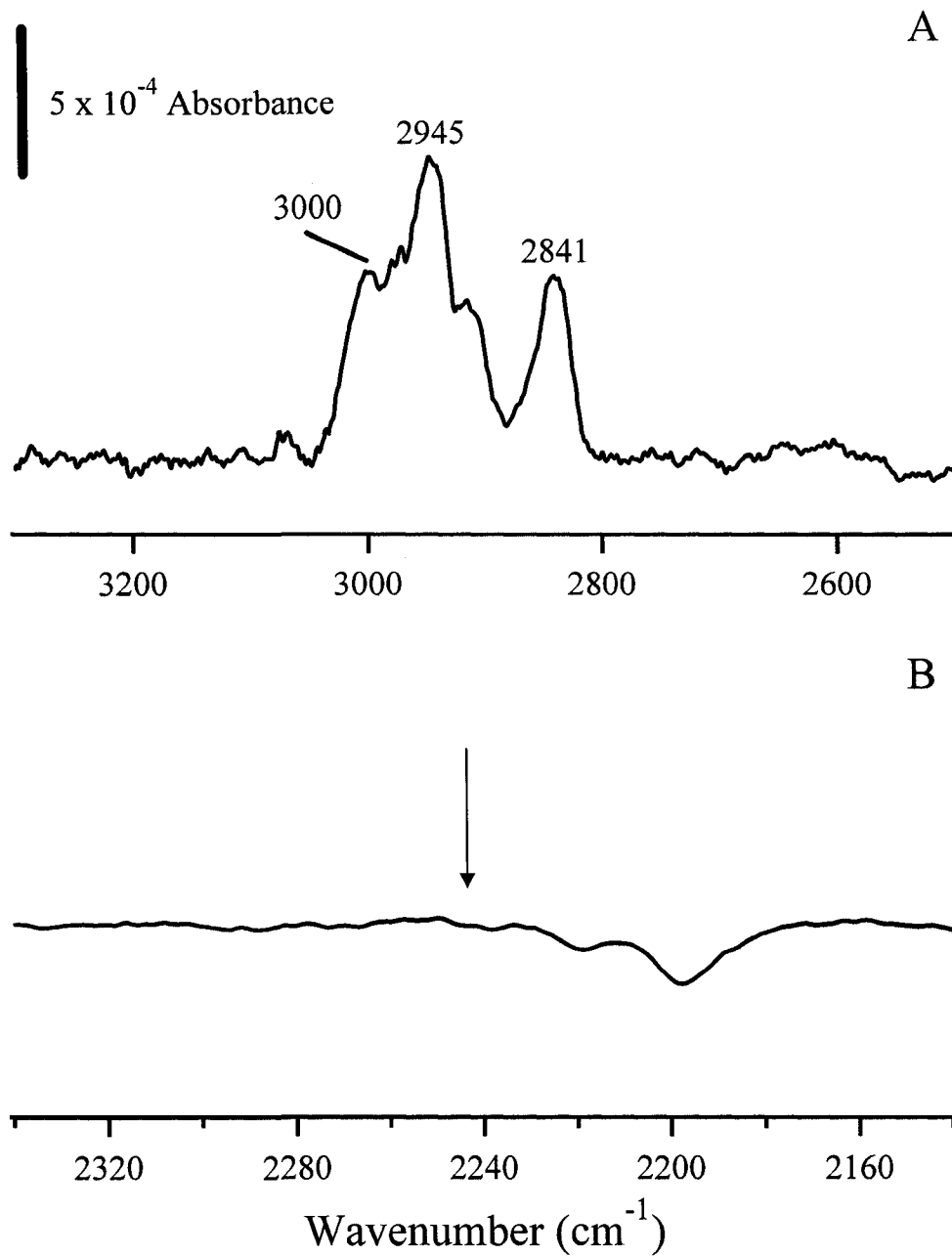


Figure 4.06. Infrared reflection absorbance spectroscopy spectra of Fast Black K electrochemically deposited on platinum. A) aliphatic region B) diazonium region with location of expected peak at 2241 cm^{-1} marked.

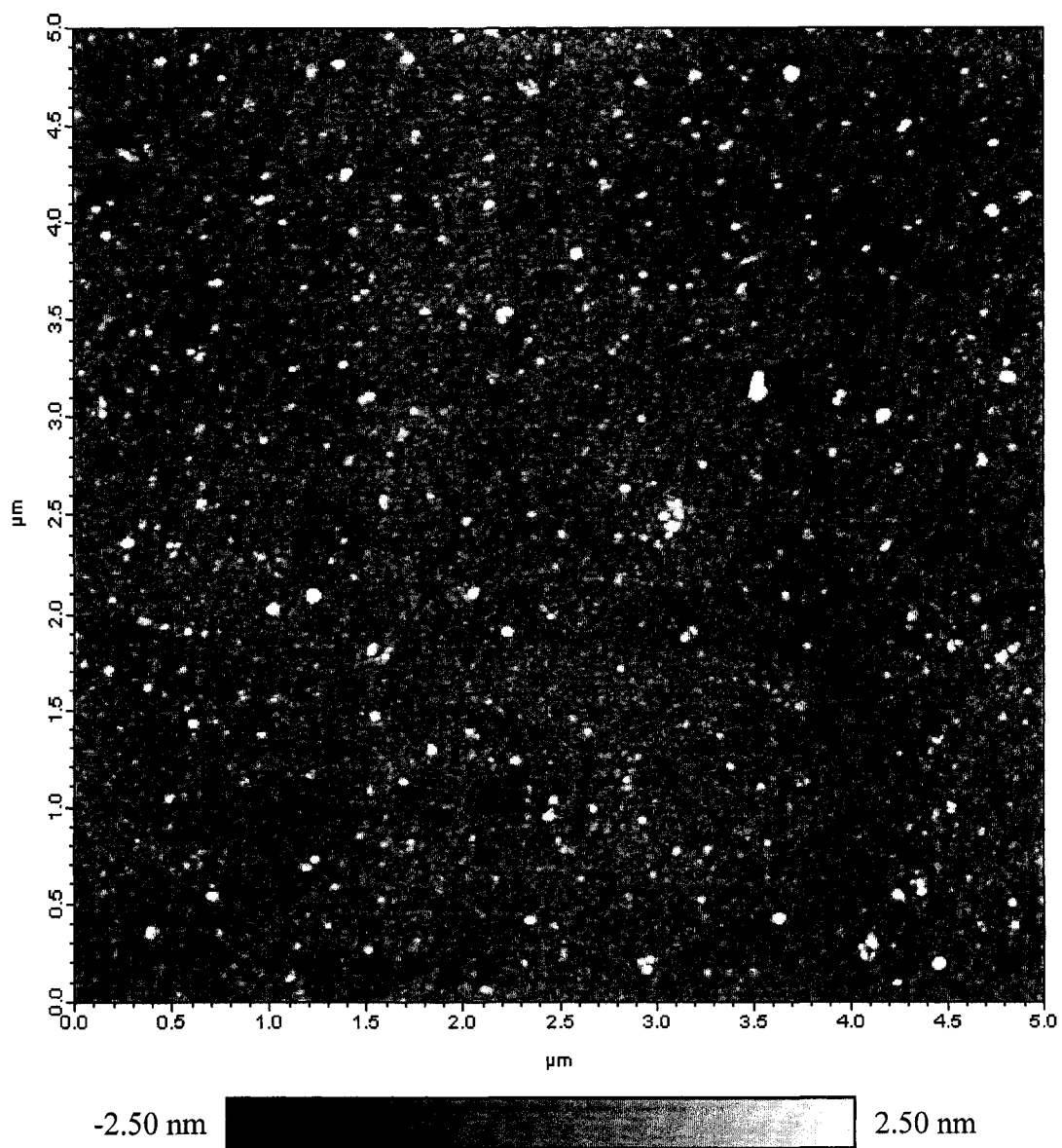


Figure 4.07. Atomic force microscopy image of Fast Black K modified glass supported platinum, $25 \mu\text{m}^2$ image size.

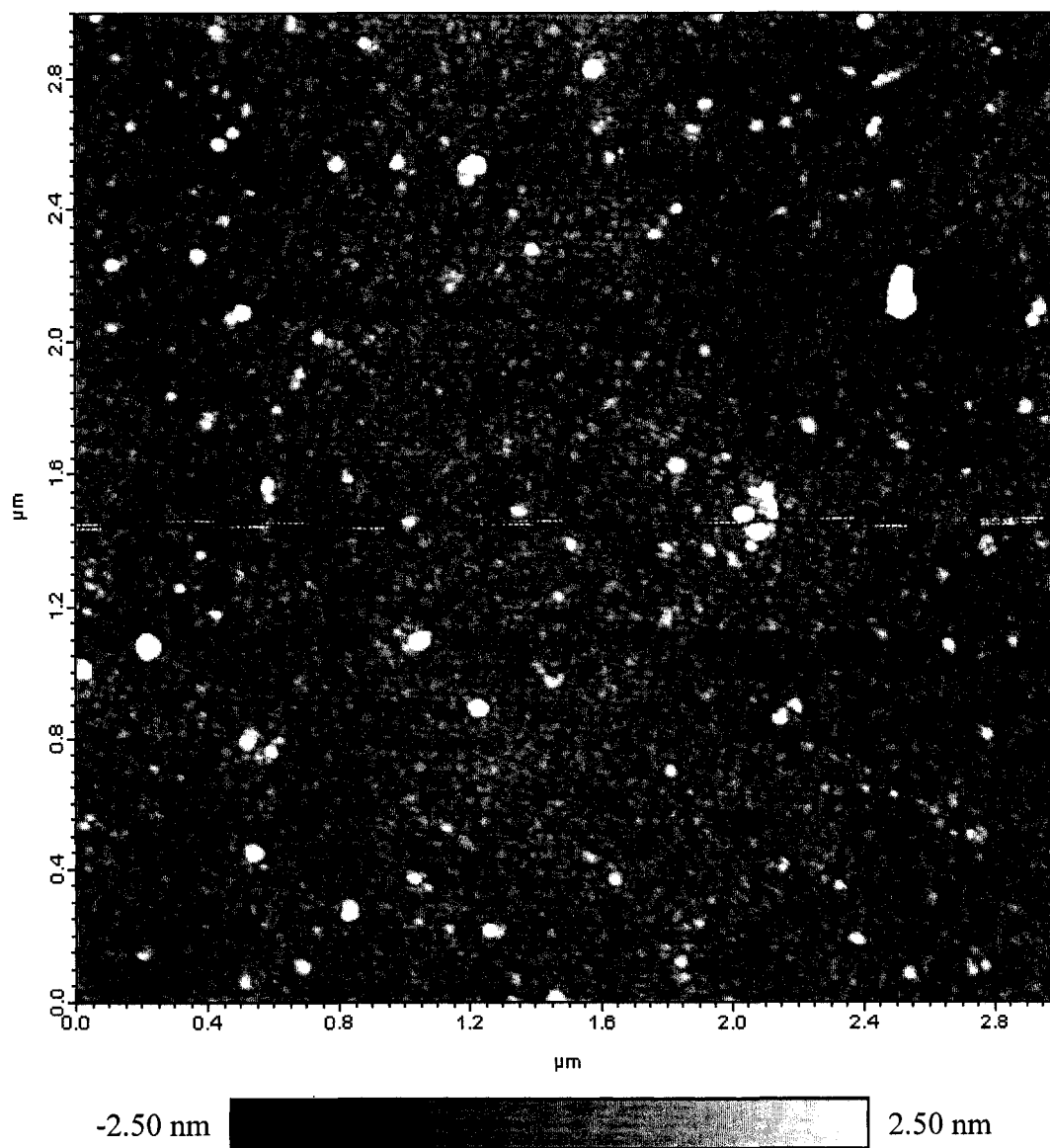


Figure 4.08. Atomic force microscopy image of Fast Black K modified glass supported platinum, $6.25 \mu\text{m}^2$ image size.

3.3 Spontaneous Attachment of Fast Black K

With the electrochemical attachment of Fast Black K achieved, the possibility of spontaneous attachment was investigated. The spontaneous self assembly of thiol, disulfides, and thio ether containing hydrocarbons on metals is a widely studied area⁴⁰⁻⁵⁸ and was used as a benchmark to compare to the spontaneous self assembly of FBK. Separate platinum slides were immersed in an acetonitrile solution of 1-dodecanethiol as well as an acetonitrile solution of tetrabutylammonium tetrafluoroborate and FBK, identical to the solutions used for the electrochemical attachment of FBK. The solutions were deaired, hermetically sealed, wrapped in optically opaque foil and allowed to react overnight. The IRRAS spectra of the thiol and diazonium self assembled samples are shown in figure 4.11. Both samples share similarity in the aliphatic region only and thus this region will be used to compare them. Summarized IRRAS peak data for spontaneously attached 1-dodacanethiol and FBK are presented in table 4.03. The IRRAS spectra for 1-dodacanethiol show all four peaks expected in the aliphatic region, the methylene symmetric and asymmetric stretches at 2854 cm^{-1} and 2924 cm^{-1} respectively, and the methyl symmetric and asymmetric stretches at 2880 cm^{-1} and 2966 cm^{-1} in that order. The peak position values for the methylene groups are shifted $3\text{-}6\text{ cm}^{-1}$ to higher wavenumbers from the expected positions whereas the methyl groups fall exactly in the location reported in the literature; this indicates a slightly lower degree of order and crystallinity of the thiol films compared to an ideal film.⁵⁹ FBK, containing only methyl aliphatic groups located on the methoxy moieties, is not expected to have as many IRRAS peaks as 1-dodecanethiol in the

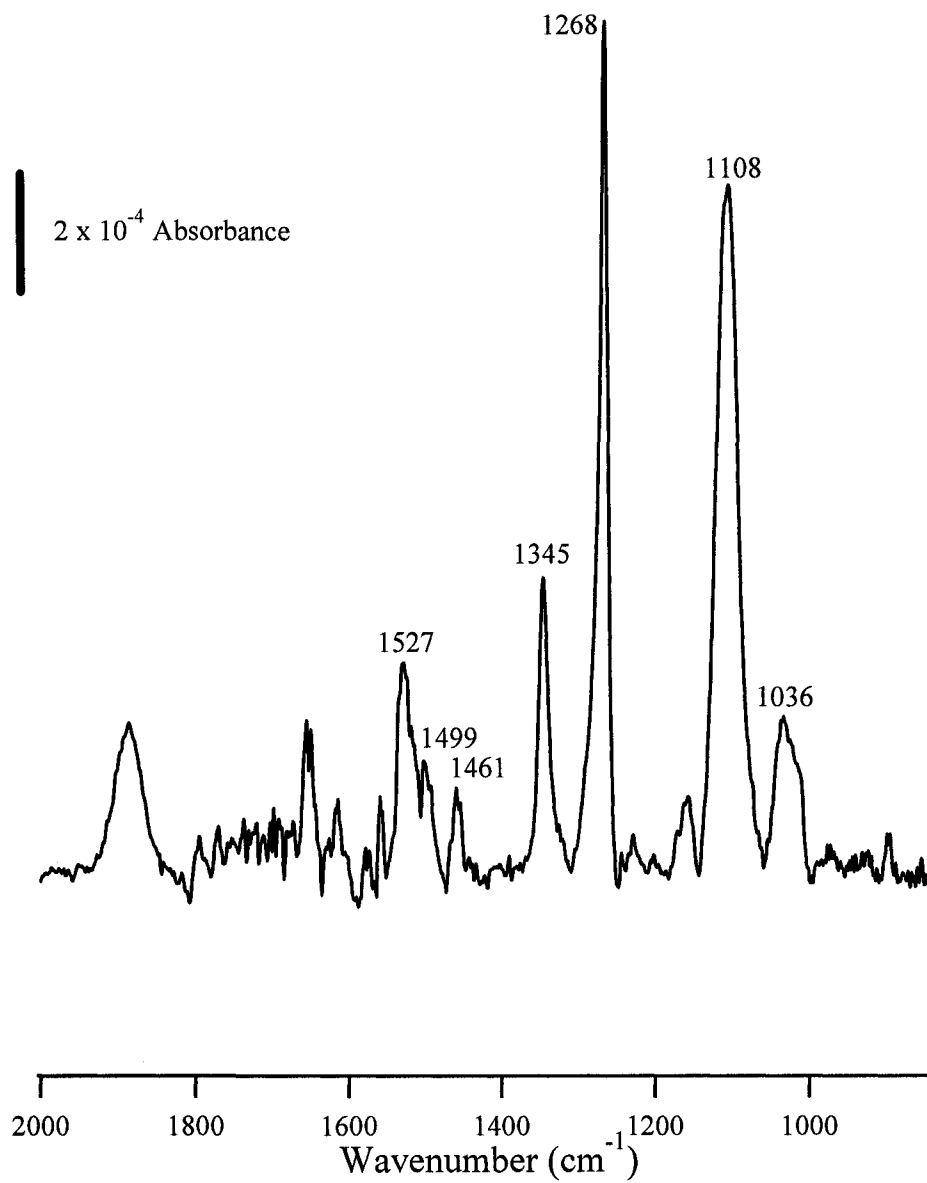


Figure 4.09. Infrared reflection absorbance spectroscopy spectra of Fast Black K self-assembled on platinum, fingerprint region.

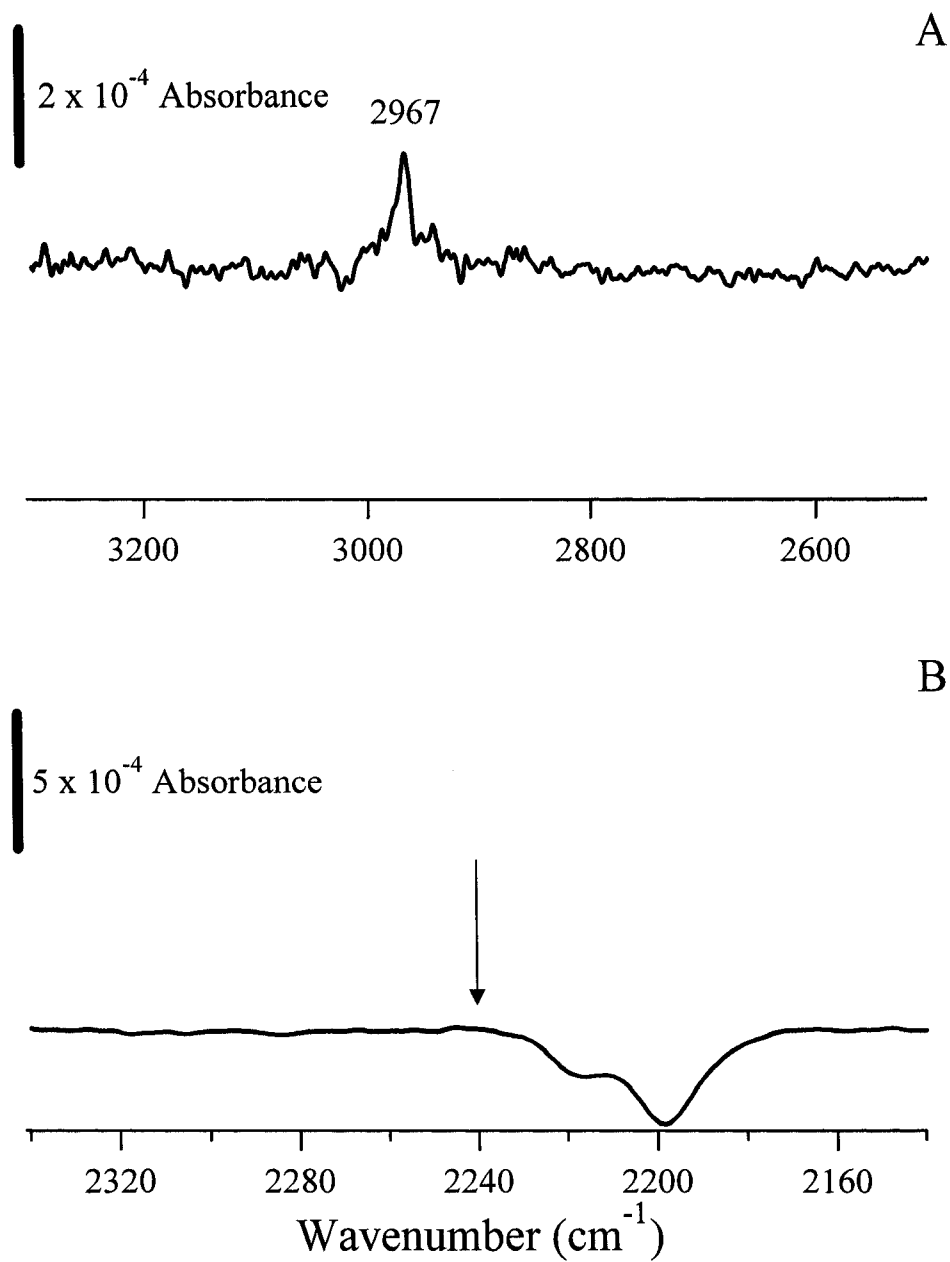


Figure 4.10. Infrared reflection absorbance spectroscopy spectra of Fast Black K self-assembled on platinum. A) aliphatic region B) diazonium region with location of expected peak at 2241 cm^{-1} marked.

aliphatic region. The methyl asymmetric stretch peak is clearly visible in the IRRAS spectra for spontaneously attached FBK. The less intense of the two modes, the symmetric stretch at 2880 cm^{-1} , is not distinguishable from the baseline noise of the spectra and thus omitted. The presence of the asymmetric methyl stretch as well as other peaks in the fingerprint region of the FBK spectrum, (figure 4.09) indicates the spontaneous attachment of FBK to platinum in some manner. Figure 4.10A shows the presence of aliphatic methylene at 2967 and figure 4.10B lacks the expected diazonium peak, similar to figure 4.06B. When the self-assembled FBK IR spectrum, figure 4.09, is compared to the IR of the electrochemically attached FBK, most of the same peaks are clearly identified, but in vastly different ratios. This indicates a much different film morphology between the electrochemically prepared film and the self-assembled films.

Peak position (cm^{-1})	Group	Peak Height (absorbance)
1-Dodecanethiol		
2854	R-CH ₂ ν_s	2.63×10^{-4}
2880	R-CH ₃ ν_s	1.25×10^{-4}
2924	R-CH ₂ ν_a	4.77×10^{-4}
2966	R-CH ₃ ν_a	3.60×10^{-4}
Fast Black K		
2967	R-CH ₃ ν_a	1.86×10^{-4}

Table 4.03. Infrared Reflection Absorbance Spectroscopy peak assignments for spontaneously attached Fast Black K and 1-dodecanethiol

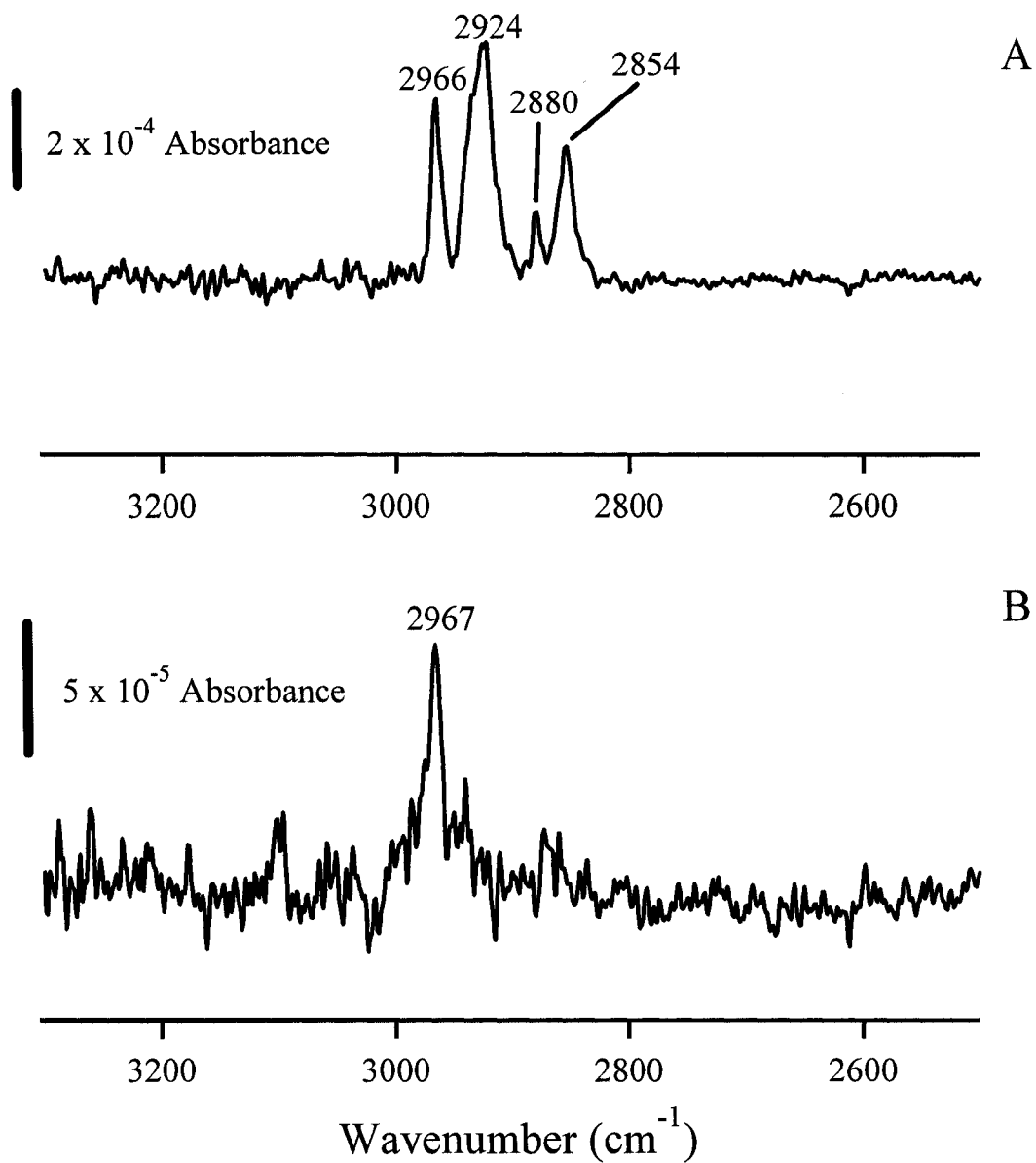


Figure 4.11. Infrared reflection absorbance spectroscopy spectra of A) 1-dodecanethiol and B) Fast Black K self-assembled on platinum.

Peak position (cm^{-1})	Group	Peak Height (absorbance)
1-Dodecanethiol displaced by Fast Black K		
2858	R-CH ₂ ν_s	1.92×10^{-4}
2882	R-CH ₃ ν_s	5.8×10^{-5}
2926	R-CH ₂ ν_a	3.97×10^{-4}
2962	R-CH ₃ ν_a	1.97×10^{-4}
Fast Black K displaced by 1-Dodecanethiol		
2850	R-CH ₂ ν_s	3.22×10^{-4}
2878	R-CH ₃ ν_s	2.36×10^{-4}
2926	R-CH ₂ ν_a	4.32×10^{-4}
2967	R-CH ₃ ν_a	5.17×10^{-4}

Table 4.04. Infrared Reflection Absorbance Spectroscopy peak assignments for spontaneously attached Fast Black K and 1-dodecanethiol displaced

Although thiol derived self assembled monolayers are known to quickly form tightly packed, regular films, the interactions with the underlying metal is relatively weak compared to a typical σ bond, 167 kJ mol^{-1} for the well-studied gold-thiol and 347 kJ mol^{-1} for a carbon-carbon σ bond.⁶⁰ To probe the relative strength of the interaction between sorbed FBK and the platinum, the FBK and 1-dodecanethiol samples discussed above were placed into a displacing solution. The displacement solution for each was sample was the other molecule of interest, that is, the displacement solution for FBK was the thiol, and the displacement solution for the thiol was FBK. The samples were allowed to react in the displacement solution overnight and the resulting films were analyzed via IRRAS, the assumption being that the more thermodynamically favoured film would remain. The IRRAS spectra for the displaced samples are presented in figures 4.12A and B. The initial difference immediately noticeable between the pre- and post-displacement spectra is the large peak intensities of the methylene symmetric and asymmetric peaks for the FBK sample that was displaced by 1-dodecanethiol, figure 4.12B. This indicates the film consists of primarily 1-dodecanethiol, with very little FBK. The spectra of 1-dodecanethiol displaced with FBK shows a dramatic intra-peak ratio shift with a larger signal for the methylene group and an overall decrease in total signal intensity. If FBK were to displace the surface bound 1-dodecane thiol one would expect the peaks associated with the methyl groups to increase relative to the methylene. One possible explanation for the observed increase in the ratio of methylene to methyl peaks is the cleaving or reaction with the terminal methyl group of 1-dodecanethiol. Another possibility is the reorientation of the 1-dodecanethiol monolayer due to the

loss of 1-dodecanethiol. The labile nature of alkane thiols and the observed decrease in overall signal makes the later explanation more likely. Although the equilibrium condition of 1-dodecanethiol is heavily skewed towards being surface bound when the 1-dodecanethiol sample was placed in a solution of FBK containing no 1-dodecanethiol in solution, it repartitioned to equilibrium conditions. It is believed the loss of surface bound 1-dodecanethiol caused the monolayer to undergo new packing with an altered tilt angle. Due to the surface selection rule of IRRAS, with respect to alkane thiols, on metals the dipoles perpendicular to the surface are greatly enhanced.⁵⁹ The peak position shift of the methylene symmetric stretch from 2854 cm^{-1} to 2858 cm^{-1} supports the rearrangement and altered packing of the monolayer to a less crystalline, more liquid like structure. Overall, the interaction of 1-dodecanethiol appears to be favoured over the interaction of FBK with platinum, leading to the conclusion that spontaneously sorbed FBK to platinum is a relatively weak interaction.

As discussed above, FBK can spontaneously sorb to the surface of platinum albeit weakly. The initial question was whether aryl diazoniums, such as FBK, can foul a counter electrode in the time frame of a typical diazonium reduction and immobilization experiment. Figure 4.13 shows the IRRAS spectra of platinum counter and working electrodes shown of the same scale. The ratio of the highest peak in each, the 1345 NO_2 ν_s band, is about 41. The ratio of the background deuterated octadecanethiol peak at 2197 cm^{-1} can be used as a pseudo-internal reference. The peak ratio of the background is 0.9, indicating a similar level of sensitivity between the two spectra. Given the semi-quantitative nature of IR it can

be assumed that the working electrode contains approximately 37 times the amount of FBK over the counter electrode. The extremely low amount of FBK left on the counter electrode coupled with the weak interaction observed between the platinum surface and spontaneously sorbed FBK make the risk of counter electrode fouling by FBK a non-issue.

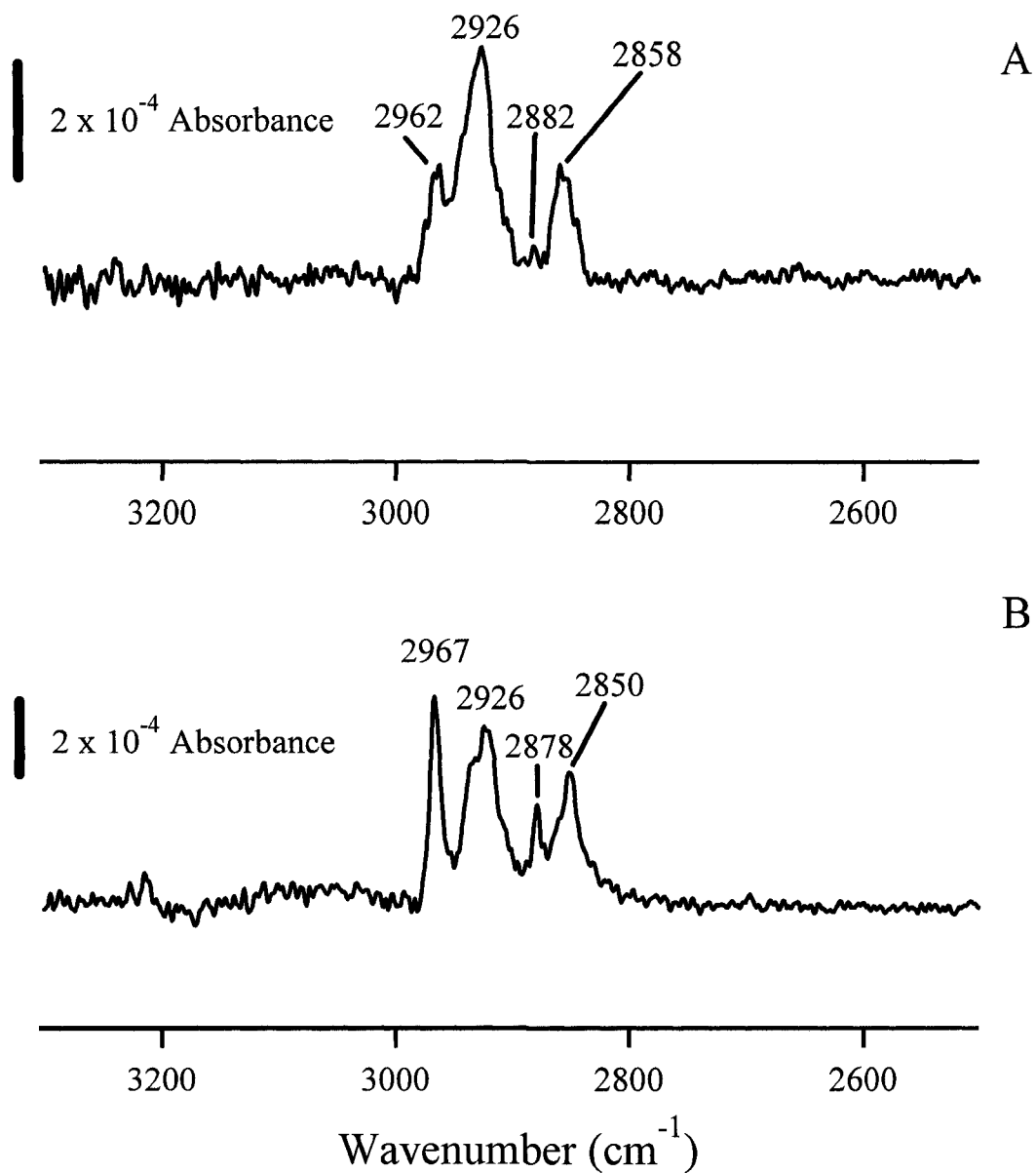


Figure 4.12. Infrared reflection absorbance spectroscopy spectra of A) 1-dodecanethiol displaced by Fast Black K and B) Fast Black K displaced by 1-dodecanethiol.

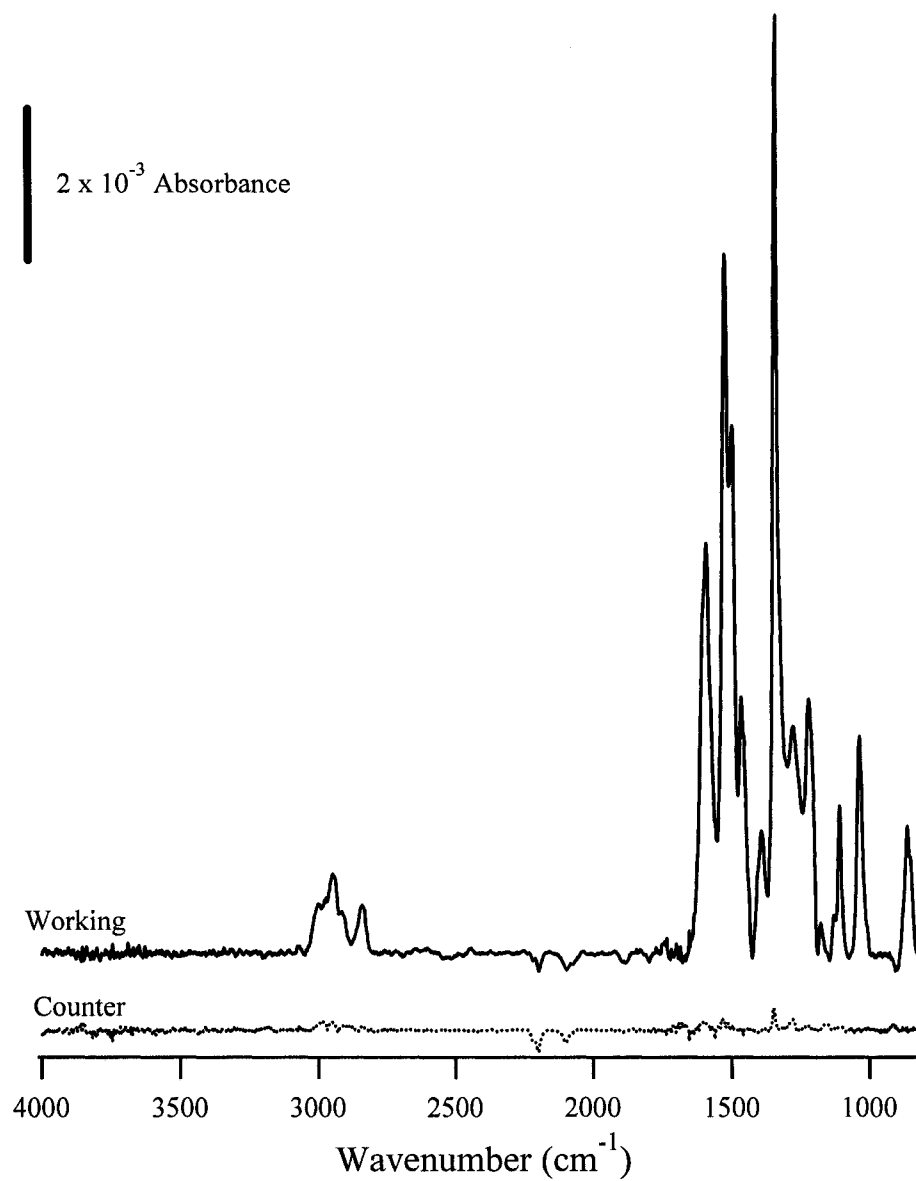


Figure 4.13. Infrared reflection absorbance spectroscopy spectra of Fast Black K on a platinum working electrode (solid) and counter electrode (dotted) after an electrochemical reduction of Fast Black K.

3.4 Electrochemical behaviour of Diazonium Modified Platinum

With the successful electrochemical attachment of diazonium derived layers to platinum electrodes, an electrochemical method to locate pin holes and defects in the newly formed film was desired; analogous to the dopamine electrochemical test for carbon. A simple experiment was devised in which protons were reduced to form molecular hydrogen from a solution of 10 mM H₂SO₄ in 1 M KCl. The electroactivity of platinum towards proton reduction is highly dependent on surface morphology and requires direct contact of the protons with the surface.^{61, 62} The initial hypothesis was that the modification of the platinum surface with a FBK diazonium derived layer would retard access of the protons to the surface and thereby inhibit the observed electrochemistry, analogous to how the electroactivity of dopamine is inhibited on carbon when a molecular layer is formed.

Before comparison to modified films, the behaviour of unmodified platinum electrodes was investigated. The cyclic voltammograms of 10 mM H₂SO₄ on unmodified platinum electrodes are presented in figure 4.14 with ΔE_p values presented in table 4.05. Surfaces were prepared using standard deposition procedures, as discussed previously in this chapter. Once the films were prepared, cyclic voltammograms were performed in the acidic media. Typical cyclic voltammograms at various scan rates, from 0.100 V/s to 0.800 V/s, are presented in figure 4.15 with ΔE_p values presented in table 4.06. To facilitate direct comparison, the cyclic voltammograms at 0.100 V/s for both the modified and unmodified platinum electrodes are presented in figure 4.16.

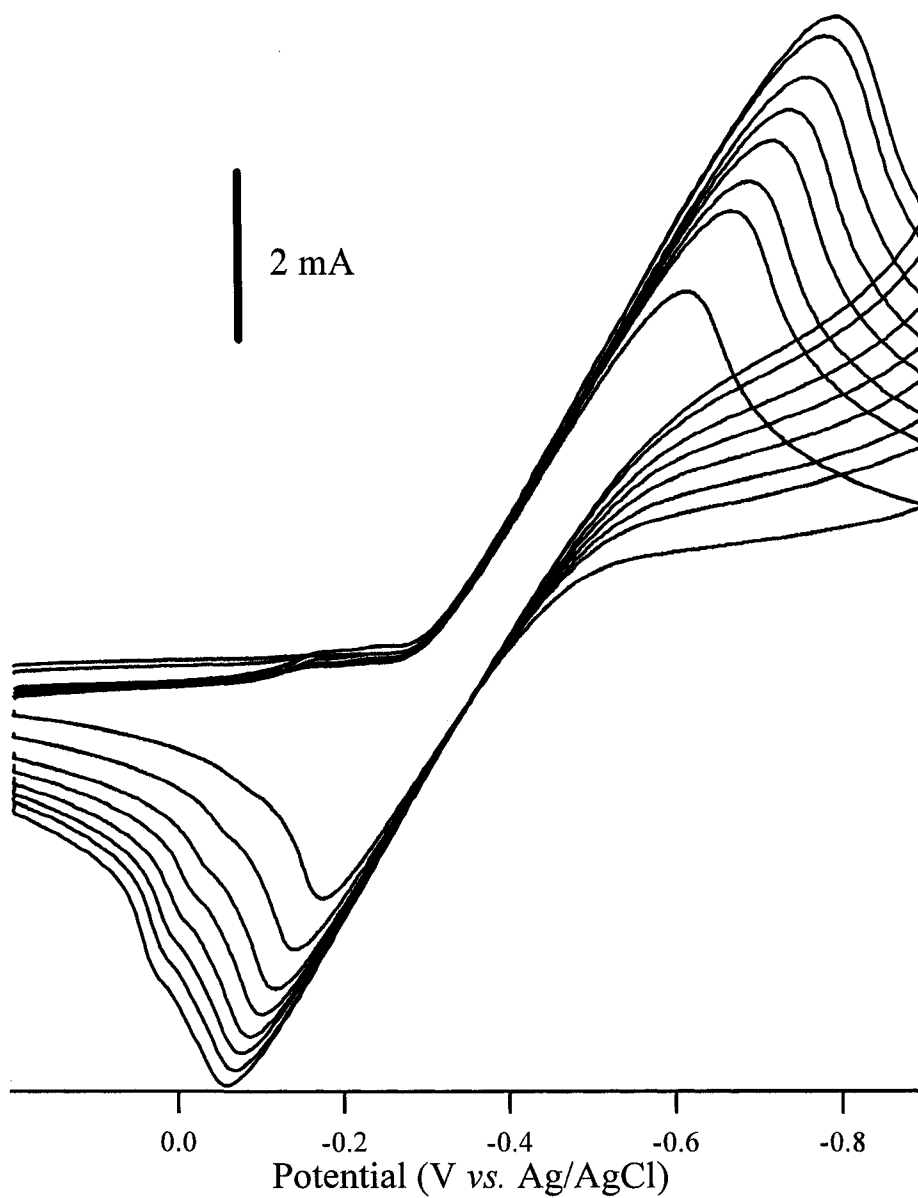


Figure 4.14. Cyclic voltammograms for the evolution of hydrogen on glass-slide platinum electrode (from lowest peak current to highest current) at 0.100, 0.200, 0.300, 0.400, 0.500, 0.600, 0.700, and 0.800 V/s.

Scan Rate (V/s)	ΔE_p (V)
0.100	0.4400
0.200	0.5260
0.300	0.5700
0.400	0.6170
0.500	0.6525
0.600	0.6829
0.700	0.7111
0.800	0.7324

Table 4.05. ΔE_p of hydrogen on platinum in 1 M KCl

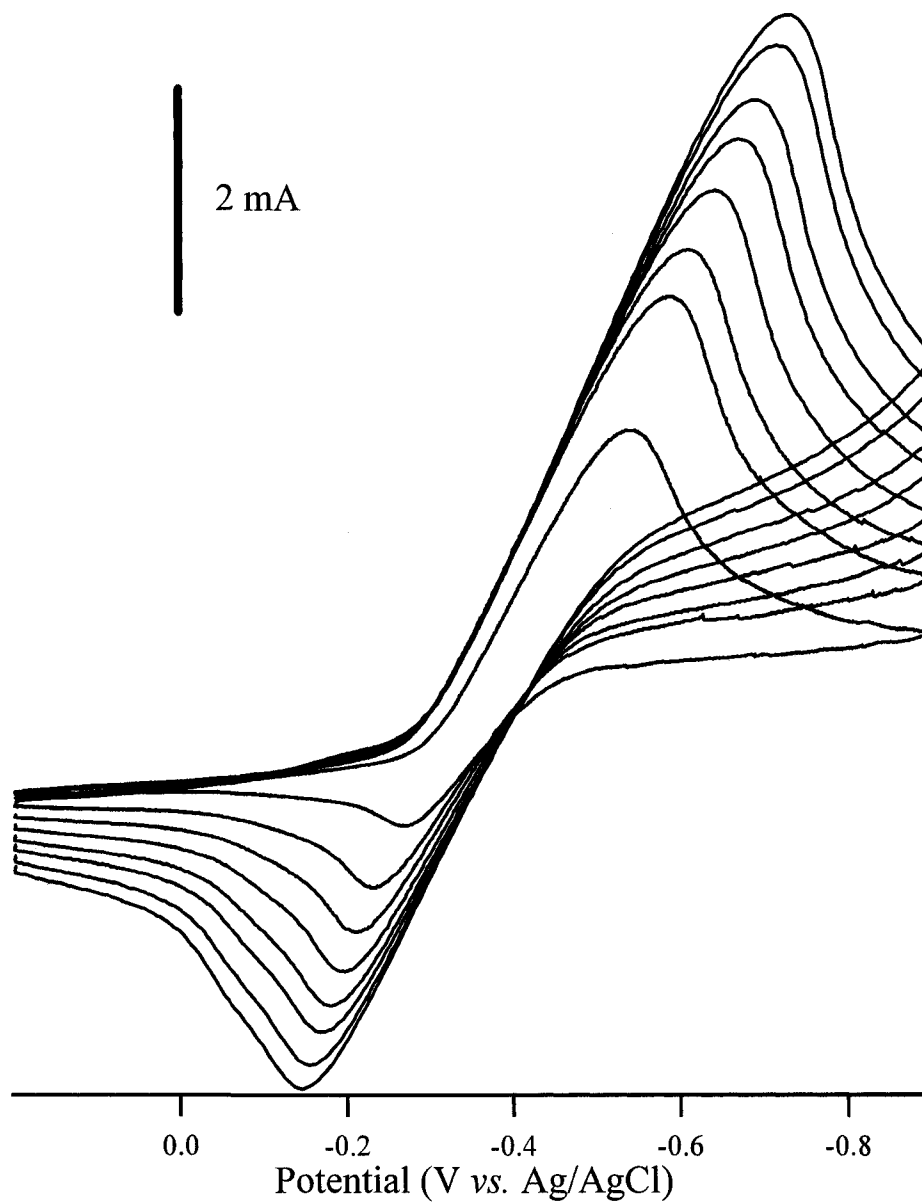


Figure 4.15. Cyclic voltammograms for the evolution of hydrogen on FBK modified glass-slide platinum electrode (from lowest peak current to highest current) at 0.100, 0.200, 0.300, 0.400, 0.500, 0.600, 0.700, and 0.800 V/s.

Scan Rate (V/s)	ΔE_p (V)
0.100	0.273
0.200	0.356
0.300	0.398
0.400	0.444
0.500	0.491
0.600	0.520
0.700	0.560
0.800	0.589

Table 4.06. ΔE_p of hydrogen on FBK modified platinum in 1 M KCl

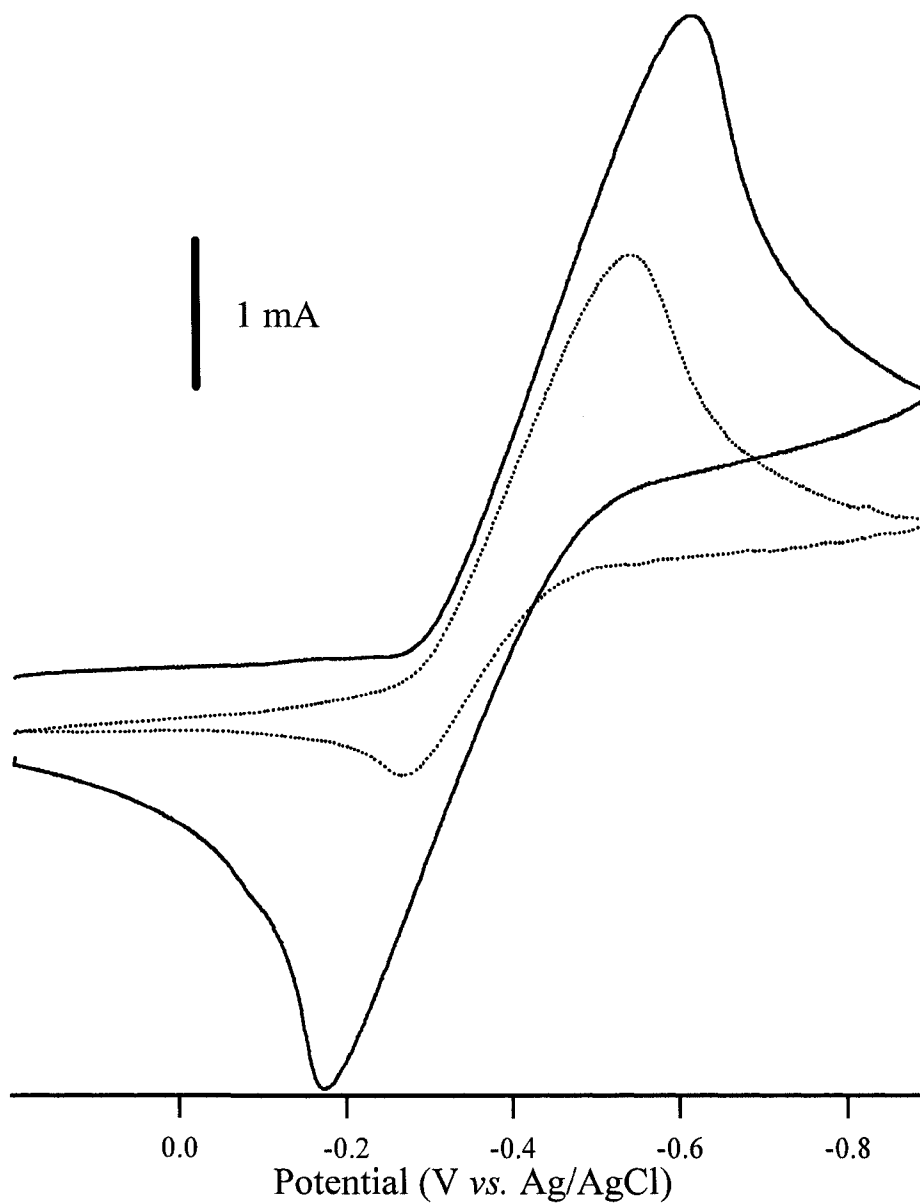


Figure 4.16. Cyclic voltammograms for the evolution of hydrogen on FBK modified glass-slide platinum electrode (dotted line) and bare glass-slide platinum electrode (solid line) at 0.100 V/s.

Immediately apparent are two distinct points: the peak current for a particular scan rate is considerably less on the modified electrode, and the ΔE_p values of the modified electrodes are also appreciably less. The anodic and cathodic peaks for the modified film are also highly asymmetric, unlike for bare platinum. Although initial investigations in the proton reduction failed to yield a test that probed surface coverage as initially hypothesized, the results were interesting enough to warrant further investigation into the electrochemical behaviour of diazonium derived films on platinum.

As discussed in section 3.1 of this chapter and presented in figure 4.03, $\text{Fe}(\text{CN})_6^{3-/4-}$ is a well behaved redox system on platinum electrodes. The electrochemical behaviour of $\text{Fe}(\text{CN})_6^{3-/4-}$ was examined on a FBK diazonium modified platinum electrode. Freshly formed platinum/FBK films were used as the working electrode and the resulting voltammograms are presented in figure 4.18. Additionally, platinum/FBK films that were used for proton reduction were also subjected to $\text{Fe}(\text{CN})_6^{3-/4-}$ cyclic voltammetry; the resulting cyclic voltammograms are presented in figure 4.19. Tabulated ΔE_p values for $\text{Fe}(\text{CN})_6^{3-/4-}$ on bare platinum, FBK modified platinum, and FBK modified platinum film that was used for hydrogen evolution are presented in table 4.07.

The act of modifying the platinum surface with FBK initially severely inhibits the electroactivity of $\text{Fe}(\text{CN})_6^{3-/4-}$, this is demonstrated by the measured ΔE_p values. After performing hydrogen reduction with the modified platinum, the electrochemical response of $\text{Fe}(\text{CN})_6^{3-/4-}$ returns to values similar to bare platinum, once again reflected in the measured ΔE_p values.

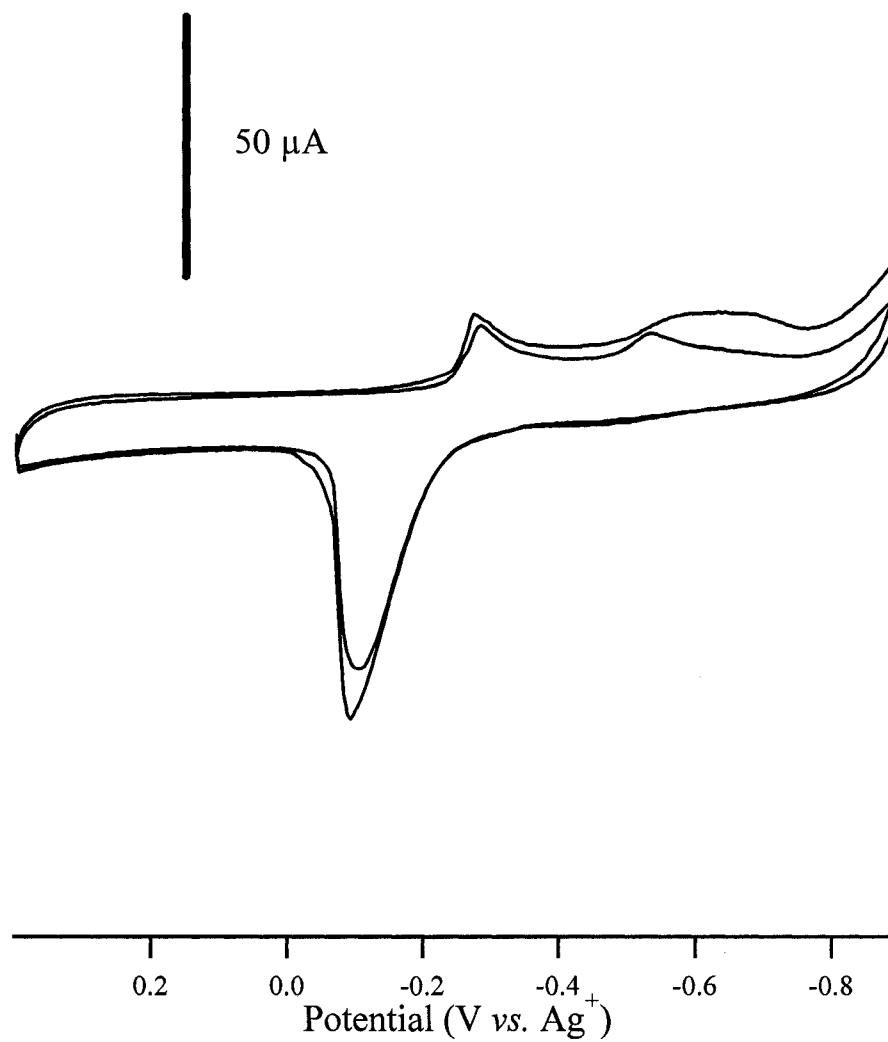


Figure 4.17. Cyclic voltammogram for platinum electrode scanned in blank acetonitrile containing tetrabutylammonium tetrafluoroborate.

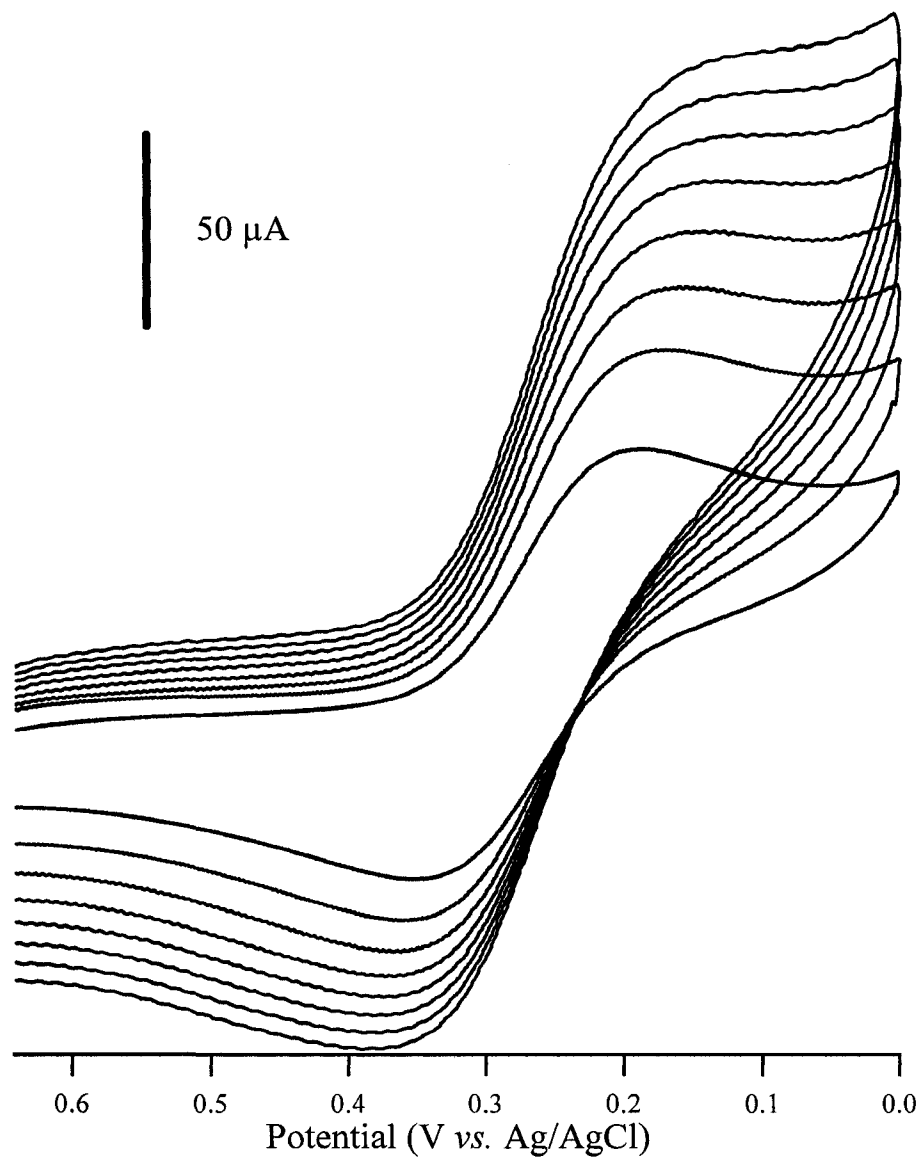


Figure 4.18. Cyclic voltammetry of $\text{Fe(CN)}_6^{3-/4-}$ on FBK modified glass-slide platinum (from lowest peak current to highest current) at 0.100, 0.200, 0.300, 0.400, 0.500, 0.600, 0.700, and 0.800 V/s.

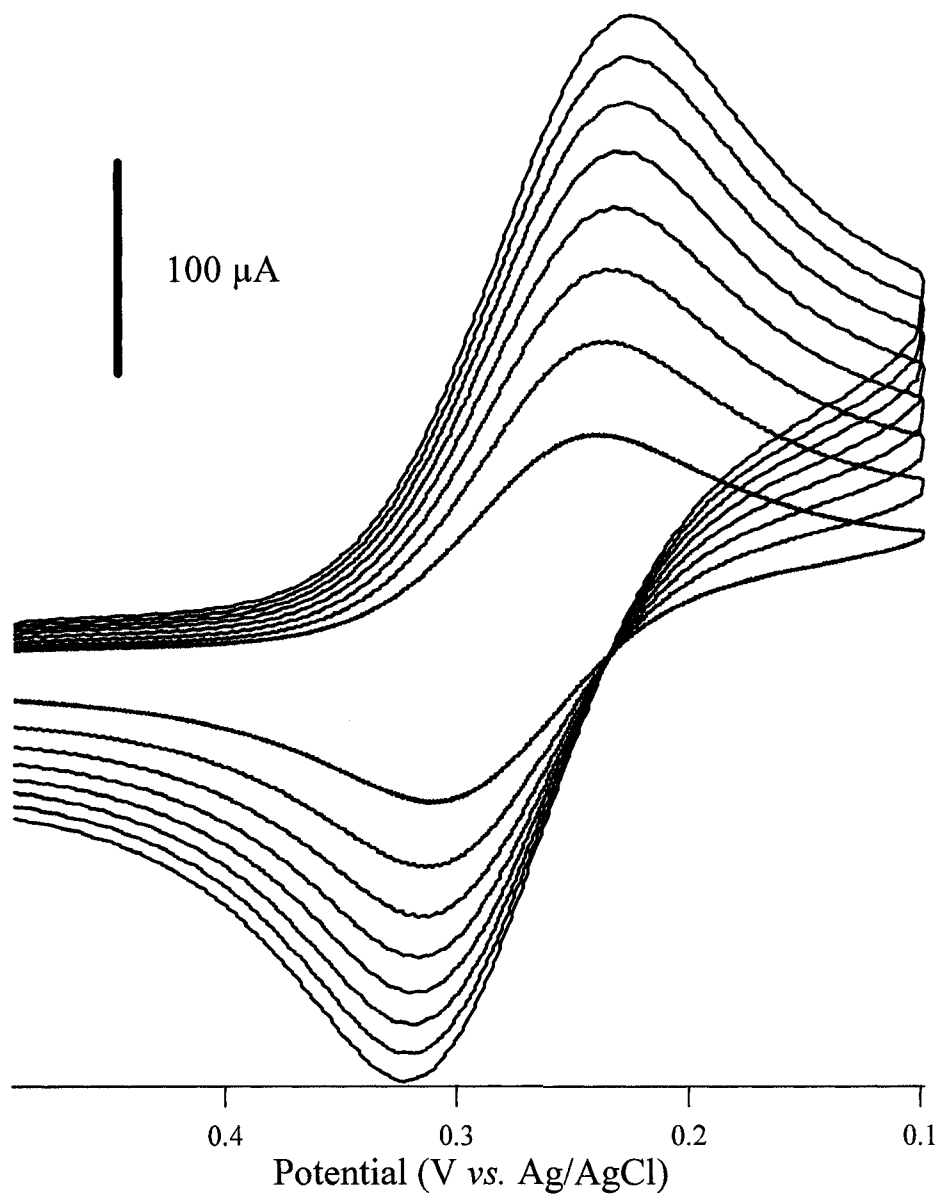


Figure 4.19. Cyclic voltammetry of $\text{Fe(CN)}_6^{3-/4-}$ on FBK modified glass-slide platinum after hydrogen evolution (from lowest peak current to highest current) at 0.100, 0.200, 0.300, 0.400, 0.500, 0.600, 0.700, and 0.800 V/s.

Scan Rate (mV/s)	ΔE_p (V)		
	Platinum	FBK modified platinum	After hydrogen evolution
0.100	0.072	0.163	0.071
0.200	0.077	0.190	0.078
0.300	0.080	0.212	0.082
0.400	0.083	0.230	0.085
0.500	0.088	Immeasurable	0.090
0.600	0.091	Immeasurable	0.094
0.700	0.091	Immeasurable	0.097
0.800	0.095	Immeasurable	0.098

Table 4.07. ΔE_p of $\text{Fe}(\text{CN})_6^{3-/4-}$ on various platinum based electrodes.

To ensure the observed response was due to the attached film and not due to the changes to the platinum during the attachment scheme, a control experiment was performed. A bare platinum electrode was scanned in blank acetonitrile containing tetrabutylammonium tetrafluoroborate. The conditions used were identical to the attachment procedures, except no FBK was included. The bare platinum films scanned in the blank solution showed no difference from the normal bare platinum films. The blank scan is presented in figure 4.17.

The observed changes in the FBK modified platinum coupled to the non-response of the control experiment suggested that behaviour is entirely due to the attached film. To further investigate the attached film and the changes observed in said film after proton reduction, IRRAS was used to investigate the films. Figure 4.20 shows the IRRAS spectra of freshly prepared FBK film (dotted trace) and FBK film after hydrogen evolution (solid trace). The peak identifications, signal intensity, and percent signal change of the two films are presented in table 4.08. It is immediately apparent that the two spectra are nearly identical. All significant peaks are located in both spectra with the only difference being in the intensity. The overall intensity change across all identified peaks is -7.6% with a large standard deviation of 21.7. With such a small percent change and a large standard deviation, one cannot statistically claim a net loss of material from the surface.

Modification of a platinum surface with FBK produces interesting kinetic results for the reduction of protons to form molecular hydrogen. The reaction appears to happen at a faster rate, but the overall flux is reduced. Furthermore, the act of

Peak Position (cm ⁻¹)	Group	Peak Height Before H ₂ evolution	Peak Height After H ₂ evolution	% change
1037	C-O-C ν_s	0.0017636	0.0011209	-36
1112	Ph-C-H in-plane bend	0.001806	0.0030796	+41
1223	C-O-C ν_a	0.0032681	0.0036865	+11
1271	Ph-C-H in-plane bend	0.0025503	0.0021372	-16
1345	NO ₂ ν_s	0.0070062	0.0053121	-24
1392	R-CH ₃ symmetric deformation	0.0018061	0.0017851	-1
1467	R-CH ₃ asymmetric deformation	0.0022566	0.0021014	-7
1499	Aromatic ring stretch	0.0041373	0.0032554	-21
1525	NO ₂ ν_a	0.0049897	0.0040163	-20
1591	Aromatic ring stretch	0.0028657	0.0027691	-3

Table 4.08. FBK peak changes after hydrogen evolution. Average change = -7.6%

SD = 21.7

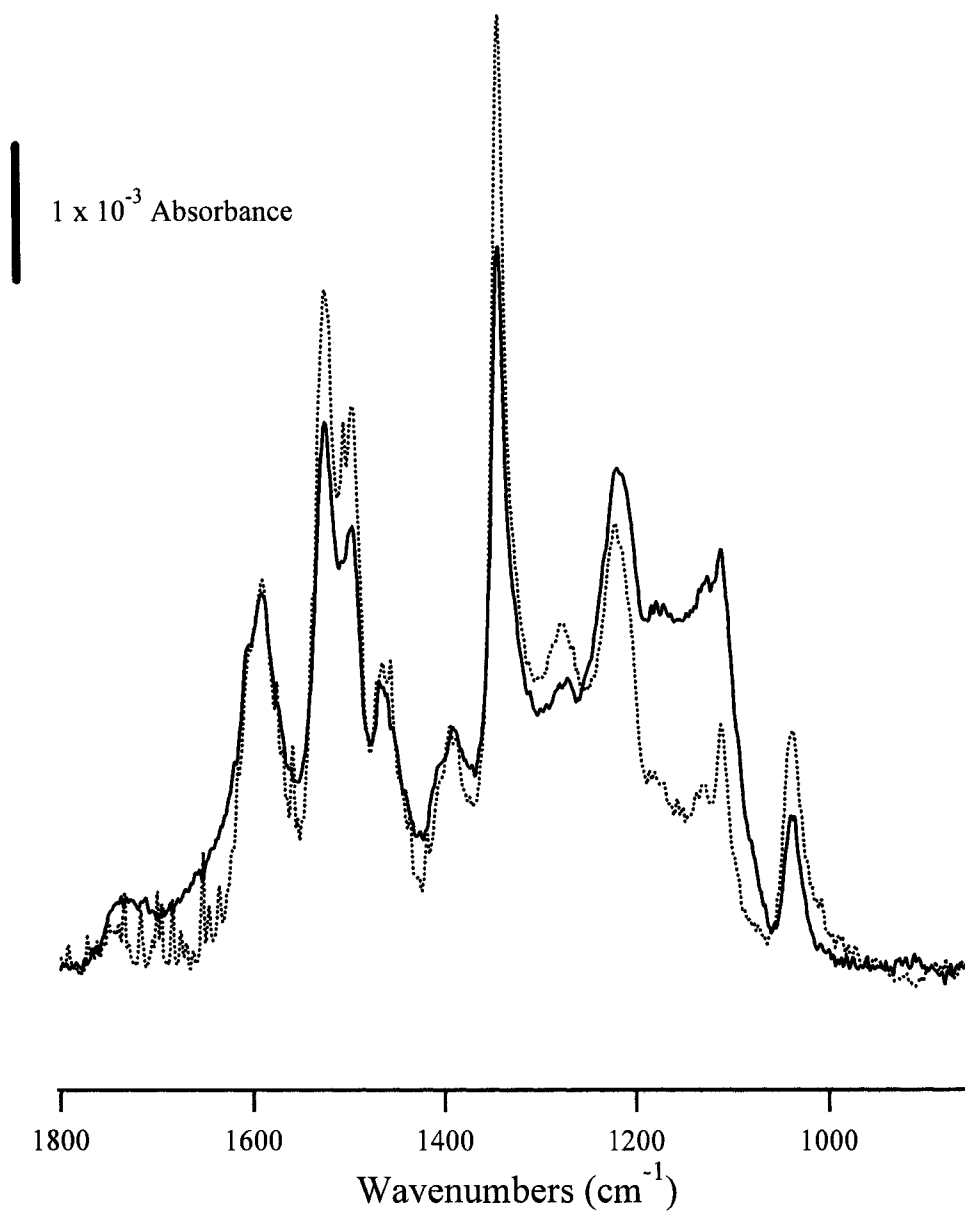


Figure 4.20. Infrared reflection absorbance spectroscopy spectra of Fast Black K on platinum. dotted – after initial attachment to platinum; solid – after the electrode was used for hydrogen evolution from 10 mM $\text{H}_2\text{SO}_4/1 \text{ M KCl}$

hydrogen evolution significantly alters the electrochemical behaviour of the film towards the standard redox probe $\text{Fe}(\text{CN})_6^{3-/4-}$.

4. Conclusions

The electrochemical reduction and subsequent attachment of Fast Black K was successfully achieved. The deliberate modification of platinum with FBK produced a thin, robust film with easily identifiable infrared spectroscopy peaks. The spontaneous sorption of FBK to platinum produces a very weakly bound film that was easily displaced by 1-dodecanethiol. This spontaneous attachment to a platinum counter electrode does not occur to a significant extent during the timeframe of a typical attachment experiment.

References

- (1) Delamar, M.; Hitmi, R.; Pinson, J.; Saveant, J. M. *Journal of the American Chemical Society* **1992**, *114*, 5883-5884.
- (2) Dirk, S. M.; Pylypenko, S.; Howell, S. W.; Fulghum, J. E.; Wheeler, D. R. *Langmuir* **2005**, *21*, 10899-10901.
- (3) Pinson, J.; Podvorica, F. *Chemical Society Reviews* **2005**, *34*, 429-439.
- (4) Chen, B.; Flatt, A. K.; Jian, H. H.; Hudson, J. L.; Tour, J. M. *Chemistry of Materials* **2005**, *17*, 4832-4836.
- (5) Allongue, P.; de Villeneuve, C. H.; Cherouvrier, G.; Cortes, R.; Bernard, M. C. *Journal of Electroanalytical Chemistry* **2003**, *550*, 161-174.
- (6) Yamada, T.; Takano, N.; Yamada, K.; Yoshitomi, S.; Inoue, T.; Osaka, T. *Japanese Journal of Applied Physics Part 1-Regular Papers Short Notes & Review Papers* **2001**, *40*, 4845-4853.
- (7) Allongue, P.; de Villeneuve, C. H.; Pinson, J. *Electrochimica Acta* **2000**, *45*, 3241-3248.
- (8) Allongue, P.; de Villeneuve, C. H.; Pinson, J.; Ozanam, F.; Chazalviel, J. N.; Wallart, X. *Electrochimica Acta* **1998**, *43*, 2791-2798.
- (9) deVilleneuve, C. H.; Pinson, J.; Bernard, M. C.; Allongue, P. *Journal of Physical Chemistry B* **1997**, *101*, 2415-2420.
- (10) Shimura, T.; Aramaki, K. *Corrosion Science* **2006**, *48*, 3784-3801.
- (11) Matrab, T.; Chehimi, M. M.; Perruchot, C.; Adenier, A.; Guillez, A.; Save, M.; Charleux, B.; Cabet-Deliry, E.; Pinson, J. *Langmuir* **2005**, *21*, 4686-4694.

- (12) Boukerma, K.; Chehimi, M. M.; Pinson, J.; Blomfield, C. *Langmuir* **2003**, *19*, 6333-6335.
- (13) Chausse, A.; Chehimi, M. M.; Karsi, N.; Pinson, J.; Podvorica, F.; Vautrin-UI, C. *Chemistry of Materials* **2002**, *14*, 392-400.
- (14) Adenier, A.; Cabet-Deliry, E.; Lalot, T.; Pinson, J.; Podvorica, F. *Chemistry of Materials* **2002**, *14*, 4576-4585.
- (15) Adenier, A.; Bernard, M. C.; Chehimi, M. M.; Cabet-Deliry, E.; Desbat, B.; Fagebaume, O.; Pinson, J.; Podvorica, F. *Journal of the American Chemical Society* **2001**, *123*, 4541-4549.
- (16) Jian, W.; Firestone, M. A.; Auciello, O.; Carlisle, J. A. *Langmuir* **2004**, *20*, 11450-11456.
- (17) Bernard, M. C.; Chausse, A.; Cabet-Deliry, E.; Chehimi, M. M.; Pinson, J.; Podvorica, F.; Vautrin-UI, C. *Chemistry of Materials* **2003**, *15*, 3450-3462.
- (18) Yu, X. W.; Ye, S. Y. *Journal of Power Sources* **2007**, *172*, 133-144.
- (19) Xu, Z. Q.; Qi, Z. G.; Kaufman, A. *Electrochemical and Solid State Letters* **2003**, *6*, A171-A173.
- (20) Xu, Z. Q.; Qi, Z. G.; Kaufman, A. *Electrochemical and Solid State Letters* **2005**, *8*, A492-A494.
- (21) Xu, Z. Q.; Qi, Z. G.; Kaufman, A. *Electrochemical and Solid State Letters* **2005**, *8*, A313-A315.
- (22) Cheng, X.; Shi, Z.; Glass, N.; Zhang, L.; Zhang, J. J.; Song, D. T.; Liu, Z. S.; Wang, H. J.; Shen, J. *Journal of Power Sources* **2007**, *165*, 739-756.
- (23) Vishnyakov, V. M. *Vacuum* **2006**, *80*, 1053-1065.

- (24) Baschuk, J. J.; Li, X. G. *International Journal of Energy Research* **2001**, *25*, 695-713.
- (25) Antolini, E. *Materials Chemistry and Physics* **2003**, *78*, 563-573.
- (26) Wee, J. H.; Lee, K. Y. *Journal of Power Sources* **2006**, *157*, 128-135.
- (27) Brandon, N. P.; Skinner, S.; Steele, B. C. H. *Annual Review of Materials Research* **2003**, *33*, 183-213.
- (28) Yano, H.; Ono, C.; Shiroishi, H.; Okada, T. *Chemical Communications* **2005**, 1212-1214.
- (29) Tsuchida, E.; Yamamoto, K.; Oyaizu, K.; Iwasaki, N.; Anson, F. C. *Inorganic Chemistry* **1994**, *33*, 1056-1063.
- (30) Okada, T.; Suzuki, Y.; Hirose, T.; Toda, T.; Ozawa, T. *Chemical Communications* **2001**, 2492-2493.
- (31) Adenier, A.; Barre, N.; Cabet-Deliry, E.; Chausse, A.; Griveau, S.; Mercier, F.; Pinson, J.; Vautrin-UI, C. *Surface Science* **2006**, *600*, 4801-4812.
- (32) Adenier, A.; Cabet-Deliry, E.; Chausse, A.; Griveau, S.; Mercier, F.; Pinson, J.; Vautrin-UI, C. *Chemistry of Materials* **2005**, *17*, 491-501.
- (33) Hurley, B. L.; McCreery, R. L. *Journal of the Electrochemical Society* **2004**, *151*, B252-B259.
- (34) Stewart, M. P.; Maya, F.; Kosynkin, D. V.; Dirk, S. M.; Stapleton, J. J.; McGuinness, C. L.; Allara, D. L.; Tour, J. M. *Journal of the American Chemical Society* **2004**, *126*, 370-378.

- (35) Stewart, M. P.; Tour, J. M.; Kosynkin, D. V.; Allara, D. L.; Dirk, S. M.; Maya, F. M. *Abstracts of Papers of the American Chemical Society* **2003**, 225, U7-U7.
- (36) Winkler, K. *Journal of Electroanalytical Chemistry* **1995**, 388, 151-159.
- (37) Peter, L. M.; Durr, W.; Bindra, P.; Gerischer, H. *Journal of Electroanalytical Chemistry* **1976**, 71, 31-50.
- (38) Bieman, D. J.; Fawcett, W. R. *Journal of Electroanalytical Chemistry* **1972**, 34, 27-39.
- (39) Kuta, J.; Yeager, E. *Journal of Electroanalytical Chemistry* **1975**, 59, 110-112.
- (40) Aliganga, A. K. A.; Duwez, A. S.; Mittler, S. *Organic Electronics* **2006**, 7, 337-350.
- (41) Forster, R. J. *Inorganic Chemistry* **1996**, 35, 3394-3403.
- (42) Frisbie, C. D.; Fritschfaules, I.; Wollman, E. W.; Wrighton, M. S. *Thin Solid Films* **1992**, 210, 341-347.
- (43) Gardner, T. J.; Frisbie, C. D.; Wrighton, M. S. *Journal of the American Chemical Society* **1995**, 117, 6927-6933.
- (44) Gatin, M.; Anderson, M. R. *Vibrational Spectroscopy* **1993**, 5, 255-261.
- (45) Haiss, W.; Nichols, R. J.; van Zalinge, H.; Higgins, S. J.; Bethell, D.; Schiffrin, D. J. *Physical Chemistry Chemical Physics* **2004**, 6, 4330-4337.
- (46) In, I.; Jun, Y. W.; Kim, Y. J.; Kim, S. Y. *Chemical Communications* **2005**, 800-801.

- (47) Kashammer, J.; Wohlfart, P.; Weiss, J.; Winter, C.; Fischer, R.; Mittler-Neher, S. *Optical Materials* **1998**, *9*, 406-410.
- (48) Kohli, P.; Taylor, K. K.; Harris, J. J.; Blanchard, G. J. *Journal of the American Chemical Society* **1998**, *120*, 11962-11968.
- (49) Lee, M. T.; Hsueh, C. C.; Freund, M. S.; Ferguson, G. S. *Langmuir* **2003**, *19*, 5246-5253.
- (50) Lenk, T. J.; Hallmark, V. M.; Rabolt, J. F.; Haussling, L.; Ringsdorf, H. *Macromolecules* **1993**, *26*, 1230-1237.
- (51) Mcdermott, C. A.; Mcdermott, M. T.; Green, J. B.; Porter, M. D. *Journal of Physical Chemistry* **1995**, *99*, 13257-13267.
- (52) Nakashima, N.; Taguchi, T.; Takada, Y.; Fujio, K.; Kunitake, M.; Manabe, O. *Journal of the Chemical Society-Chemical Communications* **1991**, 232-233.
- (53) Scherer, J.; Vogt, M. R.; Magnussen, O. M.; Behm, R. J. *Langmuir* **1997**, *13*, 7045-7051.
- (54) Schlenoff, J. B.; Li, M.; Ly, H. *Journal of the American Chemical Society* **1995**, *117*, 12528-12536.
- (55) Schonherr, H.; Ringsdorf, H. *Langmuir* **1996**, *12*, 3891-3897.
- (56) Sun, F.; Castner, D. G.; Grainger, D. W. *Langmuir* **1993**, *9*, 3200-3207.
- (57) Widrig, C. A.; Chung, C.; Porter, M. D. *Journal of Electroanalytical Chemistry* **1991**, *310*, 335-359.
- (58) Zhang, M. H.; Anderson, M. R. *Langmuir* **1994**, *10*, 2807-2813.
- (59) Porter, M. D.; Bright, T. B.; Allara, D. L.; Chidsey, C. E. D. *Journal of the American Chemical Society* **1987**, *109*, 3559-3568.

- (60) Ulman, A. *Chemical Reviews* **1996**, *96*, 1533-1554.
- (61) Maier, C. U.; Specht, M.; Bilger, G. *International Journal of Hydrogen Energy* **1996**, *21*, 859-864.
- (62) Yazici, B. *Turkish Journal of Chemistry* **1999**, *23*, 301-308.

Chapter V

Conjugation of Anticoagulants to Carbon Surfaces:

Toward Modified Implantable Materials

1. Introduction

A large number of prosthetic devices are constructed from graphitic carbon, specifically low temperature isotropic carbon (LTIC). For example LTIC is routinely used in the construction of artificial heart valves. Although LTIC has a higher degree of biocompatibility when compared to other implant materials, patients who receive LTIC artificial heart valves are required to undergo lifelong anti-coagulation therapy due to thromboembolic complications.¹ Systematic studies of the interactions between LTIC and plasma proteins by Feng and Andrade has shown LTIC tightly binds a variety of blood plasma proteins.²⁻⁶ The initial adsorption of proteins to an implant material modulates the interaction of the implant towards further blood components.

It is believed that modification of implant materials such as artificial heart valves with the bio-molecule heparin will increase bio-compatibility by decreasing the thrombosis caused by the implant. Glassy carbon was used as a substitute for LTIC due to its similarity as well as the low cost and availability.

Heparin, a highly sulfated glycosaminoglycan used medically as an anticoagulant, consists of alternating uronic acid and glucosamine, as illustrated in figure 5.01. In addition to *in vivo* medical injections, bio-materials such as polymeric

catheters are routinely coated with heparin to increase biocompatibility.⁷ Both *in vivo* and *in vitro* applications of heparin reduce thrombosis by activation antithrombin III, which in turn reduces the production of thrombin, a protein directly responsible for thrombosis.^{8,9}

Traditionally, modification of surfaces with heparin involves the use of an avidin or streptavidin pre-modified surface. Biotinylated heparin is then introduced to the avidin modified surface and heparin immobilized via biotin-avidin binding.¹⁰ This method employs well known chemistry but can suffer from unwanted interactions of avidin-biotin with the surrounding matrix. It has been shown that many heparin binding proteins interact nonspecifically with avidin and streptavidin.¹¹ A more recent modification method was developed in which albumin-heparin was immobilized on a surface via amide bond formation between surface bound carboxylic acid functional groups and free amine groups of the albumin.¹⁰ This method was shown to be both more robust and easier to perform when compared to surfaces prepared the traditional way. The heparin also retained its bioactivity when immobilized on the surface via the albumin-heparin bonding.

This chapter discusses the immobilization of heparin on the LTIC substitute, glassy carbon (GC), as well as a gold surface. The bio-activity of the heparin was also briefly probed. Two methods for immobilizing heparin on glassy carbon were developed. Each of these methods involved the direct linking of heparin, via the carboxylic acid group of some glucosamine units, with surface bound amine groups. 1-ethyl-3-(3-dimethylaminopropyl) carbodiimide hydrochloride (EDC) is a common

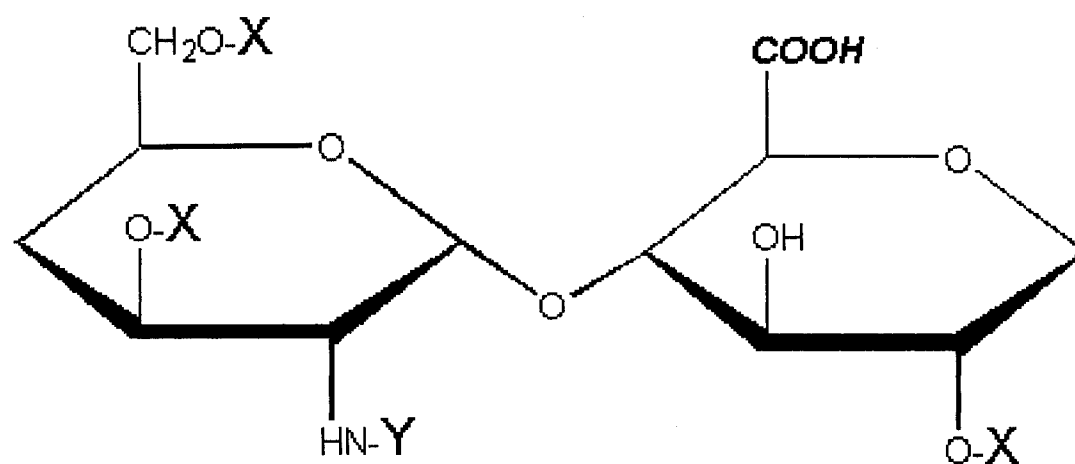


Figure 5.01. Structure of heparin, repeating dimer unit. The bold carboxylic acid is the site of surface immobilization; $\text{X} = \text{SO}_3^-$ or H^+ and $\text{Y} = \text{SO}_3^-$ or COCH_3 .

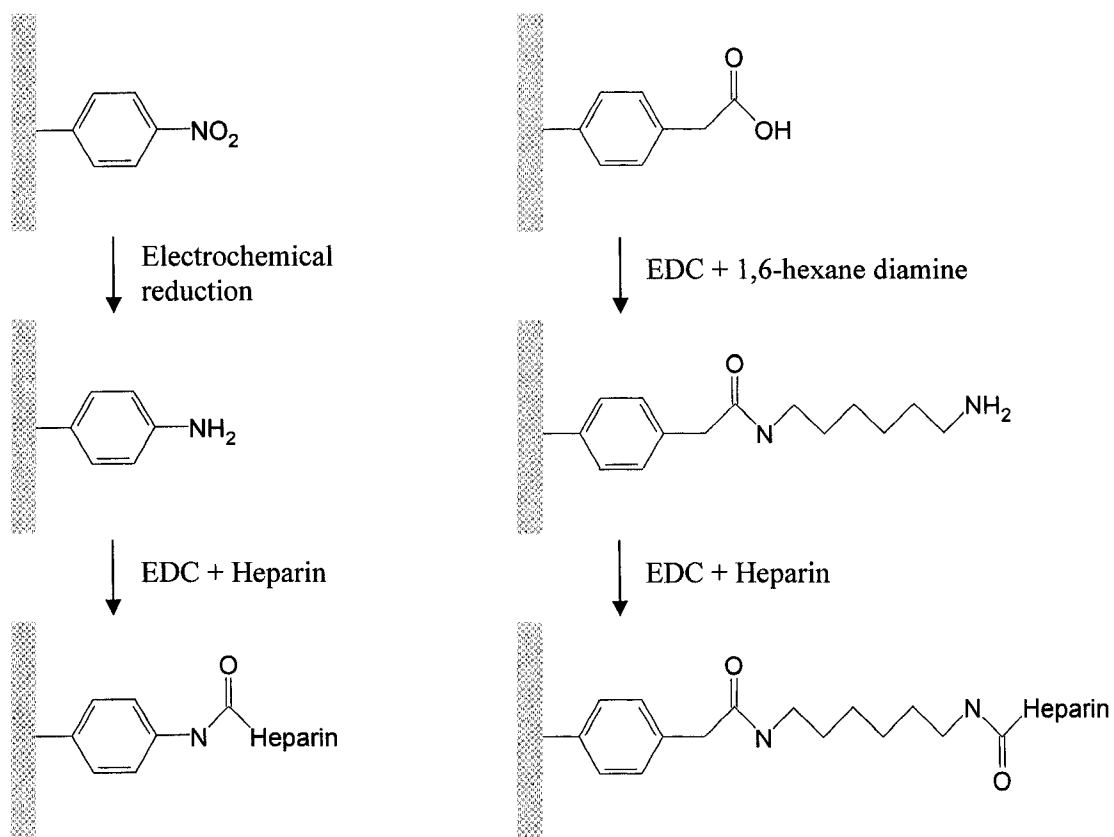


Figure 5.02. Immobilization of heparin on glassy carbon. Left scheme via attachment of p-nitrobenzene and right scheme via attachment of p-phenyl acetic acid.

carboxylic activator and was used to initiate amide bond formation. Glassy carbon surfaces were modified to contain exposed amine groups using diazonium chemistry discussed in detail in previous chapters. Two methods were employed; first p-nitrobenzene diazonium was reduced to form surface bound nitro groups which were subsequently electrochemically reduced to the amine and second, p-acetic acid diazonium was reduced to form a layer containing available carboxylic acid groups. The exposed carboxylic acid groups were coupled with 1,6-hexanediamine to create surface bound amine groups to couple heparin. Heparin was attached to the surface through amide bond formation between the surface bound amine groups and the carboxylic acid of glucosamine. Figure 5.02 outlines the two methods used to modify glassy carbon with heparin. A similar method was developed in parallel to attach heparin to the surface of gold. The same amide bond between heparin and surface amine was used, but 11-amino-1-undecanethiol was used to create the surface bound amine group. The heparin modified gold both served as a reference to compare the heparin modified glassy carbon as well as opening possibilities for heparin modified surface plasmon resonance (SPR) sensors. Heparin modified SPR sensors are not new, however they are prepared via different methods as described previously.¹⁰

2. Experimental

Solutions of p-phenyl acetic acid and p-nitrobenzene diazonium salt were prepared at 5 mM concentration in freshly distilled reagent grade acetonitrile (Caledon Laboratory Chemicals, Georgetown, Ontario) and included 0.1 M

tetrabutylammonium tetrafluoroborate (Sigma-Aldrich Canada Ltd, Oakville, Ontario, Canada) as the supporting electrolyte. All solutions were prepared fresh for each experiment set and deaerated with argon prior to use. Glassy carbon electrodes (Tokai GC-20, Electrosynthesis Corp, New York, USA) were polished successively in 1, 0.3 and 0.05 μm alumina slurries on polishing microcloth (Buehler, Lake Bluff, Illinois, USA) with sonication for 10 minutes in nanopure water after each polishing step. Electrochemical deposition of aryl layers was performed via cyclic voltammetry using a model AFCBP1 bipotentiostat (Pine Research Instrumentation, Raleigh, North Carolina, USA) running PineChem version 2.7.9. A standard three electrode cell consisting of the glassy carbon working electrode, a platinum wire counter electrode and a silver wire reference electrode was used. Electrochemical reduction of the surface bound nitro group of p-nitrobenzene was achieved via reduction in a 0.1 M KCl solution in 90% H_2O and 10% ethanol. The potential was swept from 0 V to -1.2 V vs. Ag/AgCl at 0.100 V/s.

Solutions of 11-amino-1-undecanethiol (Dojindo Laboratories, Kumamoto, Japan) were prepared at about 1 – 10 mM concentration in anhydrous ethanol (Commercial Alcohols Inc, Brampton, Ontario, Canada). Gold coated glass slides (200 nm) with a thin (less than 40 nm) chromium adhesion layer were cleaned via sonication in anhydrous ethanol for ten minutes followed by a rinse with fresh anhydrous ethanol (Commercial Alcohols Inc). Self assembled monolayers of 11-amino-1-undecanethiol on gold were prepared by immersing the cleaned gold slides in the prepared solution and allowing it to self assemble overnight. After twenty-four

hours the slides were removed from solution, rinsed with ethanol and dried with argon.

Amide bond coupling of surface bound phenyl acetic acid and 1,6-hexane diamine was achieved by incubating with aqueous 1-ethyl-3-(3-dimethyl aminopropyl) carbodiimide hydrochloride (EDC) for 24 hours. Heparin immobilization was achieved similarly by incubating the heparin with the p-aniline or 1,6-hexane diamine/p-acetic acid benzene modified surface with aqueous EDC for 72 hours.

All protein solutions were prepared at 50 $\mu\text{g}/\text{mL}$ and contained in phosphate buffered saline (PBS). PBS solutions were prepared from 10 mM phosphate at pH of 7.4 as well as 137 mM NaCl and 2.7 mM KCl. Heparin sodium salt (CAS 9041-08-1) from bovine intestinal mucosa and bovine serum albumin were obtained from Sigma (Sigma-Aldrich Canada Ltd, Oakville, Ontario, Canada) and used as received. Human fibronectin was obtained from MP Biomedicals (formerly ICN Biomedicals, Irvine, California, USA), labeled with flurocein using fluorescein isothiocyanate and purified with size exclusion chromatography via commercially available kits (Molecular Probes, Carlsbad, California, USA).

3. Results and Discussion

3.1 Electrochemical Deposition of Aryl Molecules

The electrochemical deposition of aryl molecules from the diazonium parent ion was first performed on glassy carbon electrodes.¹² Since this initial report, glassy carbon has been the most widely studied material for modification via this method.¹³⁻²² The electrochemical reduction of the aryl diazonium and subsequent formation of the reactive radical was performed via cyclic voltammetry in a solution of the diazonium and tetrabutylammonium tetrafluoroborate in acetonitrile. The attachment of p-phenyl acetic acid was achieved by sweeping the potential from 0 to -1.000 V with respect to the silver wire reference electrode at 0.200 V/s. A typical deposition cyclic voltammogram is shown in figure 5.03. The attachment of p-nitrobenzene to glassy carbon was performed in a manner nearly identical to the initial method described by Saveant¹² and a typical attachment voltammogram is shown in figure 5.04. The electrochemical reduction and subsequent attachment of p-nitrobenzene diazonium was achieved via a cyclic voltametric sweep from 0.400 V to -0.900 V with respect to the silver wire reference electrode. The reduction wave for both attachment schemes has the chemically irreversible peak indicative of diazonium reduction as discussed previously, see chapter 3, section 3.1. The reduction of the surface immobilized nitro group in p-nitrobenzene was reported by Saveant when the initial diazonium reduction and attachment was published.¹² The electrochemical reduction of nitrobenzene to aniline is a well studied reaction; the reaction is an

overall four electron wave and can be made irreversible in a protic solvent.²³ The reduction of the nitro group to an amine group occurs when the applied potential is sufficiently negative, approximately 1.1 V more negative than the reduction of the diazonium functionality. This wide separation in reduction potentials allows for selective reduction. The p-nitrobenzene can be grafted and kept as the nitro, or it can easily be converted to the amine. A typical electrochemical reduction of the phenyl nitro to the phenyl amine is presented in figure 5.05. In this work, the reduction to the amine was performed *ex-situ* in a 0.1 M KCl solution in 90% H₂O and 10% ethanol. The reduction can also be performed *in-situ* with respect to the deposition environment as initially reported.¹²

Immobilized phenyl acetic acid was coupled with a 1,6-hexane diamine linker using a water soluble carbodiimide, 1-ethyl-3-(3-dimethylaminopropyl) carbodiimide (EDC) as an activator. Carbodiimides, such as EDC, are carboxylic activating agents, and in the presence of a primary amine readily form amide bonds.²⁴ Glassy carbon surfaces with grafted p-nitrobenzene and p-phenylacetic acid/1,6-hexane diamine linker provide an available primary amine to attach heparin. The same method for attachment of the diamine linker to p-phenyl acetic acid was used to covalently bond heparin to the surface. Samples were ultra sonicated in nano-pure water to remove impurities including excess 1,6-hexane diamine, and were then incubated in aqueous solutions of EDC and heparin.

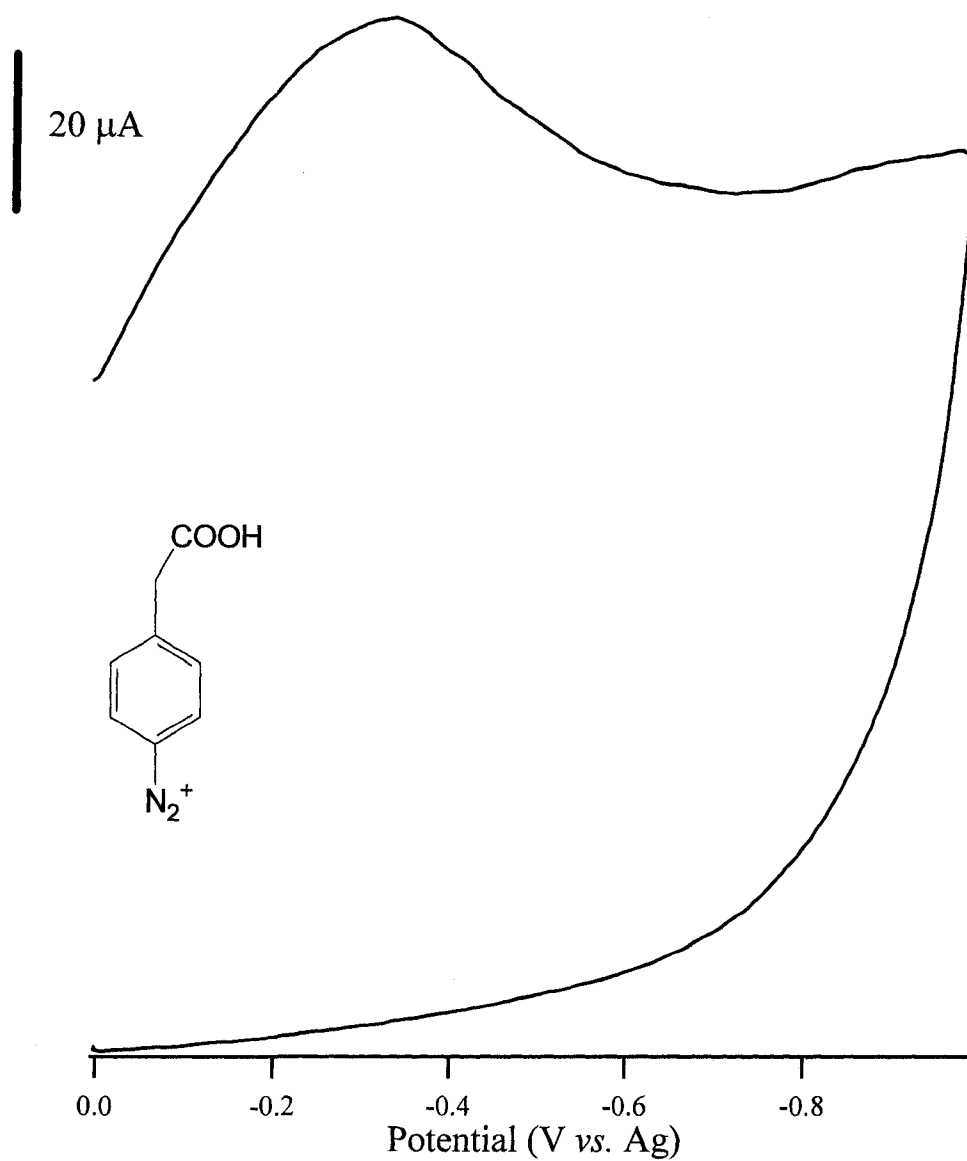


Figure 5.03. Cyclic voltammogram for the electrochemical attachment of p-phenyl acetic acid to glassy carbon from a 5 mM solution at 0.200 V/s.

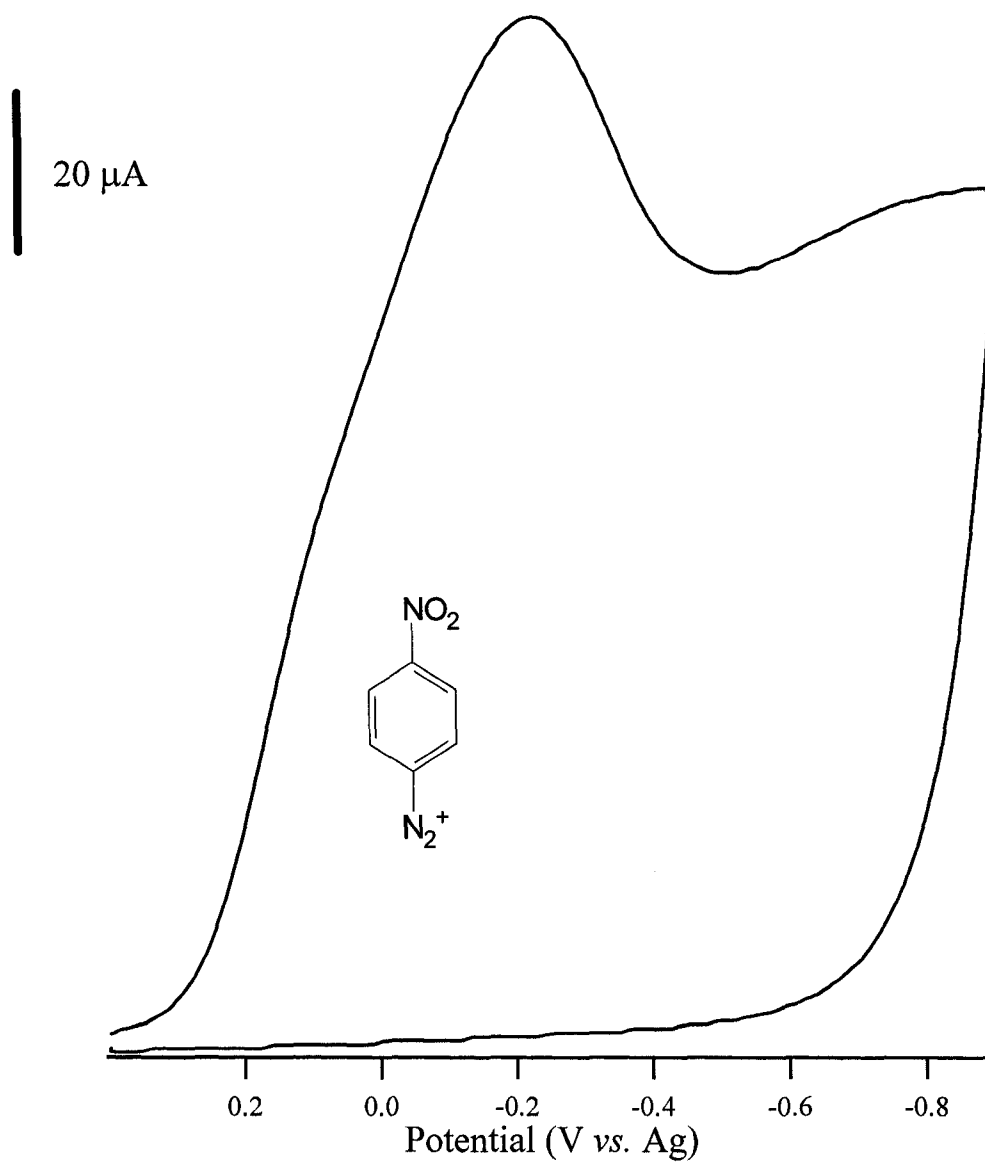


Figure 5.04. Cyclic voltammogram for the electrochemical attachment of p-nitrobenzene to glassy carbon from a 5 mM solution at 0.200 V/s.

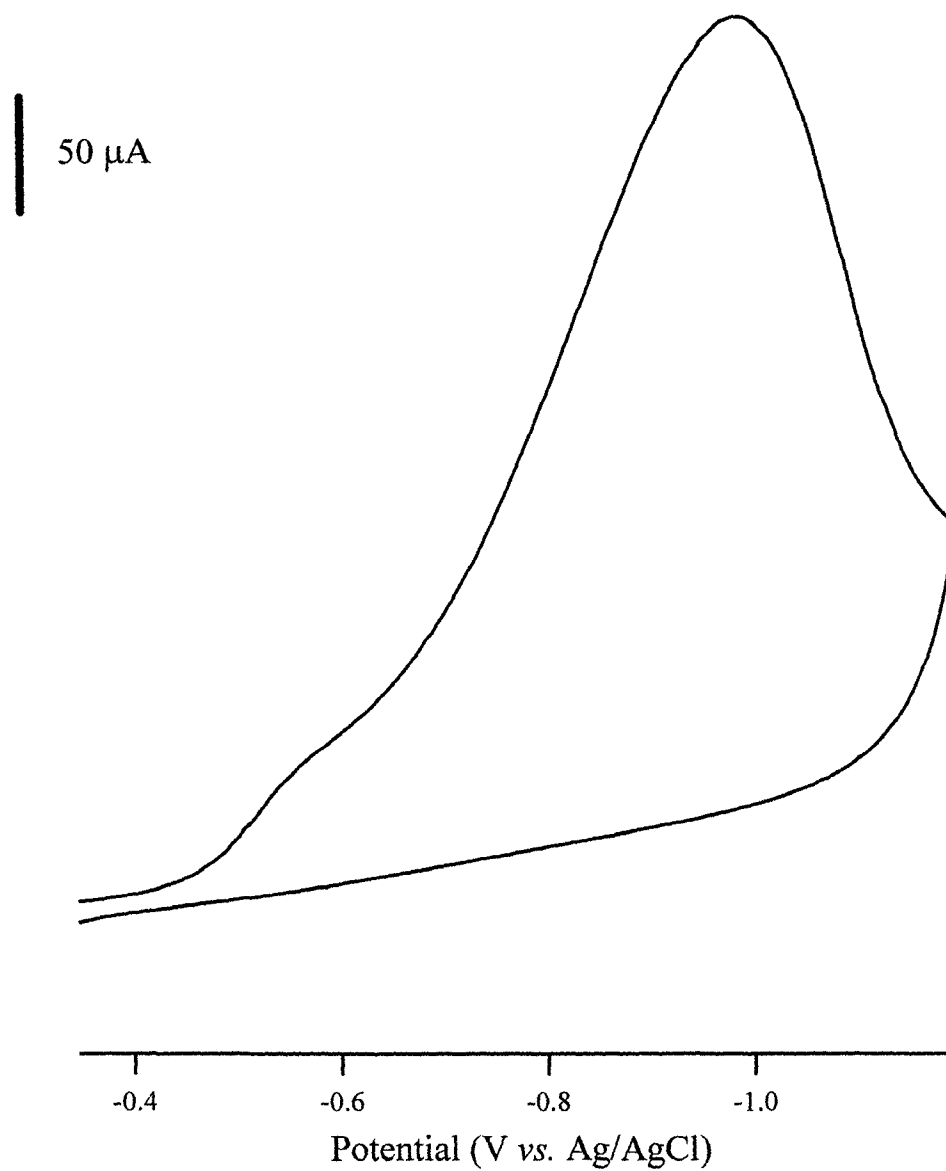


Figure 5.05. Electrochemical reduction of surface nitro group to amine in 0.1 M KCl solution in 90% H₂O and 10% ethanol, 0.100 V/s.

Infrared reflection absorption spectroscopy was used to determine successful surface immobilization. Due to the inherent poor reflection IR signal from carbon, a parallel experiment was performed on gold using the amine on monolayers of 11-amino-1-undecanethiol as the anchor point for heparin. The powder IR spectrum for heparin is shown in figure 5.06. The IRRAS spectra of immobilized heparin are shown in figures 5.07, on gold, and figure 5.08 on carbon. The peak assignments for the various spectra are presented in tables 5.01 to 5.03. Although the three spectra appear quite different upon initial inspection, two issues must be considered. First, the powdered IR spectrum is stock heparin and exists primarily as the sodium salt, and second, the IRRAS surface selection rule applies to the gold supported sample, but not the carbon supported sample.²⁵ As a result, expected bands appear with vastly different intensities and in some cases shifted positions. Despite this hindrance, the expected bands are present and identified in tables 5.01 to 5.03.

Peak Position (cm^{-1})	Function group
3427	OH ν
2939	CH ₂ /CH ₃ ν
2362	CO ₂
2342	CO ₂
1416	C-OH acid deformation
1350	C-N ν
1034	6-ring ether ν_a
939	C-OH acid deformation
816	6-ring ether ν_s

Table 5.01. Infrared peak assignments for powdered heparin.

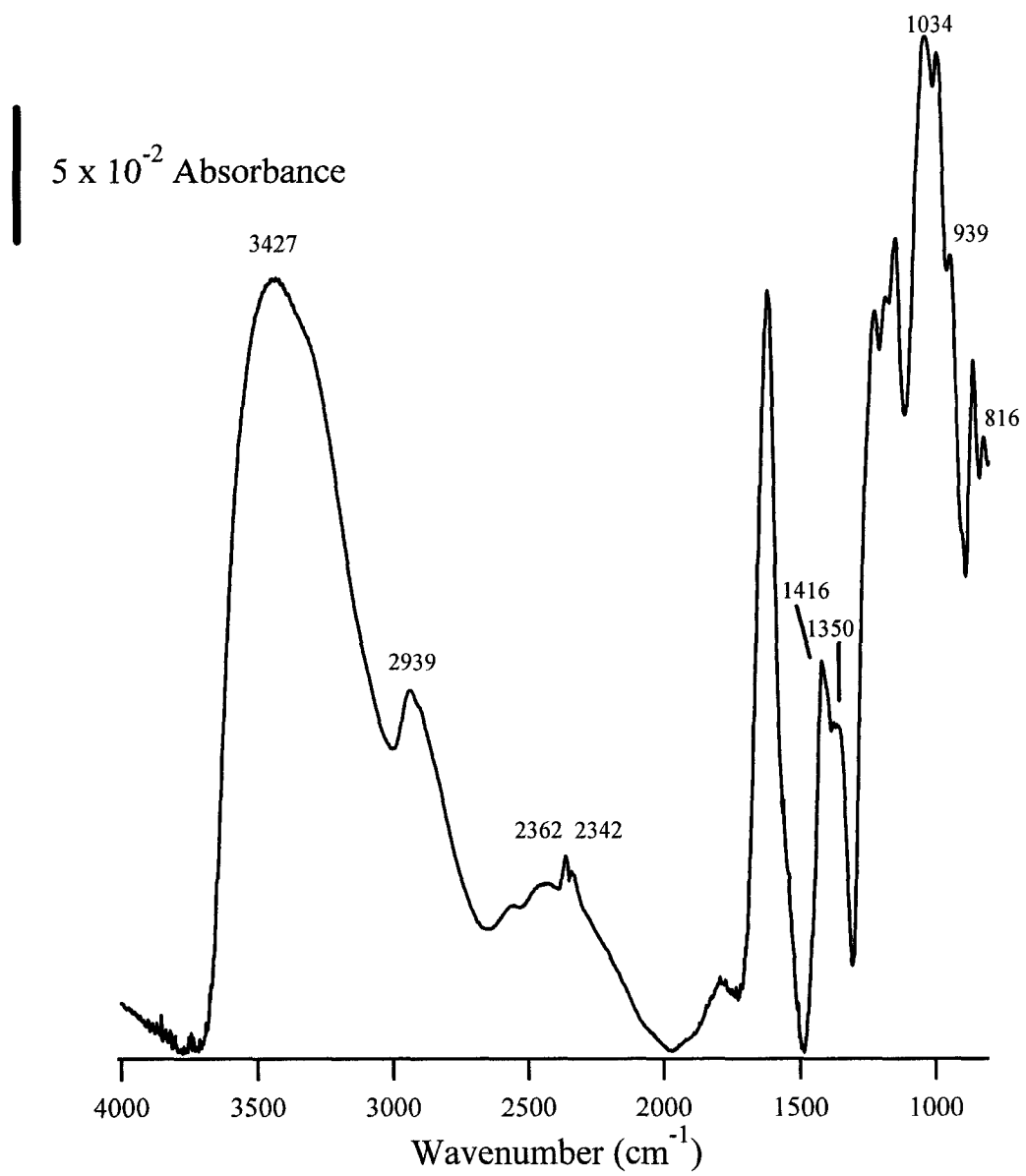


Figure 5.06. Infrared spectrum of powdered heparin.

Peak Position (cm^{-1})	Function group
3300	OH ν
2921	R-CH ₂ ν_a
2851	R-CH ₂ ν_s
1653	C=O amide 1
1539	CNH amide 2
1456	N-H bend
1381	Alkane C-H sym_def
1304	OH deformation
1259	C-O acid deformation
1194	C-O ν

Table 5.02. Infrared peak assignments for heparin bound to gold.

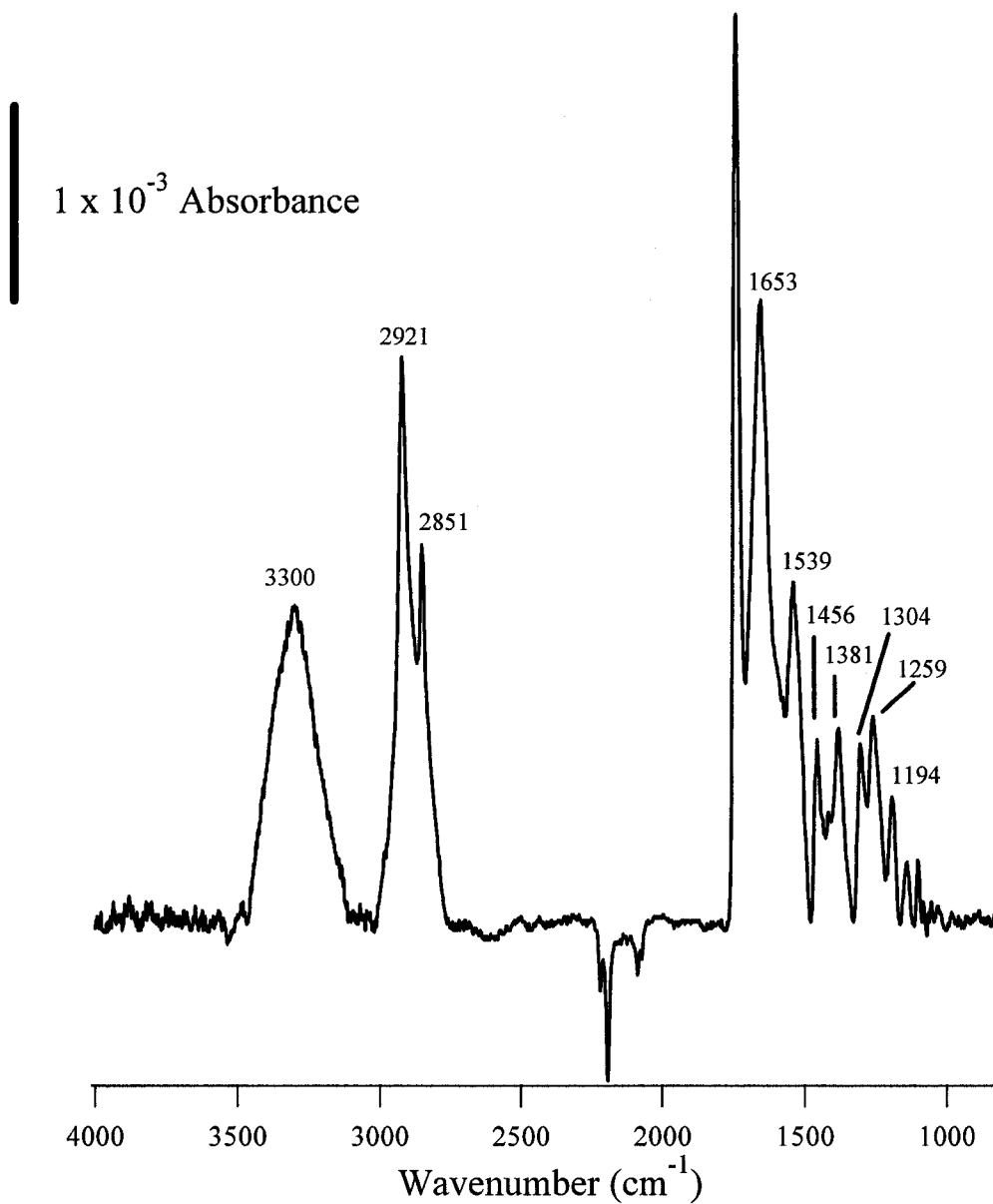


Figure 5.07. Infrared reflection absorption spectrum of heparin on gold. The negative face peaks are from the deuterated background.

Peak Position (cm^{-1})	Function group
3425	OH ν
3050	R-CH ₃ ν_a
2968	R-CH ₂ ν_a
2919	R-CH ₃ ν_s
2509	NH ν
1652	C=O amide 1
1603	NH ₂ ⁺ deformation
1523	CNH amide 2
1350	C-N ν

Table 5.03. Infrared peak assignments for heparin bound to glassy carbon

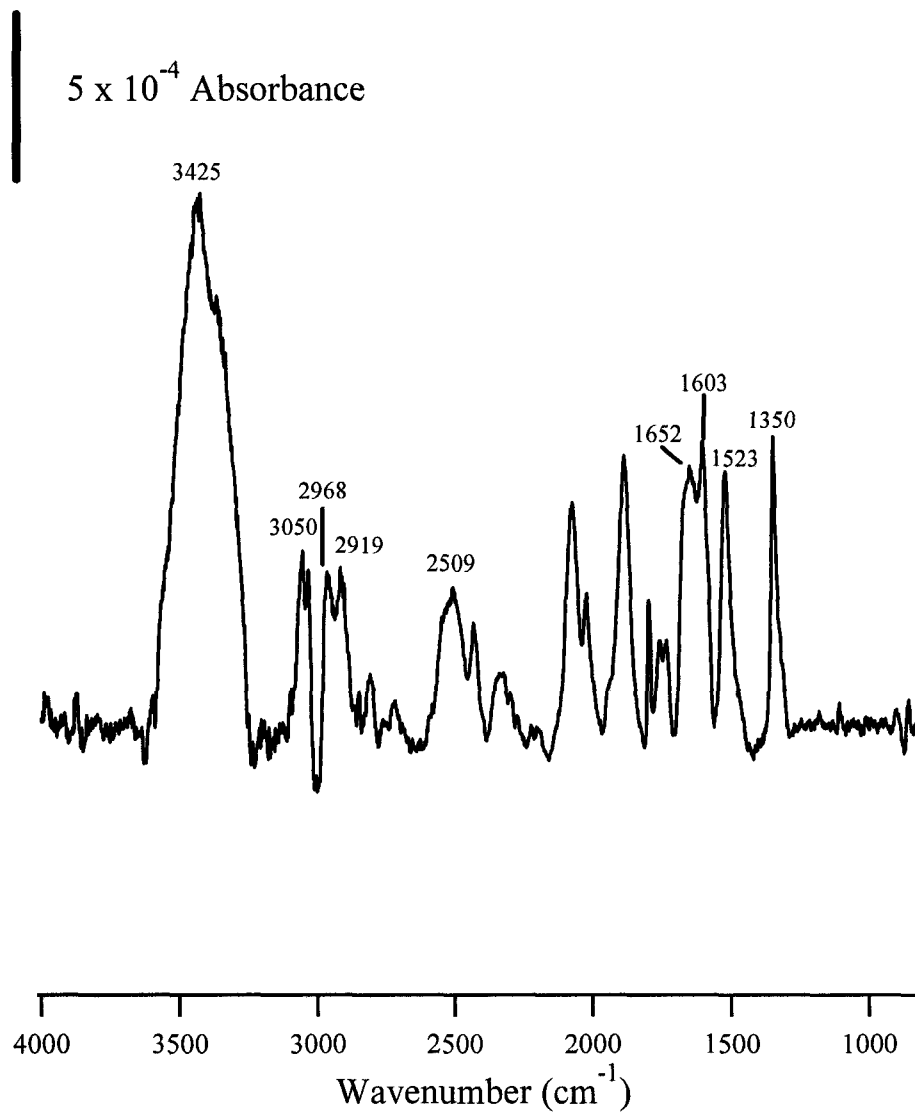


Figure 5.08. Infrared reflection absorption spectrum of heparin on glassy carbon.

3.2 Interaction of Surface Bound Heparin with Fibronectin

The infrared data presented above offers strong evidence for the successful covalent attachment of heparin to glassy carbon. For heparin modified carbon to be viable for prosthetic implants the bio activity of heparin needs to be uncompromised. In order to test the bioactivity of covalently immobilized heparin, a simple experiment was performed probing the interactions of fibronectin (Fn) with heparin. Fibronectin is a common glycoprotein found in blood plasma, extracellular matrices, and other bodily fluids. It is known to play an important role in various biological functions such as wound healing, immune response, and tumor metastasis. Fibronectin specifically binds heparin at three sites; Hep I, Hep II, and Hep III. Binding site Hep I is located near the amino terminus of Fn. Binding site Hep II is located at the opposite end, the carboxylic terminus, of Fn and is reported as having the highest affinity for heparin, upwards of 100-fold higher than that of Hep I. The final site, Hep III, is located closer to the center and is believed to play a significantly less prominent role in binding of Fn. Bovine serum albumin (BSA) was used to reduce non-specific adsorption of Fn. Bovine serum albumin is commonly used for such blocking; it readily forms a physisorbed monolayer on a variety of surfaces. The BSA monolayer reduces the non-specific adsorption of additional solution components, including other proteins.

Solutions of fluorescein isothiocyanate modified fibronectin (FITC-Fn) and BSA in PBS were incubated with the heparin modified surfaces. The surfaces studied were heparin modified via both methods previously described, surface amine

attachment and surface carboxylic acid and diamine linker methods. The incubated samples were removed from solution and rinsed with deionized water. Laser scanning confocal microscopy was used to determine the presence and relative distribution of FITC-Fn. Figure 5.09 shows the laser scanning confocal micrograph of FITC-Fn interaction with heparin immobilized on carboxylic acid terminated diazonium with a 1,6-hexane diamine linker. Figure 5.10 shows the laser scanning confocal micrograph of FITC-Fn interaction with heparin immobilized on amine terminated diazonium. For both images the lighter, red, areas indicate the presence of FITC-Fn. For both images a significantly larger amount of Fn is observed on the heparin modified area when compared to the unmodified carbon. The surface modified via carboxylic acid terminated diazonium and the 1,6-hexane diamine linker shows a greater contrast between the modified area compared to the non-modified area as well as a more even distribution of the Fn in the modified area when compared to the surface modified via the amine terminated diazonium. Both methods result in some Fn non-specifically adsorbed to the non-modified area indicating the BSA blocking was not 100% effective. The preferential attachment of Fn to the heparin modified area over the non-specific adsorption of BSA indicates that the immobilized heparin retained at least some of its bioactivity. The barrier line between the modified and unmodified area is due to residual FITC-Fn initially non-specifically adsorbed to the elastomeric o-ring used to define the modification area.

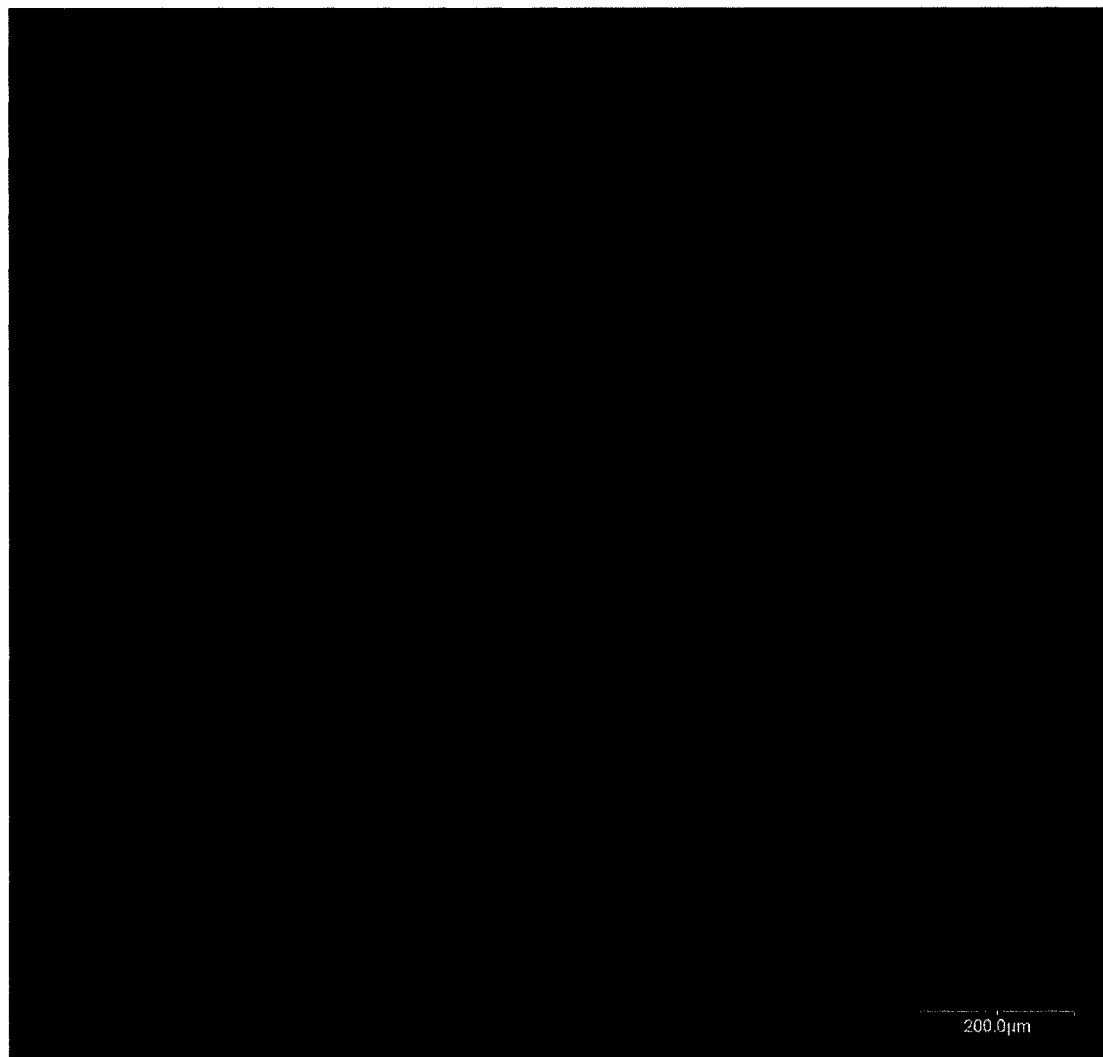


Figure 5.09. Laser Scanning Confocal Image of FITC labeled fibronectin and bovine serum albumin with heparin immobilized on carboxylic acid terminated diazonium with a 1,6-hexane diamine linker. The top right area, light red, is the heparin modified area.



Figure 5.10. Laser Scanning Confocal Image of FITC labeled fibronectin and bovine serum albumin with heparin immobilized on amine terminated diazonium. The top left area, light red, is the heparin modified area.

Similar to the method used to probe the interactions of heparin immobilized on glassy carbon with fibronectin, the same interactions were probed on a heparin modified gold surfaces. Due to the advantageous inherent traits of SPR as well as the fluorescence quenching of metallic gold, SPR was used to measure the interaction of fibronectin with heparin immobilized on gold. Figure 5.11 shows the SPR image and corresponding cross section of a gold sensor modified with heparin and the interaction with Fn and BSA. A polydimethylsiloxane (PDMS) microfluidic network was used to introduce the Fn and BSA onto the heparin modified gold SPR sensor. The sensor, with the patterned BSA and Fn, was placed in the SPR and PBS was used to rinse the surface. The SPR image was recorded under static PBS. As shown in figure 5.11 the interaction between heparin and Fn is about five times larger than the non-specific adsorption of BSA. This larger signal for Fn on heparin modified gold echoes the results observed for heparin modified carbon and indicates that gold immobilized heparin retains at least some of its bioactivity.

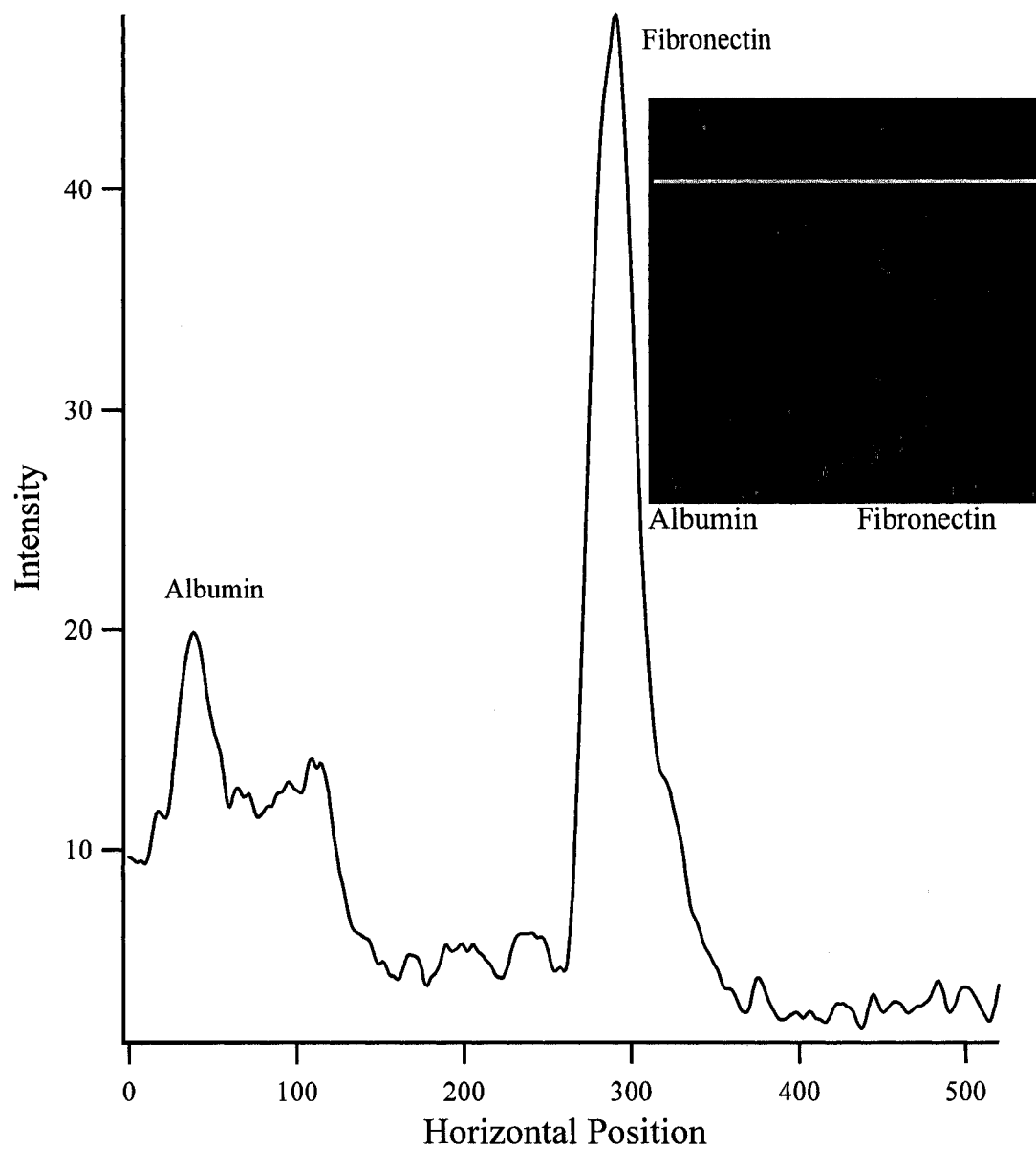


Figure 5.11. Surface plasmon resonance image, and corresponding cross section, of the interactions of bovine serum albumin and human fibronectin with a heparin modified gold SPR sensor.

4. Conclusions

Heparin has been successfully covalently attached to both glassy carbon and gold. Two methods were employed to perform the attachment to GC. The first method involved the reduction of a nitro terminated aryl diazonium and subsequent attachment to GC. The nitro groups were electrochemically reduced to amine and coupled to a carboxylic acid moiety of heparin via amide bond formation. The second method involved the electrochemical reduction of a carboxylic acid terminated diazonium and subsequent attachment to GC. A diamine linker was attached to the carboxylic acid group via amide bond formation. Heparin was attached to the second amine of the diamine linker via amide bond formation as well. Heparin was attached to gold via amide bond formation to a monolayer of amine terminated thiols. As shown by the preferential binding of Fn to heparin modified areas, it was shown that surface bound heparin retains some of its bioactivity.

The use of aryl diazoniums to modify the surface of carbon with heparin shows promising results and warrants further investigation.

References

- (1) Wang, X. H.; Zhang, F.; Li, C. R.; Zhgne, Z. H.; Wang, X.; Liu, X. H.; Chen, A. Q.; Jiang, Z. B. *Surface & Coatings Technology* **2000**, *128*, 36-42.
- (2) Feng, L.; Andrade, J. D. *Journal of Colloid and Interface Science* **1994**, *166*, 419-426.
- (3) Feng, L.; Andrade, J. D. *Journal of Biomedical Materials Research* **1994**, *28*, 735-743.
- (4) Feng, L.; Andrade, J. D. *Biomaterials* **1994**, *15*, 323-333.
- (5) Feng, L.; Andrade, J. D. *Journal of Biomaterials Science-Polymer Edition* **1995**, *7*, 439-452.
- (6) Feng, L.; Andrade, J. D. *Colloids and Surfaces B-Biointerfaces* **1996**, *6*, 149-149.
- (7) Du, Y. J.; Brash, J. L.; McClung, G.; Berry, L. R.; Klement, P.; Chan, A. K. C. *Journal of Biomedical Materials Research Part A* **2007**, *80A*, 216-225.
- (8) Olson, S. T.; Bjork, I. *Seminars in Thrombosis and Hemostasis* **1994**, *20*, 373-409.
- (9) Tanaka, K. A.; Levy, J. H. *Hematology-Oncology Clinics of North America* **2007**, *21*, 33-50.
- (10) Zhang, F. M.; Fath, M.; Marks, R.; Linhardt, R. J. *Analytical Biochemistry* **2002**, *304*, 271-273.
- (11) Marks, R. M.; Lu, H.; Sundaresan, R.; Toida, T.; Suzuki, A.; Imanari, T.; Hernaiz, M. J.; Linhardt, R. J. *Journal of Medicinal Chemistry* **2001**, *44*, 2178-2187.

- (12) Delamar, M.; Hitmi, R.; Pinson, J.; Saveant, J. M. *Journal of the American Chemical Society* **1992**, *114*, 5883-5884.
- (13) Kariuki, J. K.; McDermott, M. T. *Langmuir* **1999**, *15*, 6534-6540.
- (14) Kariuki, J. K.; McDermott, M. T. *Langmuir* **2001**, *17*, 5947-5951.
- (15) Adenier, A.; Cabet-Deliry, E.; Chausse, A.; Griveau, S.; Mercier, F.; Pinson, J.; Vautrin-UI, C. *Chemistry of Materials* **2005**, *17*, 491-501.
- (16) Adenier, A.; Barre, N.; Cabet-Deliry, E.; Chausse, A.; Griveau, S.; Mercier, F.; Pinson, J.; Vautrin-UI, C. *Surface Science* **2006**, *600*, 4801-4812.
- (17) Allongue, P.; Delamar, M.; Desbat, B.; Fagebaume, O.; Hitmi, R.; Pinson, J.; Saveant, J. M. *Journal of the American Chemical Society* **1997**, *119*, 201-207.
- (18) Baranton, S.; Bélanger, D. *Journal of Physical Chemistry B* **2005**, *109*, 24401-24410.
- (19) Brooksby, P. A.; Downard, A. J. *Langmuir* **2004**, *20*, 5038-5045.
- (20) Downard, A. J. *Langmuir* **2000**, *16*, 9680-9682.
- (21) Downard, A. J. *Electroanalysis* **2000**, *12*, 1085-1096.
- (22) Delamar, M.; Desarmot, G.; Fagebaume, O.; Hitmi, R.; Pinson, J.; Savéant, J. M. *Carbon* **1997**, *35*, 801-807.
- (23) Koryta, J.; Dvorak, J.; Kavan, L. *Principles of Electrochemistry*, Second Edition ed.; Wiley, 1993.
- (24) Nakajima, N.; Ikada, Y. *Bioconjugate Chemistry* **1995**, *6*, 123-130.
- (25) Porter, M. D.; Bright, T. B.; Allara, D. L.; Chidsey, C. E. D. *Journal of the American Chemical Society* **1987**, *109*, 3559-3568.

Chapter VI

Conclusions

1. Overall Conclusions

As discussed previously, the area of surface modification is a rich and varied field. The interest in modification of an interface is as strong as ever and shows no signs of changing in the immediate future. The aim of this thesis was three fold; to evaluate electron beam evaporated carbon films as a platform for testing the molecular electronic viability of aryl diazonium created films; to investigate the performance of the often overlooked platinum counter electrode in diazonium reduction; and finally to offer an alternative modification scheme for the introduction of biomolecules such as heparin to a surface.

The most thorough and accurate characterizations of electron beam evaporated carbon films to date has been presented. The films studied here were on the order of 50 nm thick and proved to be extremely flat with RMS roughness of less than 1 nm. The fabricated films behave extremely well as electrodes and are easily modified with standard aryl diazonium modification procedures. Under the right conditions the studied molecules could behave as rudimentary components such as a rectifier or resistor in electronic components. The use of conducting atomic force microscopy as an important tool in the emerging field of molecular electronics was demonstrated. The C-AFM is potentially an extremely powerful tool for such applications, but the unfavorable aspects were also highlighted. The C-AFM is extremely vulnerable to tip fouling and the measured current is highly dependent on applied force as demonstrated. In an effort to

aid future research of diazonium modified electron beam evaporated carbon films, a technique was developed to accurately determine molecular film thicknesses.

With the surfeit of research of aryl diazonium modification of many surfaces, platinum was investigated. Aryl diazoniums were shown to readily reduce in the presence of a platinum surface and the resulting films were stable and robust. Electrochemically created films also showed interesting kinetic behaviour that warrants further investigation. Self assembly of diazonium derived layers were weakly bound and easily displaced by thiol containing molecules. It was also demonstrated that spontaneous adsorption was not an issue on the timeframe of a typical electrochemical experiment. Fouling of the platinum counter electrode was minimal.

Finally, the well characterized diazonium derived modification of carbon was exploited to obtain two novel methods to introduce heparin to the surface of carbon. The same method, used on gold, indicated that the attached heparin retained some bioactivity. These new methods are a promising step forward in terms of modification of implant materials. With current wet chemistry techniques and the recent successful modification of various surfaces other than carbon, it is certain that this method can be extended to include many implant materials and desirable biomolecules interfaces.

2. Future Work

The C-AFM results presented are promising. The next logical step for this research is to couple it with current research by McDermott and Du involving the fabrication of nanoscale carbon devices. These devices are created from electronbeam lithography followed by pyrolyzation of the electronbeam resist. Currently structures can

be fabricated with dimensions less than 20 nm. It is feasible to create a device with a gap between electrode materials on the order of 1-2 nm. Ideally the gap would be tailored to the size of the molecule of interest. If one can attach an aryl diazonium between the two electrodes, it would provide a stable platform to test electronic properties without the added complication of applied load force. Figure 6.01 is a scanning electron microscope (SEM) micrograph of such a fabricated gap. Currently the gap, at 61 nm, is much too large to investigate small molecules as discussed in this thesis. The fabrication process would need to be refined and possibly coupled with carbon etching techniques developed in the McDermott lab in order to obtain the desired well-defined 1-2 nm gap. Electron beam lithography is a very slow technique; each individual feature must be designed sequentially. When compared to the massively parallel method of photolithography it is both extremely slow and expensive. The final step in this line of research would be the development of standard photolithography techniques coupled with carbon etching to create arrays of carbon based nanowires containing well-defined single molecule sized gaps. This would allow one to have an array of individually addressable molecules.

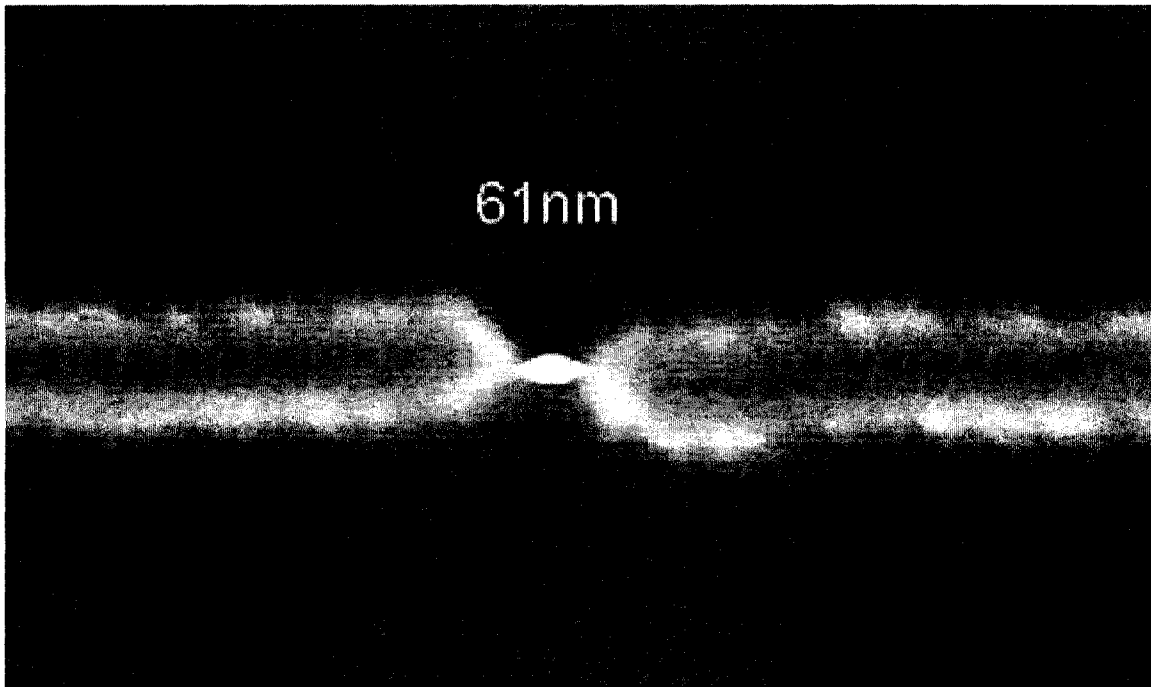


Figure 6.01. Nanogap fabricated from pyrolyzed electron beam lithography.

Chapter VII

Appendix

	1 Hz	3 Hz	5 Hz	10 Hz
Low Feedback	0.317 ± 0.080	0.383 ± 0.172	N/A	6.13 ± 7.84
Normal Feedback	0.279 ± 0.083	0.496 ± 0.108	0.420 ± 0.066	7.45 ± 7.47

Table 7.01 Noise of RMS roughness measurements of Nanoman Atomic Force Microscope, reported values are nanometers.

	1 Hz	3 Hz	5 Hz	10 Hz
Low Feedback	0.070 ± 0.029	0.073 ± 0.004	0.054 ± 0.003	0.060 ± 0.007
Normal Feedback	0.065 ± 0.012	0.059 ± 0.003	0.056 ± 0.003	0.063 ± 0.008

Table 7.02 Noise of RMS roughness measurements of Multimode Atomic Force Microscope, “E” scanner, reported values are nanometers.

Veeco brand atomic force microscope noise measurements were performed by measuring one square nanometer under normal operating conditions. Due to the extremely small scan size, the tip was effectively still. The measurements were performed at typical feedback gains used for data collection as well as in a low

feedback mode, where the gain was one half the typical working feedback. The resulting image was measured for surface roughness. The resulting surface RMS is the reported noise. Additionally, full noise spectra were also measured to help reduce environmental noise and are presented in figures 7.01 and 7.02.

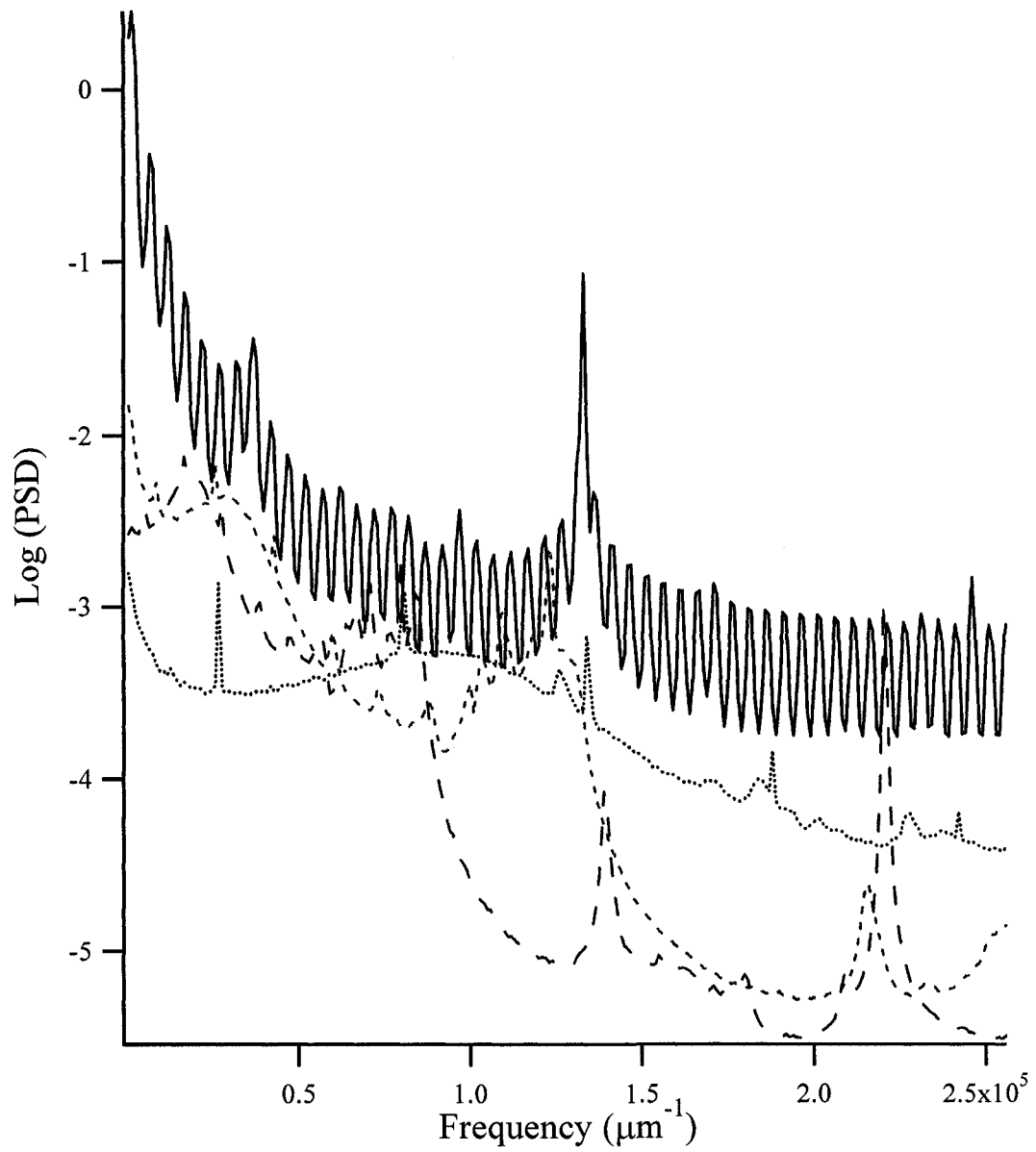


Figure 7.01 Power spectrum density of Nanoman noise at normal feedback. Solid trace at 10 Hz, long dash at 5 Hz, short dash at 3 Hz, dotted at 1 Hz.

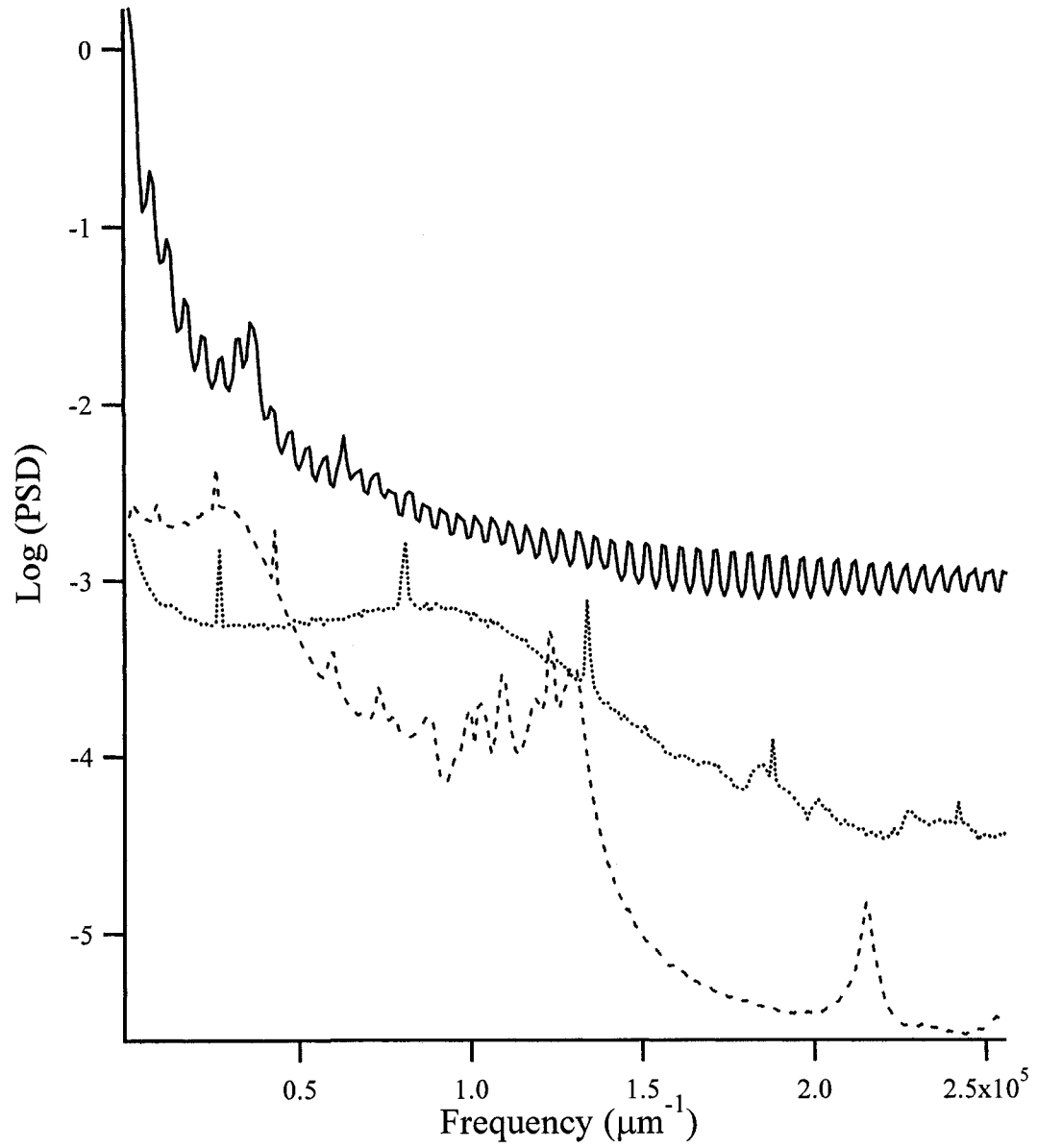


Figure 7.02 Power spectrum density of Nanoman noise at low feedback. Solid trace at 10 Hz, short dash at 3 Hz, dotted at 1 Hz.

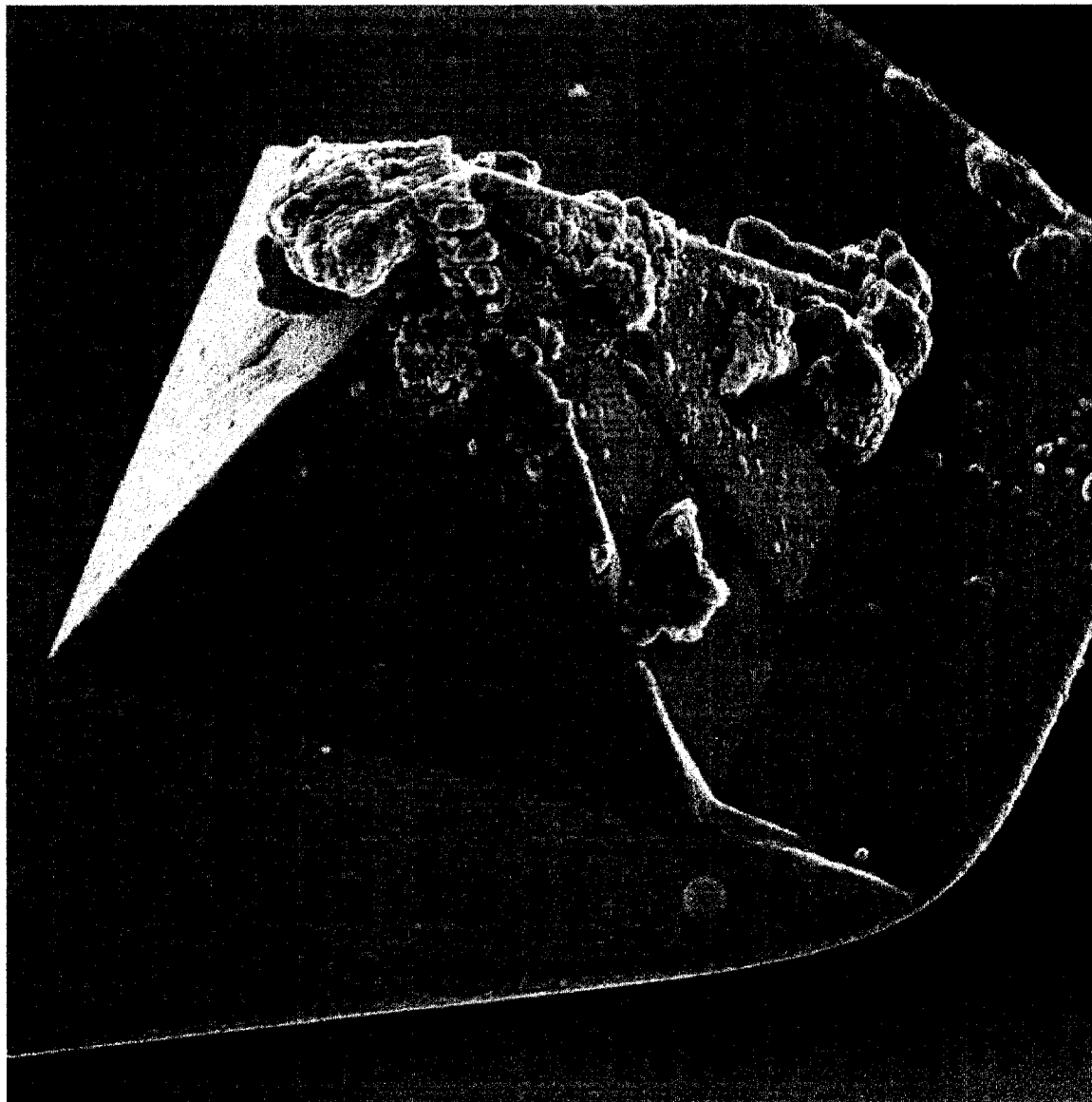


Figure 7.03 Scanning electron micrograph of a typical DNP atomic force microscope probe coated in-house with 30 nm chromium followed by 300 nm of gold. The above tip is a poor deposition present in a batch of good depositions. The image is 6.966 x 6.966 μm .

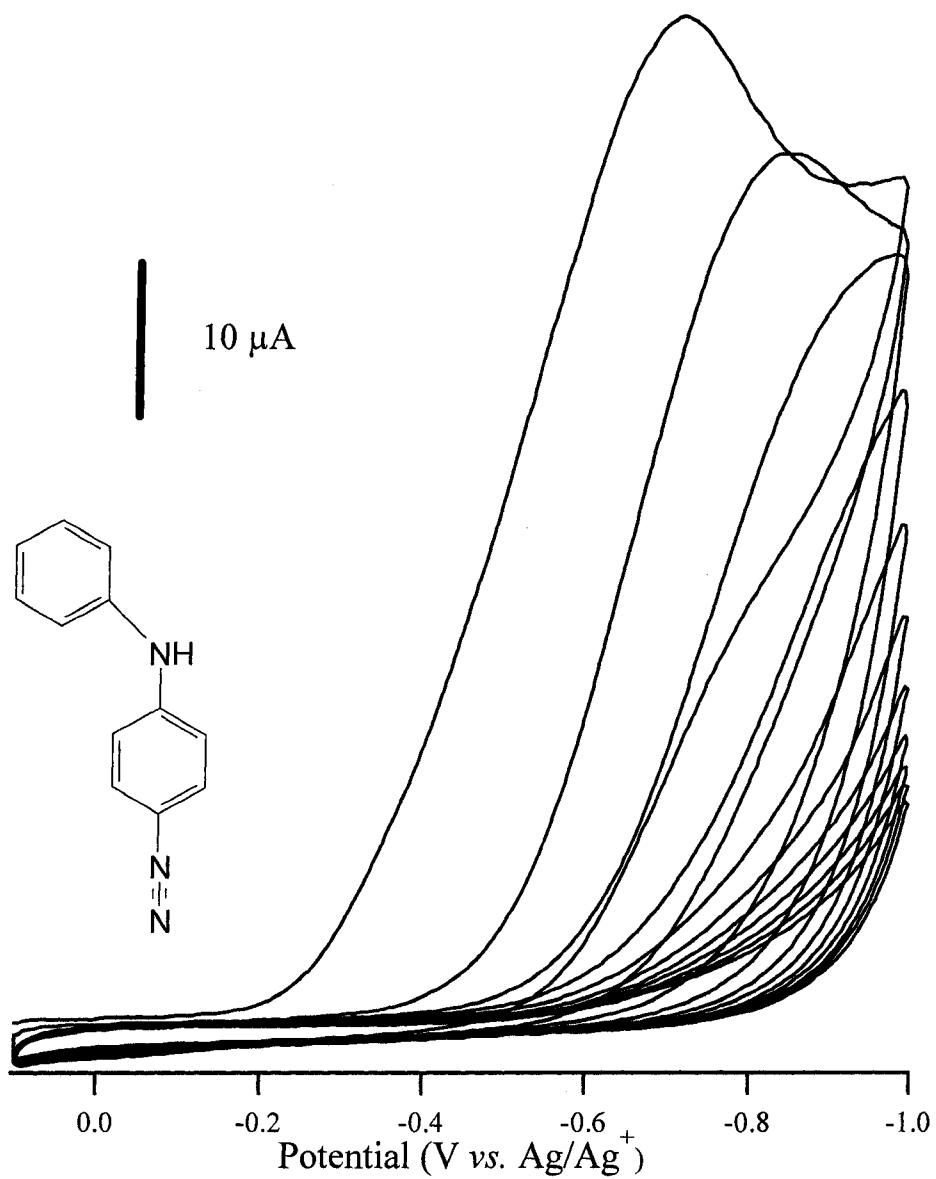


Figure 7.04 Cyclic voltammograms for electrochemical attachment of variamine blue RT to EB50; this is an example of a poorly behaved diazonium reduction and deposition. The large current after the initial scan indicates poor coverage.

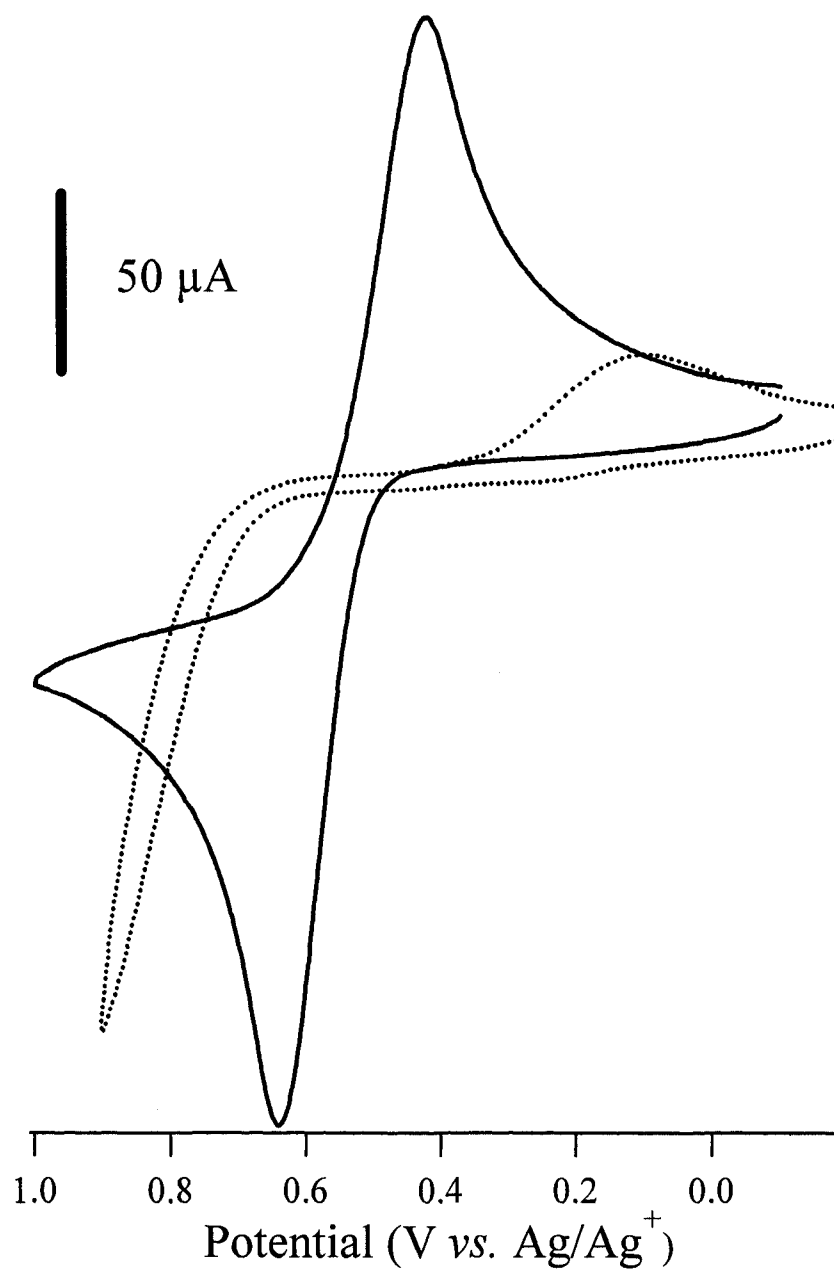


Figure 7.05 Cyclic voltammograms for the blocking of dopamine by Variamine Blue RT on EB50. Although the peaks are considerably shifted, outside of the scan window, the dopamine is still quite reactive, indicating poor coverage of variamine blue RT.

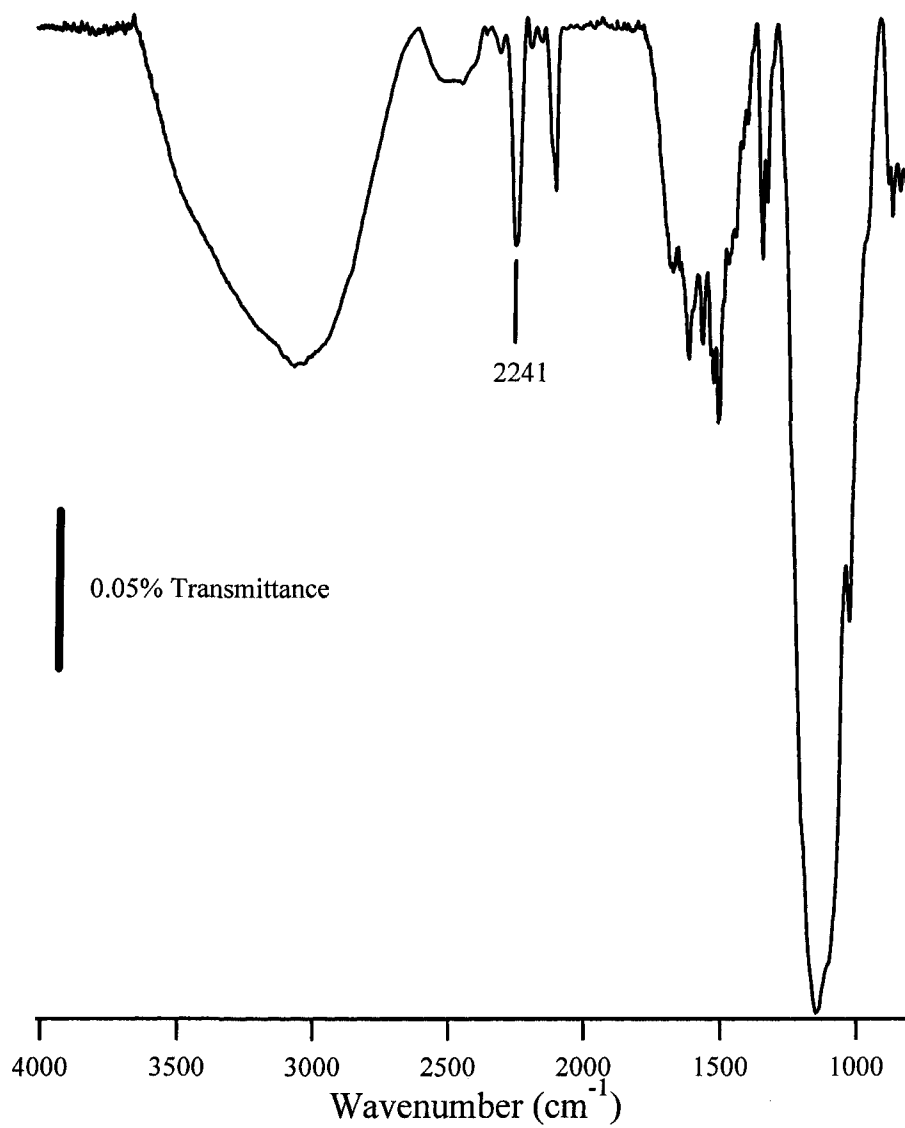


Figure 7.06. Infrared spectrum of powdered fast black K. Diazonium peak, 2241, identified.

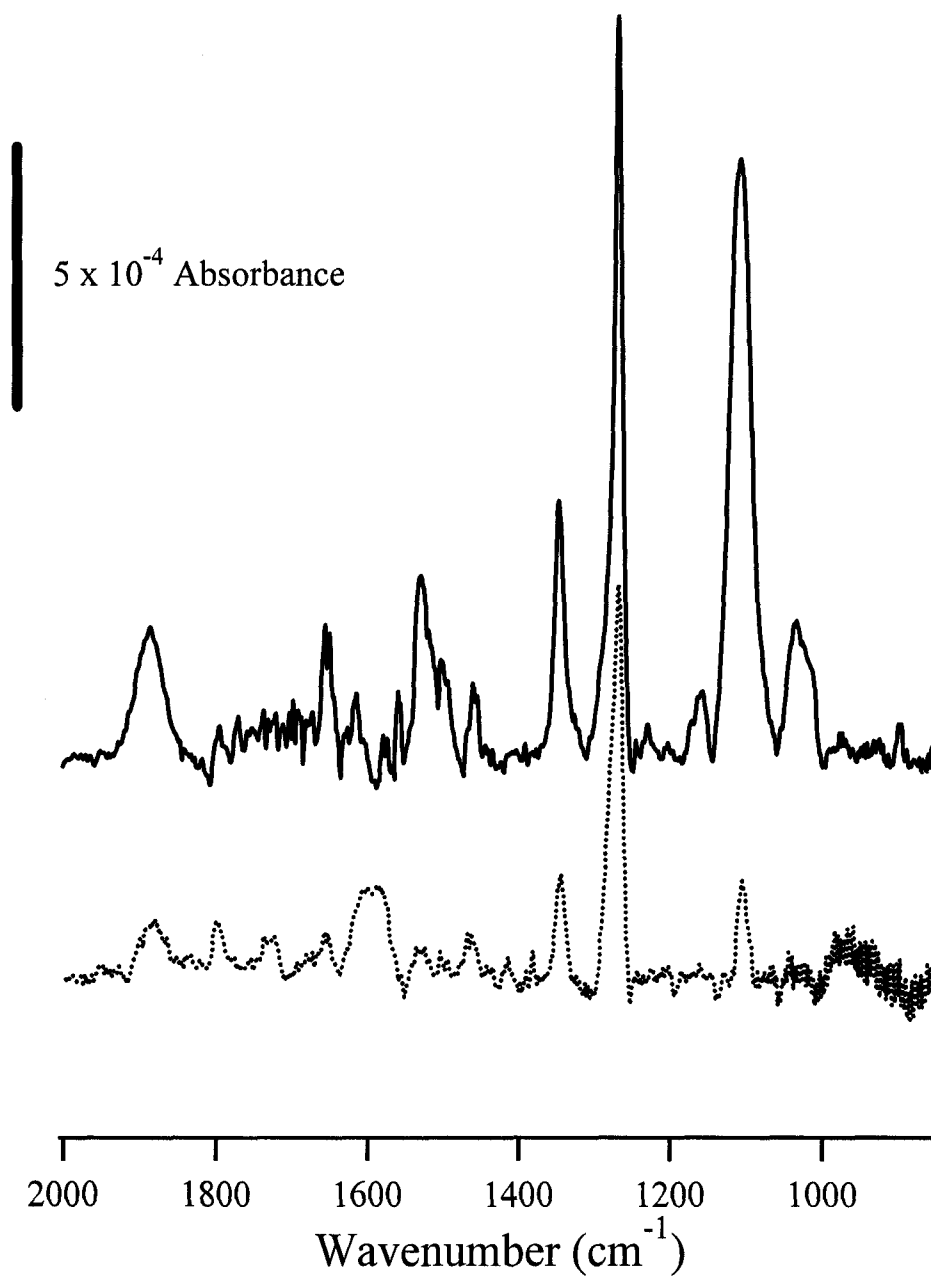


Figure 7.07. Infrared spectrum of fast black K displaced by 1-dodecane thiol. Solid – initial IR. Dotted – after displacement

Conductive AFM IV curve analyzer

The following macro was used within an Excel spread sheet to quickly import, convert and display massive amounts of current-voltage curves. The curves were required to be in text based format with sequential numbers as the file names.

Sub cafmadvanced()

' cafmadvanced Macro

' Macro recorded 24/03/2004 by Aaron W. Skelhorne

' Tested with NanoScope V6.11

' Read in the user input defined variables through a series of dialog boxes

```
Sheets("Notes").Activate  
  
v = Application.InputBox("Please enter the starting directory" & Chr(13) &  
Chr(13) & "You must include the final backslash" & Chr(13) & "i.e.  
e:\data\04_03_26\", "File Directory", "e:\cafmcures\  
  
If v = False Then  
  
End  
  
End If
```



```
x = Application.InputBox("Please enter the number of curves to import" & Chr(13)
& Chr(13) & "Total number of curves is limited to 85", "Number of Curves to
Import", "12")
```

```
' Stops program if total number of curves > 85
```

```
If x >= 86 Then
    Sheets("Data confirmation").Cells(2, 2).Value = "Error"
    Sheets("Data confirmation").Activate
    Range("B2").Select
End
End If
```

```
If x = False Then
    End
End If
```

```
y = Application.InputBox("Please enter the number of points per curves" &
Chr(13) & Chr(13) & "Total number of points per curves is limited to 32 000", "Data
Points", "1024")
```

```
If y >= 32000 Then
    Sheets("Data confirmation").Cells(4, 2).Value = "Error"
    Sheets("Data confirmation").Activate
```

```
Range("B4").Select
```

```
End
```

```
End If
```

```
If y = False Then
```

```
End
```

```
End If
```

```
z = Application.InputBox("Please enter the scan offset value", "3D Scan Offset",  
"200")
```

```
If z = False Then
```

```
End
```

```
End If
```

```
w = Application.InputBox("Please enter the sensitivity (nA/V)" & Chr(13) &  
Chr(13) & "Valid NanoScope software values are 1 and 100 nA/V", "NanoScope  
Current Sensitivity", "100")
```

```
If w = False Then
```

```
End
```

```
End If
```

```
u = Application.InputBox("Please enter the first curve name (no extension  
required)", "Input File Starting Value", "1")
```

If u = False Then

End

End If

'Clear the Data Input and Data Sheets before starting

Sheets("Data confirmation").Activate

Columns("B:IV").Select

Selection.ClearContents

Sheets("Data").Activate

Columns("A:IV").Select

Selection.ClearContents

Sheets("Modified Data").Activate

Columns("A:IV").Select

Selection.ClearContents

' Confirmation of defined variables

Sheets("Data confirmation").Activate

Range("A2").Select

ActiveCell.Value = x

Range("A5").Select

ActiveCell.Value = y

Range("A8").Select

```
ActiveCell.Value = z
```

```
Range("A11").Select
```

```
ActiveCell.Value = w
```

```
Range("A14").Select
```

```
ActiveCell.Value = v
```

```
Range("A17").Select
```

```
ActiveCell.Value = u
```

```
x1 = Range("A2").Value
```

```
x2 = Range("A2").Value
```

```
x9 = Range("A2").Value
```

```
y1 = Range("A5").Value
```

' Open data selection

```
For l = u To x2 + u - 1
```

```
Workbooks.OpenText Filename:=v & l & ".txt", Origin:=xlWindows, _
```

```
StartRow:=2, DataType:=xlFixedWidth, FieldInfo:=Array(Array(0, 1),
```

```
Array(20, 1))
```

```
Columns("A").Select
```

```
Selection.Cut
```

```
Windows("caf-m-advanced-macro.xls").Activate
```

```
Sheets("Data").Activate
```

```
Sheets("Data").Columns(3 * (1 - u) + 1).Select
```

```
Sheets("Data").Paste
```

```
Windows(1 & ".txt").Activate
```

```
Columns("B").Select
```

```
Selection.Cut
```

```
Windows("caf-m-advanced-macro.xls").Activate
```

```
Sheets("Data").Columns(3 * (1 - u) + 2).Select
```

```
Sheets("Data").Paste
```

```
Sheets("Data").Cells(1, 3 * (1 - u) + 3).Value = ("Scan-" & 1)
```

```
Sheets("Data").Cells(1, 3 * (1 - u) + 2).Value = ("I-" & 1 & " (nA)")
```

```
Sheets("Data").Cells(1, 3 * (1 - u) + 1).Value = ("mV-" & 1)
```

```
Windows(1 & ".txt").Activate
```

```
ActiveWindow.WindowState = xlNormal
```

```
ActiveWindow.Close SaveChanges:=False
```

```
Next 1
```

```
For j = 1 To x
```

```
    For i = 1 To y
```

```
Sheets("Data").Cells(i + 1, 3 * j).Value = z * j + i - z
```

```
Next i
```

```
Next j
```

```
For k = 1 To x1
```

```
Next k
```

' Sensitivity adjustment

```
For p = 1 To x9
```

```
For q = 1 To y1
```

```
Sheets("Data").Cells(q + 1, 3 * p - 1).Value = Sheets("Data").Cells(q + 1, 3 * p -
```

```
1) * w
```

```
Next q
```

```
Next p
```

' Copy Data to Modified Data Sheet

```
Sheets("Data").Activate
```

```
Columns("A:IV").Copy
```

```
Sheets("Modified Data").Activate
```

```
Range("A1").Select
```

```
ActiveSheet.Paste
```

```
Range("A1").Select
```

```
' Home "Data Input" sheet
```

```
Windows("caf-m-advanced-macro.xls").Activate
```

```
Sheets("C-AFM Curves").Activate
```

```
Range("A1").Select
```

```
ActiveWindow.WindowState = xlMaximized
```

```
' Gives warning if sensitivity <> 1 OR 100
```

```
Sheets("Data confirmation").Cells(1, 2).Value = "Messages"
```

```
If w <> 1 Then
```

```
    If w <> 100 Then
```

```
        Sheets("Data confirmation").Cells(3, 2).Value = "Warning"
```

```
        Sheets("Data confirmation").Activate
```

```
        Range("B3").Select
```

```
        ActiveWindow.WindowState = xlMaximized
```

```
    End If
```

```
End If
```

End Sub

Conductive AFM IV averaging macro

Similar to the above analyzer, this macro was used within an Excel spread sheet to import and average a large number of current-voltage curves.

```
Sub cafmaverage()
```

```
'
```

```
' cafmaverage Macro
```

```
' Macro recorded 24/03/2004 by Aaron W. Skelhorne
```

```
'
```

' Read in the user input defined variables through a series of dialog boxes

```
Sheets("Notes").Activate
```

```
v = Application.InputBox("Please enter the starting directory" & Chr(13) &
```

```
Chr(13) & "You must include the final backslash" & Chr(13) & "i.e.
```

```
e:\data\04_03_26\", "File Directory", "e:\cafmcures\")
```

```
If v = False Then
```

```
End
```

```
End If
```

```
x = Application.InputBox("Please enter the number of curves to import" & Chr(13)
```

```
& Chr(13) & "Total number of curves is limited to 256", "Number of Curves to
```

```
Import", "12")
```

' Stops program if total number of curves > 256

If x >= 257 Then

Sheets("Data confirmation").Cells(2, 2).Value = "Error"

Sheets("Data confirmation").Activate

Range("B2").Select

End

End If

If x = False Then

End

End If

y = Application.InputBox("Please enter the number of points per curves" &
Chr(13) & Chr(13) & "Total number of points per curves is limited to 32 000", "Data
Points", "1024")

If y >= 32000 Then

Sheets("Data confirmation").Cells(4, 2).Value = "Error"

Sheets("Data confirmation").Activate

Range("B4").Select

End

End If

If y = False Then

End

End If

w = Application.InputBox("Please enter the sensitivity (nA/V)" & Chr(13) &
Chr(13) & "Valid NanoScope software values are 1 and 100 nA/V", "NanoScope
Current Sensitivity", "100")

If w = False Then

End

End If

u = Application.InputBox("Please enter the first curve name (no extension
required)", "Input File Starting Value", "101")

If u = False Then

End

End If

'Clear the Data Input and Data Sheets before starting

Sheets("Data confirmation").Activate

Columns("B:IV").Select

Selection.ClearContents

Sheets("Extend").Activate

Columns("A:IV").Select

Selection.ClearContents

Sheets("Retract").Activate

Columns("A:IV").Select

Selection.ClearContents

' Confirmation of defined variables

Sheets("Data confirmation").Activate

Range("A2").Select

ActiveCell.Value = x

Range("A5").Select

ActiveCell.Value = y

Range("A11").Select

ActiveCell.Value = w

Range("A14").Select

ActiveCell.Value = v

Range("A17").Select

ActiveCell.Value = u

x1 = Range("A2").Value

x2 = Range("A2").Value

```
x9 = Range("A2").Value
```

```
y1 = Range("A5").Value
```

' Open data selection

```
' Import potential
```

```
Workbooks.OpenText Filename:=v & u & ".txt", Origin:=xlWindows, _  
StartRow:=2, DataType:=xlFixedWidth, FieldInfo:=Array(Array(0, _  
1), Array(20, 1), Array(40, 1))
```

```
Columns("A").Select
```

```
Selection.Cut
```

```
Windows("caf-m-average-macro.xls").Activate
```

```
Sheets("Average").Activate
```

```
Sheets("Average").Columns(1).Select
```

```
Sheets("Average").Paste
```

```
Windows(u & ".txt").Activate
```

```
ActiveWindow.WindowState = xlNormal
```

```
ActiveWindow.Close SaveChanges:=False
```

```
Windows("caf-m-average-macro.xls").Activate
```

```
Sheets("Average").Cells(1, 1).Value = "Potential"
```

' Import current

```
For l = u To x2 + u - 1
```

```
Workbooks.OpenText Filename:=v & l & ".txt", Origin:=xlWindows, _  
StartRow:=3, DataType:=xlFixedWidth, FieldInfo:=Array(Array(0, _  
1), Array(20, 1), Array(40, 1))
```

```
Columns("B").Select
```

```
Selection.Cut
```

```
Windows("caf-m-average-macro.xls").Activate
```

```
Sheets("Extend").Activate
```

```
Sheets("Extend").Columns(1 - u + 1).Select
```

```
Sheets("Extend").Paste
```

```
Windows(l & ".txt").Activate
```

```
Columns("C").Select
```

```
Selection.Cut
```

```
Windows("caf-m-average-macro.xls").Activate
```

```
Sheets("Retract").Activate
```

```
Sheets("Retract").Columns(1 - u + 1).Select
```

```
Sheets("Retract").Paste
```

```
Windows(1 & ".txt").Activate
```

```
ActiveWindow.WindowState = xlNormal
```

```
ActiveWindow.Close SaveChanges:=False
```

```
Next l
```

' Sensitivity adjustment

```
For p = 1 To x9
```

```
For q = 1 To y1
```

```
Sheets("Extend").Cells(q, p).Value = Sheets("Extend").Cells(q, p) * w
```

```
Sheets("Retract").Cells(q, p).Value = Sheets("Retract").Cells(q, p) * w
```

```
Next q
```

```
Next p
```

' Home "Data Input" sheet

```
Windows("caf-m-average-macro.xls").Activate
```

```
Sheets("Extend").Activate
```

```
Range("A1").Select
```

```
ActiveWindow.WindowState = xlMaximized
```

' Gives warning if sensitivity <> 1 OR 100

```
Sheets("Data confirmation").Cells(1, 2).Value = "Messages"
```

```
If w <> 1 Then
```

```
    If w <> 100 Then
```

```
        Sheets("Data confirmation").Cells(3, 2).Value = "Warning"
```

```
        Sheets("Data confirmation").Activate
```

```
        Range("B3").Select
```

```
        ActiveWindow.WindowState = xlMaximized
```

```
    End If
```

```
End If
```

```
End Sub
```